LEABHARLANN CHOLÁISTE NA TRÍONÓIDE, BAILE ÁTHA CLIATH | TRINITY COLLEGE LIBRARY DUBLIN
Ollscoil Átha Cliath | The University of Dublin

Terms and Conditions of Use of Digitised Theses from Trinity College Library Dublin

Copyright statement

All material supplied by Trinity College Library is protected by copyright (under the Copyright and Related Rights Act, 2000 as amended) and other relevant Intellectual Property Rights. By accessing and using a Digitised Thesis from Trinity College Library you acknowledge that all Intellectual Property Rights in any Works supplied are the sole and exclusive property of the copyright and/or other IPR holder. Specific copyright holders may not be explicitly identified. Use of materials from other sources within a thesis should not be construed as a claim over them.

A non-exclusive, non-transferable licence is hereby granted to those using or reproducing, in whole or in part, the material for valid purposes, providing the copyright owners are acknowledged using the normal conventions. Where specific permission to use material is required, this is identified and such permission must be sought from the copyright holder or agency cited.

Liability statement

By using a Digitised Thesis, I accept that Trinity College Dublin bears no legal responsibility for the accuracy, legality or comprehensiveness of materials contained within the thesis, and that Trinity College Dublin accepts no liability for indirect, consequential, or incidental, damages or losses arising from use of the thesis for whatever reason. Information located in a thesis may be subject to specific use constraints, details of which may not be explicitly described. It is the responsibility of potential and actual users to be aware of such constraints and to abide by them. By making use of material from a digitised thesis, you accept these copyright and disclaimer provisions. Where it is brought to the attention of Trinity College Library that there may be a breach of copyright or other restraint, it is the policy to withdraw or take down access to a thesis while the issue is being resolved.

Access Agreement

By using a Digitised Thesis from Trinity College Library you are bound by the following Terms & Conditions. Please read them carefully.

I have read and I understand the following statement: All material supplied via a Digitised Thesis from Trinity College Library is protected by copyright and other intellectual property rights, and duplication or sale of all or part of any of a thesis is not permitted, except that material may be duplicated by you for your research use or for educational purposes in electronic or print form providing the copyright owners are acknowledged using the normal conventions. You must obtain permission for any other use. Electronic or print copies may not be offered, whether for sale or otherwise to anyone. This copy has been supplied on the understanding that it is copyright material and that no quotation from the thesis may be published without proper acknowledgement.

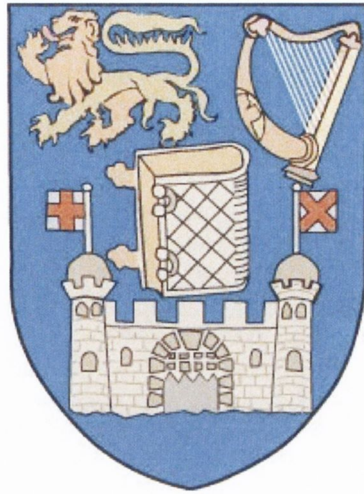

Ab-initio study of the electronic and vibrational properties on low-dimensional nanostructures made of layered transition metal di-chalcogenides

by

Kapildeb Dolui

A thesis submitted for the degree of

Doctor of Philosophy

School of Physics

Trinity College Dublin

July 15, 2013

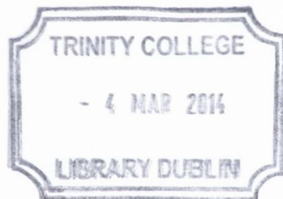

Thesis 10196

Declaration

I, Kapildeb Dolui, hereby declare that this thesis has not been submitted as an exercise for a degree at this or any other University.

It comprises work performed entirely by myself during the course of my Ph.D. studies at Trinity College Dublin. I was involved in a number of collaborations, and where it is appropriate my collaborators are acknowledged for their contributions.

I agree that the Library may lend or copy this thesis upon request.

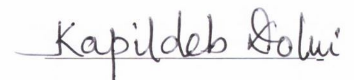

Kapildeb Dolui

The mathematical framework of quantum theory has passed countless successful tests and is now universally accepted as a consistent and accurate description of all atomic phenomena.

———————————

Erwin Schrödinger

Abstract

The controlled modulation of the electronic and phonon properties of low dimensional materials via external perturbations such as electric fields, doping, and strain, do represent an important step in the development of the next generation of nano-electronic devices. While Graphene and carbon nanotubes have thus far dominated the research into low-dimensional nono-electronics, layered di-chalcogenide materials have late attracted considerable attention as well.

Density functional theory (DFT) and density functional perturbation theory (DFPT) have emerged as state-of the art methods for computing the ground state of the many-body systems, and its vibrational properties, respectively. Here, electronic and phonon's structures are determined using *ab-intio*-DFT/DFPT codes. More advanced electronic-structure method, namely the Green's function quasi-particle approach, are employed in addition to the DFT framework.

First, we perform a systematic study of the dependence of the electronic and magnetic properties in a MoS_2 monolayer on the anion (S), cation (Mo) substitution, considering different non-metals, transition metals and halogens dopants. Most dopants appear as deep-donors with in the band gap, however for some dopants we find n-type and also p-type character. Adsorption of alkali metals shifts the Fermi energy into the MoS_2 conduction band, making the system n-type as well. Moreover, the adsorption of charged molecules is considered, which occurs in an ionic liquid environment. This is found to lead to both n- and p-type conductivity, depending on the charge polarity of the adsorbed molecules. In addition, by studying the disorder of MoS_2/SiO_2 interface, we have been able to identify two surface defects which can generate either n- or p-doping in MoS_2.

Next we investigate the electronic structure of MoS_2 armchair nanoribbons in the presence of an external static electric field. Such nanoribbons, which are nonmagnetic and semiconducting, exhibit a set of weakly interacting edge states whose energy position determines the bandgap of the system. We show that, by applying an external transverse electric field, E_{ext}, the nanoribbons bandgap can be significantly reduced, leading

to a metal-insulator transition beyond a certain critical value. Moreover, the presence of a sufficiently high density of states at the Fermi level in the vicinity of the metal-insulator transition leads to the onset of Stoner ferromagnetism that can be modulated, and even extinguished, by E_{ext}. In the case of bi-layer nanoribbons we further show that the bandgap can be changed from indirect to direct by applying a transverse field, an effect which might be of significance for opto-electronics applications.
In addition to the 1-D structures represented by nanoribbons, we also investigated the electronic properties of different sizes of monolayer triangular MoS_2 nanoclusters. Depending on the edge termination (such as Mo-edge or S-edge) and the percentage of S coverage at the edges, a nanocluster is classified as magnetic or non-magnetic. We show that by applying a transverse electric field, E_{ext}, the gap between the highest occupied and lowest unoccupied molecular orbitals can be decreased and that eventually at a certain critical E_{ext}, a non-magnetic nanocluster becomes spin polarized with a spin moment of 2 μ_B.

Finally, we investigate the electronic and phonon properties of bulk, and both pristine and doped TiS_2 monolayer. The bandgap of monolayers opens for iso-electronic doping with oxygen replacing sulfur and the bandgap opens linearly as the O-concentration increases. We observe a Kohn anomaly in bulk phonon dispersion. In contrast, our DFT calculations using the local density approximation, show that monolayer exhibits charge density wave (CDW) instability. The CDW can be tuned either by compressive strain or by oxygen doping. We observe that both the bandgap and the CDW phase strongly depend on the functional used in the DFT calculations.

Acknowledgements

During my postgraduate study, I have received a lot of support and encouragement from many people. Without their helps and supports, this thesis would not have been possible.

First of all, I would like to express my gratitude to my supervisor Prof. Stefano Sanvito for giving me the opportunity to work in his prestigious group. I have benefited greatly from his advice and teaching during my PhD. His continuous encouragements always help me to overcome the difficulties faced during my PhD.

I would like to thank to Dr. Andrea Droghetti who is one of my office-mate. He helped me a lots at the beginning of my PhD to be familiarized with the computational Density Functional Theory. I have received a lots of scientific discussions from him through out this study. I want to convey my special thanks to him for giving the companion at the office during the week-end.

Next, thanks goes to Dr. Ivan Rungger who is my another office-mate. We have exchanged a lots of scientific discussion at any times when I needed. Whenever, I get any kinds of technical problems, I used to stop him very often to clear our my confusions. Thanks to him for being so kind to me.

I would like to thank to Dr. Chaitanya Das Pemmaraju, who was a former postdoc in our group. Before he moves to California, USA, I used to receive many discussions about my work.

I would like to thank to Mr. Awadhesh Narayan for sharing scientific updates and ideas with me.

I would like to thank to Dr. Clotilde Cucinotta with whom I have started to work collaboratively from the last year.

Besides, I would like to thank to all of my present members of the group: Thomas James Cathcart, Sandip Bhattacharya, Gokaran Shukla, Akinlolu Akande, Maria Tsoneva, Tom Archer, Igor Popov, Aaron Hurley, Amaury melo souza, Jacopo Simoni, and the former members of the group: Ruairi Hanafin, Sankar Kesanakurthi, Xihua Chen, Nuala Mai Caffrey, Nadjib Baadji, Mauro Mantega, and Anna Pertsova. Thanks you all for creating such friendly and pleasant environments in the group and for your supports.

I would like to convey a special thank to my friends Dr. Aurab Chakraborty, Dr. Debasish Saha, and Mr. Suvendu Mandal for providing me the scientific informations electronically across the continents,

I am truly thankful to my examiners Prof. Charles Patteson and Prof. Thomas Heine for their time, exceptionally helpful comments and inspiring discussions during the Viva exam.

I would also like to thank Stefania, who is taking care of all administrate and financial issues and has been extremely helpful and supportive.

The computer resources and the help with our local machines have been provided by the TCHPC stuff members, who all have been very helpful.

I also gratefully acknowledge the financial support of Science Foundation of Ireland that made this work possible.

Finally, I would like to express a very special gratitude to my parents and two elder sisters. They are always supportive to my decisions and interests both in academia and social life.

Contents

Declaration iii

Abstract v

Acknowledgements vii

List of Figures xiii

1 Introduction 1
- 1.1 Low dimensional nanostructures . . . 1
- 1.2 Materials demand for Applications . . . 2
- 1.3 Materials used in current electronics . . . 4
- 1.4 Layered Transition Metal Di-chalcogenides . . . 6
- 1.5 LTMD's Nanostructures . . . 10
- 1.6 Dissertation Layout . . . 12

2 Theoretical Methods 15
- 2.1 Electronic Structure Problem . . . 15
- 2.2 The Born-Oppenheimer Approximation . . . 16
- 2.3 Non-interacting electronic system . . . 17
- 2.4 Hartree-Fock Theory . . . 18
- 2.5 Density Functional Theory . . . 20
  - 2.5.1 The Hohenberg-Kohn Theorem . . . 21
  - 2.5.2 The Kohn-Sham Scheme . . . 21
  - 2.5.3 Approximated Exchange Correlation Functional . . . 23
  - 2.5.4 The interpretation of Kohn-Sham eigenvalues . . . 27
- 2.6 Beyond DFT: G_0W_0 method . . . 28
- 2.7 Equilibrium Geometry and Phonon Spectrum . . . 30
- 2.8 Computational Methods . . . 32
  - 2.8.1 Basis Sets . . . 32

2.8.2 Pseudo-potential 33
2.8.3 DFT Codes 35

3 Effects of impurities and of the substrate on a MoS_2 monolayer 37
3.1 Introduction 37
3.2 Effect of Impurities 41
3.2.1 Thermodynamics of impurity formation energy and transition level 41
3.2.2 Methodology 45
3.2.3 Electronic properties of bulk and monolayer 46
3.2.4 Substitutional doping 48
3.2.4.1 S substitutional doping 48
3.2.4.2 Mo substitutional doping 51
3.2.5 Doping by adsorption 55
3.2.5.1 Alkali atom adsorption 55
3.2.5.2 Adsorption of molecular ions 57
3.2.6 Robustness of the results against the choice of XC functional:HSE06 61
3.2.7 Conclusion 63
3.3 Effects of SiO_2 substrate 64
3.3.1 Methodology 64
3.3.2 Defect-free SiO_2 interface 65
3.3.3 SiO_2/MoS_2 composite with siloxane reconstruction 67
3.3.4 SiO_2/MoS_2 composite with silanol reconstruction 73
3.3.5 Robustness of the results against the choice of XC functional: ASIC 74
3.3.6 Conclusion 75

4 Electric Field Effects on Low Dimensional Nanostructures 77
4.1 Computational details 80
4.2 Electric field effect on MoS_2 Nanoribbon 81
4.2.1 Nanoribbon Structure 81
4.2.2 Electronic structure of MoS_2-ANR 81
4.2.3 Response of a MoS_2-ANR to E_{ext} 85
4.2.4 Bi-layer and multi-layer MoS_2-ANR 93
4.2.5 Electrically driven magnetism 96
4.2.6 Edge termination 99
4.2.7 Cr doped ANR 102
4.2.8 Conclusion 105
4.3 Electric Field Effects on Triangular Nanoclusters (TNCs) 106
4.3.1 MoS_2 nanoclusters 106
4.3.2 Hubbard model 111
4.3.3 Conclusion 114

5 The electronic and phonon properties of pristine and oxygen doped TiS_2 115

5.1 Introduction 115
5.2 Methodology 119
5.3 Electronic Properties with oxygen doping 121
5.3.1 Pristine bulk and single layer 121
5.3.2 Oxygen doping on a monolayer 123
5.3.3 Oxygen doping on nanoribbon 126
5.4 Phonon Properties of bulk and single layer 128
5.5 Conclusion 132

6 Conclusions and Future Work **135**

7 Publications stemming from this work **141**

Bibliography **143**

List of Figures

1.1 Schematic representation of a typical MX_2 bulk structure 7
1.2 Band scheme showing the electron energy (E) versus the DOS for MX_2 8
1.3 Schematics of the phonon mode 11

3.1 Unit-cell of bulk and monolayer MoS_2 38
3.2 Schematic molecular structures of ILs 40
3.3 Supercell of impurity doped MoS_2 45
3.4 Bandstructure of multi-layer MoS_2 47
3.5 Bandstructure and PDOS for monolayer MoS_2 48
3.6 DOS and PDOS for S substitutional (n-type) 50
3.7 DOS and PDOS for S substitutional (p-type) 51
3.8 DOS and PDOS for Mo substitutional (n-type) 52
3.9 DOS and PDOS for Mo substitutional (p-type) 54
3.10 DOS and PDOS for alkali metals adsorption(n-type) 56
3.11 DOS and PDOS for Nb-Cs co-doping 57
3.12 Schematic diagrams of the EDL transistor 58
3.13 Schematic diagram of EDL transistor operation and band for electron doping 59
3.14 Ions adsorption on MoS_2 surface 60
3.15 DOS and PDOS for ion-adsorption 60
3.16 DOS and PDOS for selective doping (HSE06 functional) 62
3.17 SiO_2 surface structure 66
3.18 Geometry of pristine MoS_2/SiO_2 hybrid structure 67
3.19 DOS and PDOS for SiO_2/MoS_2 68
3.20 Schematic band diagram for MoS_2 placed on the defect SiO_2 substrate . 69
3.21 Geometry of defective SiO_2/MoS_2 hybrid structure 70
3.22 DOS for defective SiO_2/MoS_2 (GGA) 72
3.23 DOS for defective SiO_2/MoS_2 (ASIC) 74

4.1 Nanoribbon structures 82
4.2 Symmetric ANR Vs Antisymmetric ANR 82
4.3 Bandstructure and LDOS of the CB, VB for 10-ANR 83
4.4 Variation of bandgaps and the lattice constant with width of ANRs . . 84
4.5 variation of the bandgaps with a transverse E_{ext} 85
4.6 Non-spin polarized bandstructure of a MoS_2 10-ANR for large field . . 87

4.7 Tight-binding model for two linear chain 88
4.8 The variation of the k_c-vector as a function of applied bias 90
4.9 Variation of the bandgap ΔE_g as a function of the n-ANR width 91
4.10 Field-induced charge density distribution along the nano-ribbon 92
4.11 Charge density accumulation Vs E_{ext} 92
4.12 The bandstructure for a multi-layered MoS_2 8-ANR 93
4.13 The bandstructure of a MoS_2 8-ANR bi-layer in the presence of a transverse electric field 94
4.14 variation of bandgap for multi-layered ANR 95
4.15 The non-spin polarized DOS at the critical field E_c 96
4.16 Variation of the magnetic moment per ribbon cell, m, as a function of the external electric field E_{ext} 97
4.17 The band-structure of the 24-ANR plotted for different E_{ext} 98
4.18 Evolution of the bandgap in an external electric field of a 24-ANR with different edge terminations 100
4.19 Magnetic moment as a function of the E_{ext} for a 24-ANR with different edge terminations 101
4.20 The atomic structure of the MoS_2-ANR with Cr dopants 103
4.21 Bandstructure of a Cr doped 10-ANR 103
4.22 Variation of the magnetic moment with the electric field for Cr doped MoS_2 10-ANR 104
4.23 Size dependent structural progression of single layer MoS_2 nanoclusters 107
4.24 The wavefunctions of the HOMO and LUMO states for different size MoS_2-TNCs 108
4.25 The effect of an E_{ext} on the TNC ($n = 4$) 109
4.26 The spin-polarized HOMO and LUMO energy levels Vs E_{ext} for MoS_2-TNC 109
4.27 The effect of a planar E_{ext} on MoS_2-TNC 110
4.28 The variation of the gap with the planar E_{ext} for MoS_2-TNC 111
4.29 Two site Hubbard Model 112
4.30 Variation of V_{ST} in Hubbard model 113

5.1 Unit-cell of bulk TiS_2 116
5.2 Schematic representation of charge density wave 119
5.3 Bandstructure and PDOS for bulk TiS_2 122
5.4 Bandstructure and PDOS for TiS_2 monolayer 123
5.5 The bandstructure and PDOS of monolayer TiSO alloy 124
5.6 Oxygen doping in TiS2 monolayer 126
5.7 Oxygen doped TiS_2 nanoribbon structure 127
5.8 Phonon dispersion of bulk and monolayer TiS_2 129
5.9 The atomic displacement of the optical modes 129
5.10 Banstructure of TiS_2 in CDW phase 130
5.11 Phonon dispersion of doped and strained monolayer TiS_2 131

To my family.

Chapter 1

Introduction

1.1 Low dimensional nanostructures

In low-dimensional (LD) systems, the motion of quasi-particles such as electrons, phonons, or photons is restricted from exploring the full three dimensional world. During the last few decades LD quantum physics has become increasingly interesting due to a constant stream of striking discoveries, such as Fermi liquid theory, the quantum Hall effect, ballistic conductance quantization, quantum phase transitions, Coulomb blockade in quantum dots, giant magneto-resistance (GMR), *etc.* Furthermore LD structures have attracted increased interest as a platform for present as well as future potential applications in electronic devices such as highly efficient low power lasers, single electron transistors, quantum computers, *etc.* A LD system typically consists of a large number of atoms and molecules, but its size is small enough so that electrons have to be considered at the quantum mechanical level at least along one direction. More precisely, in a LD structure the system's size is larger than a microscopic length a_0 (the Bohr radius), but yet smaller than the phase coherent length, L_ϕ, which is the characteristic length beyond which an electron losses phase coherence. L_ϕ generally depends on the dimension, the temperature and the electronic structure of the system.

LD physics has recently illuminated some difficult questions such as how disorder (impurities, for example) and electron-electron interactions affect the dynamics of a quantum system. In fact, the study of the combined effects of disorder and electron-electron interaction in condensed matter physics is currently a problem of enormous interest. LD nanostructures have unusual but interesting electronic and transport properties due

to their small size and quantum confinement. As an example, we mentioned that the ballistic flow of electrons in narrow channels for distances less than the mean free path has been observed experimentally [1]. There are many important distinctions between systems in different dimensions and those in their bulk form, such as the effective mass which, in general, depends on the the electron's propagation direction and can even vary with position. Another important distinction between systems with different dimensions is their density of states, $N(\epsilon)$ [the number of states per unit volume in the energy range ϵ to $\epsilon+d\epsilon$]. In general one finds, $N(\epsilon) \propto \epsilon^{\frac{d}{\alpha}-1}$, where d is the dimension of the system, and the power α depends on the quasi-particle type, *i.e.* $\alpha = 1$ for phonons and photons and $\alpha = 2$ for electrons. In comparison with a bulk (3D) object, the higher surface to volume ratio associated to the LD nanostructures results in the dominance of surface effects (e.g., composition, bonding and surface states/defects) over the materials properties (electrical, thermal, mechanical, catalytic, optical *etc*). Such LD systems have potential for major applications in nanodevices as their performance, for example the gas sensing ability, largely depends on environmental conditions/adsorbates, surface scattering, and surface trapping.

1.2 Materials demand for Applications

Over the past four decades, the performances of semiconductor electronics have been improved gradually by 'scaling-down' or reducing the dimensions of field effect transistors (FETs). However, size-scaling has enhanced the complexity of the technology, where transistor miniaturization is succeeded by integration of a large number of transistors into a single integrated circuit called a microprocessor. Since 1971, this constant scaling-down has enabled us to follow Moore's law [2]: the transistor count per microprocessor doubles every 18 months, leading to a significant improvement in performance and price reduction [3]. Nowadays a micro-processor is constructed incorporating a few billions metal-oxide semiconductor FETs (MOSFETs), whose channel length, *i.e.* distance between the source and the drain electrodes in FET, is shrunk down to 20-30 *nm*. At such a scale, quantum effects such as the onset of electron quantum tunneling through potential barriers, limit the ability to confine charges in a densely packed array. Unfortunately, the size-scaling of FETs is expected to attain a fundamental limit in the near future. Therefore research has been recently focused in searching for alternative device concepts and novel materials to be implemented in existing device.

In order to continue progress, one is left with two options. One route is to explore entirely new physical phenomena, for example spin transistors [4] or single electron devices [5]. The second option is to implement the existing FET concept with novel promising materials.

In a basic FET structure, the conductivity of a channel is controlled by the gate electrode via application of an electric field. The channel material, usually semiconductor, needs to meet some primary requirements. Firstly, the semiconductor should have bandgap of at least 0.4 eV so that the conductivity can be switched off (required for digital logic operation) [6]. An on/off ratio (*i.e.* the ratio of the on-state to the off-state conductance) of 10^4-10^7 is generally require for effective switching [7]. Next, a high charge carrier mobility in the semiconductor is required for fast operation.

Beside the specific need for new semiconducting materials in digital electronic devices, researchers are also busy in searching for promising materials with all kinds of electronic phases for other potential applications such as opto-electronics, molecular-sensing, catalysis and thermo-electrics. For example, metallic thin-films are required as transparent electrodes in display technology [8], whereas insulating films are promising as dielectrics for capacitors [9], gate insulators [10], energy storage [11], and memory devices [12, 13]. Moreover, the stacking of individual materials such as metal/semiconductor/semiconductor/metal could lead to hetero-junction solar cells. Performances of these devices primarily depend on the electronic, vibrational, optical, and chemical properties of the material. For example, for opto-electronic devices such as solar cells, light emitting diodes (LEDs), photo-detectors, and transparent displays, the ability to absorb/emit light is directly determined by the electronic bandstructure. In fact, photons can not be absorbed/emitted at an energy smaller than the material bandgap energy. This is the case for direct bandgap semiconductors. In contrast, for the indirect bandgap one, additional energy must be absorbed or emitted in a phonon assisted transition to supply the difference in momentum, reflecting the much less efficient absorption or emission of photons. Another interesting example is associated with developing high-performance thermo-electric materials for electric power generation from a heat source. The figure of merit of thermo-electric materials is usually defined by $ZT = S^2\sigma T/(\kappa_e + \kappa_l)$ where, S is the Seebeck coefficient, σ the electrical conductivity, T the absolute temperature, while κ_e, κ_l are the electron and the lattice's contributions respectively to the parasitic thermal conductivity. In another words, the thermo-electric efficiency is improved by engineering independently the phonon and the electronic properties of a material [14, 15].

1.3 Materials used in current electronics

Since 1960 silicon has been used as the primary material to fabricate the semiconducting channel between the source and drain in the FET. Silicon has been successful till the present mainly due to its abundance and consequent low manufacturing price for MOSFETs. Of course, there are several other reasons: 1) it is easy to dope to make n/p-type semiconductor, 2) there is an easy accessible oxide (SiO_2), which performs nicely as an insulating substrate, and 3) there is a significant body of experience accumulated to control the materials processing and it physical properties. However, silicon does not appear as promising for many other applications. One example is flexible electronics for which Si is too brittle and its carrier mobility is too low [16]. Thus, when the application changes, other semiconductors can be used. For instance SiC, GaN, Ge, and GaAs have been all used for more specialized applications such as high power electronics, high temperature electronics, photovoltaics and LEDs.

In materials design for nanotechnology, metal oxides such In_2O_3, SnO_2, and ZnO are attractive because of the efficient progress made in fabricating their nanostructures, such as nanosheets, nanorods, nanoribbons and nanoparticles [17, 18]. These materials display a number of interesting properties, such as large optical bandgap leading to transparency, high photo-electric yield, and sometimes room-temperature ferromagnetism. As such these materials have widespread use in applications, including transparent conductors, solid state sensors, and solar cells [8]. In particular, thin-film transistors made of metal oxide have some advantages over those made of Si: the mobility is higher than that of silicon and relatively cheap large scale production is possible due to their low temperature fabrication. Moreover, metal oxides with wide bandgaps ($\sim$ 3.0-5.0 eV) such as ZrO_2, Al_2O_3, TiO_2 and HfO_2 are traditionally used for designing nano-dielectrics for high-κ (κ=dielectric constant) dielectric devices [19]. The major problem with metal oxides is that their electronic properties are extremely sensitive to point defects, such as vacancies or interstitial dopants, which arise during the materials growth. For instance, ZnO is an optically efficient ultra-violet bandgap semiconductor, but it may display a green, yellow and blue photo-luminescence because of the presence of defects [20, 21].

Carbon nanotubes (CNTs) were identified as ideal for certain areas of electronics over two decades ago. The first transistor using a single walled CNT was demonstrated in 1998 [22]. Interestingly, in a individual CNT the mobility can be as high as 10^5

$cm^2/V{\cdot}s$ [23] and one can achieve an on/off ratio exceeding 10^5 [24]. However, nanotubes can exhibit many electronic structures from metallic to semiconducting depending on the precise arrangement of the C atoms (the CNT chirality). Over the last decade it has become clear that sorting nanotubes by precise electronic type will be an inefficient process not suitable to large scale electronics. In addition it remains unclear how arrays of billions of nanotubes could be addressed. This has led to slow progress in finding a commercial use for CNTs. Although, it has been shown that transistors could be made from networks of metallic and semiconducting CNTs, upon the application of gate-bias, the semiconducting tubes turned off and the metallic ones burnt out with a high current. This is a serious disadvantage for realistic application [25]. On the contrary, the nanotubes thin-films can be considered in other device applications such as display devices. This has worked very well but it is becoming clear that they are not good enough for industrial applications, again partly because of the presence of semiconducting nanotubes [26]. Thus the presence of semiconducting nanotubes suppresses the possibility of potential applications requiring metallicity while the presence of metallic nanotubes complicates applications requiring semiconducting systems.

Conjugated polymers and other similar organic molecules were first shown to display electro-luminescence nearly 20 years ago [27]. Since then, polymer thin films of these materials have been used in photodiodes [28], solar cells [29], lasers [30], transistors [31] as well as LEDs [32]. Their main advantage is that they can be processed in the liquid phase, which makes device fabrication straightforward. However, due to their conjugated nature, they are prone to photo-oxidization and so must be produced and used in inert environments. This is a significant problem. Thus, all the nanostructures of made materials such as silicon, oxides, organic polymers, and other forms of carbon appear to have both potential and problems as electronic materials.

Recently, graphene (the 2D allotrope of carbon) has received much attention due to its unique and unusual electronic [33], thermal [35] and optical [34] properties. Graphene can be exfoliated from graphite, a layered material, where graphene monolayers are stack together by weak van der Waals forces. Surprisingly, just after six years from the first synthesis of graphene [36], in 2010, the Nobel prize was awarded to Andre Geim and Konstantin Novoselov. A new direction in science and technology at the 2D *flatland* was opened. It was then suggested that devices based on layered materials, such graphene may become an alternative to the dominant silicon-based electronics. These are expected to overcome some of the limitations imposed by miniaturization. Although graphene displays a mobility exceeding 10^6 $cm^2/V{\cdot}s$ [37], its application to

Bulk	**Bandgap (eV) (ΔE_g)**	**Electron mobility (cm^2/V-s) (μ)**	**Electrical Resistivity (Ω-cm) (ρ)**	**Thermal conductivity (W/m-K) (κ)**
Graphite	-0.4 (semi-metal) [41]	20x10^3 [41]	(5-30)x 10^{-6} [42]	25-470 [42]
Si	1.12 (indirect)[45]	90-1400 (doping 10^{20}-10^{14} cm^{-3})[43]	10^3 [45]	149 [45]
BN	5.2 (direct)[46]	$\sim$ 200 [46]	$\sim 10^{14}$ [47]	(30-600) [47]
Bi_2Te_3	0.21 (direct) [44]	1140 [44]	-	3.0 [44]
MoS_2	1.23 (indirect) [48]	100 [49]	$\sim 10^4$ [50]	4.17-18.06 [51]

TABLE 1.1: Experimentally observed physical, electrical, and thermal properties of some layered materials, together with those of Silicon (Si) shown for comparison.

nano-electronics is hindered by the lack of a bandgap, *i.e.* the conductivity can not be switched off upon applying a gate bias. An electronic bandgap can be as large as 200 meV opened by by patterning graphene into a nanoribbon. This however reduces drastically the mobility to $\sim$200 cm^2/V·s [38]. A similar reduction and bandgap opening happens when graphene is deposited on a suitable substrate [39], or when molecules are absorbed at the surface [40]. The bandgap problem of graphene then boosted the search for other classes of inorganic layered materials such as BN, $BiSe_2$, Bi_2Te3 and transition metal di-chalcogenides (TMDs) (for example, MoS_2) to be used in nano-electronics. In Table 1.1 we list the physical, electrical and thermal properties of some interesting layered structure materials together with those of Si for comparison. For example, BN triggered tremendous research interest due its exceptional thermal conductivity, high chemical stability and extreme robustness and its possible potential applications in optics and opto-electronics [57, 58, 59]. In contrast, Bi_2Se_3 and Bi_2Te_3 are potential candidates for thermo-electronic applications [60, 61]. More generally, layered TMDs become attractive due their large variation of electronic phases such as semiconductors, metals and superconductors.

1.4 Layered Transition Metal Di-chalcogenides

Layered transition metal di-chalcogenides (LTMDs) are a class of materials with the stoichiometry MX_2, where M is a transition metal from the IV, V, VI, VII, VIIIB and VIIIC group, while X is a chalcogen (S, Se or Te). There are about 40 LTMDs in

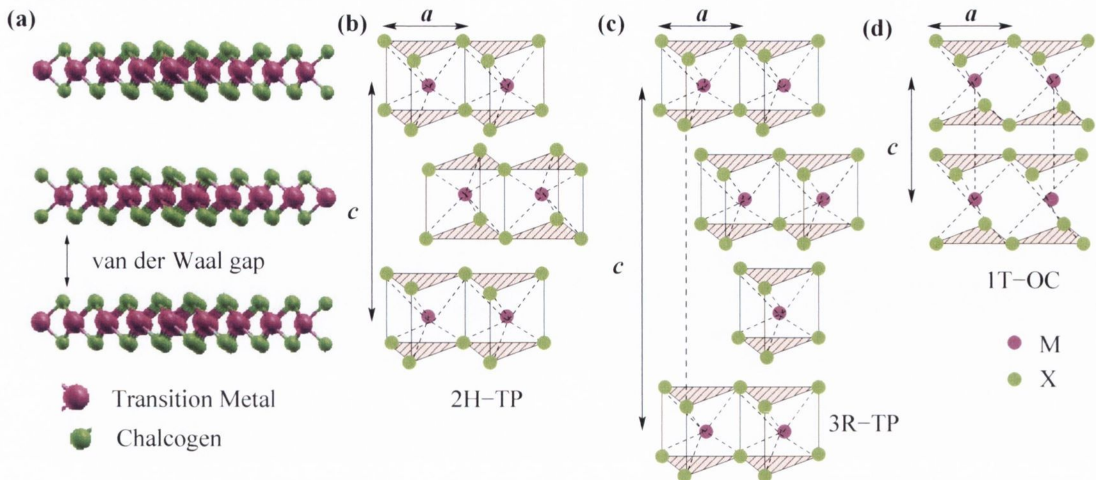

FIGURE 1.1: (a) Schematic representation of a typical MX_2 bulk structure, with the metal atoms (M) in magenta and the chalcogen atoms (X) in green. Schematic representations of the MX_2 structural polytypes: (b) 2H-TPC (two monolayers per unit cell, hexagonal symmetry, trigonal prismatic coordination), (c) 3R-TPC (three monolayers per unit cell, hexagonal symmetry, trigonal prismatic coordination), and (d) 1T-OC (one monolayer per unit cell, hexagonal symmetry, octahedral coordination). In the panel (b-d) the metal atoms (M) are solid magenta circles and the chalcogen atoms (X) are solid light green circles. The lattice constant, a, varies from 3.1 Å to 3.7 Å for different LTMDs [63]. The index c indicates the number monolayer incorporated in the unit cell for different stacking orders, and the interlayer spacing, "van der Waal gap", is $\sim$ 6.5 Å [63].

nature. In these layered materials, the M ions are covalently bonded to the X ones to form a X-M-X sandwich layer, in which two individual planes of hexagonally arranged chalcogens are connected via a similar hexagonal plane of M atoms. Each X-M-X sandwich layer interacts with the neighboring sandwich layer only through van der Waals forces to form a bulk crystal. Thus the distance between the sandwich layers is called "van der Waals gap" [shown in Fig. 1.1(a)]. The stacking orders of the sandwich layers and the coordination of the metal atoms lead to a variety of polytypes for those layered materials (shown in Fig. 1.1). The entire family of LTMDs display either hexagonal or rhombohedral symmetry and additionally the metal atom has octahedral or trigonal prismatic coordination. The electrical and magnetic properties of LTMDs are characterized by the ligand field splitting of transition metal's d states, resulting from the metal's d orbitals and the chalcogens p ones [62, 63]. Additionally, the electronic phase of LTMDs depends on the degree to which the non-bonding d bands are occupied (see Fig. 1.2). For example, the presence of 1 non-bonding d electron orbital results in NbS_2 to be a metal. In contrast, MoS_2 is a semiconductor due to 2 electrons filling the

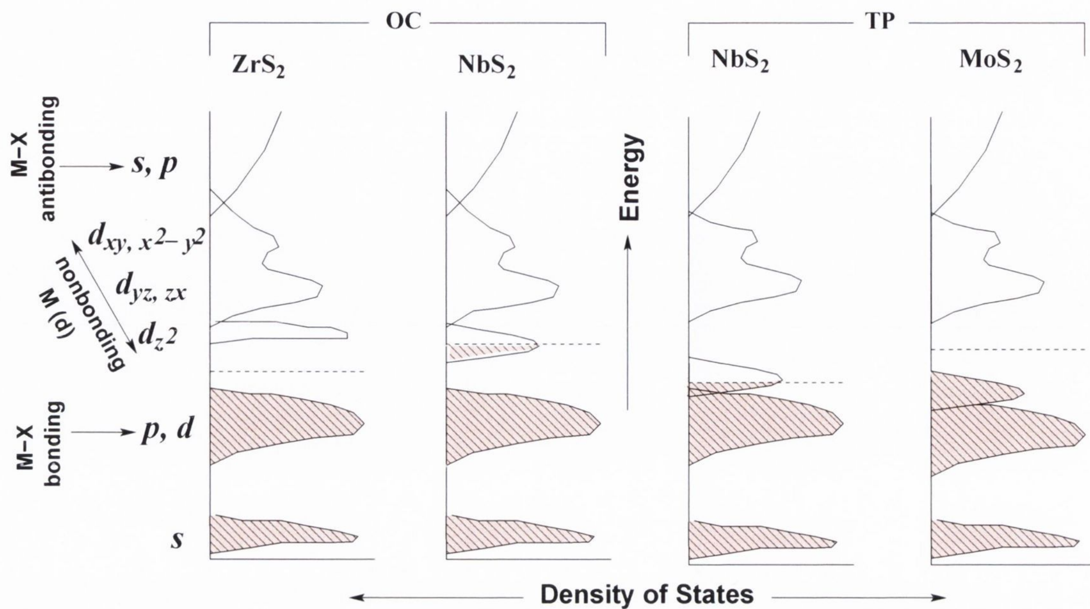

FIGURE 1.2: Band scheme showing the electron energy (E) versus the density of states, for some Representatives of MX_2, *i.e.* from the group VI (ZrS_2), the group V (NbS_2), and VI (MoS_2). OC and TPC denote the octahedral and trigonal prismatic coordinations respectively. The occupied states are shown shaded, and the dash line indicated the Fermi energy.

non-bonding d orbital [65]. In Table 1.2 the crystallographic types and the electronic properties of the class LTMDs are summarized.

Due to the presence of a weak van der Waals force between the layers, the LTMDs family displays very anisotropic properties both electronically and mechanically. The electrical conductivity perpendicular to the planes differ significantly from that in plane. For example, in the case of MoS_2 the perpendicular conductivity is reduced by at least two orders of magnitude from that in plane [63]. It is also notable that the so-called intra-layer phonon modes, A_{1g}, which involve intra-layer X-X bonding, are many times stronger than the so-called layer-layer modes E^1_{2g}, which involve bonding across the "van der Waals gap" [64] [see Fig. 1.3(a)]. This fact produces an anisotropy not only in the mechanical properties such as the compressibility, but also in the thermal ones. Due to the unique electronic and phonon characteristics, the LTMDs show many interesting phenomena. For example, intercalation of organic molecules or alkali metals inside the "van der Waals gap" can tune superconductivity and several electron-phonon driven lattice instabilities [63, 65].

M \ X_2	$-S_2$ CT	$-Se_2$ CT	$-Te_2$ CT	Electronic and magnetic characteristics.
IV $[d^2]$ Ti, Zr, Hf	OC	OC	OC	Diamagnetic semiconductors. $E_g \sim$ 0.2-2 eV, $\rho \sim 1$ ohm-cm. $TiSe_2/Te_2$ exhibits CDW [52, 53].
V $[d^3]$ V, Nb, Ta	OC (V) TPC(Nb) TPC/DOC(Ta)	OC(V), TPC(Nb), TPC/DOC(Ta)	DOC	Narrow band metal, $\rho \sim 10^4$ ohm-cm. Pauli paramagnet $\rightarrow$ band antiferromagnet. Selenides and tellurides exhibit both CDW and superconductivity ($T_c < 10$K) [54, 55, 56].
VI $[d^4]$ Mo, W	TPC	TPC	DOC TPC (Mo)	(i) The undistorted compounds: Diamagnetic semiconductors, $\rho \sim 1$ ohm-cm, $E_g \sim$ 1-2 eV; (ii) The distorted compounds: semi-metals, $\rho \sim 10^{-3}$ ohm-cm, diamagnetic.
VII $[d^5]$ Tc, Re	DOC	DOC	DOC	Small gap diamagnetic semiconductors.
VIIIB $[d^7]$ Co, Rh, Ir	- (Ir)	- (Ir)	OC	Metal. IrS_2/Se_2-semiconducting.
VIIIC $[d^8]$ Ni, Pd, Pt	OC (Pt)	OC (Pt)	OC	(i) Tellurides-metals, $\rho \sim 10^-5$ ohm-cm. Pauli paramagnetic. $PdTe_2$-superconductor. (ii) $PdS_2/PdSe_2$, PtS_2/Se_2-diamagnetic semiconductors, $E_g \sim 0.4$ eV, $\rho \sim$ 1 ohm-cm.

TABLE 1.2: Structure types, electrical and magnetic properties of LTMDs. Notations: CT$\rightarrow$ Crystallographic Types, OC$\rightarrow$ octahedral coordination, TPC$\rightarrow$ trigonal prismatic coordination, DOC$\rightarrow$ distorted octahedral coordination, $E_g \rightarrow$ bandgap, $\rho \rightarrow$ electrical conductivity, CDW $\rightarrow$ charge density wave. The table is adopted from Ref. [63]

1.5 LTMD's Nanostructures

In the last few years, several experimental techniques have been employed to produce 2D nanosheets down to the single layer from inorganic layered materials [66]. For industrial applications, one needs to have a manufacturing protocol that is scalable to large volumes at a reasonable cost. In this context, Coleman *et al.* have been recently pioneered a straightforward technique, namely liquid exfoliation, which can efficiently produce 2D nanosheets from a variety of inorganic layered compound such as BN, Bi_2Te_2, MoS_2, WS_2, $MoSe_2$, $MoTe_2$, $TaSe_2$, $NbSe_2$ and $NiTe_2$ [67]. The virtue of the layered materials is that ultra-thin flakes exhibit, in general, of high crystal quality. Moreover, many interesting properties emerge from having atomically thick layers due the quantum confinement. For example, the bulk indirect bandgap of the MX_2 (M=Mo, W) family becomes direct in the monolayer limit, as demonstrated by the emergence of a room-temperature photo-luminescence (PL) [68, 69, 70, 71] and the fact that the PL intensity depends on the material's thickness. In fact, photo-transistor and photo-detector devices made of the ultra-thin layers MoS_2 and WSe_2 have been reported having better performances over silicon and germanium based ones [72, 73]. In contrast, the A_{1g} and E^1_{2g} phonon modes change monotonically with the thickness of the LTMDs.

As a representative of the LTMDs family, the variation of those phonon modes with the layer numbers for MoS_2 is shown in Fig. 1.3(b). Consequences of these results, namely the evolution of the PL intensity or the A_{1g} and E^1_{2g} Raman activated frequencies are utilized to identify the numbers of a layers of layered compound [69, 74, 75] [see the Fig. 1.3]. While, atomic force microscopy (AFM) [75] is the most direct way to identify the number of layers, the method is hindered by the time consuming process of the characterization. Scanning electron microscopy (SEM) or transmission electron microscopy (TEM) could also be employed here [76], but they are problematic due to electron-beam induced deposition and by radiation which could have significant impact on the atomic displacement [77]. However, optical imaging tools are developed in a simple way for rapid characterization of the samples [78].

Beside the recent huge progresses in making 2D nanostructures of TMDCs, other dimensional nanostructures such as 1D like nanowires [80], nanoribbons [81, 82], nanotubes [83, 84]; and 0D like nanoclusters [85], nanorods [86], nanoflowers [87], and nanoparticles [88] have been explored their properties for potential applications [85,

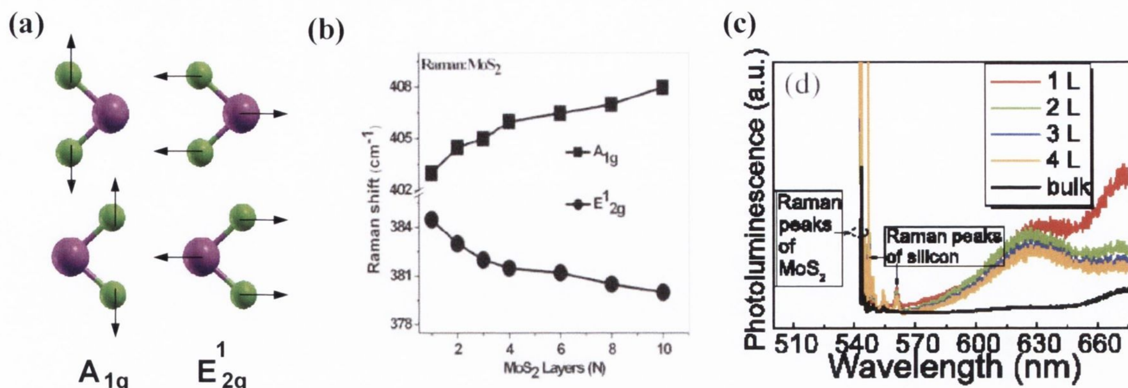

FIGURE 1.3: (a) Schematics of the intra-layer phonon mode A_{1g}, and the inter-layer phonon mode E^1_{1g} for bulk MoS_2. The experimental variation of the phonons modes A_{1g} and E^1_{2g} (b) and the photo-luminescence with the number of layers for a prototypical MX_2, MoS_2 (c). Panel (b) is taken from the Ref. [75] and (c) from the Ref. [79].

87, 89, 90]. For example, several experimental and theoretical investigations have been devoted to MoS_2 nanoclusters, since very small ($\sim$ 2 nm) nanoclusters are reported to be candidates for hydrodesulfurization catalysis due the presence of metallic edge states [91, 92].

While low dimension nanostructures made of layered materials have the potential to transform the electronic industry, several fundamental issues such as how the electronic and phonon properties change in the reduced dimensions, need to be resolved before such materials are incorporated into devices at an industrial scale. In this thesis, we discuss the effects of dimensionality on the electronic and phonon properties of LTMDs and the possibility of manipulating those properties by applying external perturbations such as doping, electric field and strain.

1.6 Dissertation Layout

The main focus of this work is to examine the electronic and phonon properties of TMDCs using density functional theory (DFT), density functional perturbation theory (DFPT), and the Green's functions formalism. As a representatives of the LTMDs large family, our studies are centered on LD nanostructures of MoS_2 and TiS_2. Their electronic properties are compared with those of other layer materials such as BN, $TiSe_2$, HfS_2, and ZrS_2.

Chapter 2: The theoretical methods required to investigate the electronic and phonon properties of real materials are introduced. The many-body electronic structure problem is discussed and, in order to solve this problem, an overview is given on density functional theory. As DFT is a ground state theory, one needs to consider other methods to estimate a fundamental quantity of the electronic structure such the bandgap, which depends on the excited states of the system. In this context, the Green's function method is introduced. Finally, the density function perturbation theory (DPFT) is introduced to study the phonon properties of the system.

Chapter 3: We study the electronic properties of bulk as well as monolayer MoS_2 by using *ab initio* DFT as it is implemented in the SIESTA program. *Ab-initio* DFT calculations are performed within a systematic study of the electronic and the magnetic properties of doped MoS_2 monolayers in order to search for suitable p-type and n-type dopants. The dopants are added both via S/Mo substitution and as absorbates. Moreover, the adsorption of charged molecules on the surface of monolayer MoS_2 is considered. This is found to lead to n-type and p-type conductivity, depending on the charge polarity.

Chapter 4: A nanoribbon is constructed by patterning an infinite 2D nanosheet of MoS_2. Again here the *ab-initio* studies are carried out on the electronic structure of narrow nanoribbons ($\sim$ 1-3 nm), where the carriers are laterally confined to form a quasi-1D system. Then, the MoS_2 nanoribbons response to an external electric field has been studied with the aim of tuning their electronic properties (bandgap). A tight-binding model is presented in order to explain a few interesting phenomena, such as the tuning of the bandgap and the shifting of the direct bandgap from the Γ point to another point in the Brillouin zone upon the application of an electric field. The issue of the robustness of the electric field effects against the different types of edge terminations is addressed.

Then we extend the study of the external electric field effects to other lower dimensional structures, such as nanoclusters, where the edge structures have been thoroughly characterized by the recent experiments.

Chapter 5: We investigate the electronic and phonon properties of another prototype LTMD, namely TiS_2. Our study mainly focuses on the oxygen substitutional doping at the S site of a TiS_2 monolayer by using both the DFT and Green's function methods. Then the evolution of the TiS_2 phonon properties with the dimension in TiS_2 (*i.e.* going from 3D bulk to a 2D monolayer) is studied by using DFPT.

Chapter 6: We draw some general conclusion and highlight possible directions for future work.

Chapter 2

Theoretical Methods

2.1 Electronic Structure Problem

In condensed matter physics the electronic structure problem is characterized by the collective motion of electrons and nuclei interacting via Coulomb forces. The steady-state motion is described by the time independent Schrödinger wave equation,

$$\hat{H}\Psi = E\Psi\,, \tag{2.1}$$

where $\hat{H}$ is the Hamiltonian operator for the quantum mechanical many-body wave-functions Ψ. For the non-relativistic system consisting of N_e electrons and N_N nuclei, the total $\hat{H}$ is described by,

$$\hat{H} = -\frac{1}{2}\sum_{K=1}^{N_N}\frac{\nabla^2_{\mathbf{R}_K}}{M_K} - \frac{1}{2}\sum_{k=1}^{N_e}\nabla^2_{\mathbf{r}_k} + \sum_{K<S}^{N_N}\frac{Z_K Z_S}{|\mathbf{R}_K - \mathbf{R}_S|} - \sum_{k=1}^{N_e}\sum_{K=1}^{N_N}\frac{Z_K}{|\mathbf{r}_k - \mathbf{R}_K|} + \sum_{k<s}^{N_e}\frac{1}{|\mathbf{r}_k - \mathbf{r}_s|}, \tag{2.2}$$

where the first and second terms are the kinetic energy of the nuclei and the electrons respectively. The third, the forth and the last term are the nucleus-nucleus, the electron-nucleus and the electron-electron Coulomb interaction respectively. $\mathbf{R}_K$ and $\mathbf{r}_k$ denote the positions of the Kth nucleus of mass M_K and the kth electron of mass m_e respectively. Note that, in these definitions, we have introduced the atomic units

($\hbar = m_e = e = 1$), which will be used throughout this work. The structure and properties of a system are governed by the above eigenvalue equation, however, finding an exact analytic solution of the Eq.(2.1) is almost impossible even for a small molecule like H_2. In addition, numerical solutions are cumbersome and extremely computationally demanding modern computers even in the simplest case of a few electron system. The problem can not be solved exactly for nano-scale objects, for which one has to deal with a few hundreds of atoms. To simplify the problem without sacrificing the accuracy of the ultimate solutions, one needs to rely on some approximation such as Born-Oppenheimer approximation, discussed below.

2.2 The Born-Oppenheimer Approximation

The many-body wavefunction Ψ in Eq. (2.1) depends both on electronic (x_k) and the nuclear (X_K) degrees of freedom, in which their positions as well spin coordinates (σ_k) are included, e.g $x_k = (\mathbf{r}_K, \sigma_k)$. Thus,

$$\Psi = \Psi(x_1, x_2, ...x_k, ..., x_{N_e}; X_1, X_2, ...X_K, ..., X_{N_N}). \tag{2.3}$$

A major step to simplify the problem is to separate out the movement of the nuclei and the electrons through the Born-Oppenheimer (BO) approximation [93]. This is based on the fact that the nuclear masses are much heavier ($\sim 10^3$) than the electron mass so that the nuclei move much slower than the electrons. Consequently, in the reference frame of the electrons the nuclei can be considered to be at rest (*i.e.*, the kinetic energies of the nuclei vanish) and the electrons move in the static field generated by the nuclei plus the other electrons. Then, the total Hamiltonian $\hat{H}$ (Eq.(2.2) takes the form of the electronic Hamiltonian $\hat{H}_e$, which can be written as,

$$\hat{H}_e = \hat{T}_e + \hat{V}_{eN} + \hat{V}_{ee}, \tag{2.4}$$

where

$$\hat{T}_e = -\frac{1}{2}\sum_{k=1}^{N_e} \nabla^2_{\mathbf{r}_k}, \tag{2.5}$$

$$\hat{V}_{eN} = -\sum_{k=1}^{N_e}\sum_{K=1}^{N_N} \frac{Z_K}{|\mathbf{r}_k - \mathbf{R}_K|}, \tag{2.6}$$

$$\hat{V}_{ee} = \sum_{k<s}^{N_e} \frac{1}{|\mathbf{r}_k - \mathbf{r}_s|} . \tag{2.7}$$

The Schrödinger equation for the entire system (electrons plus nuclei) reduces to the form,

$$\hat{H}_e(\{x_k\})\Psi^e(\{x_k\}) = E(\{X_K\})\Psi^e(\{x_k\}) , \tag{2.8}$$

where, the energy eigenvalues E are parametrized by the nuclear coordinates $(\{X_K\})$, reflecting the fact that now one has only to consider the electronic coordinates $\{x_k\}$, whereas the nuclear coordinates become a set of parameters of the electronic system.

2.3 Non-interacting electronic system

Within the BO approximation, Eq.(2.8) suggests that the electronic wavefunctions belong to $3N_e$ dimensional space, *i.e.* $\Psi \in \Re^{3N_e}$, meaning that extracting the properties of the interacting electronic system is still a nontrivial task. This is due to the presence of the term $\hat{V}_{ee}$, which couples all the electronic coordinates. However, the problem becomes much simpler for the case of a non-interacting electronic system where $\hat{V}_{ee}$ vanishes or is set to zero. Then, the Hamiltonian $\hat{H}_e$ (Eq. 2.4) transforms into a sum of N_e individual one-electron Hamiltonians $\hat{h}$. Thus,

$$\hat{H}^{non} = \sum_{k=1}^{N_e} \hat{h}_k = \sum_{k=1}^{N_e} \left[-\frac{1}{2}\nabla^2_{\mathbf{r}} - \sum_{K=1}^{N_N} \frac{Z_K}{|\mathbf{r} - \mathbf{R}_K|} \right], \tag{2.9}$$

and the corresponding Schrödinger wave equation becomes

$$\hat{H}^{non}\Phi = E^{non}\Phi. \tag{2.10}$$

The eigenfunction Φ can be constructed as a Slater determinant (an anti-symmetric product of the N_e occupied one-electron eigenfunctions $\psi_\alpha\{\mathbf{x}\}$), which also satisfies the

eigenvalue equation $\hat{h}\psi_\alpha = \varepsilon_\alpha\psi_\alpha$,

$$\Phi = \frac{1}{\sqrt{N_e!}}\det[\psi_\alpha(x_\beta)] = \frac{1}{\sqrt{N_e!}}\begin{vmatrix} \psi_1(\mathbf{x}_1) & \psi_1(\mathbf{x}_2) & ... & \psi_1(\mathbf{x}_{N_e}) \\ \psi_2(\mathbf{x}_1) & \psi_2(\mathbf{x}_2) & ... & \psi_2(\mathbf{x}_{N_e}) \\ . & . & . & . \\ . & . & . & . \\ . & . & . & . \\ \psi_{N_e}(\mathbf{x}_1) & \psi_{N_e}(\mathbf{x}_2) & ... & \psi_{N_e}(\mathbf{x}_{N_e}) \end{vmatrix}. \tag{2.11}$$

This takes into consideration the Pauli exclusion principle: two or more fermions (electrons) cannot occupy the same spin orbitals simultaneously. Note that both the spatial ($\mathbf{r}$) and spin (σ) part are included in ψ_α, *i.e.* $\psi_\alpha\{x\} = \psi_\alpha\{\mathbf{r},\sigma\}_{\alpha=1}^{N_e}$. Since $\hat{h}$ commutes with the $\hat{s}_z$ component of the electron spin σ, either $\sigma = +\frac{1}{2}(\uparrow)$ or $\sigma = -\frac{1}{2}(\downarrow)$ can be chosen as a one-electron quantum number. The total energy E of this system is simply the sum of the eigenvalues (ε_α) of the N_e occupied single particle states, *i.e.*,

$$E^{non} = \sum_{\alpha=i}^{N_e}\varepsilon_\alpha. \tag{2.12}$$

Simultaneously, the total electron density is given by $\sum_{\alpha=1}^{N_e}|\psi_\alpha(\mathbf{r})|^2$.

2.4 Hartree-Fock Theory

The original interacting problem, *i.e.*, the Schrödinger equation in Eq. (2.8), is the counterpart to the wavefunction variational principle [95], namely for any trial wavefunction, Ψ_t, the total energy of the system $E[\Psi_t]$ functional is always greater than the ground state energy, E_0. Thus,

$$E[\Psi_t] = \left[\frac{\langle\Psi_t|\hat{H}|\Psi_t\rangle}{\langle\Psi_t|\Psi_t\rangle}\right] \geq E_0, \tag{2.13}$$

where the equality is satisfied only for the ground state wavefunction, $\Psi_t = \Psi_0$. Here $\hat{H}$ is the Hamiltonian described in Eq.(2.4)

$$\langle\Psi_t|\hat{H}|\Psi_t\rangle = \sum_{\sigma_1,...\sigma_{N_e}}\int d\mathbf{r}_1...d\mathbf{r}_{N_e}\Psi_t^*(\mathbf{x}_1,...,\mathbf{x}_{N_e})\hat{H}\Psi_t(\mathbf{x}_1,...,\mathbf{x}_{N_e}), \tag{2.14}$$

and

$$\langle \Psi_t | \Psi_t \rangle = \sum_{\sigma_1,...\sigma_{N_e}} \int d\mathbf{r}_1...d\mathbf{r}_{N_e} |\Psi_t(\mathbf{x}_1, ..., \mathbf{x}_{N_e})|^2 . \tag{2.15}$$

Ψ_t can be constructed in a general way, however the wavefunction Φ of the non-interacting system is useful for this purpose. Therefore our general interacting problem is rephrased in a way where the Slater-determinant eigenstates [94] of $\hat{H}^{non}$ are utilized to construct an orthonormal basis for the expansion of the antisymmetric eigenstates of $\hat{H}$, the interacting Hamiltonian. The many-body solution is found by minimizing $E[\Psi_t]$ with the methods of Lagrange multipliers. Thus,

$$\delta[\langle \Psi | \hat{H} | \Psi \rangle - E \langle \Psi | \Psi \rangle] = 0, \tag{2.16}$$

and the Hartree-Fock (HF) equation for the N_e one-electron wavefunctions $\{\psi_\alpha\}_{\alpha=1}^{N_e}$ takes the form,

$$\hat{f}_\alpha \psi_\alpha = \Big\{ -\frac{1}{2}\nabla_{\mathbf{r}}^2 - \sum_{K=1}^{N_N} \frac{Z_K}{|\mathbf{r} - \mathbf{R}_K|} \Big\} \psi_\alpha \tag{2.17}$$

$$+ \sum_{\beta=1}^{N_e} \int d\mathbf{r}' \frac{|\psi_\beta(\mathbf{r}')|^2}{|\mathbf{r} - \mathbf{r}'|} \psi_\alpha(\mathbf{r}) - \sum_{\beta=1}^{N_e} \sum_{\sigma} \int d\mathbf{r}' \frac{\psi_\beta^*(\mathbf{r}')\psi_\alpha(\mathbf{r}')}{|\mathbf{r} - \mathbf{r}'|} \psi_\beta(\mathbf{r}) = \varepsilon_\alpha \psi_\alpha.$$

Here the eigenvalues (ε_α orbital energies) of the Fock operator $\hat{f}_\alpha$ are Lagrange multipliers which take into account the orthonormality of the one-particle orbitals. Note that a self-consistent field (SCF) approach is needed to solve the problem, since the orbitals determine part of their own effective potential. Koopman's theorem [96] provides a physical interpretation of the orbitals energies, ε_α, which approximate the negative of the vertical ionization energy, defined as the energy required to remove an electron from the orbital ψ_α, *i.e.*, $\varepsilon_\alpha = E_{N_e} - E_{N_e-1}^{\alpha}$. Koopman's theory is valid for all the occupied levels within HF formalism. Within HF theory, electron-electron interaction is approximately considered by the third and fourth term of Eq.(2.17). These are called the electrostatic Hartree potential and the non-local exchange potential, respectively. The non-local exchange is entirely due to the antisymmetric nature of the wavefunction and does not have a classical counterpart. Within HF theory, the approximated wavefunction captures partially the nature of a many electron system, however it can never replace the exact wavefunction. As such, the total energy determined by the HF theory (E^{HF}) always exceeds the exact ground state energy E_0 and the difference the

correlation energy, E_C^{HF}, written as:

$$E_C^{HF} = E_0 - E^{HF}. \tag{2.18}$$

The difference mainly comes from quantum mechanical many particle contributions to the total energy which are not captured by a single Slater determinant wavefunction. Precisely, it originates from neglecting the electronic correlation caused by the instantaneous repulsion of the electrons. Furthermore, even for HF theory the computational cost grows rapidly with the number of electrons ($\sim N^4$). Therefore, a different approach is needed to tackle a realistic system of interacting electrons. Indeed, Density Functional Theory (DFT) achieves this by mapping the many-body wavefunction $\Psi\{\mathbf{r}_i\}_{i=1}^{N_e}$ onto the electron density $n(\mathbf{r})$ as the basic quantity of interest.

2.5 Density Functional Theory

The main idea behind the DFT formalism is that the total energy of the interacting electronic system can be written as a universal functional of the equilibrium electron density $n(\mathbf{r})$. For a collection of N_e interacting electrons, the spin-polarized density $n^\sigma(\mathbf{r})$ is defined by

$$n^\sigma(\mathbf{r}) = N_e \sum_{\{\sigma_i\}_{i=2}^{N_e}} \int d\mathbf{r}_2 d\mathbf{r}_3 ... d\mathbf{r}_{N_e} |\Psi(\mathbf{x}_1, \mathbf{x}_2, ..., \mathbf{x}_{N_e})|^2 \tag{2.19}$$

subjected to the constraint $\langle\Psi|\Psi\rangle = 1$. Here $\sigma = \uparrow (\frac{1}{2})$ or $\downarrow (-\frac{1}{2})$ is the z-component of the spin and

$$n(\mathbf{r}) = n_\uparrow(\mathbf{r}) + n_\downarrow(\mathbf{r}), \tag{2.20}$$

Also,

$$\sum_{\{\sigma_i\}_{i=2}^{N_e}} \int d\mathbf{r}\; n^\sigma(\mathbf{r}) = N_e. \tag{2.21}$$

As a consequence the electronic structure problem reduces to a three spatial-dimensional one, regardless of the number of electrons in the system, while the many-electron wavefunction $\Psi\{\mathbf{r}_i\}_{i=1}^{N_e}$ depends on the $3N_e$ spatial coordinates.

2.5.1 The Hohenberg-Kohn Theorem

The foundation of the DFT is based on the Hohenberg-Kohn theorems [97], summarized by the following statements:

I. The ground states density $n_0(\mathbf{r})$ of a system of interacting particles uniquely determines the external potential V_0 within an additional constant. Since $n_0(\mathbf{r})$ considers the entire spectrum of many-body Hamiltonian except for a constant shift of the energy, the ground and excited states of the many-body wavefunction can be extracted, implying that $n_0(\mathbf{r})$ uniquely and completely determines all properties of the system.

II. For a given external potential $V_{ext}[n^\sigma]$, the total energy functional $E[n^\sigma]$ is written as

$$E[n^\sigma] = T[n^\sigma] + V_{ee}[n^\sigma] + V_{ext}[n^\sigma], \tag{2.22}$$

where the $T[n^\sigma]$ and $V_{ee}[n^\sigma]$ are the kinetic energy and the electron-electron interaction energy functionals. As the total energy is a functional of the electron density, the variational principle provides that for any trial density, $n_t(\mathbf{r})$, the total energy exceed the true ground state energy E_0, *i.e.* $E_0 \leq E[n_t]$, where the equality sign holds if and only if $n_t = n_0$.

Note that $F_{HK}[n^\sigma] = T[n^\sigma] + V_{ee}[n^\sigma]$ is a universally valid functional as it does not depend on the external potential of the specific system. Unfortunately, the universal functional $F_{HK}[n^\sigma]$ is unknown, implying that properties of a system are still impossible to extract with this framework. This problem is overcome by the Kohn-Sham scheme [98] discussed below.

2.5.2 The Kohn-Sham Scheme

The Kohn-Sham formalism maps a many-body interacting electronic systems into a systems of non-interacting electrons moving in a Kohn-Sham effective potential, which generates the identical ground state density and energy as those of the interacting system. The Kohn-Sham total energy functional, $E[n(\mathbf{r})]$, is expressed as,

$$E[n(\mathbf{r})] = T_s[n(\mathbf{r})] + \int d\mathbf{r}\; n(\mathbf{r})\; V_{ext}(\mathbf{r}) + U_{ee}[n(\mathbf{r})] + E_{xc}[n(\mathbf{r})], \tag{2.23}$$

where first term is the non-interacting kinetic energy functional, the second term is the interaction of the electrons with the external potential, $V_{ext}(\mathbf{r})$, the third term is the

classical Coulomb repulsion (Hartree) energy of the electron density $n(\mathbf{r})$, *i.e.*

$$U_{ee}[n(\mathbf{r})] = \frac{1}{2}\int d\mathbf{r}\int d\mathbf{r}'\frac{n(\mathbf{r})n(\mathbf{r}')}{|\mathbf{r}-\mathbf{r}'|}, \tag{2.24}$$

and the last term is the exchange-correlation (XC) energy, E_{xc}, which is defined to include everything neglected by the first three terms, *i.e.*

$$E_{xc}[n(\mathbf{r})] = T[n(\mathbf{r})] - T_s[n(\mathbf{r})] + V_{ee}[n(\mathbf{r})] - U_{ee}[n(\mathbf{r})]. \tag{2.25}$$

E_{xc} is not known exactly and needs to be approximated. Here the fundamental difference between the DFT and HF formalisms is that HF theory includes the exchange energy exactly, whereas DFT can capture both exchange and correlation effects in an approximate way. Finally in the KS-DFT method, the following set of one-particle Schrödinger-like equation, called Kohn-Sham equation can be obtained:

$$\left[-\frac{1}{2}\nabla^2_{\mathbf{r}} + V_{KS}[n(\mathbf{r})]\right]\psi_\alpha^{KS}(\mathbf{r}) = \varepsilon_\alpha\psi_\alpha^{KS}(\mathbf{r}). \tag{2.26}$$

Here $\psi_\alpha^{KS}(\mathbf{r})$ are the Kohn-Sham one-electron orbitals, which satisfy the orthonormality condition, *i.e.* $\langle\psi_\alpha^{KS}(\mathbf{r})|\psi_\beta^{KS}(\mathbf{r})\rangle = \delta_{\alpha\beta}$ and the KS effective potential V_{KS} is identified by,

$$V_{KS}[n(\mathbf{r})] = V_{ext}(\mathbf{r}) + \int d\mathbf{r}'\frac{n(\mathbf{r}')}{|\mathbf{r}-\mathbf{r}'|} + V_{xc}[n(\mathbf{r})], \tag{2.27}$$

where second term is the Hartree potential, V_H, and V_{xc}, is the exchange-correlation potential written as a functional derivative of the exchange correlation energy with respect to the density, *i.e.*

$$V_{xc}[n(\mathbf{r})] = \frac{\delta E_{xc}[n]}{\delta n(\mathbf{r})}. \tag{2.28}$$

The charge density is constructed in the following way,

$$n(\mathbf{r}) = \sum_{\alpha=1}^{N_e}\Theta(\mu-\varepsilon_\alpha)|\psi_\alpha^{KS}(\mathbf{r})|^2. \tag{2.29}$$

The step function Θ ensures that the summation is taken over all the occupied KS orbitals that minimize the total energy functional. The chemical potential, μ, satisfies the condition,

$$\int d\mathbf{r}\; n(\mathbf{r}) = N_e. \tag{2.30}$$

This implies that Eq.(2.26) can be solved by a self-consistent approach. Now with the orbitals $\psi_{KS}(\mathbf{r})$, the noninteracting kinetic energy can be calculated with the formula

$$T_s[n(\mathbf{r})] = \sum_{\alpha} \Theta(\mu - \varepsilon_\alpha) \langle \psi_\alpha^{KS}(\mathbf{r})| - \frac{1}{2}\nabla_{\mathbf{r}}^2 |\psi_\alpha^{KS}(\mathbf{r})\rangle. \tag{2.31}$$

Within the KS scheme, the total ground state energy E_{KS} does not apprear as the sum of the eigenvalues of the KS equation, [Eq. (2.26)], rather it is expressed as

$$E_{KS} = \sum_{\alpha=1}^{N_e} \Theta(\mu - \varepsilon_\alpha)\, \varepsilon_\alpha + E_{xc}[n] - \int d\mathbf{r}\; n(\mathbf{r}) V_{xc}[n(\mathbf{r})] - \frac{1}{2}\int d\mathbf{r} d\mathbf{r}' \frac{n(\mathbf{r})n(\mathbf{r}')}{|\mathbf{r} - \mathbf{r}'|}, \tag{2.32}$$

where the additional last three terms refer to the so called "double counting" corrections.

2.5.3 Approximated Exchange Correlation Functional

In principle, the KS ansatz enables us to predict the exact ground state density. However, in practice, the form of the XC-correlation energy E_{xc} is unknown and it needs to be approximated.

Local Density Approximation (LDA)

Indeed, Kohn and Sham proposed in their original work [98], the local density approximation (LDA) for the $E_{xc}[n(\mathbf{r})]$. Here, $E_{xc}[n(\mathbf{r})]$ at the position $\mathbf{r}$ depends only on the electron density at that given position, *i.e.*

$$E_{xc}^{LDA}[n(\mathbf{r})] = \int d\mathbf{r}\; n(\mathbf{r})\; \epsilon_{xc}[n(\mathbf{r})]. \tag{2.33}$$

The functional $\epsilon_{xc}[n(\mathbf{r})]$ is the exchange-correlation energy density for a homogeneous electron gas of density $n(\mathbf{r})$ [100, 101] and it is parametrized by using Quantum Monte Carlo methods [99] to reproduce highly accurate exact results. Although the LDA simplifies $E_{xc}[n(\mathbf{r})]$ by assuming that the electron density is homogeneous, it works reasonably well even in a system where the electron density is rapidly varying. This is accomplished by the fact that the underestimated correlation energy is compensated by the overestimated exchange energy. In general, the LDA overestimates the binding energies of the solids, while their bond-lengths typically are underestimated. This

approximation can be generalized to spin-polarized systems where it is called the Local Spin Density Approximation (LSDA), *i.e.* the $E_{xc}^{LDA}[n(\mathbf{r})]$ is modified as,

$$E_{xc}^{LSDA}[n_\uparrow(\mathbf{r}), n_\downarrow(\mathbf{r})] = \int d\mathbf{r}\; n(\mathbf{r})\; \epsilon_{xc}[n_\uparrow(\mathbf{r}), n_\downarrow(\mathbf{r})], \tag{2.34}$$

where, $n_\downarrow(\mathbf{r})$ and $n_\uparrow(\mathbf{r})$ are spin-up and spin-down electron densities respectively.

Generalized Gradient Approximation (GGA)

The inhomogeneity of the electron density is considered explicitly through the generalized gradient approximation (GGA) [102], where E_{xc} is a functional of the electron density and the gradient of the electron density,

$$E_{xc}^{GGA}[n_\uparrow(\mathbf{r}), n_\downarrow(\mathbf{r})] = \int d\mathbf{r}\; n(\mathbf{r})\; \epsilon_{xc}[n_\uparrow(\mathbf{r}), n_\downarrow(\mathbf{r}), \nabla n_\uparrow(\mathbf{r}), \nabla n_\downarrow(\mathbf{r})]. \tag{2.35}$$

Different flavors of GGA functional have been developed [103, 104, 105, 106] to capture more accurate features of the inhomogeneous system. GGA usually provides better results than LDA in calculating the bond-length, binding energy and atomization energies of solids and molecules.

Hybrid Functional

Hybrid functional was initially proposed within the framework of the adiabatic connection approach [107, 108], where the electron-electron interaction term gradually enters into noninteracting systems. Generally, the hybrid functionals $E_{xc}^{Hyb}[n(\mathbf{r})]$ are constructed such that these contain a fraction of exact HF exchange with LDA or GGA exchange and correlation, *i.e.* $E_{xc}^{Hyb}[n(\mathbf{r})]$ can be formally written as

$$E_{xc}^{\text{Hyb}}[n(\mathbf{r})] = aE_x^{\text{HF}} + (1-a)E_x^{\text{LDA(GGA)}} + E_c^{\text{LDA(GGA)}} \tag{2.36}$$

where the coefficient a is either determined experimentally or estimated theoretically. One of the most popular hybrid functional used in the condensed matter physics community is the HSE06 [109]. In that case E_{xc} is written as

$$E_{xc}^{\text{HSE}} = \frac{1}{4}E_x^{\text{HF,sr},\mu} + \frac{3}{4}E_x^{\text{PBE,sr},\mu} + E_x^{\text{PBE,lr},\mu} + E_c^{\text{PBE}}, \tag{2.37}$$

where (sr) and (lr) denote the short- and long-range parts of the respective exchange interaction (either HF or PBE exchanges). E_x^{PBE} and E_c^{PBE} denote the exchange and correlation energies calculated within the GGA [102]. The separation is obtained by decomposing the Coulomb kernel into the following expression

$$\frac{1}{r} = S_\mu(r) + L_\mu(r) = \frac{\text{erfc}(\mu r)}{r} + \frac{\text{erf}(\mu r)}{r} \tag{2.38}$$

where $r = |\mathbf{r} - \mathbf{r}'|$, and μ are the parameters to define the range-separation and they are related to a characteristic distance, $(2/\mu)$, at which the short-range interactions become negligible. The parameter μ is optimized empirically to a value approximately in the ranges $0.2 - 0.3$ Å^{-1} [109]. By using this hybrid functional, lattice constants and bulk moduli of solids are predicted more accurately than by the standard semi-local functional LDA/GGA [150].

LDA + Hubbard U (LDA+U)

The basic problem with the LDA/GGA functional is that the exchange correlation potential is orbital independent. Therefore, for a system containing "correlated" orbitals (d/f electronic shells) which produce strong correlation among themselves, LDA/GGA can not properly describe such system. This problem can be overcome by introducing LDA+U method, where electrons are classified into two parts: delocalized s/p electrons which are well described by LDA/GGA and localized d/f electrons for which additional energy term (Hubbard U [110]) is required to describe the d-d/f-f Coulomb interactions. In this method, a new energy functional E_{xc}^{LDA+U} is written [111, 112, 113] as

$$E_{xc}^{LDA+U} = E_{xc}^{LSDA} + E^U[\{p_m^\sigma\}] - E^{dc}[\{p_m^\sigma\}], \tag{2.39}$$

where E^U is the Hubbard energy, E^{dc} is the double counting term and both of the them depend on the orbital occupation p_m^σ of the correlated orbitals. Several forms of the E_{xc}^{LDA+U} have been suggested to date. Particularly, in a simple and transparent form [114, 115], the U parameter is redefined as an effective parameter $U_{\text{eff}} = U - J$ (J is the intra-atomic exchange energy for electrons) and the last two term in the Eq.(2.39) take the form,

$$E^U - E^{dc} = \frac{U_{\text{eff}}}{2} \sum_I \sum_{m\sigma} \left[p_{mm}^{K\sigma} - \sum_{m'} f_{mm'}^{K\sigma} p_{m'm}^{K\sigma} \right]. \tag{2.40}$$

Here the index of the atomic position K is separated out from the magnetic quantum number m and an off-diagonal population $p^{K\sigma}_{mm'}$ is introduced in the form $p^{K\sigma}_{mm'} = \sum_\alpha \langle\psi^\sigma_\alpha|\hat{P}^{K\Phi}_{mm'}|\psi^\sigma_\alpha\rangle$, where $\hat{P}^{K\Phi}_{mm'} = |\Phi^K_m\rangle\langle\Phi^K_{m'}|$. In Eq.(2.39) the correction added to the LDA functional depends on the two parameter U and J and they are chosen in such a way as to reproduce the particular properties of the system of interest. Therefore the method is not considered as fully *ab-initio*. Within this approximation the energy of the occupied strongly correlated orbital shifts to a lower level in energy while those of the unoccupied ones move the opposite way. This approximation describes transition metals and rare earth elements quite well.

Self Interaction Correction (SIC)

One of the fundamental problems associated with the semi-local functionals (LDA/GGA) is the presence of self interaction (SI) [116]. This is the unphysical interaction of an electron in a given KS orbital with the Hartree and XC potential generated by itself. Although exact DFT is SI free, generally LDA/GGA functionals include SI. Note that within HF theory the SI of occupied orbitals is exactly cancelled out. However, such a cancellation occurs partially when semi-local functionals are used and the rigorous condition of DFT,

$$U_{ee}[n^\sigma_\alpha] + E_{xc}[n^\sigma_\alpha, 0] = 0, \tag{2.41}$$

for the orbital density $n^\sigma_\alpha = |\psi^{KS}_{\alpha\sigma}|^2$ of a fully occupied KS orbital, $\psi^{KS}_{\alpha\sigma}$ is not satisfied. The SI is of significant impact for systems with highly localized states. In contrast, it tens to vanish for delocalized states as the charge extends over the crystal resulting a rapid decrease of the coulomb interaction ($\sim \frac{1}{N_e}$).
Since in a solid SIC is not uniquely defined, many different methods have been proposed in DFT calculations to explicitly reduce the effect of the SI via generating an orbital-dependent potential (see Ref. [117] for a review). These are generally based on the work of Perdew and Zunger [116]. Another alternative work, the atomic-SIC (ASIC) approximation is used in this thesis because it is computationally inexpensive and its foundation is described in Ref. [119]. The method is based on the work of Vogel *et al.* [118]. Later this work was extended by Filipptti and Spaldin [120]. The great advantage of the SIC formalism over the LDA+U method is that the selection of the strongly correlated is not required and there is no need for the parameters such as U, and J.
The ASIC approach provides a good description of a large range of materials [121, 122,

123]. Specifically, the computed bandgap and band alignment of semiconductors have a better agreement with experiment. However for some metals it provides a non-physical result, namely it may open an artificial gap (note that metals should be SI free).

2.5.4 The interpretation of Kohn-Sham eigenvalues

As mentioned earlier, the KS formalism maps the many body interacting problem onto N_e non-interacting one-electron problem with same ground state electron-density and ground state-energy. However, the KS eigenvalues are just a mathematical construct, namely they are the Lagrange multipliers needed to minimize the functional and to impose the orthonormality of the KS eigenfunctions. Moreover, it can be shown that the KS single Slater determinant wavefunction does not describe the true many-body wavefunction. Therefore, the significance of the eigenvalues and eigenfunctions needs to be justified. Indeed, the mathematical meaning of the KS eigenvalues is provided by Janak's theorem [127]: the KS eigenvalue, ε_α, can be expressed as the first order derivative of the total energy with respect to the states occupation, *i.e.*

$$\varepsilon_\alpha = \frac{\partial E}{\partial n_\alpha}, \tag{2.42}$$

In principle, the KS eigenvalues do not correspond to the energy of the actual excited states. However, it been shown shown [128] that in exact DFT, the highest occupied energy level ε_{HOMO} (for finite systems) is equal to the negative of the ionization energy (I), *i.e.* $\varepsilon_{HOMO} = -I$. For a solid system, this is equivalent to the fact that the chemical potential μ in exact DFT is same as the true Fermi energy [127]. Although this relation is rigorous for the exact exchange-correlation potential, in many cases 'I' can be calculated by taking total energy differences, *i.e.* $I = E(N_e - 1) - E(N_e)$, where $E(N_e)$ is the ground state energy of the system containing N_e interacting electrons. Similarly, the electron affinity, A, can be extracted from $A = E(N_e) - E(N_e + 1)$. This refers to the fact that the electron affinity of a system of N_e electrons is equal to the ionization energy of a system of $(N_e + 1)$ electrons.
It is stated that in the KS formalism only the highest occupied KS level has a physical meaning. However, in practice the KS eigenstates and the bandstructures are routinely compared to the experimental bandstructure of real systems. The bandgap of molecular or semiconducting systems containing N_e electrons is defined [94, 129] as

$$\Delta_{bg} = -[E(N_e) - E(N_e - 1)] + [E(N_e + 1) - E(N_e)], \tag{2.43}$$

$$= \begin{cases} I - A & \text{(molecules)} \\ \mu(N_e+1) - \mu(N_e) & \text{(semiconductor)} \end{cases} \tag{2.44}$$

where $E(N_e)$, A, $\mu(N_e)$ are the ground state energy, the electron affinity and the chemical potential (solid) of the system containing N_e interacting electrons, respectively. The predicted KS bandgap Δ_{bg}^{KS} for solid semiconductors or molecules, *i.e.* the energy difference between the highest occupied (ε_{HOMO}) and lowest unoccupied (ε_{LUMO}) energy level, is not expected to be the real gap of the system due to the derivative discontinuity [129] of the energy XC functional E_{xc} at integer occupancy. Thus,

$$\left.\frac{\delta E_{xc}[n]}{\delta n(\mathbf{r})}\right|_{N_e+\delta} - \left.\frac{\delta E_{xc}[n]}{\delta n(\mathbf{r})}\right|_{N_e-\delta} = \Delta^{xc}, \tag{2.45}$$

where, δ is the infinitesimal variation of the total electron N_e. Meanwhile, the actual gap Δ_{bg}^{actual} is defined as

$$\Delta_{bg}^{actual} = \Delta_{bg}^{KS} + \Delta^{xc} \tag{2.46}$$

Since, Δ^{xc} is positive, the predicted KS bandgaps are expected to be smaller than the real one. In another word, unless the derivative discontinuity is accurately captured, one must be careful of the DFT calculations in which extracting information depends on the bandgap and the position of the KS-HOMO level. Specifically, the LDA functional does not have a derivative discontinuity in the exchange-correlation potential. Therefore, the predicted bandgap is typically underestimated by a considerable amount, for example it is around 50 % for weakly correlated semiconductors [130].

2.6 Beyond DFT: G_0W_0 method

Photoemission (PE) [131] and inverse photoemission (IPE) [132] spectroscopy are the main experimental methods used to probe, respectively, the occupied and unoccupied states of real systems. Usually PE/IPE spectra are interpreted in terms of single particle excitations. It was mentioned before that DFT eigenvalues are not the real single-particle excitation energies. Therefore, in order to compare theory with PE/IPE, one needs to introduce the concept of quasi-particle energies for the interacting many electronic (N_e) system. The many-body α^{th} eigenstate follows the Schödinger equation $\hat{H}_e|N_e,\alpha\rangle = E(N_e,\alpha)|N_e,\alpha\rangle$, where $\hat{H}_e$ is the many-body Hamiltonian and $E(N_e,\alpha)$ is total energy defined as $E(N_e,\alpha) = \langle N_e,\alpha|\hat{H}|N_e,\alpha\rangle$. The αth excitation energy ε_α of the many-body states created by the addition and removal of an electron in the

PE/IPE process and the corresponding transition amplitude $\psi_\alpha(\mathbf{r})$ are defined

$$\left.\begin{array}{l}\varepsilon_\alpha = E(N_e+1,\alpha) - E(N_e)\\ \psi_\alpha(\mathbf{r}) = \langle N_e|\hat{\psi}(\mathbf{r})|N_e+1,\alpha\rangle\end{array}\right\} \quad \text{for } \varepsilon_\alpha \geq E_F. \tag{2.47}$$

$$\left.\begin{array}{l}\varepsilon_\alpha = E(N_e) - E(N_e-1,\alpha)\\ \psi_\alpha(\mathbf{r}) = \langle N_e-1,\alpha|\hat{\psi}(\mathbf{r})|N_e\rangle\end{array}\right\} \quad \text{for } \varepsilon_\alpha < E_F. \tag{2.48}$$

Here, the field operator $\hat{\psi}(\mathbf{r})$ annihilates an electron from the many-body states $|N_e+1\rangle$ or $|N_e\rangle$, and E_F is the Fermi energy of the system. In Eq. (2.47), ε_α is interpreted as the excitation energy from the N_e-electron ground state with total energy $E(N_e)$ into an excited state of the (N_e+1)-electron system with total energy $E(N_e+1)$ upon addition of one electron. Similarly, upon removal of one electron from the system ε_α, corresponds to the total energy difference of the excited $N_e - 1$-electrons system and the ground states [see Eq.(2.48)].
Now the excited state energy ε_α and the wavefunction ψ_α are solutions of the equation

$$\left[\hat{h}(\mathbf{r}) + V_H(\mathbf{r})\right]\psi_\alpha(\mathbf{r}) + \int d\mathbf{r}'\Sigma^{G_0W_0}(\mathbf{r},\mathbf{r}';\varepsilon_\alpha)\psi_\alpha(\mathbf{r}') = \varepsilon_\alpha\psi_\alpha(\mathbf{r}) \tag{2.49}$$

where, $\hat{h} = T_S + V_{ext}$ (T_S = single particle kinetic energy term) and V_H is the Hartree potential. Using the Hedin's G_0W_0 approximation [133], the self energy $\Sigma^{G_0W_0}$ is given by

$$\Sigma^{G_0W_0}(\mathbf{r},\mathbf{r}';\varepsilon) = \frac{i}{2\pi}\int d\omega' e^{-i\omega'\delta}G_0(\mathbf{r},\mathbf{r}';\omega+\omega')W_0(\mathbf{r},\mathbf{r}';\omega'). \tag{2.50}$$

where δ is an infinitesimal time and $G_0(\mathbf{r},\mathbf{r}';\omega)$ is the single particle Green's function which is defined by the equation [134]

$$G_0^{-1}(\mathbf{r},\mathbf{r}';\omega) = [\omega - \hat{h}(\mathbf{r}) - V_H(\mathbf{r})]\delta(\mathbf{r}-\mathbf{r}'). \tag{2.51}$$

W_0 is the screened Coulomb interaction. The non-interacting Green's function [136] is given by,

$$G_0(\mathbf{r},\mathbf{r}';\omega) = \sum_\alpha \frac{\phi_\alpha^*(\mathbf{r})\phi_\alpha(\mathbf{r}')}{\omega - \varepsilon_\alpha^0 \pm i\delta_\alpha} \tag{2.52}$$

where, ε_α^0 and ϕ_α are the eigenvalues and the eigenstates of the non-interacting system. Then the screened Coulomb interaction W_0 can be calculated from the polarizability function

$$P_0(\mathbf{r},\mathbf{r}';\omega') = -\frac{i}{2\pi}\int d\omega' G_0(\mathbf{r},\mathbf{r}';\omega+\omega')G_0(\mathbf{r}',\mathbf{r};\omega') \tag{2.53}$$

and the bare Coulomb potential V_{ee} are related by the Dyson-type equation $W_0 = V_{ee} + V_{ee}P_0W_0$ [137]. Although the formalism of the quasi-particle Eq. (2.49) is formally simple, it is difficult to solve due to the non-local self energy term. However, the DFT can be helpful in this task. DFT can reproduce the exact ground-state and within the KS scheme it follows the equation

$$\left[\hat{h} + V_{ext} + V_{xc}\right]\psi_\alpha^{KS} = \varepsilon_\alpha^{KS}\psi_\alpha^{KS}. \tag{2.54}$$

Combining Eq.(2.49) and (2.54) and using the first order perturbation theory [135], the quasi-particle energies $\varepsilon_{\mathbf{k}\alpha}^{QP}$ are written as,

$$\varepsilon_\alpha^{QP} = \varepsilon_\alpha^{KS} + \langle\psi_\alpha^{KS}(\mathbf{r})|\Sigma^{G_0W_0} - V_{xc}|\psi_\alpha^{KS}(r)\rangle. \tag{2.55}$$

It is found that the G_0W_0 correction applied to the KS schemes based on the Hybrid functional (HSE06) yields overall agreement with the experimental bandgaps, while improvements are generally small when LDA/GGA semilocal functionals are used [150].

2.7 Equilibrium Geometry and Phonon Spectrum

Many physical properties of solids such as the specific heat, the thermal conduction, the resistivity of metals, the optical spectra, the superconductivity *etc*, depend on the lattice (phonon) dynamics. Such dynamics, within the BO approximation is determined by the Schrödinger equation given by,

$$\left[-\frac{1}{2}\sum_{K=1}^{N_N}\frac{\nabla_{\mathbf{R}_K}^2}{M_K} + \sum_{K<S}^{N_N}\frac{Z_KZ_S}{|\mathbf{R}_K - \mathbf{R}_S|} + \hat{H}_e(\mathbf{r};\mathbf{R})\right]\Psi(\mathbf{r};\mathbf{R}) = E(\mathbf{R})\Psi(\mathbf{r};\mathbf{R}), \tag{2.56}$$

where $\hat{H}_e(\mathbf{r};\mathbf{R})$ is the electronic part of the Hamiltonian as described in the Eq.(2.4). For a system of interacting electrons moving in a static field of nuclei, the ground state energy $E_0(\mathbf{R})$ is defined as

$$E_0(\mathbf{R}) = E_0^{el}(\mathbf{r};\mathbf{R}) + E^{Nu}(\mathbf{R}) \tag{2.57}$$

with $E^{Nu}(\mathbf{R})$, being the nucleus-nucleus interaction energy, *i.e.*

$$E^{Nu}(\mathbf{R}) = \sum_{K<S}^{N_N} \frac{Z_K Z_S}{|\mathbf{R}_K - \mathbf{R}_S|}. \tag{2.58}$$

Taylor series expansion of the total energy $E(\mathbf{R})$ of a dynamical system about the equilibrium structure at $\mathbf{R} = \mathbf{R_0}$ is given by

$$E(\mathbf{R}) = E_0(\mathbf{R}_0) + \sum_K \mathbf{F}_K \, \delta\mathbf{R}_K + \frac{1}{2}\sum_{KS} C_{KS} \, \delta\mathbf{R}_K \delta\mathbf{R}_S + ... \tag{2.59}$$

In the Eq.(2.59), the $\mathbf{F}_K$ and the C_{KS} are identified as the force acting on the Kth nucleus and the interatomic force constant between the Kth and the Sth nucleus, respectively. Thus,

$$\mathbf{F}_K = -\frac{\partial E(\mathbf{R})}{\partial \mathbf{R}_K}\bigg|_{\mathbf{R}_0} \tag{2.60}$$

$$C_{KS} = \frac{\partial^2 E(\mathbf{R})}{\partial \mathbf{R}_K \partial \mathbf{R}_S}\bigg|_{\mathbf{R}_0} \tag{2.61}$$

The first order energy derivative in Eq.(2.60) can be calculated by using the Hellman-Feynman theorem [138] and the equilibrium structure is found by solving the equation $\mathbf{F}_K = 0$. In contrast, within the linear response formalism [139, 140], C_{KS} can be written in the form,

$$C_{KS} = \int \frac{\partial n(\mathbf{r};\mathbf{R})}{\partial \mathbf{R}_S} \frac{\partial V(\mathbf{r})}{\partial \mathbf{R}_K} + \int n(\mathbf{r};\mathbf{R}) \frac{\partial^2 V(\mathbf{r})}{\partial \mathbf{R}_K \partial \mathbf{R}_S} d\mathbf{r} + \frac{\partial^2 E^{Nu}(\mathbf{R})}{\partial \mathbf{R}_K \partial \mathbf{R}_S}. \tag{2.62}$$

Here, $n(\mathbf{r}, \mathbf{R})$ is the ground states electronic density at the nuclear position $\mathbf{R}$, $\delta V(\mathbf{r})$ is the external perturbation to the potential $V(\mathbf{r})$ acting on the interacting electrons when the nucleus are fixed. Within the DFT framework, the $V(\mathbf{r})$ is replaced by the KS potential V_{KS} [see the Eq.(2.27)] and the C_{KS} can be calculated with by using the density functional perturbation theory (DFPT) [140].
The phonon frequencies ω can be obtained by diagonalizing the $C_{KS}^{\alpha\beta}$ matrix, *i.e* by solving the secular equation

$$\sum_{S,\beta} (C_{KS}^{\alpha\beta} - M_K \omega^2 \delta_{KS} \delta_{\alpha\beta}) U_S^{\beta} = 0, \tag{2.63}$$

where U_S^{β} is the βth Cartesian component of the displacement vector $\delta\mathbf{R}_S$. In crystals, the frequencies are classified by a wavevector $\mathbf{q}$. Phonon $\omega(\mathbf{q})$ and displacement

patterns $\widetilde{U}_t^{\beta}(\mathbf{q})$ are determined by the secular equation:

$$\sum_{t,\beta} \left(\widetilde{C}_{st}^{\alpha\beta} - M_s \omega_q^2 \delta_{st} \delta_{\alpha\beta}\right) \widetilde{U}_t^{\beta} = 0. \tag{2.64}$$

Here, M_s is the mass of the sth atom in one unit cell. $\widetilde{C}_{st}^{\alpha\beta}$ is the Fourier transform of $C_{st}^{\alpha\beta}$ at $\mathbf{q}$, *i.e.*

$$\widetilde{C}_{st}^{\alpha\beta}(\mathbf{q}) = \sum_{\mathbf{R}} e^{-i\mathbf{q}\cdot\mathbf{R}} C_{st}^{\alpha\beta}. \tag{2.65}$$

This approach allows us to calculate the phonon spectra throughout the entire Brillouin zone but it is limited to the harmonic approximation.

2.8 Computational Methods

KS-DFT schema have been implemented in many different numerical codes in recent days. These enable the electronic structure and crystal structure calculations. However, the accuracy of the results as well as the computational costs depend on the two main features of the specific numerical DFT code:
I. The type of the basis set used to expand the KS eigenfunctions, the electronic density and the KS potential.
II. The efficiency to capture the effect of the core electrons residing close to the nucleus.

2.8.1 Basis Sets

Within the numerical DFT method, the KS eigenfunctions are typically expanded by using two popular classes of basis set, namely plane waves and atom-centered linear combination of atomic orbitals (LCAO).

Plane waves

In a solid where the electrons move in a periodic potential, the Bloch theorem ensures that their wavefunctions can be obtained from the Fourier expansion over a set of plane waves [141]. This leads to the fact the KS eigenfunction can written as

$$\psi_\alpha(\mathbf{r}) = \sum_{\mathbf{k}} C_{\alpha\mathbf{k}} u_{\alpha\mathbf{k}}(\mathbf{r}) e^{-i\mathbf{k}\cdot\mathbf{r}} \tag{2.66}$$

where $\mathbf{k}$ denote the wave vector and the summation is taken over the entire Brilloiun zone. $u_{\alpha\mathbf{r}}$ is the periodic Bloch function. The increasing value of $|\mathbf{k}|$ makes the computational power costly. The numerical accuracy is set by truncating the plane wave basis set such that the highest electronic kinetic energy $\frac{|k^2|}{2} < E_{cut}$.

Linear Combination of Atomic Orbitals (LCAO)

Another approach used in the molecular physics community constructs the eigenvectors with analytic functions, such as Slater type orbitals or numerical atomic orbitals. Typically, the eigenvectors are constructed from a finite number of atom centered basis functions,

$$\psi_{\alpha}(\mathbf{r}) = \sum_{\beta} C_{\alpha\beta}\phi_{\beta}(\mathbf{r}), \tag{2.67}$$

where $\phi_{\beta}^{K}(\mathbf{r})$ is a numerical basis function centered on the Kth atom that decays rapidly from the nucleus. Within the LCAO scheme the $\phi_{\beta}^{K}(\mathbf{r})$ orbitals are chosen to be atomic orbitals, *i.e* they are products of radial functions $\phi_{nl}^{K}(r_K)$ and spherical harmonics $Y_{lm}^{K}(\theta, \varphi)$. Thus,

$$\phi_{\beta}^{K}(\mathbf{r}) \equiv \phi_{nlm}^{K}(\mathbf{r}) = \phi_{nl}^{K}(r_I)Y_{lm}^{K}(\theta, \varphi), \tag{2.68}$$

where, n, l, m refer to the principal, azimuthal and the magnetic quantum numbers, respectively. The values of l, and m may be arbitrarily large. Generally several orbitals with same angular dependence are used to construct the basis set, formally known as multiple-ζ basis sets [125].
The main advantage of using plane wave calculations is that it is easy to handle relatively large systems due to the availability of efficient fast Fourier transform techniques [126]. For non-periodic systems plane waves basis become inefficient computationally. However, localized basis sets like LCAO are helpful in that purpose.

2.8.2 Pseudo-potential

Electrons in solids and molecules arrange in a valence part and a core part, with the chemical bonding, and the electron conduction being mainly determined by the valence electrons. In contrast, core electrons remain unperturbed by the chemical environment, *i.e.* the effects on their energy levels are small. Therefore, in order not to include the core electrons explicitly, the pseudo-potential (PP) approach is introduced [124]. Here,

the individual contributions of the core electrons and the nuclear potential is incorporated into a single effective potential that acts on valence electrons. The great advantage of this technique is that it reduces the number of basis functionals needed to construct the electron density.

Real-wavefunctions for the valence electron are replaced by the pseudo-wavefunctions, which are constructed in such way to match to the real wavefunctions beyond a certain length r_c (the cut off radius) and having the oscillating part of the core region replaced by a nodeless smooth function. Consequently the electronic large kinetic energy induced in the core region is roughly compensated by the large potential energy from the coulomb interaction. The PP is constructed by considering the fact that it has to be norm-conserving [142], *i.e.* the norm of the true and the pseudo-wavefunction must be same. Note that a PP needs to be created separately for the each individual atomic species and the pseudo-eigenvalues of the valence electrons should match the real ones for the chosen atomic configuration. The above constraints lead to the fact that the pseudo-potential can be separated into two parts: a local potential $V_{local}(r)$ describing the region $r > r_c$ and a non-local potential described the region $r < r_c$. The semilocal form (depending on the angular momentum l) of the pseudo-potential $V_l(r)$ can be transformed into a fully nonlocal form as proposed by Kleinman and Bylander [143]. Another important criterion to construct a pseudo-potential is transferability [142], *i.e*, the $V_l(r)$ and the all electron potential are equal beyond r_c. Thus, $\delta V(r) = 0$ for r_c. Some DFT codes deal with a specific class of pseudo-potentials called ultra-soft [144, 145] in which the non-conserving constraint is lifted, but the transferability criterion is still present. Therefore the pseudo-wavefunctions can be made much smoother than with standard PP. Consequently, the computational cost is much cheaper as the the number of basis functional is reduced.

A drawback of the pseudo-potential approach is that often a complicated nonlinear core correction is necessary [146] for systems where the overlap between the core and the valence electron densities is significant. This deficiency can be eliminated by using an approach called the project-augmented wave (PAW) method [147, 148]. Unlike the PP approach, the PAW method includes the nodal features of the valence orbitals. In this approach, linear transformation is used to rebuild the all electron wavefunctions from the pseudo wavefunctions [147, 148]. The great advantage of this method is that it not only gives computational efficiency but also the accuracy of results obtained from all electron methods is achieved [149].

2.8.3 DFT Codes

In this thesis, several DFT codes (SIESTA, VASP, QUANTUM ESPRESSO) are employed to study the electronic and phonon properties of the materials. Many electronic structure calculations are carried out using a development version of SIESTA [125]. In the SIESTA code, the pseudo-potentials are norm-conserving and the LCAO method is used to construct the basis sets. Within our group, many useful features like the atomic self-interaction correction (ASIC) functional [119] and the LSDA+U are implemented additionally to the standard SIESTA code.

Two other DFT codes, VASP [150] and QUANTUM ESPRESSO [151] are used to study the electronic structure of a few materials. A plane-wave basis set is used in both of them. Both PAW and ultra-soft pseudo-potential are included in the VASP code while QUANTUM ESPRESSO uses both norm-conserving and ultra-soft pseudo-potentials. Specifically, calculations based on the GW method are carried out with VASP while phonon properties studied with QUANTUM ESPRESSO.

Chapter 3

Effects of impurities and of the substrate on a MoS_2 monolayer

3.1 Introduction

Molybdenum di-sulfide (MoS_2) is a prototypical LTMD. Structurally, MoS_2 consists of covalently bonded S-Mo-S atoms arranged in 2D hexagonal planes (monolayers), which in its bulk form are stacked together by weak van der Waals (vdW) forces [152] (see Fig. 3.1). In the most stable structure of bulk MoS_2, the Mo atom coordination is trigonal prismatic (2H-MoS_2) and the space group of bulk MoS_2 is P63/mmc (point group D_{6h}^4). Bulk MoS_2 has an indirect bandgap of 1.23 eV, with the valence band maximum (VBM) located at Γ, and the conduction band minimum (CBM) along the Γ to K line in the Brillouin zone [see Fig. 3.1(d)]. It has been widely explored as a lubricant [153], catalyst [154], and a lithium ion battery anode [155] in the past. Many interesting properties have been found in bulk MoS_2. For example, superconductivity has been induced by intercalating alkali metals, with a critical temperature of up to 6.9 K ($Rb_{0.3}MoS_2$) [156, 157].

Recently, MoS_2 based LTMDs have been investigated due to the possibility of creating low dimensional nano-structures for a variety of applications [158, 159]. The experimental techniques used to fabricate such thin films include micro-mechanical cleavage, solution based exfoliation, laser-thinning, thermolysis, chemical vapor deposition (CVD), and electrochemical lithiation [160]. The aim is to produce thin-flakes

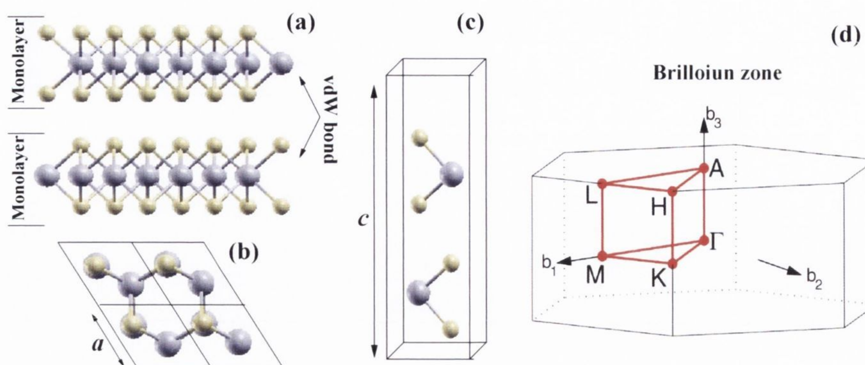

FIGURE 3.1: (a) MoS_2 bulk and monolayer. (b) and (c) Top and side view of the bulk MoS_2 unit cell. The primitive vectors are $\vec{a}_1 = (\frac{1}{2}a, \frac{\sqrt{3}}{2}a, 0)$, $\vec{a}_2 = (\frac{1}{2}a, \frac{\sqrt{3}}{2}a, 0)$, and $\vec{a}_3 = (0, 0, c)$. (d) The high symmetry k-points in the Brillouin zone of hexagonal crystal structure.

of MoS_2 in large-scale, keeping the cost of the synthesis low while preserving a sufficient quality of the film at the same time [160]. Such 2D nanostructures are gaining growing attention due to their potential for future nano-electronics applications, owing to their unusual physical, optical and electrical properties, which are a consequence of the quantum confinement associated to their ultra-thin structure [161]. Interestingly, the electronic properties of MoS_2 have a strong dependence on its thickness, *i.e.* the bandgap of MoS_2 increases with decreasing thickness, and at the monolayer limit the bandstructure exhibits a direct bandgap, leading to a photo-luminescence signal [69]. Therefore, light emitting devices such as photo-transistors [162] can be realized using a monolayer MoS_2, where the possibility of n- and p-type doping of MoS_2 is a key factor. Recently a photo-transistor based on a mechanically exfoliated monolayer MoS_2 nanosheet was fabricated, and a better photoresponsive was demonstrated when compared with graphene-based devices [159]. In particular, since MoS_2 monolayers have a direct bandgap of 1.90 eV, they may be a semiconducting alternative to graphene despite its large carrier mobility of up to $\sim 10^5$ cm^2/V·s), especially considering that graphene does not have a bandgap in its pristine form. The bandgap in graphene can be opened by making nanoribbons [163] or depositing graphene on substrates [164], at the cost however of deteriorating the carrier mobility due to edge and impurity scattering [165]. On the other hand, the absence of dangling bonds, high crystallinity, and the low dimensionality, make the performance of the LTMDs comparable to currently existing Si transistors at the scaling limit [166, 167, 168]. In fact, a monolayer MoS_2 transistor has recently been demonstrated at room temperature with a mobility in the range of 200-1000 cm^2/V·s, on/off current ratios of 10^8, and with low standby

power dissipation [169, 170]. This large mobility is obtained due to dielectric screening by using a top gate with high-κ dielectric materials [171]. On the other hand the room-temperature mobility is as low as ~0.5-3 $cm^2/V.s$ with the bottom gate only configuration [169].

Interestingly, both n-type [169, 172, 173, 174] and p-type [175, 176] conductivities have been reported in ultra-thin MoS_2 layers deposited on SiO_2. The conducting behavior of MoS_2 therefore seems to depend on the experimental details and an explanation for the specific current polarity (n- or p-type) remains far from clear. Note that no intentional doping was introduced in the experiments mentioned above, so that the origin of the different carrier types should be either intrinsic to the MoS_2 layer, to the substrate, or it can be due to the interaction between the two.

The possible creation of Mo and/or S vacancies during the growth can not be the cause of the varying conductive properties, since vacancies create deep levels at midgap in the bandstructure of a MoS_2 monolayer [177]. One possible way to set the conducting character in a well defined way is by substitutional doping. Although there are studies of specific dopants in single layer MoS_2 [177, 178, 179], so far to our knowledge there are no systematic studies which investigate the possibility to tune the conductivity by substitutional doping in single layered MoS_2. Moreover, the interfaces of the materials play a crucial for controlling the conductive properties of ultra-thin devices. For example, in a liquid-gated electric double layer transistor, the ions can modulate the electronic properties from insulator to metal through chemical doping in the channel at a finite bias [180]. Compared with other dopants, such as metals and light atoms, ionic liquids have several advantages as surface dopants: a large variety of such ionic complexes are available, and they can accumulate more carriers than conventional solid state gated transistors. In fact, ambipolar transistor operation has been achieved using thin flakes of MoS_2 in an ionic liquid-gated environment [181].

An ionic liquid (IL) is a molten salt, which consists of an inorganic anion and usually a large asymmetric organic cation. Due to the large size of their constituents and the typical chemical nature of the anions, the charges on the ions of these salt are diffuse. Consequently the electrostatic forces between the anions and cations become very weak and anisotropic. This results in difficulties to form a crystalline structure. Therefore they usually exist in liquid phase at room temperature. ILs are extensively used as solvent in chemical processes for synthesis and catalysis [182]. The structure of ILs is similar to that of table salt, namely as sodium chloride crystal made of positive sodium

ions and negative ions, not molecules. Schematic molecular structures of typical ionic liquids (ILs) are shown in Fig. 3.2.

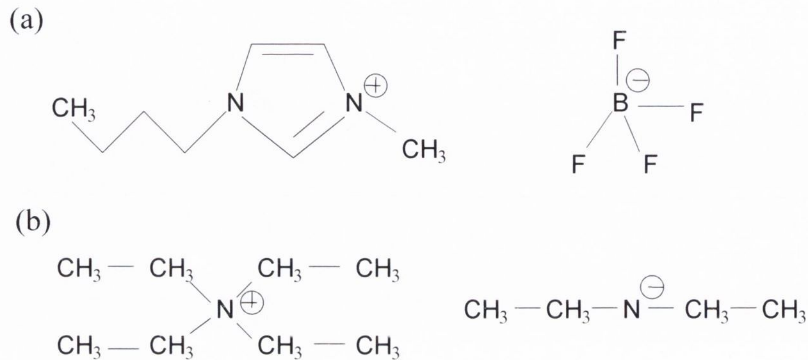

FIGURE 3.2: Schematic molecular structure of two ionic liquids (ILs). (a) 1-Butyl-3-methylimidazolium tetrafluoroborate and (b) N,N-diethyl-N-(2-methoxyethyl)-N-methylammonium bis(trifluoromethylsulphonyl-imide), DEME-TFSI. Left and right panels show the cations and anions, respectively.

Unlike ionic liquids, which usually act as a top gate dielectric, the substrate generally acts as a back gate dielectric in field effect transistors. Notably, disorder at the semiconductor/substrate interface in general plays a crucial role in determining the conductive properties of ultra-thin devices. For example, for GaAs nanowires it has been demonstrated that upon decreasing the nanowire diameter the interface-mediated conductivity gradually becomes dominant over the bulk one [183]. Since MoS_2 monolayers are placed on insulators in practically all device architectures, it is important to identify the possible effect the substrate has on the conductivity.

The defects responsible for the conductive properties of low dimensional devices are expected to be extrinsic in nature, such as charged impurities at the interface between the conductive channel and the substrate. These lead to an inhomogeneous Coulomb potential for both conduction and valence band electrons. Such charge traps have been identified to be in the form of adsorbates or defects at the surface of the underlying substrate in the case of graphene [184, 185]. Likewise, temperature dependent transport measurements on thin MoS_2 layers, down to the monolayer limit, suggest that trapped charges at the SiO_2 surface could be responsible for the observed n-type behavior, when MoS_2 is deposited on SiO_2 [186].

In general when charge traps are located at an interface, they influence the depletion/accumulation of electrons in the conducting channel up to a certain thickness,

which is proportional to the channel screening length. This distance depends on different physical features, such as the nature and the density of the traps, and the electronic properties of the channel. For conventional semiconductors it typically reaches up to a few nanometers. For instance it has been recently demonstrated that charge trap states at the substrate/channel interface significantly affect the conductivity of GaAs nanowires up to diameters of about 40-70 nm [183]. More dramatic effects are expected for layered compounds down to the single layer limit, in which essentially all the atoms are at the interface with the substrate, and the channel vertical dimension is certainly shorter than the screening length. Recently a reduction in conductivity with increasing MoS_2 film thickness has been observed in MoS_2-based transistors, where SiO_2 was used as the back gate [187]. This suggests that for the MoS_2/SiO_2 system the transport is interface-mediated, since intrinsic defects, homogeneously distributed in MoS_2, would not lead to any dependence of the conductivity on thickness.

In this chapter we have carried out two key investigations on monolayer layer MoS_2. Firstly, in Sec. 3.2 we systematically study the effects of impurities on the electronic structure of monolayer MoS_2. We also calculate formation energies to evaluate the stability of different systems, with the aim of finding possible candidates for n- and p-type semiconducting character. Specifically here we consider the impurities such as halogens, non-metals, transition metals, and alkali metals from the periodic table. The changes of the conductive properties of the monolayer MoS_2 due molecular ions (NH_4^+ and BF_4^-) absorbed at the surface are investigated.

Secondly, in Sec. 3.3 we aim to shed some light on the effects that trap states at the SiO_2 surface have on the conductive properties of MoS_2/SiO_2 hybrid systems. In particular we consider the case when the traps are due to impurities such as immobile Na and H atoms, as well as O-dangling bonds.

3.2 Effect of Impurities

3.2.1 Thermodynamics of impurity formation energy and transition level

Many important physical properties in a semiconductor, such as electrical conductivity and optical absorption, are often controlled by impurities in a semiconductor. These

properties play a crucial role in the efforts to boost the performance of a device for technological applications. To achieve such control, an extensive knowledge of the thermodynamic processes to control doping in semiconductor is required. In this context the energy position of the impurity levels, their formation energy and their thermodynamic transition levels, which are either deep or shallow in the bandgap, are the key quantities which need to be considered. The electronic states created by an impurity can be characterized experimentally by techniques such as photo-luminescence (PL) spectroscopy [20], sometimes generated by high energy electron irradiation [188]. The likelihood of such impurity formation can be directly estimated from a reciprocal function of the formation energy.

The formation energy of an impurity refers to the energy required to incorporate the impurity into a semiconductor host. The impurity formation energy can be estimated by a mathematical expression which is given by

$$E_{\text{form}}(X^q) = E_{\text{tot}}(X^q) - E_{\text{tot}}(\text{bulk}) - \sum_i n_i\mu_i + q(E_{\text{F}} + E_{\text{VBM}} + \Delta V), \tag{3.1}$$

where X^q denotes the impurity X in the charge state q, $E_{\text{tot}}(\text{bulk})$ and $E_{\text{tot}}(X^q)$ are total energies calculated for the pristine supercell and for the same supercell containing an impurity X, respectively. Here n_i is the number of species i added ($n_i > 1$) to or removed ($n_i < 1$) from the supercell and μ_i are the corresponding chemical potentials of species. E_{F} is the Fermi energy with respect to the valence band maximum level, E_{VBM}, in the bulk and ΔV is a correction term due to the fact that the supercell is charged [189]. The chemical potential largely depends on the experimental growth conditions. For example, in the case of MoS_2 monolayer it can be Mo-rich, S-rich or in between. Therefore in order to assess the solubility of an impurity one needs to consider the possible range of the chemical potentials. Under extreme Mo-rich conditions, the Mo chemical potential, μ_{Mo}, sets to an upper bound, *i.e.* $\mu_{\text{Mo}}^{max} = \mu_{\text{Mo}}(\text{bulk})$. Indeed, in thermodynamic equilibrium the Mo chemical potential can not exceed the energy of bulk Mo. If it does exceed, we will no longer be able to grow MoS_2. Similarly, the upper limit of the S chemical potential, μ_S, is given by $\mu_{\text{S}} = \mu_{\text{S}}(\text{S}_2)$, *i.e.*, the energy of S in the S_2 molecule. In contrast, the lower limit for the chemical potential can be estimated by minimizing the MoS_2 Gibbs free energy, $G_f(\text{MoS}_2)= \mu_{Mo} + 2\mu_S$. For the temperature in question, $T < T_F$ (T_F is the Fermi temperature) the free energy [190] is written as $G_{\text{solid}} \simeq E_{\text{solid}} + f_{\text{vib}}$, where E_{solid} and f_{vib} are the electrostatic energy and the vibrational energy, respectively. At in low temperature the contribution from

the vibrational energy is neglected. This means that $G_{\text{solid}} \approx E_{\text{solid}}$. In our theoretical approach, the ground-state electronic structure of the system is determined at the absolute zero temperature limit, *i.e*, $G_f = H_f$, where H_f is the enthalpy. The boundary of μ_{Mo} and μ_{S} are given by

$$\mu_{\text{Mo}}(\text{bulk}) > \mu_{\text{Mo}} > \mu_{\text{Mo}}(\text{bulk}) + \Delta H_f(\text{MoS}_2), \tag{3.2}$$

$$\mu_{\text{S}}(\text{S}_2, \text{molecule}) > \mu_{\text{S}} > \mu_{\text{S}}(\text{S}_2, \text{molecule}) + \frac{1}{2}\Delta H_f(\text{MoS}_2), \tag{3.3}$$

respectively. The chemical potentials can be estimated from the expression given by

$$\mu_{\text{Mo}} = E_{\text{tot}}(\text{Mo}, \text{bulk}) + \Delta H_f(\text{MoS}_2), \tag{3.4}$$

$$2\mu_{\text{S}} = E_{\text{tot}}(\text{S}_2, \text{molecule}) + \Delta H_f(\text{MoS}_2). \tag{3.5}$$

The total energies are calculated by considering that Mo is in a bulk metallic body-centered cubic (bcc) structure and S_2 is in the molecular phase. Similarly the formation enthalpy of bulk MoS_2 ,$\Delta H_f(\text{MoS}_2)$, can be calculated from the expression,

$$\Delta H_f(\text{MoS}_2) = E_{\text{tot}}(\text{MoS}_2, \text{bulk}) - \left[E_{\text{tot}}(\text{Mo}) + E_{\text{tot}}(\text{S}_2)\right]. \tag{3.6}$$

The $\Delta H_f(\text{MoS}_2)$ is estimated to -2.86 eV (with respect to bulk S), which is in good agreement with the experimental value of -185.3 kJ/mol (-1.92 eV) [192]. An impurity with high formation energy is always unlikely to form, since considerable energy is required for their incorporation into a semiconductor, whereas the driving force to lowering the energy of the system is large. In this work, we assume that MoS_2 is prepared at the Mo(S)-rich condition for anions (cations) substitutions, so there is no need to add ΔH_f term to μ_{Mo} and μ_{S} [see Eqs. (3.4) and (3.5)]. Beside we consider that the impurity states reside in a charge neutral state, *i.e.*, $q = 0$. The importance of the charged states is discussed below.

Most impurities, incorporated in a semiconductor can be found in multiple charging states. Moreover, impurity levels are usually created in the bandgap of the semiconductor. These levels play a key role for identifying the impurity center experimentally. However, the transitions between different charging states occur always for the levels which are relevant for experiments. These kind of levels can be characterized by the deep-level transient spectroscopy (DLTS) experiment and temperature dependent Hall experiments (reflects in the thermal ionization energy) for deep and shallow impurity

levels, respectively [189]. The relevant levels can not be directly extracted from by the Kohn-Sham energies, calculated for the impurity incorporated semiconductor.

The thermodynamic transition level, $\epsilon(q_1/q_2)$, is defined as the position of the Fermi level at which the formation energies of an impurity in its two charge states, say q_1 and q_2 become equal. Then $\epsilon(q_1/q_2)$ can be written as

$$\epsilon(q_1/q_2) = E_{\text{VBM}} + \frac{E(X^{q_2}) - E(X^{q_1})}{q_1 - q_2} \tag{3.7}$$

and the transition level can be calculated by using the total energy method, where $\epsilon(q_1/q_2)$ is expressed as

$$\epsilon(q_1/q_2) = [\{E_{\text{bulk}}(X^{q_1}) - E_{\text{bulk}}(X^{q_2})\} + \{E(X^{q_2}) - E(X^{q_1})\}]/(q_1 - q_2). \tag{3.8}$$

Here $E_{\text{tot}}(X^q)$ is the total energy of the supercell with an impurity X in the charging state q and $E_{\text{bulk}}(X^q)$ is the total energy for the same pristine supercell in the same charging state. We note that in this work we do not calculate transition energy levels, considering the fact that the impurity resides in a charge neutral state.

State-of-the-art first principle calculations, using density functional theory (DFT) have a major impact on the understanding of impurities in semiconductors. With the help of total energy calculations, it has become feasible to investigate the atomic structures of semiconductor doped by impurities. For this purpose the use of DFT-LDA has been well justified [189], since only total energies difference are meaningful here. The main drawback of the DFT-LDA is that it can not describe accurately the properties of excited states. It is observed that the bandgap is usually underestimated by LDA [191]. Due to the bandgap problem, the impurity states are incorrectly described and the formation energy of impurity may include a large error, particularly for charged states. Many corrections schemes such as LDA+U [113], GGA [224], GGA+U [113], SIC [116], ASIC [232] and hybrid Hartree-Fock DFT [109] have been introduced to solve this problem. For an estimation of such quantities, described by the excited states one needs to go beyond DFT and use the schemes such as GW approach and quantum Monte Carlo. However, these are computationally expensive compared to DFT-LDA approach. In this work, we only consider DFT-LDA and hybrid Hartree-Fock DFT (DFT-HSE06).

3.2.2 Methodology

To investigate the electronic and magnetic properties of a MoS_2 monolayer with impurities, *ab-initio* calculations are performed using density functional theory [97, 98] within the local spin density approximation (DFT-LSDA) of the exchange and correlation using the Ceperly-Alder parametrization [193], as implemented in the SIESTA code [125]. In our calculations, double-ζ polarized [195] numerical atomic orbitals basis sets are used for all atoms, and the Troullier-Martins scheme is used for constructing norm-conserving pseudo-potentials [194]. A (5×5) supercell (15.66 × 15.66 $\AA^2$), is constructed to simulate the single impurity effects in the monolayer MoS_2 [see Fig. 3.3(a)]. An equivalent plane wave cutoff of 250 Ry is used for the real space mesh, and the Brillouin zone sampling is done by using a (5×5×1) Monkhorst-Pack grid. Periodic boundary conditions are applied, and a vacuum layer of at least 15 Å is placed above the monolayer to minimize the interaction between the adjacent layers. The conjugate gradient method is used to obtain relaxed geometries. All atoms in the supercell are allowed to relax, until the forces on each atom are less than 0.02 eV/Å.

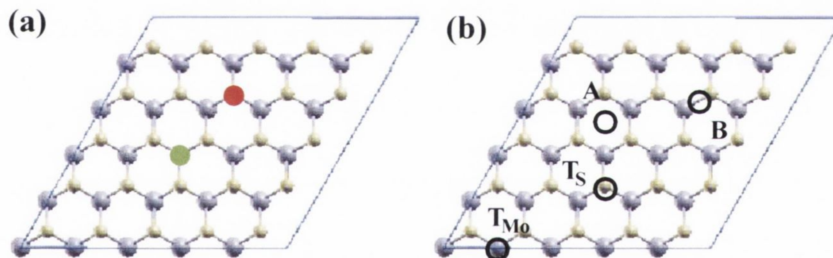

FIGURE 3.3: (a) The simulated (5×5) supercell of a doped MoS_2 monolayer where a Mo is substituted by a transition metal: Y, Zr, Nb, Re, Rh, Ru, Pd, Ag, Cd (solid red) and a S is substituted by the nonmetals P, N, and As, as well as by the halogens F, Cl, Br, and I (solid green). (b) The (5×5) supercell of an alkali atom (black circle) absorbed at different positions (T_{Mo}, T_S, A and B). Color code: light grey → Mo, light yellow → S

The formation energy is defined as

$$E_{form} = E_{tot}(MoS_2^*{+}X) - E_{tot}(MoS_2) - E_{bulk}(X) + E_{bulk}(host),$$

where $E_{tot}(MoS_2^*{+}X)$ is the total energy derived from a calculation with a substitutional atom X, $E_{tot}(MoS_2)$ is the total energy of the corresponding pristine MoS_2 monolayer supercell, $E_{bulk}(X)$ and $E_{bulk}(host)$ are the energies of a substitutional atom X and a

host atom Mo (S) respectively in their bulk (diatomic molecule) forms for the Mo (S) substitutions. On the other hand, the adsorption energy can be written as follows:

$$E_{\text{ads}} = E_{\text{tot}}(\text{MoS}_2\text{+Y})\text{-}E_{\text{tot}}(\text{MoS}_2)\text{-}E_{\text{bulk}}(\text{Y}),$$

where E_{tot} refers to our total energy results and E_{bulk} to the energy of an adsorbate Y in its bulk form. To find the most stable configuration for adsorption, we consider four different positions labelled T_{S} (adsorbate on top of S), T_{Mo} (adsorbate on top of Mo), A (adsorbate above the center of the hexagonal ring of MoS_2), and B (above the middle of the Mo-S bond) [see Fig. 3.3(b)]. We observe that the in-plane lattice constant of the system incorporated with an impurity converges to that of the pristine supercell, when its size is as large as (5×5). Moreover, the impurity formation energy or adsorption energy has indeed converged for this cell size.

In order to verify that the calculated impurity level alignments are robust against the choice of exchange correlation functional, we repeat the calculations for the main results using the screened hybrid functional of Heyd-Scuseria-Ernzerhof (HSE06) [199]. All DFT calculations based on the HSE06 functional are carried out with the projector augmented wave (PAW) pseudo potential plane-wave method [196] as implemented in the VASP code [197]. A 3×3×1 Monkhorst-Pack [198] **k**-point grid and a plane wave energy cutoff of 500 eV are used for the HSE06 calculations.

3.2.3 Electronic properties of bulk and monolayer

Our systematic study begins with calculating the electronic properties of MoS_2 in its bulk form. The optimized bulk MoS_2 unit cell parameters are $a = b = 3.137$ Å, $c/a = 3.74$, while the S-Mo-S bonding angle is 82.64°. These values are in good agreement with previous theoretical calculations [200] and also with the experimental ones of $a = b = 3.16$ Å, $c/a = 3.89$ [201]. The Mo-S bond length in bulk MoS_2 is found to be 2.42 Å, again in close agreement with the experimental value of 2.41 Å [201] and to the earlier theoretical estimate of 2.42 Å [63]. Bulk MoS_2 is a semiconductor and we predict an indirect bandgap of 0.64 eV between the Γ point and a point half way along the Γ-K line [see Fig. 3.4(a)]. Our calculated bandgap is smaller than the experimental one of 1.23 eV [200, 201] but it is in good agreement with existing density functional theory (DFT) calculations at the local spin density approximation (LSDA) level [200, 202]. It is well known that the LSDA systematically underestimates the

bandgap, so that such result is not surprising. However, we note here that the LSDA underestimation affects our results only at a marginal quantitative level.

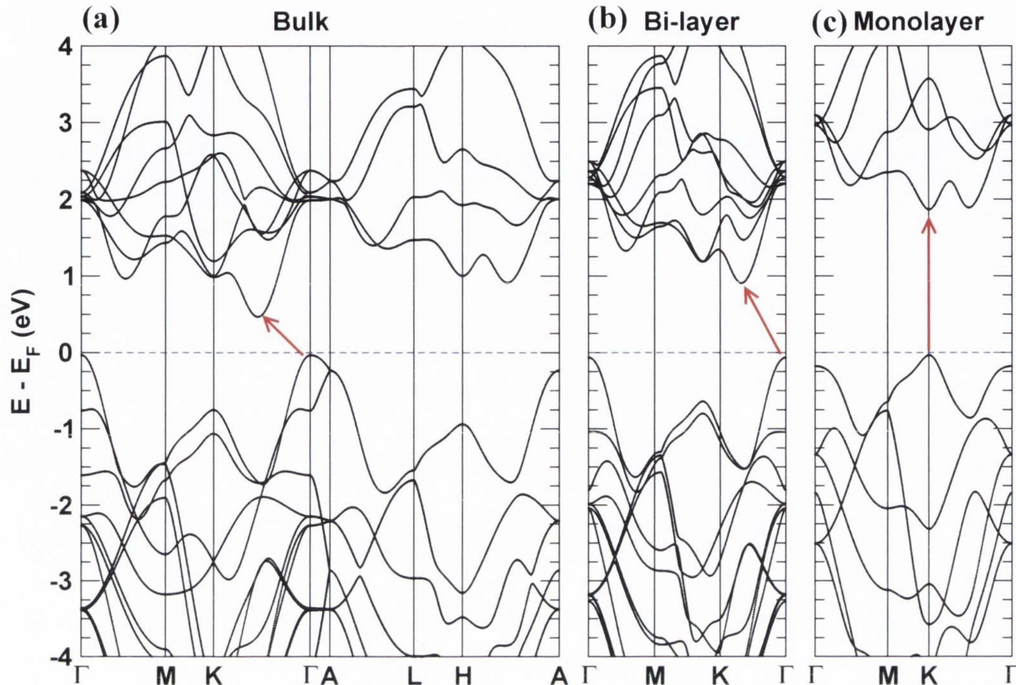

FIGURE 3.4: Calculated LDA-bandstructures of (a) bulk MoS_2, (b) bi-layer MoS_2, (c) monolayer MoS_2. The solid arrows indicate the position of the bandgap. Bulk MoS_2 and the bi-layer are characterized by an indirect bandgap. At the monolayer limit MoS_2 becomes a direct bandgap semiconductor. The blue dotted line indicates the valence band maximum.

Next we move to study the electronic properties of a single MoS_2 layer. Our optimized lattice constant, $a = b$, is now 3.132 Å, and therefore slightly smaller than that in the bulk. Such a value is in close agreement with the experimentally observed one of 3.15 Å [203]. Our calculations show that as the number of layers is decreased from the bulk to a few layers, the minimum of the lowest unoccupied band shifts from half way along the Γ-K line to K, with a single MoS_2 layer exhibiting a direct bandgap at K [see Fig. 3.4]. A similar conclusion was reached by comparing scanning photoelectron microscopy to DFT calculations [204]. For monolayer MoS_2 the bandgap becomes direct at the K point [see Fig. 3.4(c)]. This fact has been recently observed experimentally [69]. The computed LDA-bandgap of 1.86 eV is in good agreement with a recent experimental value of 1.90 eV [172], as well as a previous theoretically predicted value of 1.70 eV [205]. Both for the bulk and the single layer the bandstructure around the Fermi level, E_F, is derived mainly from Mo-4*d* orbitals, although there are smaller

contributions from the S-3p via hybridization within the layer [see the Fig. 3.5]. This is in good agreement with previous calculations [178].

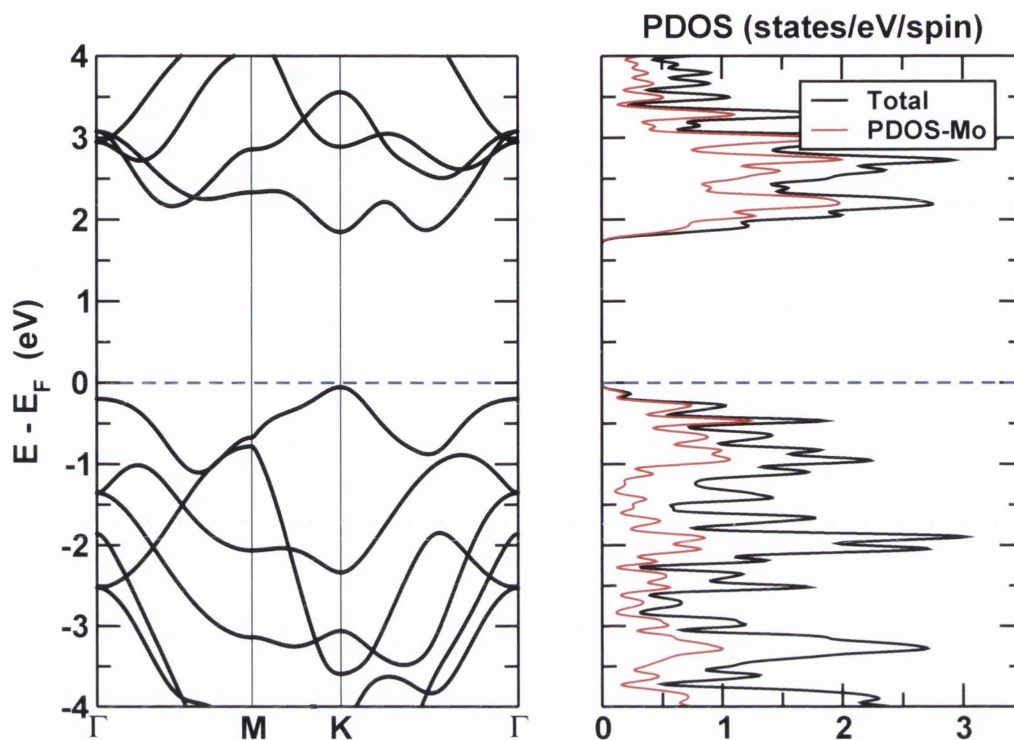

FIGURE 3.5: Left: The LDA-bandstructure of monolayer MoS_2. Right: The total DOS (black) and the projected DOS on Mo-4d (red) for monolayer MoS_2. The electronic states in DOS are Gaussian broadened by 0.05 eV.

Next, in the Sec. 3.2.4 and the Sec. 3.2.5, we study the effects on the electronic structure of monolayer MoS_2 due to substitutional doping and due to surface-adsorption of alkali atoms and of ionic molecules, for n-type and p-type dopants. We evaluate formation and adsorption energies for all dopants to infer the likelihood of formation in experiment (Table 3.1).

3.2.4 Substitutional doping

3.2.4.1 S substitutional doping

We begin by substituting a surface S atom with elements from the halogen family (F, Cl, Br, I), in order to create possible n-type impurities in the MoS_2 monolayer, since these have one more p electrons than S. We present the DOS for all the halogen

Impurity	$m(\mu_B/\text{defect})$	$E_{\text{form}}(\text{eV})$
F, Cl, Br	1.00	0.60 (F), 1.93 (Cl), 2.16 (Br)
I	0.00	2.53
N, P	1.00	2.90 (N), 1.89 (P)
As	0.00	1.91
Re	1.00	2.05
Ru	2.00	3.05
Rh	3.00	4.15
Pd	4.00	5.63
Ag	2.57	7.28
Cd	1.58	6.11
Nb, Zr, Y	0.00	-0.19 (Nb), -0.48 (Zr), 0.52 (Y)

TABLE 3.1: The theoretically calculated (DFT-LSDA) magnetic moment per defect, m, and the formation energy, E_{form}, of different substitutional dopants in the MoS_2 monolayer.

family (see Fig. 3.6). As a representative system, we start by illustrating results of the Cl doping, since the other ones are similar. The Cl doped MoS_2 monolayer has a magnetic ground state, where an occupied defect level is formed at about 0.4 eV below the CBM. The corresponding minority state is located above the CBM and is empty. These defect levels originate from the hybridization between the Cl-3p and the Mo-4d states. Similarly to the Cl substitution, for both F and Br dopants (iso-electronic to Cl) the systems are paramagnetic, having a magnetic moment (per defect) of $\approx 1\ \mu_B$. In the case of the F substitutional for S, the spin-splitting is larger than that of the Cl, whereas it is smaller for the Br substitutional case. Eventually, when substituting S with iodine, the system becomes nonmagnetic, but the impurity level is still located well below (0.3 eV) the CBM [see Fig. 3.6(d)].

We then investigate the possibility of p-type doping by replacing a S atom with an element from the group VA in the periodic table (N, P, As). When replacing S with N the system has a magnetic ground state [Fig. 3.7(a)], with a moment of $1\mu_{\text{B}}$ and ~0.20 eV of exchange splitting. In both spin channels gap states are introduced above the VBM, which are formed by a hybridization between the N-2p and the Mo-4d valence band states. Similarly, when substituting S with P, the system is again magnetic, but the defect states are rigidly shifted closer to the VBM of the pristine MoS_2 monolayer in both spin channels, with a spin splitting similar as before. Finally for the As substitutional case, the defect states shift even more towards the VBM. Additionally, the spin-splitting vanishes and the system becomes p-type semiconducting. The partially

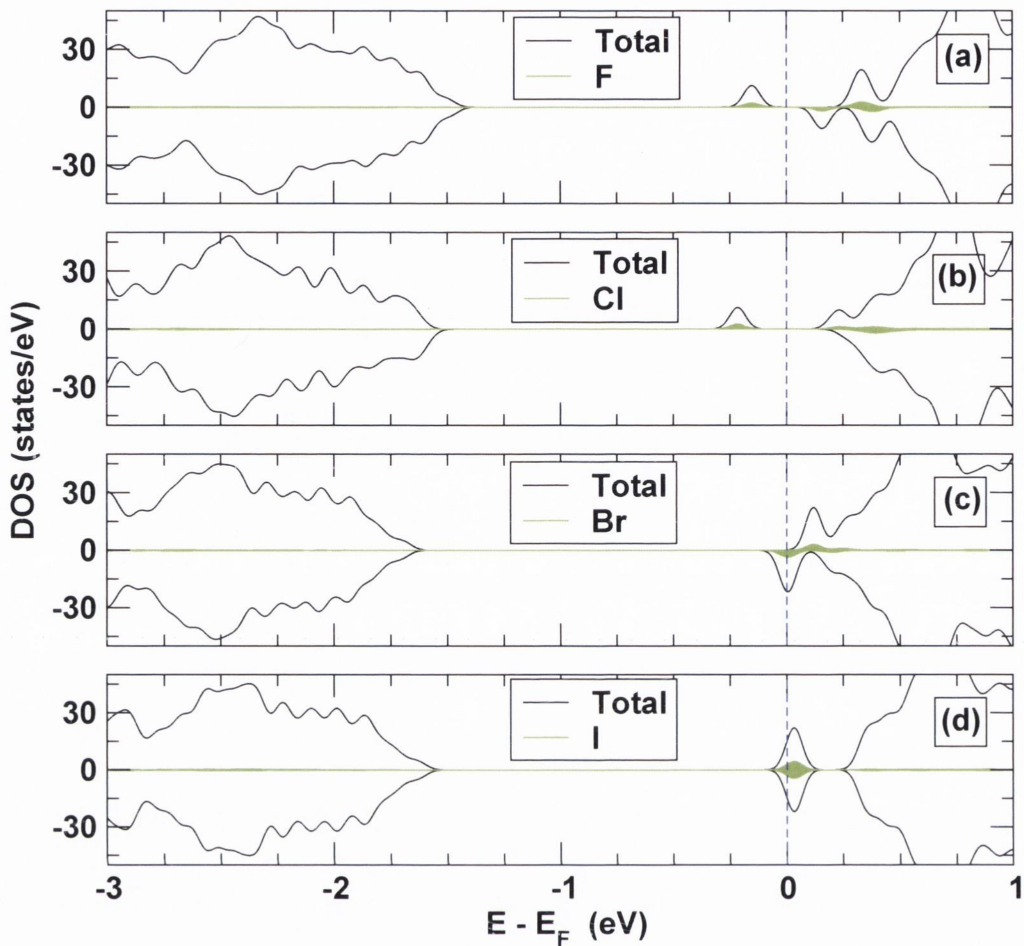

FIGURE 3.6: LSDA-DOS for one S in the MoS_2 supercell replaced by (a) F, (b) Cl, (c), Br and (d) I. Negative values refer to minority spins, positive values to majority spins. The blue dashed line indicates the Fermi energy, the colored shaded areas indicate the DOS projected onto the dopants. The electronic states in DOS are Gaussian broadened by 0.05 eV.

unoccupied impurity band however shows very little dispersion and is split off the valence band by ~0.08 eV. It is formed mainly by As-4p and Mo-4d states. In Fig. 3.7 the progressive shift to lower energies of the defect levels, when going from N to P to As, is visible.

To summarize, for S substitutional doping most dopants create localized, spin-split gap states. The spin-splitting reduces and the states move towards the VBM/CBM when increasing the atomic number of the dopant. Doping with As gives the most promising DOS for p-type doping, since its non-spin polarized defect band is very close to the VBM. For n-type doping, among the considered dopants the donor states are located rather far from the CBM of MoS_2, and are therefore localized states. We

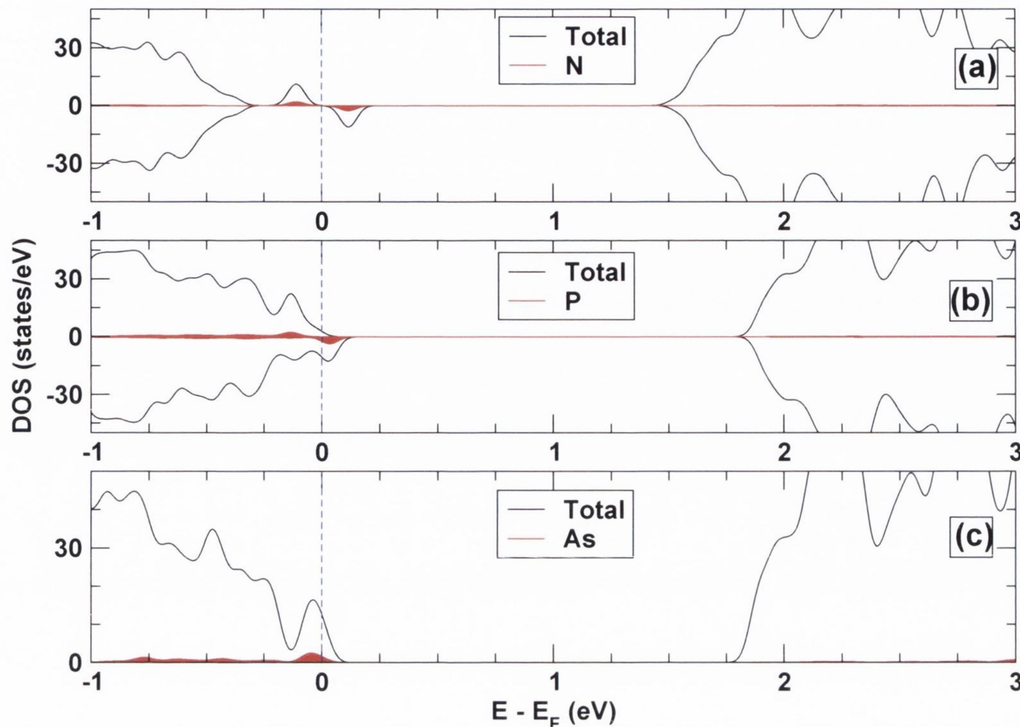

FIGURE 3.7: LSDA-DOS for one S in the MoS_2 supercell replaced by (a) N, (b), P and (c) As. Negative values refer to minority spins, positive values to majority spins. The blue dashed line indicates the Fermi energy, the colored shaded areas indicate the DOS projected on the dopants. The electronic states in DOS are Gaussian broadened by 0.05 eV.

note that in all cases the formation energies are rather large (see Table 3.1), so that substituting the S atoms with dopants in single MoS_2 might be difficult to achieve experimentally. However, the formation of S vacancies in MoS_2 monolayers has been recently demonstrated [206]. Therefore, it might be possible to realize the considered S substitutions by filling up induced S vacancies with the above mentioned dopants.

3.2.4.2 Mo substitutional doping

Next we consider substitution of a Mo atom with different transition metal atoms, each of them having a different number of electrons in the d orbitals. Specifically, we consider all the atoms in the periodic table from Y to Cd, with the exception that instead of Tc we use Re due to the radioactivity of Tc. We find that for all the systems where the substitutional atoms have larger d occupancy than Mo, the ground state is magnetic. In Table 3.1 we list the magnetic moments per defect for all the different transition metals.

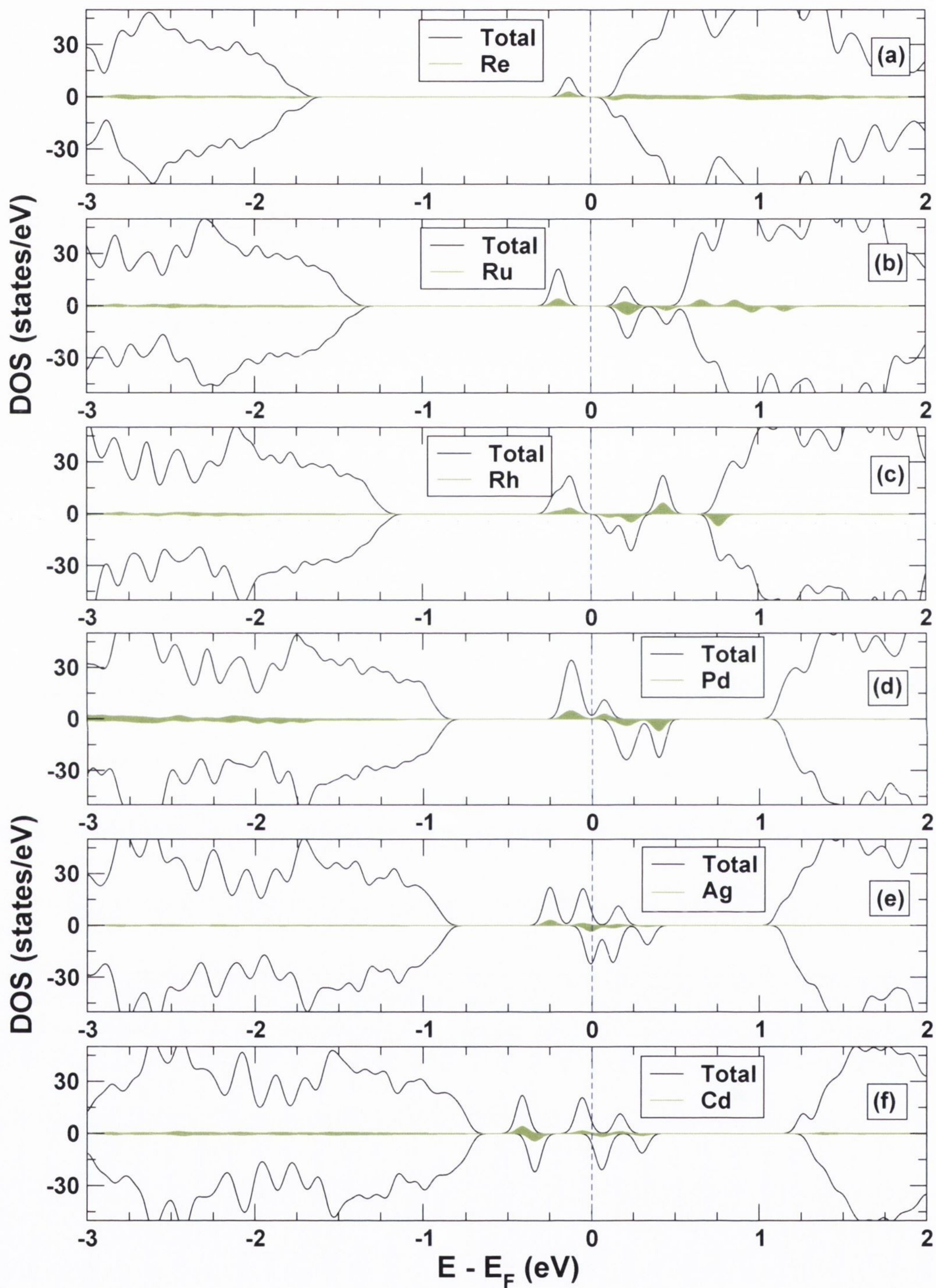

FIGURE 3.8: LSDA-DOS for one Mo in the MoS_2 supercell replaced by (a) Re, (b) Ru, (c) Rh, (d) Pd, (e) Ag and (f) Cd. The blue dashed line indicates the Fermi energy, the colored shaded areas indicate the DOS projected on the dopants. The electronic states in DOS are Gaussian broadened by 0.05 eV.

When Re replaces a Mo atom, 1 extra electron is added to the supercell. This extra electron goes into a majority spin gap state [Fig. 3.8(a)], located 0.3 eV below the CBM, with the Fermi energy located between this state and the CBM, and the system therefore has a magnetic moment of 1 μ_B/supercell. The DOS is similar to the Cl S-substitutional doping [Fig. 3.6(b)]. In a non-spinpolarized calculation for a Re doped MoS_2 monolayer the donor level is created at about 0.2 eV below the CBM. The magnetic ground state is however lower in energy than the nonmagnetic state by 82 meV/supercell. The non-spinpolarized result is similar to previous non-spinpolarized calculations [207] on Re doped MoS_2 nanotubes, where it was found that the donor level is situated at 0.19 eV below the CBM, and where it is suggested that Re could be an n-type dopant for MoS_2 nanotubes. We note that single crystals of Re-doped MoS_2 have been grown by chemical vapor deposition [208].

For the remaining transitions metal dopants having a larger *d*-orbitals occupancy than Re, an increasing number of gap states are formed, and the excess electrons go into those gap states rather than into the MoS_2 conduction band (see Fig. 3.8). The Fermi energy is always in the MoS_2 energy gap, and it moves further away downwards from the MoS_2 CBM as the number of excess *d* electrons increases. The excess electrons first fill up the majority spins of the host *d*-orbitals, until the magnetic moment reaches the largest value of 4 μ_B for Pd, and then the magnetic moment decreases when the excess electrons start to populate the minority spins states.

We move to study the possibility of obtaining a p-type system, starting by replacing Mo with Nb, which has one less electron than Mo. The substitutional doping by a Nb atoms does not change significantly the bond lengths. Moreover it does not change the DOS profile significantly, but the Fermi energy is shifted below the VBM due to the removal of one electron [Fig. 3.9(a)]. The newly created defect states are rather delocalized and range up to third nearest neighbor Mo atoms. The states around the VBM mainly originate from hybridized *d* orbitals of Nb and Mo. The valence band looks sufficiently dispersive in our DFT bandstructure, therefore the mobility is expected to be rather large. The formation energy of the Nb doped system is -0.19 eV, which is in good agreement with the formation energy of -0.21 eV [209], obtained theoretically for Nb substitution in bulk MoS_2. Our results suggest that Nb is a promising candidate for a p-type dopant in monolayer MoS_2. An experimental study [210] shows that Nb substituted (concentration of 15-25 %) MoS_2 nanoparticles can be synthesized, and that they also exhibit p-type character. For all the other considered substitutional dopants with less *d* electrons than Mo (Y and Zr) the ground states are also nonmagnetic (see

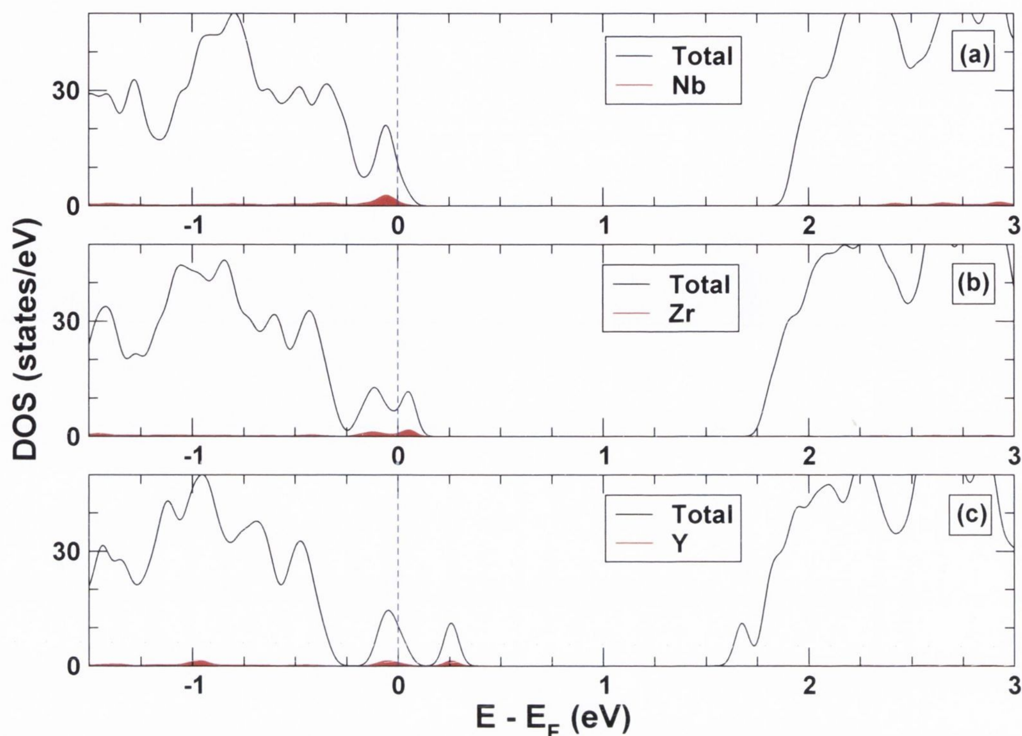

FIGURE 3.9: LSDA-DOS for one Mo in the MoS_2 supercell replaced by (a) Nb, (b) Zr and (c) Y. The blue dashed line indicates the Fermi energy, the colored shaded areas indicate the DOS projected on the dopants. The electronic states in DOS are Gaussian broadened by 0.05 eV.

Table 3.1). However, in contrast to Nb doping, the defect states become less hybridized with the VBM and produce split off acceptor-levels above the VBM for both Zr and Y doping [see Fig. 3.9(b),(c)].

Next we evaluate the pairing energy between two Nb atoms in a 6×6 supercell. In Table 3.3 we list the energy difference δE between the configuration where the two impurities are placed at the nearest, and where they are placed at the farthest distance from each other. The result suggests that in the case of Nb pairs the dopants try to stay close to each other in the MoS_2 monolayer. Based solely on the pairing energy, Nb dopants would tend to form clusters, however this cluster formation is likely to be inhibited in experiments due to the large energy barrier for moving the transition metals in the MoS_2 plane from one site to another one.

To summarize, for Mo substitutions with extra d electrons the donor states are located deep inside the gap (> 0.2 eV below the CBM), with Re being the dopant with the smallest activation energy, and the formation energies are large (Table 3.1). On the contrary, p-type doping by substituting a Mo with transition metals such as Nb and

Zr creates acceptor states just at the VBM, and the formation energies are also small (Table 3.1). In a recent experiment[211] the formation of Mo vacancies in bulk MoS_2 via proton irradiation is observed, which have a finite magnetic moment. If such experiments can be performed for a single MoS_2 layer, it might then be possible to fill up the induced vacancies by the transition metal dopants considered here.

3.2.5 Doping by adsorption

The results of the previous section show that neither by Mo substitution with transition metals nor by S substitution with nonmetal elements is it possible to obtain shallow donor states. Another route to obtain n-type character in a MoS_2 monolayer is by adsorbing H and alkali metals (Li, K, Cs). This possibility is addressed here. In the second part of this section we then consider adsorbed molecular ions as dopants for both n- and p-type character.

3.2.5.1 Alkali atom adsorption

For alkali metals adsorption on the MoS_2 surface, we find that T_{Mo} [see Fig. 3.3(b)] is the energetically most favorable site for all considered adsorbates. This is also suggested experimentally [212] as well as predicted by a previous theoretical calculation [217]. All the adsorption energies are large and negative (Table 3.2).

We start by considering Cs adsorption. When Cs is adsorbed there is no significant structural change in the geometry of the MoS_2 monolayer. The DOS in Fig. 3.10(a) shows that the Cs-6*s* electron is transferred to the CBM Mo-4*d* orbitals. For Li and K the electronic structure is similar [see Fig.3.10(b),(c)]. In contrast, in the case of adsorbed H atoms we obtain a spin-split (1 eV) midgap state [see Fig.3.10]. This result in the H-adsorbed case is in good agreement with recent theoretical results [206].

The pairing energy of Cs-Cs and of Nb-Cs pairs is given in Table 3.3. Nb-Cs pairs might originate in a mixed n- and p-type system. Note that in this case Cs is adsorbed on top of either Nb or Mo whereas Nb substitutes Mo. It is energetically more favorable by about 200 meV to put the Cs atom on top of Nb rather than on top of Mo, which is caused by the attraction of the oppositely charged ions. For this lowest energy configuration, the DOS is similar to the one of the pristine MoS_2, since the valence band states are completely filled, so that the Fermi energy is midgap (see Fig. 3.11).

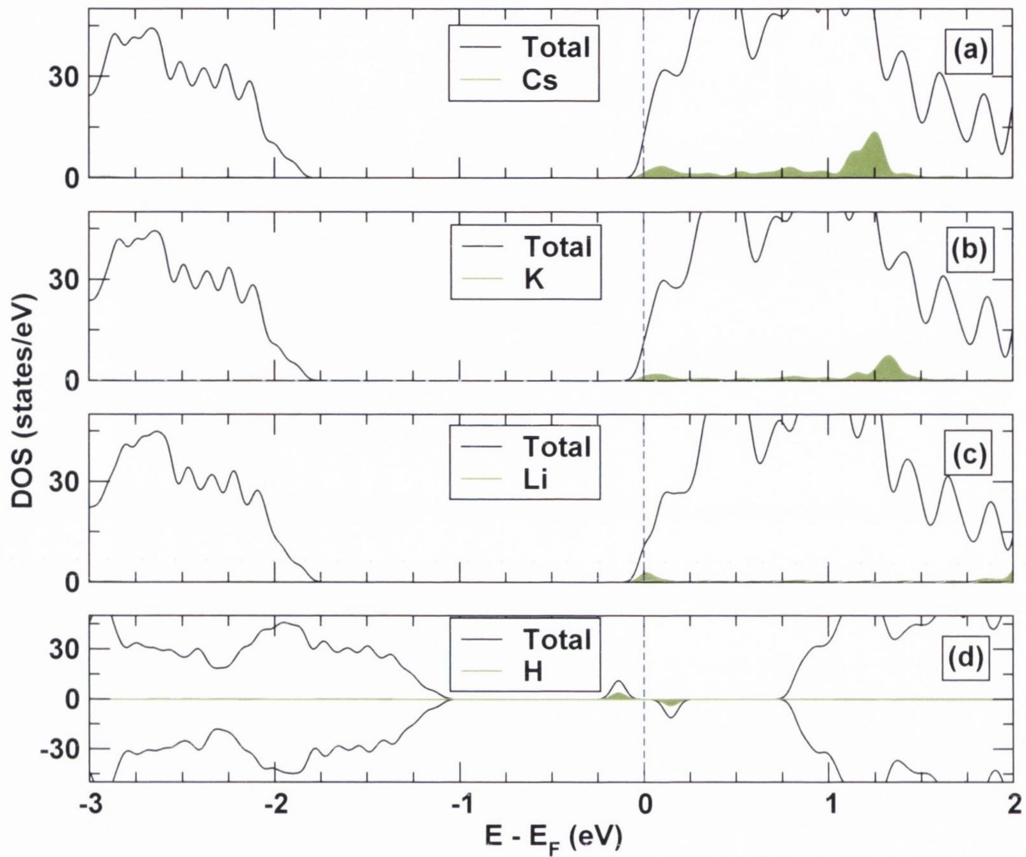

FIGURE 3.10: LSDA-DOS for (a) Cs, (b) K, (c) Li and (d) H adsorbed on the MoS_2 supercell. The blue dashed line indicates the Fermi energy, the colored shaded areas indicate the DOS projected on the adsorbates. The electronic states in DOS are Gaussian broadened by 0.05 eV.

Adatoms	E_{ads} (eV)
Cs	-0.79
K	-0.82
Li	-0.98

TABLE 3.2: Theoretically calculated (DFT-LSDA) adsorption energy for different alkali metal adsorbed on the MoS_2 monolayer.

Pairing between	δE (meV)
Nb-Nb	-157
Nb-Cs	-218
Cs-Cs	-166

TABLE 3.3: Theoretically calculated (DFT-LSDA) pairing energy for co-doping in the MoS_2 monolayer.

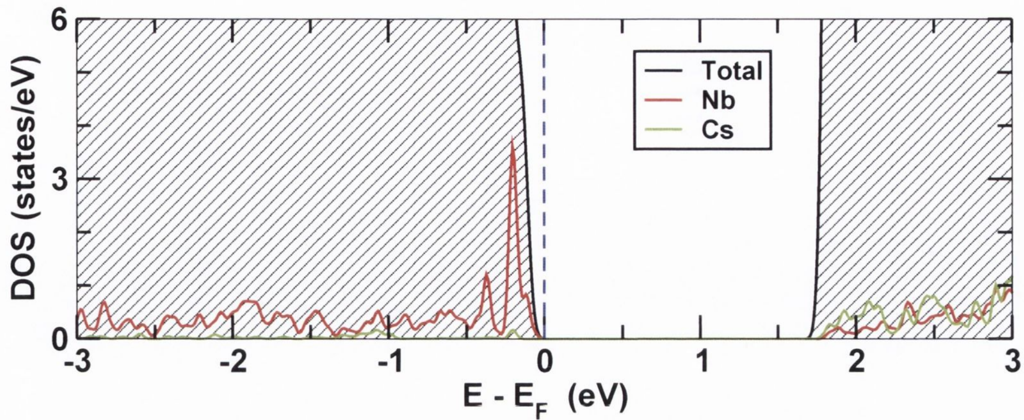

FIGURE 3.11: LSDA-DOS for a MoS_2 supercell, where a single Mo is replaced by Nb, and where a Cs atom is adsorbed. The blue dashed line indicates the Fermi energy, the colored curves indicate the DOS projected on the dopants. The electronic states in DOS are Gaussian broadened by 0.05 eV.

To summarize the properties of adsorbed alkali metals, we find that these release their valence s electron at the CBM. Moreover the adsorption energies are large. Therefore, they are promising candidates for n-type doping of MoS_2. This is different to H adsorption, where midgap states are formed. Various experimental studies have been performed on the intercalation of alkali metals in bulk MoS_2 [218], which indicates that this should be possible also in the single layer limit.

3.2.5.2 Adsorption of molecular ions

Electric double layer (EDL) transistors with ionic liquids acting as gate dielectrics have recently emerged as promising devices tools, where the electrical properties of a solid can be controlled by electrostatic carrier doping [180, 219]. A schematic diagram for such a device concept is shown in Fig. 3.12. By applying a gate bias to the ionic liquid, an electric double layer is formed between the interface of the liquid and the solid (see Fig. 3.12), where the polarity of the molecular ions on the surface of the semiconductor can be reversed by changing the polarity of the gate bias. The EDL at the ILs/solid surface can be regarded as nano-scale capacitor potentially displaying a huge capacitance. As a result the accumulation of charges along the transport channel occurs at a high density level (10^{14} cm^{-2}), which is practically impossible to reach in conventional transistors made with solid gate dielectrics. This can even lead to phase transitions in the solid. Metal-superconductor and metal-insulator transitions have been demonstrated in $KTiO_3$ [220] and VO_2 [180], respectively by using EDL gating.

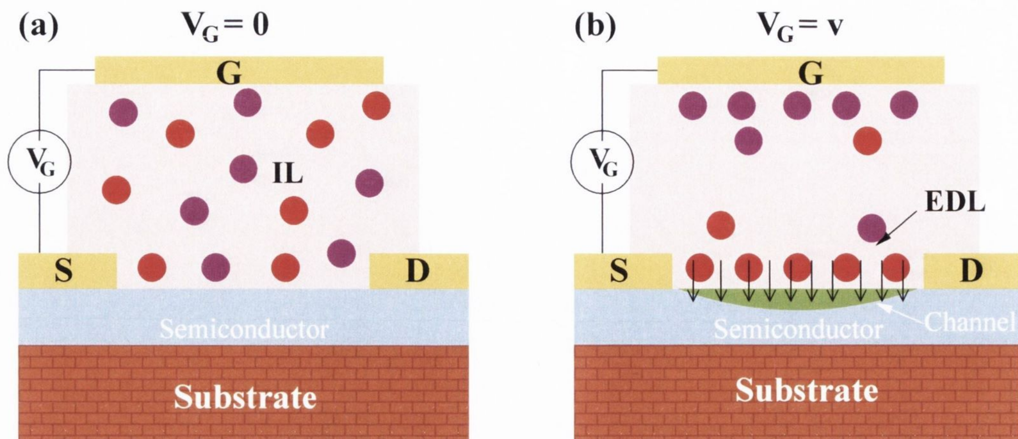

FIGURE 3.12: Schematic diagrams of the EDL transistor operation with an ionic liquid electrolyte. Here, "S" indicates the source, "D" indicates the drain, and "G" indicates the gate. The solid circles denote the ions in the liquid, where the different colors represent cations and anions. (a) Without an applied gate bias (V_G=0), cations and anions are uniformly distributed and both adsorbed at the interface of the semiconductor with equal probability. (b) With a finite applied bias at the gate ($V_G = v$), cations or anions adsorb predominantly at the gate electrode, depending on the bias polarity, and the oppositely charged ions adsorb predominantly on the semiconductor. These adsorbed ions will emerge an electric field (black arrows, direction depends on the polarity of ions) and lead to an accumulation of a screening charge at the semiconductor surface, which implies a large surface carrier concentration.

It has been reported that a large electric field, generated by a nano-capacitor, induces not only electrostatic charge accumulation but also an electrochemical reaction between the liquid and the solid [213]. This electrochemical reaction represents another mechanism to induce conduction in the solid channel through chemical doping by ions. This type of chemical doping occurs at relatively large bias. Indeed, a distinct bias regime of chemical as well as electrostatic doping has been reported in $SrTiO_3$ in a liquid gated arrangement [213]. It has been shown that chemical doping has a significant contribution for large bias (above 3.7 eV). This study clarifies some issues regarding the doping mechanism in the EDLT devices. However, regardless of the chemical doping, the accumulation of the charge (induced electrostatically) is maintained due to charge injection from the electrodes in the EDLT devices. The operation of highly flexible MoS_2 thin-film transistors in an ionic liquid gated dielectric has been demonstrated recently [221]. Although we do not consider any electrode in our study, we discuss the effects of the adsorbed molecular ions on MoS_2 monolayer at high impurity density limit (10^{14} cm^{-2}). Here we simulate the situation where the charges in the solid comes from the ions as they have usually a low electron ionization potential (anion) and a

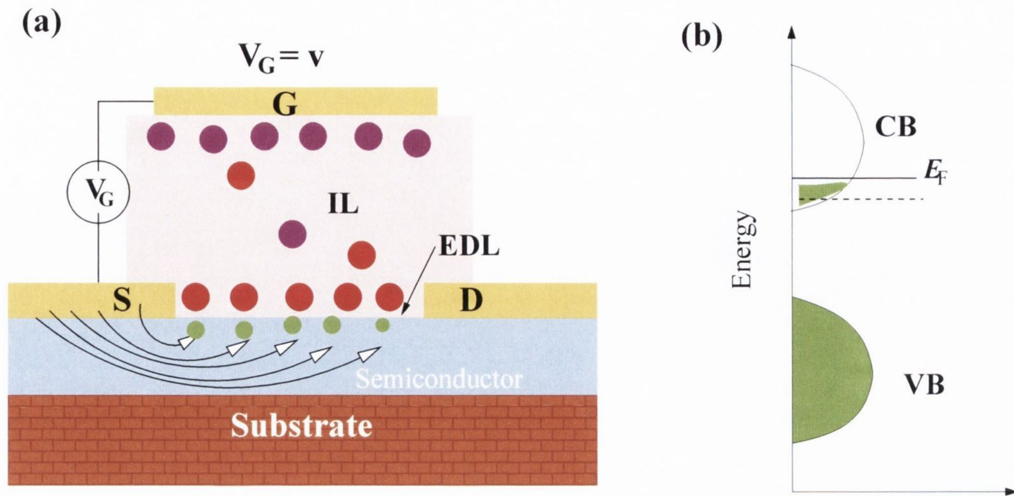

FIGURE 3.13: (a) Schematic diagrams of the EDL transistor operation with an ionic liquid electrolyte at finite positive bais $V_G = v$. The accumaled charges (green solid) transfer from the electrode to MoS_2. Other symbols and levels are same as shown in Fig.3.12. (b) Schematic band diagram for charge transfer (here electron) to the MoS_2. When for each positively charges ions one electron is transfered from the lectrode to MoS_2, the Fermi level (E_F) is denoted by solid black line, whereas the dashed black line is for a fractional charge-transfer. The VB and CB denote, respectively the valence and conduction band of MoS_2.

high electron affinity (cation) as compared to the solid. Although large variety of ionic complexes are available experimentally, here we consider only NH_4^+ and BF_4^- ions. We note that the electronic ionization potential of NH_4 and electron affinity of BF_4 are respectively, $\sim$ 0.42 eV [214], and $\sim$ 6.86 [215], whereas the electron affinity is $\sim$ 4.0 eV for bulk MoS_2 [216]. Therefore one may expect that the ions release electrons to MoS_2 (in the case of NH_4) or take electrons from MoS_2 (in the case of BF_4) to induce a conducting channel.

In experiments charged layers of ions are absorbed on MoS_2 surfaces. It will induce a large electric field, which repels/attracts the electrons in MoS_2 (see Fig. 3.12). Therefore, this will partially transfer electrons/holes from the MoS_2 to the electrodes in the EDLT devices [see Fig. 3.13(a)]. In our calculations, with a neutral system we implicitly assume that for each ion one electron is transfered from the electrode to MoS_2. This represents an upper limit for the charge transfer. Otherwise, the charges transfered would be a fraction of an electron for each ion [see Fig. 3.13(b)].

In our calculations, we place the NH_4 and BF_4 ions on the 5×5 MoS_2 supercell (see Fig. 3.14). This corresponds to an impurity density of $\sim 10^{14}$ cm^{-2}. We find that the energetically favorable adsorption sites are T_S for the cation, and T_{Mo} for the anion.

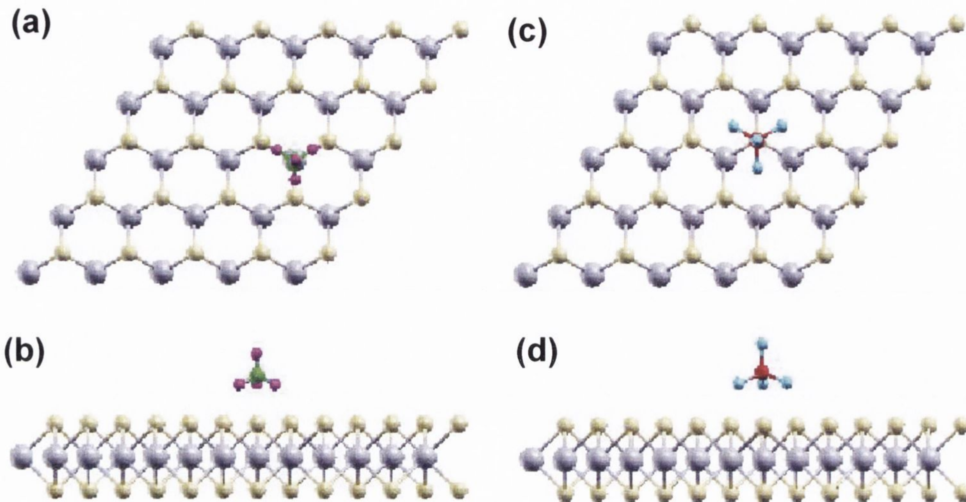

FIGURE 3.14: The optimized geometries for (a, b) NH_4^+ and (c, d) BF_4^- ions adsorbed on the MoS_2 monolayer. In (a) and (c) the top view is shown, whereas in (c) and (d) the side view is shown. Pink spheres indicate H, green spheres N, cyan spheres F, and red spheres B.

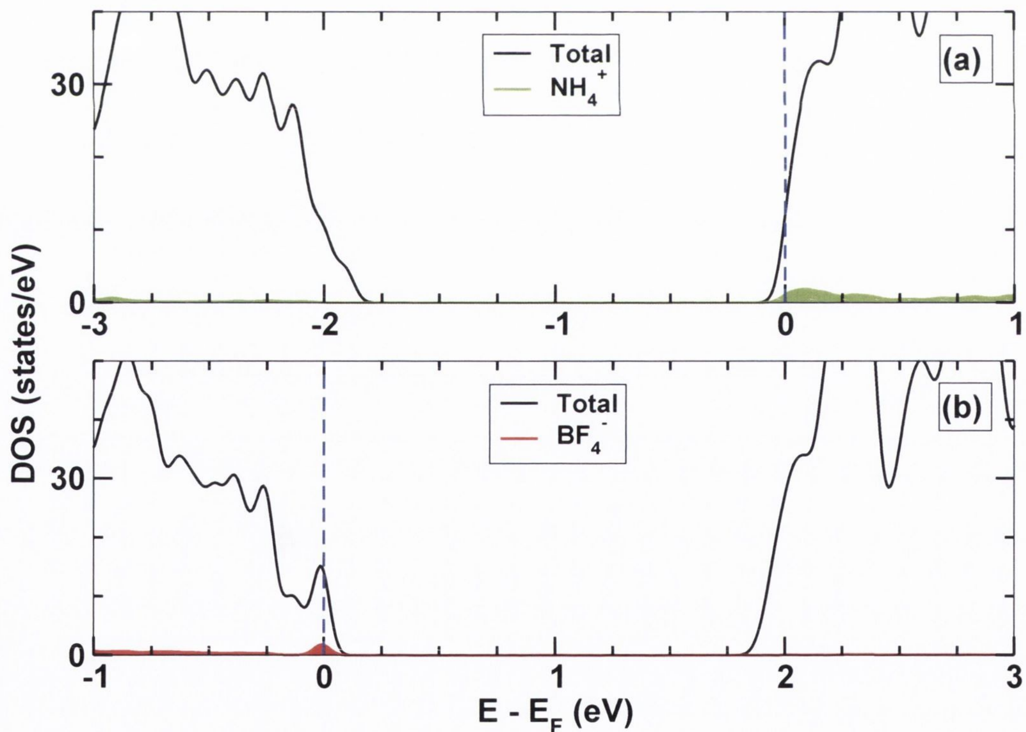

FIGURE 3.15: LSDA-DOS for (a) NH_4^+ and (b) BF_4^- adsorbed on the MoS_2 supercell. The blue dashed line indicates the Fermi energy, the colored shaded areas indicate the DOS projected on the adsorbates. The electronic states in DOS are Gaussian broadened by 0.05 eV.

In Fig. 3.15(a) the DOS is shown for NH_4 adsorption. It can be seen that the NH_4 releases one electron into the MoS_2 CBM, resulting in a n-type channel in the MoS_2 monolayer. On the other hand, if BF_4 is adsorbed, it obtains one electron from the MoS_2 [see Fig. 3.15(b)], thereby shifting the Fermi energy below the VBM of MoS_2, so that the system is p-type. This also confirms that these adsorbed molecules are indeed ionized to NH_4^+ and BF_4^- when put on MoS_2. In a liquid gated transistor arrangement, the anions/cations are brought close to the surface of the channel by applying a bias at the gate. Therefore, for this system, depending on the polarity of the gate bias the MoS_2 is indeed predicted to have a n- or p-type conducting channel. Clearly this effect is maximized for a single layer of MoS_2 when compared to thicker structures. In fact, conductivity measurements [181] on MoS_2 show that it decreases from going from a thin layer to bulk in an ionic liquid gated environment. Moreover, depending on the polarity of bias, it is found that the conductivity indeed switches from n-type to p-type.

3.2.6 Robustness of the results against the choice of XC functional:HSE06

Finally, in order to verify that the impurity level alignment presented in the previous sections is robust against the choice of exchange correlation functional, we repeat our calculations using the HSE06 exchange and correlation functional. The MoS_2 lattice constant obtained using the HSE06 functional is 3.165 Å, which is only slightly larger than the LDA value of 3.137 Å. For a pristine MoS_2 monolayer at this relaxed lattice constant HSE06 exhibits a direct bandgap of 2.10 eV (compared to a LDA gap of 1.86 eV at 3.137 Å), which is rather similar to the gap obtained applying the atomic self-interaction correction [see Sec. 3.3.5]. This is however larger than the optical bandgap of 1.90 eV measured experimentally for MoS_2 monolayers [172]. The apparent contradiction can be solved by noting that the optical excitations involve excitons with a large binding energy of the order of 1 eV, as confirmed by many-body calculations [243]. Thus, one expects that the true quasi-particle spectrum has a bandgap of approximately 1.9+1=2.9 eV, in good agreement with that computed with the *GW* scheme, either at the first order level [243] (2.82 eV) or self-consistently [244] (2.76 eV).

In Fig. 3.16 we report the results for four representative choices of doping, namely for Nb substitutional doping, as well as for Cs, NH_4 and BF_4 adsorption. The calculations

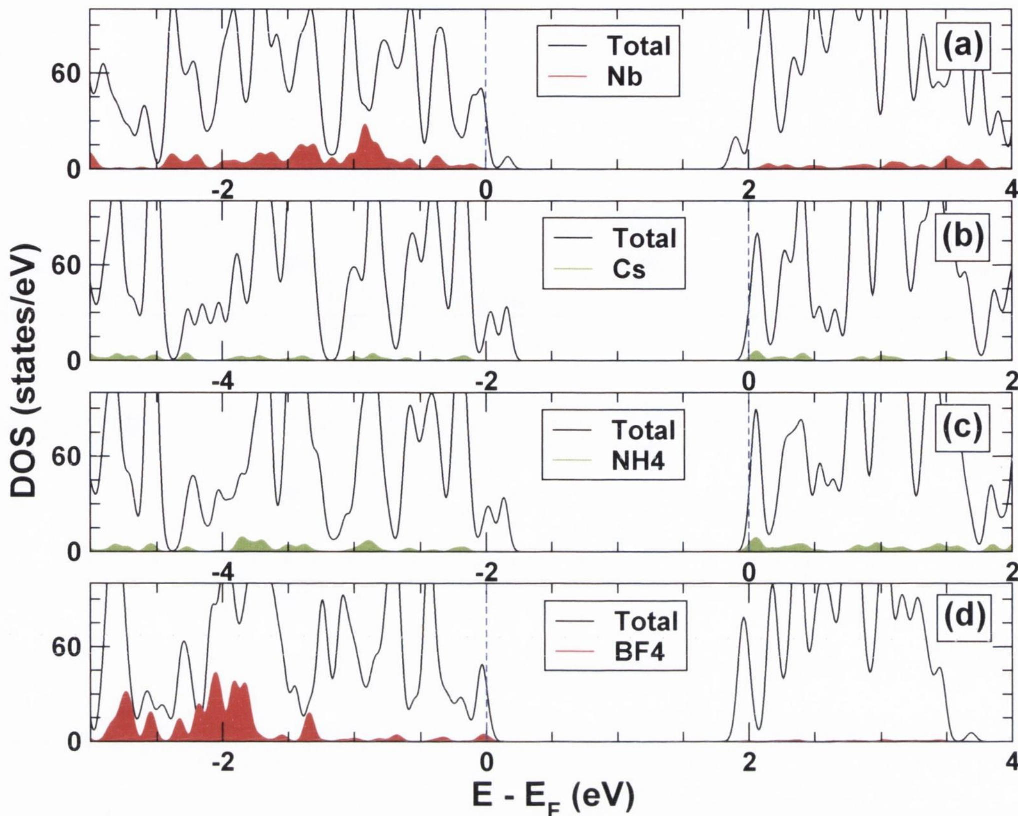

FIGURE 3.16: DOS for the doped monolayer MoS_2, calculated with the HSE06 functional: (a) Nb substitutional doping, and (b) Cs, (c) NH_4, as well as (d) BF_4 adsorbed on the MoS_2 surface. The blue dashed line indicates the Fermi energy, the colored shaded areas indicate the DOS projected on the adsorbates. The electronic states in DOS are Gaussian broadened by 0.05 eV.

	$E_{\text{form}}/E_{\text{ads}}$ (eV)	
Impurity	LDA	HSE06
Nb	-0.19	-0.14
Cs	-0.79	-0.89

TABLE 3.4: Theoretically calculated (DFT-LDA/HSE06) formation and adsorption energy, respectively for Nb doped and Cs adsorbed on the MoS_2 monolayer.

are carried with the same structures used in the previous sections, in order to make a direct comparison with the presented results. We find that for all four cases the main difference to the LDA results is just a minor change in the bandgap, while the impurity levels with respect to the respective Fermi energies are placed at the same positions observed in the LDA calculations. Moreover, the formation energies are similar to the LDA values (see Table 3.4).

3.2.7 Conclusion

We have carried out a systematic study on the changes to the electronic structure of a MoS_2 monolayer induced by dopants. We considered substitutional doping for both Mo and S, as well as doping by adsorption. S substitution with nonmetals and Mo substitution with transition metals create deep donor levels inside the bandgap of the MoS_2 monolayer for most of the considered dopants. Via substitutional doping we find that it is possible to obtain p-type MoS_2 by replacing a Mo atom with a Nb. For making MoS_2 n-type on the other hand we find only rather deep donor levels when substituting Mo with transition metals, with Re being the one with the smallest activation barrier. A N-type character can also be achieved by adsorbing alkali metals. As a last class of dopants we consider adsorption of ionic molecules, which can occur during electric double layer formation when MoS_2 is contact with in an ionic liquid. These show high potential for inducing large carrier concentrations, both electrons or holes, within the MoS_2 monolayer. Moreover, the changes to the carrier densities induced by ionic liquids are expected to be a general property of LTMDs in such environments.

3.3 Effects of SiO_2 substrate

3.3.1 Methodology

In order to investigate the influence of a SiO_2 substrate on the electronic properties of a MoS_2 monolayer, *ab-initio* calculations are performed by using density functional theory (DFT) [97, 98] within the generalized gradient approximation (GGA) of the exchange and correlation (XC) functional as introduced by Perdew, Burke and Ernzerhof (PBE) [224] and numerically implemented in the SIESTA code [125]. In our calculations, a double-ζ polarized [195] numerical atomic orbital basis set is used for all the atoms and the Troullier-Martins scheme is employed for constructing norm-conserving pseudo-potentials [225]. An equivalent plane wave cutoff of 350 Ry is chosen in all the simulations and the Brillouin zone is sampled by using an equivalent k-grid cutoff of 17 Å. Relaxed geometries are obtained with the conjugate gradient method, where all the atoms in the supercell are allowed to relax until the force on each atom is less than 0.02 eV/Å.

A trap state is usually formed when an energy level associated with either a defect or an impurity appears within the energy gap of the host material. Such trap states influence the charge transport properties mainly in two ways. Firstly, if the traps become charged, they will capture a hole or an electron from the environment. This produces a modification of the electrostatic potential, which in turns shifts the level alignments in the system, and thus affects the conductivity. Secondly, they can also increase the carrier concentration and provide pathways for electrons or holes to hop. The efficiency of this process depends on the amount of localization of the states associated with the defect site. If the energy of the localized gap state is close to either the valence band maximum (VBM) or the conduction band minimum (CBM), then at a given temperature some of these charges will be transferred either to the conduction or to the valence band, where they may contribute to increase the system conductivity.

Whether or not one can describe with *ab initio* calculations such mechanisms depends crucially on the ability of computing accurately the energy levels of the system. The use of the GGA (or of the local density approximation - LDA) for electronic structure calculations of defect levels is, in general, problematic. One reason is the typical underestimation of the energy gap and the related incorrect alignment of the energy levels of hybrid systems. For instance an artificially reduced bandgap may erroneously

bring deep traps in resonance with either the conduction or the valence band [226, 227]. A second source of error is the incorrect description of the charge localization at the defect site, a feature that usually leads to defects being predicted ions of to be too shallow [228]. Atomic self-interaction correction (ASIC) [229, 230] has been proved to overcome these deficiencies [231, 232]. Therefore we also perform additional LDA+ASIC calculations to verify the robustness of the LDA/GGA results. In particular we set the ASIC scaling parameter to $\alpha = 0.5$, a value which is generally appropriate to mid-gap insulators [229].

3.3.2 Defect-free SiO_2 interface

Substantial experimental efforts have been devoted to deposit ultra-thin MoS_2 layers onto SiO_2 in order to demonstrate transistor operation, down to the single layer limit [169, 172, 176]. Usually amorphous oxides are used as substrates. However, in order to avoid the computational complexity of a highly disordered structure, a crystalline SiO_2 substrate is simulated here instead. This also allows us to systematically determine the effects of individual defects and impurities on the electronic structure of a MoS_2 layer. Our unit cell is constructed as a slab containing at least 6 Si atomic layers of α-quartz and an adsorbed MoS_2 monolayer. At least 15 Å of vacuum are included at the slab boundaries to avoid the spurious interaction between the slab periodic images. We consider the modified oxygen-terminated (0001) SiO_2 surface in order to simulate the most experimentally relevant conditions.

Two primary structures for the oxygen-terminated SiO_2 (0001) surface are possible, depending on whether the termination is with the siloxane group (Si-O-Si) or with the silanol one (Si-OH). Both surfaces can form depending on the surface treatment [233]. The siloxane reconstruction at room temperature forms an O-terminated surface with an outermost six-membered ring structure, as shown in Fig. 3.17(a, b). Under annealing in ambient conditions it becomes hydroxylated (Si-OH) and the reconstruction transforms into the silanol one, which presents on the surface a zigzag H-bonded network [see Fig. 3.17(c, d)]. In both cases in our simulations the dangling bonds on the Si-terminated bottom surface are saturated by hydrogen.

The optimized lattice constants of the pristine SiO_2 and MoS_2 are 4.91 Å and 3.19 Å, respectively. We therefore construct a hexagonal supercell in the plane, with a 9.69 Å-long side, so that the lattice mismatch between SiO_2 and MoS_2 is minimized to $\sim$1.2 %.

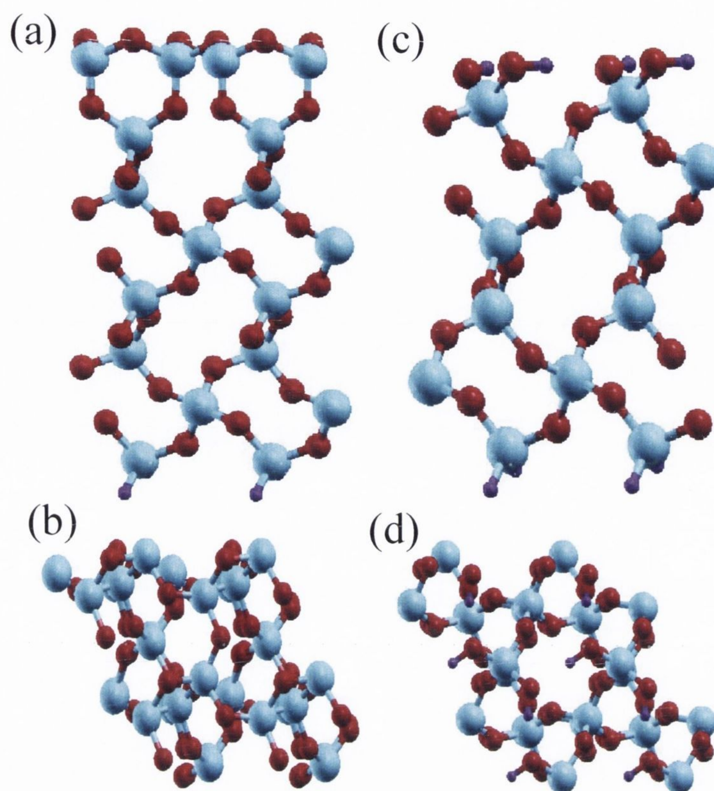

FIGURE 3.17: Side and top views of reconstructed structures for the O-terminated SiO_2 (0001) surface (a and b), and the fully hydroxylated SiO_2 (0001) one (c and d) (color code: cyan $\rightarrow$ Si, red $\rightarrow$ O, violet $\rightarrow$ H).

The GGA calculated bandgap of SiO_2 and of a MoS_2 monolayer are 6.20 eV and 1.49 eV, respectively. The small strain applied to the MoS_2 monolayer changes the electronic structure only slightly. The bandgap remains direct at the K point and it is only reduced by 0.22 eV from the value of 1.71 eV obtained for the unstrained case. Similarly to the case of graphene [234], we expect that the electronic structure of a MoS_2 monolayer is only marginally affected by its local arrangement on the SiO_2 substrate. Therefore, as a representative configuration we use the arrangement of Fig. 3.18, where an oxygen atom is situated at the hollow site of the Mo surface triangles.

We start our discussion by presenting the properties of the defect-free hybrid MoS_2/SiO_2 system. The equilibrium distances, d_0, between the SiO_2 and the MoS_2 surfaces are 3.01 Å and 2.98 Å for siloxane and silanol, respectively. Here d_0 is defined as the vertical separation between the top-most O layer in the SiO_2 surface and its nearest S layer in MoS_2. These values are similar to the distance between two MoS_2 monolayers that we calculate to be 3.17 Å. The binding energy of the MoS_2/SiO_2 system is given by $E_\mathrm{b} = E_{\mathrm{MoS_2}} + E_{\mathrm{SiO_2}} - E_{\mathrm{MoS_2/SiO_2}}$, where $E_{\mathrm{MoS_2}}$, $E_{\mathrm{SiO_2}}$, and $E_{\mathrm{MoS_2/SiO_2}}$ are total

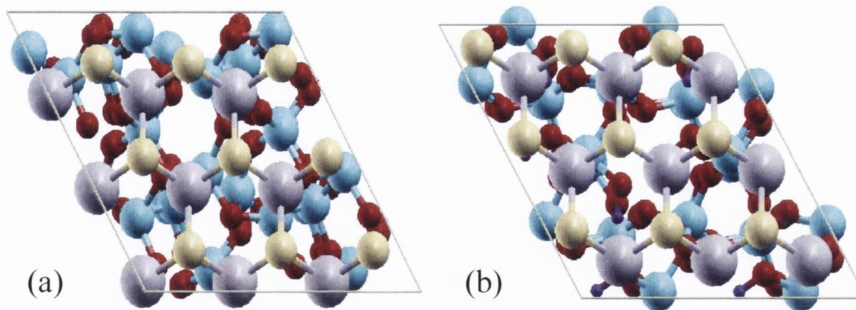

FIGURE 3.18: Top view of the optimized structure of MoS_2 placed on a defect-free (a) siloxane and (b) silanol surface (color code: light grey → Mo, yellow → S, cyan → Si, red → O, violet → H).

energies of the isolated MoS_2, the isolated SiO_2 slab, and of the MoS_2/SiO_2 hybrid system, respectively. We find E_b for siloxane and silanol to be respectively 0.14 eV and 0.16 eV per primitive MoS_2 unit cell. These binding energies are close to that between two MoS_2 layers (0.20 eV/unit cell), which are bound together by the rather weak van der Waals forces. As such, our results show that MoS_2 is weakly bound also to the SiO_2 surface, in agreement with recent experimental results that have measured the interaction between MoS_2 and an underlying SiO_2 substrate to be negligible [204].

Note that in general GGA-type XC-functionals do not describe accurately van der Waals forces. However, it has been shown that the LDA/GGA is able to reproduce the interlayer spacing and the binding energy of layered chalcogenides [235]. We have then verified that our calculated d_0 for bulk MoS_2, $d_0 = 3.08$ Å, is in good agreement with the experimental value of 2.96 Å [157] and also with the previously calculated theoretical estimate of 3.05 Å [236]. Moreover, in order to take into account possible small deviations of the relaxed distance from the experimental value due to the XC functional used, we have evaluated the electronic structure for d_0 within the range $d_0 \pm 0.5$ Å, and we have found that the results change little with varying the distance.

3.3.3 SiO_2/MoS_2 composite with siloxane reconstruction

We now move to study the electronic structure of a MoS_2 monolayer deposited on SiO_2 by starting with the siloxane surface. In particular we consider first the situation where SiO_2 is defect-free. Fig. 3.19(c) shows the density of states (DOS) of the hybrid SiO_2/MoS_2 system, which remains semiconducting with a bandgap of 1.48 eV, i.e. with the same bandgap as a free-standing MoS_2 monolayer with the same lattice parameters.

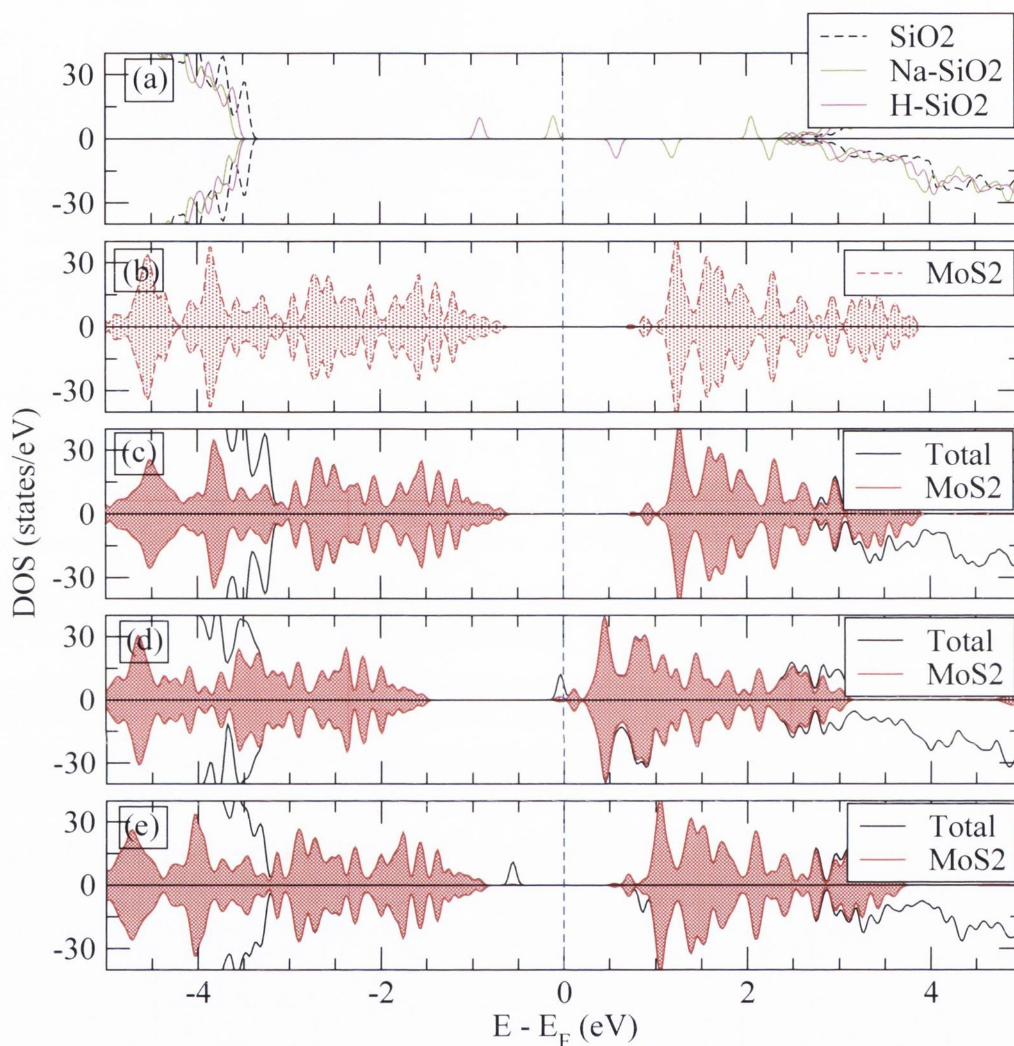

FIGURE 3.19: Electronic structure of the SiO_2/MoS_2 hybrid system when various defects are present at the SiO_2 siloxane surface. (a) The total GGA-DOS for the defect-free surface (black, dashed curves), and when either Na (green, solid curves), or H adsorbed (magenta, solid curves) are adsorbed. (b) The DOS of a pristine free-standing MoS_2 monolayer. The total DOS and the PDOS for MoS_2, when the MoS_2 monolayer is placed on the defect-free siloxane surface (c), on a siloxane surface with one adsorbed Na (d), or with one adsorbed H (e). The blue dashed vertical line indicates the Fermi level, which has been set to zero in all the panels. The red shaded areas indicate the MoS_2 PDOS. Positive and negative DOS are respectively for spin up (majority spins) and spin down (minority spins) electrons.The electronic states in DOS are Gaussian broadened by 0.05 eV.

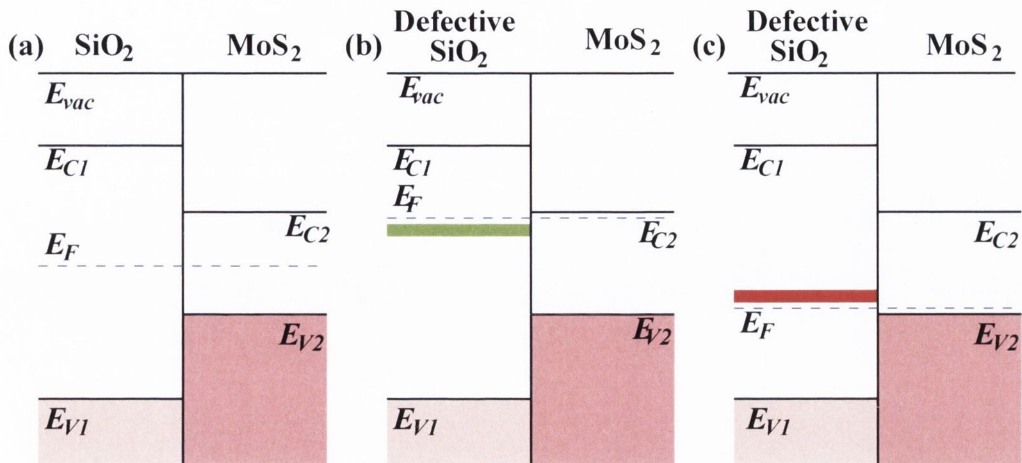

FIGURE 3.20: Schematic band diagram for MoS_2 placed on the defect SiO_2 substrate (a), and on a substrate including a defect-induced donor (b) or acceptor (c) level. This demonstrates the modulation of the conductivity from n-type to p-type as the impurity state redefines the Fermi energy in the oxide. The energy levels E_V, E_C, E_F and E_{vac} define the valence band maximum (VBM), the conduction band minimum (CBM), the Fermi energy, and the vacuum level, respectively. The subscripts 1 and 2 refer to SiO_2 and MoS_2, respectively. The blue dashed-lines indicate the Fermi energy of the hybrid system (common to SiO_2 and MoS_2). The thick green line in (b) indicates the donor level and the thick red line in (c) represents the acceptor state in the oxide. Note that in general due to charge transfer from MoS_2 to the gap states, and the related dipole formation, the level alignment between E_{V1} and E_{V2} will also change in the defective systems.

Both the valence and the conduction bands of the hybrid compound are associated with MoS_2. We note that the projected DOS (PDOS) over MoS_2 extends into the SiO_2 bandgap, and the total DOS of the combined material is essentially given by the superposition of the DOS of the pristine slab of SiO_2 [Fig. 3.19(a)] and of the MoS_2 monolayer [Fig. 3.19(b)]. Both the conduction and the valence bands of SiO_2 are located at least 1.5 eV away from those of MoS_2. As a consequence, no charge transfer between the substrate and MoS_2 occurs. One of the basic criteria for a selection of the gate oxide is fulfilled here, namely that the oxide should have a band offset of over 1 eV for both the conduction and valence band in order to create a large barrier for both electrons and holes [237]. Our results show that the conductivity of MoS_2 is not influenced by the underlying defect-free SiO_2 substrate. Therefore the measured n-type or p-type conducting properties of MoS_2 on SiO_2 must be due to defects and impurities.

Localized states, arising from impurities or defects within the oxide substrate or at the interface with the conducting channel, can redefine the effective Fermi level of the

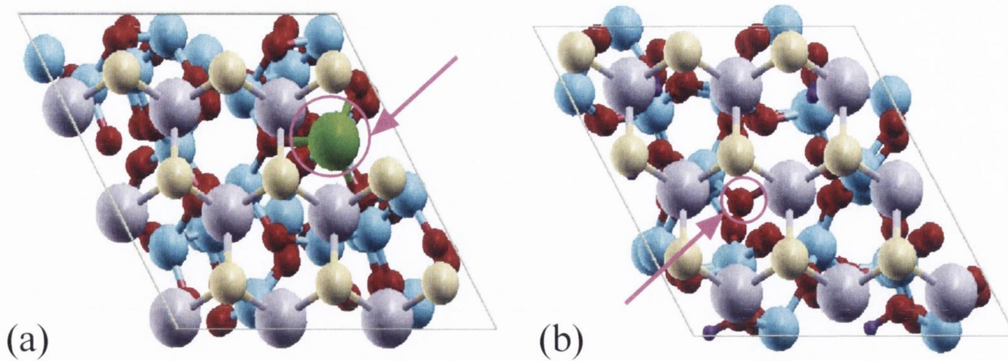

FIGURE 3.21: The optimized geometries for MoS_2 placed on (a) the siloxane surface incorporating a Na impurity and (b) the dangling oxygen bond on the silanol surface, obtained by removing a H atom. The arrows indicate the positions of the defects on the surface (Color code: green $\rightarrow$ Na, while the other colors are the same atoms as in Fig. 3.18). The arrows indicate the location of the impurities/defects.

hybrid system, as illustrated schematically in Fig. 3.20. Depending on the alignment of the gap states with respect to the MoS_2 valence and conduction bands, the system can switch from n-type [see Fig. 3.20(b)] to p-type [see Fig. 3.20(c)]. Therefore, such trap states are expected to give significant contributions to the conductivity of these low dimensional systems. In the layered structure considered in this work, the trap states are expected to be located at the interface between the LTMDs and the substrate, not in the LTMDs themselves, which usually are highly defect-free. Trap states at the SiO_2 surface can have a wide range of origins, such as immobile ionic charges, SiO_2 surface dangling bonds, and foreign impurities adsorbed on the surface [238]. In the literature, densities of trap states on SiO_2 are reported in the range [239] 10^{10}-10^{14} cm^{-2}. As representative dopants, here we consider two possible candidates: Na atoms and SiO_2 surface oxygen dangling bonds.

During synthesis and sample preparation, SiO_2 can adsorb relatively light impurities such as Na and K [240] at its surface. In order to simulate the effects of such impurities on the electronic structure of the MoS_2 channel a single Na atom is placed on top of the siloxane SiO_2 surface. Given the lateral dimension of our supercell, this corresponds to an impurity density of $\sim 10^{14}$ cm^{-2}, which is close enough to recently reported values of trap states densities, reaching up to $\sim 10^{13}$ cm^{-2} for thin MoS_2 layers deposited on SiO_2 [166, 187]. The most energetically favorable binding position for Na is found to be at the center of the surface oxygen triangle [see panel (a) of Fig. 3.21]. A Na adatom adsorbed on a pristine SiO_2 surface creates a deep donor state in the DOS, with a single particle level at about 2 eV below the SiO_2 CBM [see Fig. 3.19(a)]. Note that such

a state is singly occupied and therefore spin-splits in our spin-polarized calculations, with the empty minority spin state (spin down) laying approximately 1 eV below the CBM and 1 eV below the Fermi level.

When a MoS_2 monolayer is deposited over the the Na-doped SiO_2 surface, d_0 increases to 3.24 Å at the edges of our unit cell, whereas at the Na site the O-S distance becomes 3.45 Å. The enlargement of the binding distance compared to that of the pristine SiO_2/MoS_2 system is a direct consequence of the Na intercalation at the interface. The electronic structure of the composite is strongly affected by the presence of the Na ion, as shown in Fig. 3.19(d). Also in this case the total DOS appears as a direct superposition of those of SiO_2 and MoS_2. However the presence of the Na filled state shifts the Fermi level, which now gets pinned just below the MoS_2 CBM. The resulting DOS around E_F is thus that of the defect-free MoS_2 conduction band with the addition of a Na-derived impurity level positioned below it. Hence, the gap state is moved below the Fermi energy, resulting in a very small activation energy for the transfer of electrons from Na to the MoS_2 conduction band. This is the situation schematically presented in figure 3.20(b), which leads to n-doping.

If we now replace Na with H on the SiO_2 siloxane surface, the associated filled gap state lies deep in the SiO_2 bandgap [see Fig. 3.19(a)], despite the fact that H and Na share the same *s*-like valence. The same situation persists in the composite [see Fig. 3.19(e)], where the H-derived filled spin-up level remains at mid-gap, approximately 0.5 eV above the VBM, while the empty spin-down one is nearly resonant within the conduction band. This situation however does not leads to doping so that H can not influence the conductivity of the MoS_2/SiO_2 structure. The quantitative difference found between the results for the Na and the H case show that, in order to obtain n-type character, only impurities with rather small ionization potential are relevant. These can transfer one electron to the MoS_2 conduction band with small activation energy. The activation energy is a key factor in the determination of the threshold voltage, V_{th}, required to operate a transistor in the on-state. As a consequence, the experimentally measured values for V_{th}, which show a large variation for different samples [186], are then attributable to varying concentrations and properties of the trap states from sample to sample.

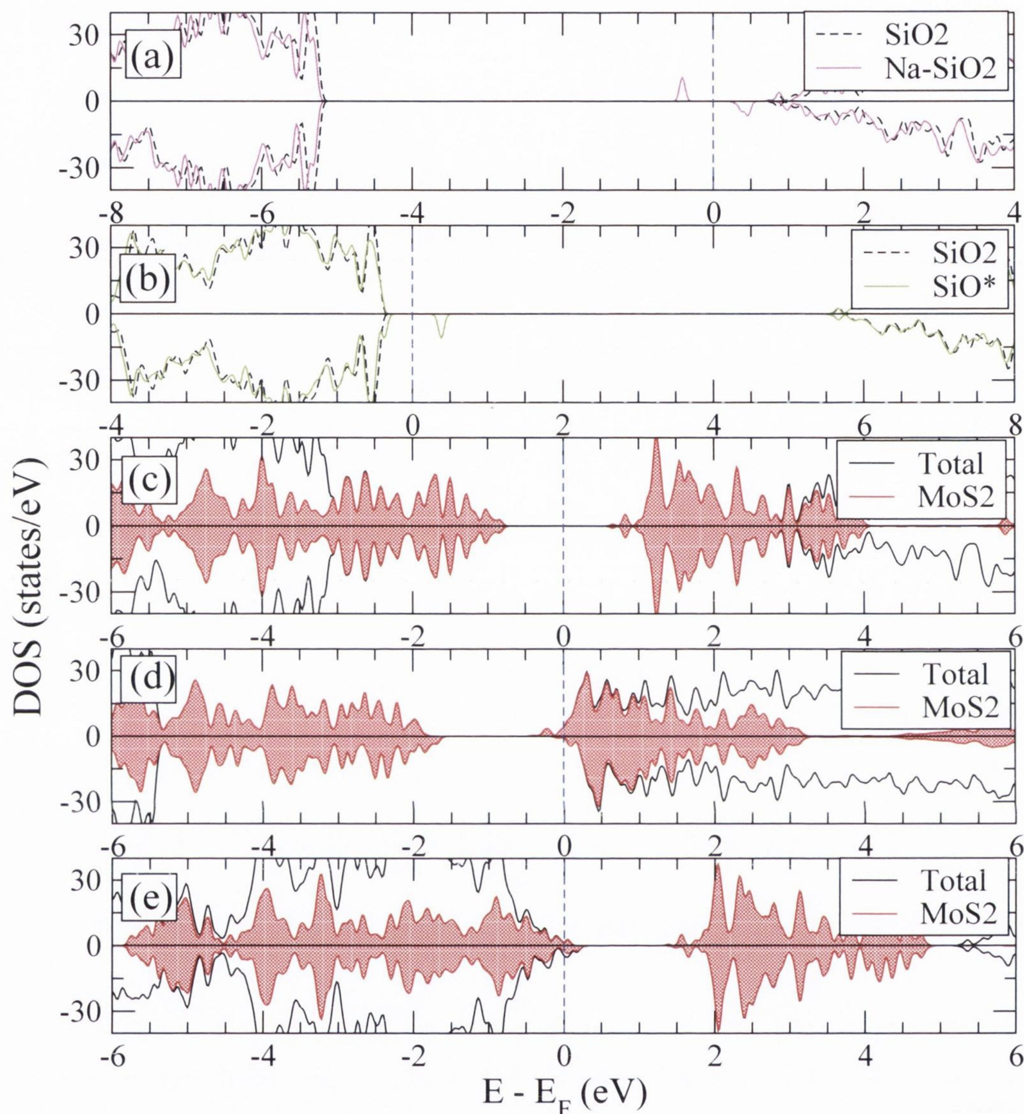

FIGURE 3.22: Electronic structure of the SiO_2/MoS_2 hybrid system when various defects are present at the SiO_2 silanol-reconstructed surface. (a) GGA-DOS for the defect-free surface (black, dashed curve) and for the one where on a Na atom in placed at the hollow site. (b) The GGA-DOS for the defect-free surface (black, dashed curve) and for the one where one O dangling bond is induced by a single H removal (green, solid curve labelled as SiO*). The total DOS and the MoS_2 PDOS for the SiO_2/MoS_2 composite when the MoS_2 monolayer is placed on (c) the defect-free surface, (d) on the surface with a single adsorbed Na atom, and (e) on the surface with a O dangling bond created by removing a single H atom. The blue dashed line indicates the Fermi energy, which is set to zero in all panels. The red shaded areas indicate the MoS_2 PDOS. Positive and negative DOS are respectively for spin up (majority spins) and spin down (minority spins) electrons. The electronic states in DOS are Gaussian broadened by 0.05 eV.

3.3.4 SiO_2/MoS_2 composite with silanol reconstruction

Next we move to examine the case of the SiO_2 surface with silanol reconstruction, whose DOS is presented in Fig. 3.22(b). Similarly to the siloxane case, the PDOS for the defect-free MoS_2/SiO_2 composite [see Fig. 3.17(c)] corresponds to a superposition of the DOS of the isolated MoS_2 [Fig. 3.19(b)] and SiO_2 [Fig. 3.22(b)] components, indicating weak interaction between the two materials. When a Na atom is intercalated between the silanol surface and the MoS_2 layer, we find that the system becomes n-type [Fig. 3.22(d)], in the same way as for the siloxane surface. This indicates that Na is an efficient n-dopant for MoS_2 on SiO_2 regardless of the surface reconstruction.

In general thermal annealing of the silanol surface creates under-coordinated oxygen atoms (Si-O*). These appear as stable surface defect centers and act as typical charge traps in oxygen rich SiO_2 [241], since they are able to capture an extra electron in their dangling bond. In our calculations, such defects are created on the Si-OH surface by removing a H atom from the top surface [see Fig. 3.21(b)]. For such a defect we find that the empty acceptor state is created ~0.9 eV above the SiO_2 VBM [see Fig. 3.22(b)]. Once MoS_2 is layered onto the surface, the value of d_0 at the boundary of our H-deficient unit cell is d_0 = 2.98 Å, which is approximately equal to that for the pristine surface, whereas at the dangling bond site the O-S distance is significantly reduced to 2.68 Å. When placing the MoS_2 monolayer on this defective surface, the dangling bond state gets filled by capturing an electron from the MoS_2 valence band, so that the Fermi energy now lies just below the MoS_2 VBM [see Fig. 3.22(e)]. This is the level alignment presented in Fig. 3.20(c), which makes the composite p-type. Note that the rather high density of oxygen dangling bonds in our system causes a large surface charge density dipole, which shifts the MoS_2 DOS downwards in energy by more than 1 eV with respect to the SiO_2 substrate. By modulating the density of such defect types one may be able to change such a shift.

We observe that for SiO_2 siloxane surface the impurity levels are much less deep in the bandgap ($\sim$ 1.5 eV) than that of the SiO_2 silanol surface (see Fig.3.19 and 3.22). So we expect a large energy shift of the VB (CB) of SiO_2 with respect to that of the VB (CB) MoS_2 band-edges, for example as shown in Fig.3.19(d) and 3.22(d). Here we mention that the large impurity concentration (10^14 cm^{-2}) in SiO_2 siloxane surface may be the cause for a closure of the impurity levels in the bandgap.

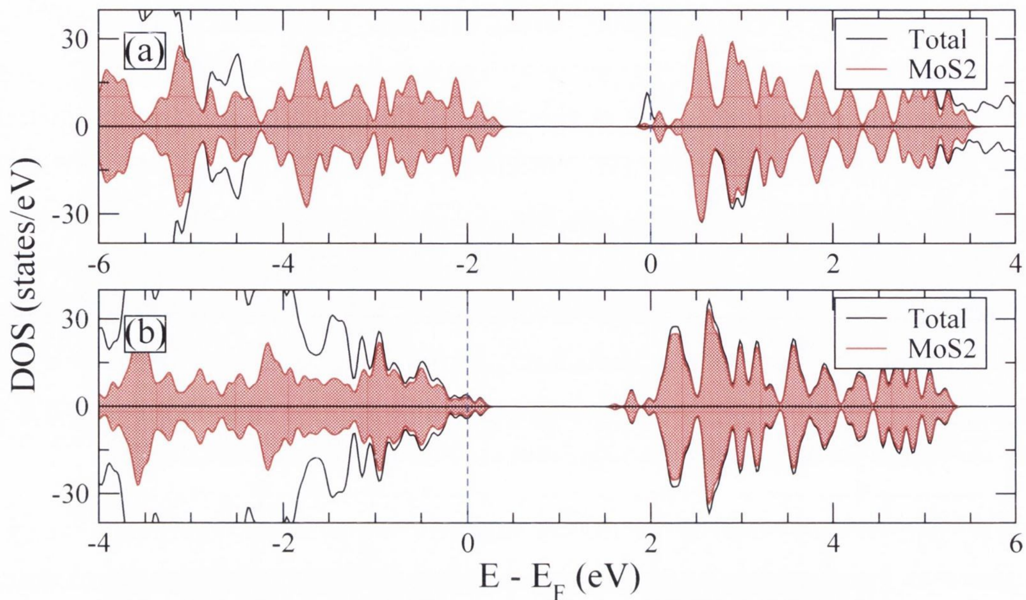

FIGURE 3.23: Density of states for the defective SiO_2/MoS_2 composite calculated with the ASIC XC functional. In panel (a) we report the DOS for the siloxane reconstruction with an intercalated Na atom [corresponding to Fig 3.19(d)], while in (b) that for the silanol reconstruction and an O dangling bond obtained by removing a surface H atom [corresponding to 3.22(e)]. The electronic states in DOS are Gaussian broadened by 0.05 eV.

3.3.5 Robustness of the results against the choice of XC functional: ASIC

Finally, in order to verify that the calculated level alignment is robust against the choice of exchange and correlation functional, we have repeated our calculations by using the ASIC scheme. As expected the ASIC functional increases the bandgap of MoS_2 and SiO_2 respectively to 1.73 eV and 8.02 eV (for the same strained hybrid structure used in the previous sections). In the case of SiO_2 this brings the calculated value sensibly closer to the experimental one of 8.9 eV [242], as expected from the ASIC when dealing with an insulator whose valence and conduction bands have different orbital content [229, 230].

The situation for MoS_2 is more complicated and deserves a detailed discussion. In this case the bandgap is defined by bands dominated mainly by Mo-d orbitals and the ASIC opens it only marginally. For a free-standing MoS_2 monolayer the ASIC ($\alpha = 0.5$) returns a direct bandgap of 2.03 eV (compared to a GGA gap of 1.71 eV).

Note that the LDA value is 1.86 eV so that the LDA already partially opens the gap with respect to the GGA. It is also notable that an enhancement of the screening parameter α to $\alpha = 1$ (full atomic correction) produces a marginal further increase of the gap to 2.10 eV. Comparing GGA, LSDA, ASIC, and HSE06, we therefore find only minor quantitative difference in the size of the bandgap [see Sec. 3.2.6].

We now go back to the SiO_2/MoS_2 composite and in Fig. 3.23 we report two representative results for the case of Na adsorbed on the siloxane surface and for that of the O dangling bond on the silanol one. We find that for the first case, although the bandgaps of the two parent materials are both increased, the Fermi energy is still pinned at the bottom of the MoS_2 conduction band [Fig. 3.23(a)]. As a consequence Na still leads to n-type semiconducting character with a small activation barrier. Similarly the O dangling bond on the silanol-terminated surface leads to p-type semiconducting character [see Fig. 3.23(b)], with the Fermi energy positioned below the MoS_2 valence band. This indicates that our two main results remain unchanged whether calculated at the GGA or ASIC level, i.e. they are robust with respect to the choice of exchange-correlation functional.

3.3.6 Conclusion

The effects of the SiO_2 substrate on the conductivity of a semiconducting MoS_2 monolayer are investigated. The defect-free SiO_2 surface does not affect significantly the electronic properties of MoS_2 due to their weak mutual interaction. The conductive properties of MoS_2 do not change and SiO_2 appears as an ideal gate material. However, when Na atoms are placed at the SiO_2/MoS_2 interface, a shallow donor trap state is created just below the CBM of the hybrid SiO_2/MoS_2 composite. The small activation energy ($\sim$0.10 eV) makes the hybrid MoS_2/Na-SiO_2 system an n-type semiconductor even for rather low temperatures. Interestingly, the behavior is different for H adsorption, where the impurity level is created $\sim$0.9 eV below the CBM, resulting in a stable localized charge that cannot be easily promoted to the CBM and does therefore not affect the conductivity.

In contrast, in the case of oxygen dangling bonds on the silanol-terminated SiO_2 surface, the Fermi energy of the MoS_2/SiO_2 system is located just below (0.03 eV) the VBM, making the system a p-type semiconductor. These results show that the conductivity of ultra-thin semiconducting LTMDs changes from n-type to p-type depending on the

charge-polarity of the traps, as well the energy level alignment of the trap states within the LTMDs band gap. These kinds of trap state at the SiO_2 surface are likely to be the origin of the observed change in conductance in different experimentally realized MoS_2-based transistors. Intriguingly, our results suggest the possibility of intentionally doping MoS_2 by depositing different adsorbates over the substrate SiO_2 surface. This can pave the way for a new strategy in the design of two-dimensional devices, where the electronic properties of the channel are engineered by manipulating those of the substrate.

Chapter 4

Electric Field Effects on Low Dimensional Nanostructures

Over the past several years one dimensional (1D) nanostructures, such as nanotubes, wires, rods, belts and ribbons have attracted growing interest from researchers keen to investigate the wide array of photophysical, photochemical and electron-transport properties that are unique to their dimensionality [245, 246]. The study of these nanostructures has also been facilitated by recent advances in nano-lithographic techniques [247], such as electron beam or focused-ion-beam (FIB) writing [248, 249] and X-ray or extreme-UV lithography [250], whereby such 1D systems can be readily fabricated in the research laboratory. From a nanotechnology perspective, 1D structures offer a range of potential applications that are different from those provided by their 2D and 3D counterparts [245, 251].

While carbon nanotubes (CNTs) remain the most widely studied 1D nanostructures to date, nanowires (NWs) and nanoribbons (NRs) have lately received increasing attention as possible alternatives. In particular the fact that the electronic structure of NRs can be modified by manipulating their edges, which usually are more reactive than the bulk, offers a powerful tool for customizing such nanostructures to a particular application. A recent experiment has shown that in nanoscale electronics, semiconducting NRs have comparable or exceeding performance to that of single crystals as their carrier mobility values, and on-off current ratio (in field effect transistor) have been enhanced [252]. For these reason recent times have witnessed an explosion of theoretical and experimental studies on NRs. Primarily these have been devoted to graphene NRs (GNRs) [38, 253, 254] but many other materials have been either made or predicted in the NR form.

These include BC_3 [255, 256], BN [257, 258, 259], ZnO [260, 261, 262], Si [263, 264] *etc.* Intriguingly for some of these, a magnetic [262, 264] or even a half-metallic ground state has been predicted.[265]

Alongside different dimensional nanostructures, the investigation of semiconductor nanoclusters (0D) has recently attracted considerable of experimental and theoretical interest [266, 267, 268, 269]. The spatial confinement of electrons in very small nanoclusters can induce size-dependent properties in the electronic structure of nanoclusters. For instance, they may exhibit a distinct functional change in, for example, optical, magnetic, or electronic properties [266]. Varying the size of nanoclusters or applying an external perturbation allows the electron affinity and ionization potential of the nanoclusters to be tuned, which may affect the rate of charge transfer [270]. One of the major motivations to study nanoclusters is to explore the current device technology in which better performance could be achieved compared to other nanostructures. For example, for a large area application, such as LEDs (light emitting diode) and photovoltaics, nanoclusters have the advantage of having size tunable absorption and emission [270].

Much intensive research has been devoted to tuning the bandstructure due to confinement induced quantization of the continuous band states [271]. In general, the ability to control the electronic properties of materials by an external perturbation such as an electric field, a magnetic field, strain, light, external doping is at the heart of modern science and technology. In many cases, an electric field can change the carrier concentration and the mobility in a semiconductor [36]. Particularly, an external transverse electric field (E_{ext}) can tune the electronic and magnetic properties in various nanostructures. For example, a transition from insulator to half-metal has been demonstrated theoretically [272] in *zigzag* GNRs. Moreover, Agapito *et al.* have studied the magnetism under E_{ext} applied on a single layer nanoclusters suggesting a potential application in spintronics devices [273].

From the parent MoS_2 single-layer crystal several nanostructures can be made. In fact a number of preparation methods for MoS_2 nanostructures including nanowires [80], nanoribbons [81, 275], nanotubes [274], triangular nanoclusters [277], and nanometer flowers [276] have been reported. All these nanostructures have been traditionally studied in the context of catalysis for desulfurization processes [277, 278], nanolubrication [279] and as thermoelectric materials [205]. More recently MoS_2 has also attracted attention as a potential electronic material. In particular, recently MoS_2 NRs transistors with high on-off ratio ($\sim 10^7$) have been demonstrated [187]. Here we explore a

different aspect, namely how the electronic properties of MoS_2 armchair nanoribbons (ANRs) can be manipulated by the application of an external electric field, E_{ext}. In particular we look at the possibility of inducing a metal-insulator transition in the nanoribbons, and at the associated magnetic moment formation via the Stoner mechanism[1] in the search for a large magneto-electric effect. Our study thus complements those already reported in the literature for graphene [272], BN [257], BC_3 [255] and AlN [280]. Next we extend this study of electric field effects onto single layer nanoclusters.

We are interested in studying the electronic structure of ANRs, although at present there is no experimental evidence for such type of edge termination. In contrast DFT calculations show the relative stability between the armchair and zigzag NRs [288]. However, in case of WS_2 (isostructural to MoS_2) monolayered zigzag edges have been identified recently through scanning transmission electron microscopy (STEM) [281]. Moreover, for graphene (most widely studied among the 2D layered materials) the formation of the zigzag and armchair edges have been characterized in a controlled way [282]. In this context, experimentally it has been reported that different types of edges terminations are present in MoS_2 monolayer nano-cluster [158]. Moreover, the formation of various edges structures also observed in these clusters depends on the growth conditions [158]. Therefore here we shed some light on the edges terminations of an ANR in the section 4.2.6. We note that following this work, an armchair nanoribbon has been synthesized using top-down fabrication technique [283].

Impurities in ANRs can generally change the ribbon's electronic and magnetic properties, *i.e.* these are an important factor in tuning the material for specific applications. Intrinsic impurities, which mainly form during the synthesis or under ambient conditions are crucial in such kind of nanostructures as their properties are ruled entirely by the edge's construction. In this work we study the effect of Cr substitutional in place of Mo in a ANR. The main motivation behind this study is to explore a way for inducing magnetism in a semiconducting ANR. Cr, in fact, is isovalent to Mo (it is one row up in the periodic table), but possesses partially filled $3d$ shell (in contrast to the $4d$ shell

[1] The basic idea behind the Stoner criterion [298] is as follows. Due to the localized density of states, electrons will experience a strong Coulomb repulsion if they occupy the same orbital, in which case they must have opposite spin orientation due to the Pauli exclusion principle. Therefore, to reduce the Coulomb energy, it is energetically favorable for the electrons to occupy different orbitals with the same spin (*i.e.* generating a non magnetic moment) instead of having parallel spin configuration. To accomplish this, electrons must be transferred to previously unoccupied orbitals with higher kinetic energy. Essentially, the Stoner criterion establishes a balance between Coulomb repulsion, Pauli exclusion principle, and an increased kinetic energy explicitly for continuous electronic bands.

of Mo), which can support a magnetic moment. We know that the exchange energy is relatively large for light atoms such as Cr (as compared to Mo). Although, there is no experimental study on Cr doped MoS_2-NRs, similar experimental as well as theoretical investigations have been conducted on transition metals doped (such as Co, Ni) MoS_2 nanoclusters, due their potential application as catalytically active materials [278]. Recently Ataca *et al.* have studied the electronic structure of atoms absorbed on the ANR's surfaces and their studies an important information towards its functionalization [303]. In addition, Cr-doped bulk MoS_2 have been synthesized and are promising for tribiological applications under a high humidity environment [284]. Interestingly a monolayer $Mo_{1-x}W_xS_2$ alloy (W is also isoelectronic to Mo) has been synthesized [285]. Such alloying are important to tune the electronic and mechanical properties, which may have potential for bandgap engineering and their edge-structure-related catalytic behaviors [285].

4.1 Computational details

Electronic structure calculations are performed using density functional theory (DFT) and the Ceperly-Alder parametrization [193] of the local spin density approximation (LSDA) to the exchange and correlation functional. In particular we employ the SIESTA code [125]. A double-ζ polarized [195] numerical atomic orbital basis set for Mo and S is used together with the Troullier-Martins scheme for constructing norm-conserving pseudo-potentials [194]. The pseudo-potentials are generated by treating the following electronic states as valence states : Mo: $5s^1 5p^0 4d^5 4f^0$; S: $3s^2 3p^4 3d^0$. An equivalent plane wave cutoff of 250 Ry is chosen for the real space grid. The Brillouin zone is sampled using a $(1 \times 100 \times 1)$ Monkhorst-Pack grid for the NRs, while for the single layer triangular nanoclusters (TNCs) the Γ-point is only employed in the calculations. In both cases, periodic boundary conditions have been included and a vacuum layer of at least 15 Å is placed at the edges of the ribbon both in plane, and out of plane in order to suppress the interaction between the ribbon periodic images, whereas the vacuum layers are placed along all directions in the case of TNCs. The conjugate gradient method is used to optimize the geometry, where all the atoms in the unit cell are allowed to relax under the action of the external electric field until the forces on each atom are less than 0.03 eV/Å.

In our calculation we do not consider explicitly any correction terms, which arise due to the dipole when an external field is applied to the cell. Due to periodic boundary conditions, the image charge will then be repeated. Here we use a vacuum separating between cells large enough that such electrostatic interaction between the image charges can be neglected. Indeed we observe that the electronic structure does not change when the length of vacuum region is as large as 25 Å.

4.2 Electric field effect on MoS_2 Nanoribbon

4.2.1 Nanoribbon Structure

Each layer of bulk MoS_2 is used as the 2D template for constructing the NRs. Similarly to C nanotubes [286], MoS_2 NRs may be described by 2D primitive lattice vectors, $\vec{a}$ and $\vec{b}$, of the parental 2D structure and two integer indices (n, m) [287], so that the chiral vector is defined as $\vec{C_h} = n\vec{a}+m\vec{b}$. Three types of NRs can thus be identified: *zigzag* for $n = m$, *armchair* for $n \neq 0$, $m = 0$, and *chiral* for $n \neq m$ [see the Fig. 4.1(a)]. MoS_2-ANRs are nonmagnetic semiconductors irrespective of their size, whereas the *zigzag* nanoribbons (ZNRs) are predicted to be metallic and magnetic [288]. Since our goal is that of describing an electric-field induced metal-insulator transition, our starting point must consist of NRs with an insulating ground state. Nevertheless, the electric field effect also has been studied in *zigzag* nanoribbons [289]. As such we consider only ANRs. As a matter of notation, following several previous studies [257, 288, 290], we identify the different sized MoS_2 ANRs as n-ANR, where n is the number of dimer lines across the terminated direction of the 2D MoS_2 layer, *i.e.* across the non-periodic dimension of the nanoribbon [see Fig. 4.1(b)]. The multilayer ribbons are constructed by placing single layer ribbons on top of each other with an ABA stacking [291].

4.2.2 Electronic structure of MoS_2-ANR

In Fig. 4.1(b) the optimized geometry of a MoS_2 10-ANR is shown (the periodicity is along the y-direction). For symmetric ANRs (n odd) the two edges have mirror reflection symmetry, while this is not the case for the antisymmetric ones (n even). Our calculations show that the two possible ribbon configurations are energetically degenerate (see Fig. 4.2), meaning that the total energy per atom scales with the ribbon

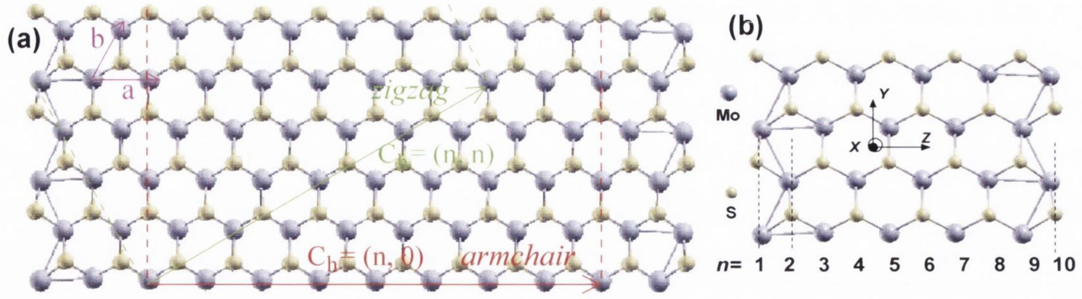

FIGURE 4.1: (a) Structural relation between a single layer 2D MoS_2 sheet and a nanoribbon. The vector $\vec{a}$ and $\vec{b}$ are the primitive vectors for the MoS_2 lattice. The chiral vectors $\overrightarrow{C_h} = n\vec{a} + m\vec{b}$ is specified by (n, m). The $(n, 0)$ direction (red arrow) and the (n, m) (green arrow) direction indicate the "armchair" and "zigzag" edge respectively and the corresponding dotted lines denote the periodic direction of the nanoribbons. (b) The optimized structure of a MoS_2 10-ANR. The ribbon is periodic along the y direction. Color code: grey (dark grey) = Mo, yellow (light grey) = S.

size but does not depend on the ribbon symmetry. We have then checked that the electronic properties and their dependence on the external electric field are insensitive to the ribbon geometry and here data are presented only for the asymmetric case. In

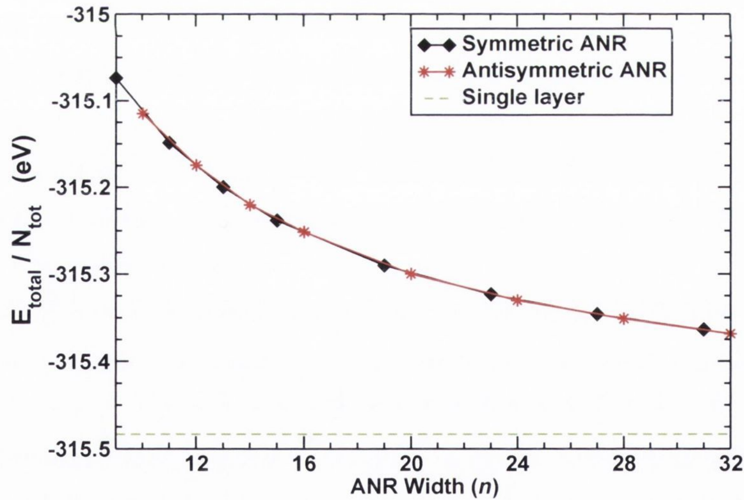

FIGURE 4.2: Total energy per atom for various n-ANRs as a function of n. Note that the symmetric (n odd) and antisymmetric (n even) congurations are energetically degenerate.

order to determine the ground state of the different n-ANRs, we have first carried out both spin-unpolarized and spin-polarized total energy calculations including geometry optimization. We take the case of a 10-ANR as an example and we use its electronic structure to discuss the general properties of such a NRs class. From the bandstructure

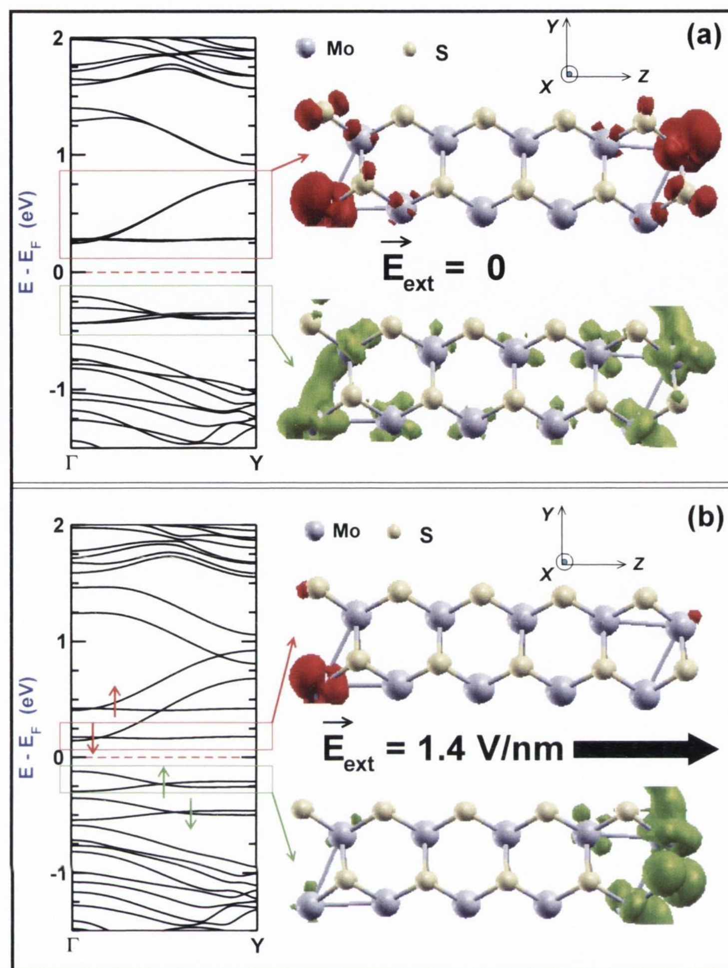

FIGURE 4.3: Electronic structure of a 10-ANR as a function of an external transverse electric field, E_{ext}. In (a) we present: (left) the band structure and (right) the LDOS respectively of the CB (top) and VB (bottom) for $E_{\text{ext}} = 0$. In (b) the same quantities are shown for $E_{\text{ext}} = 1.4$ V/nm. The LDOS are taken over the energy range indicated by the red (dark gray) and green (light gray) boxes respectively above and below the Fermi level (see band-structure). Note that in both cases the CB and VB are characterized by states located at the NR edges.

[shown in Fig. 4.3(a)], it is clear that a 10-ANR is a non-magnetic semiconductor with a direct (LSDA) bandgap of 0.45 eV at the Γ point. This is in agreement with previous calculations [288]. The local density of states (LDOS) of the conduction band (CB) and valence band (VB) [shown in Fig. 4.3(a)] indicates that the electronic states around E_{F} are completely localized at the ANR's edges. The CB and the VB originate from a hybridized mix of Mo-4d and S-3p orbitals with the hybridization being stronger in the VB than in the CB.

Such results are relatively independent of the ribbon size, and unlike graphene NRs, all

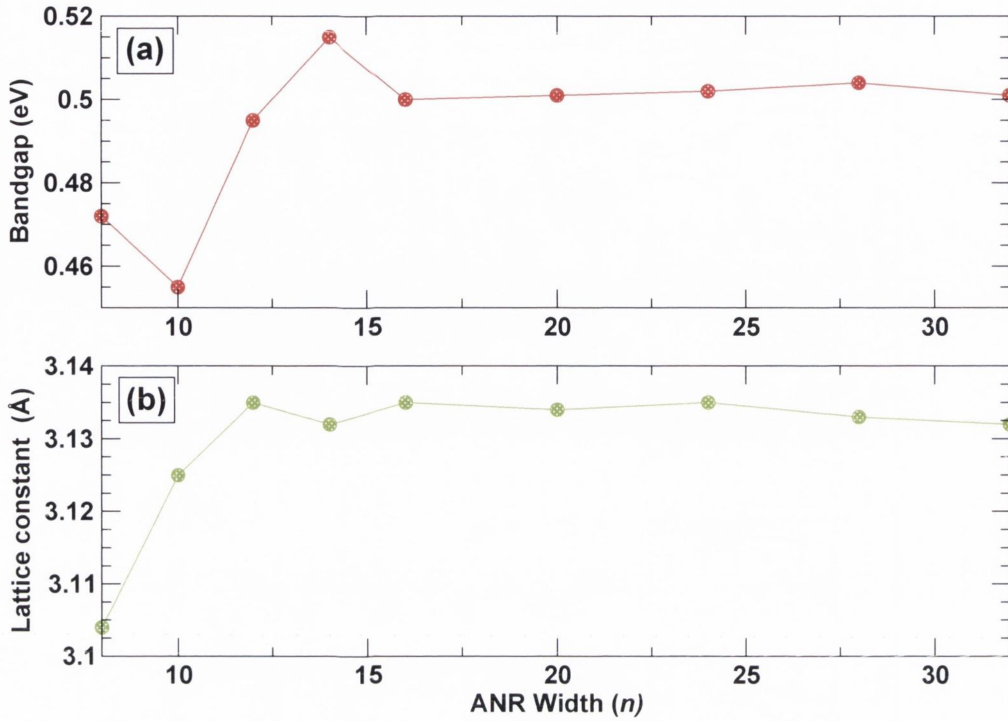

FIGURE 4.4: Variation of (a) the elementary LSDA bandgaps and (b) the lattice constants with width of ANRs.

the MoS_2 ANRs are semiconducting. For the smaller n-ANRs ($n \leq 24$), the bandgap oscillates in magnitude with increasing n and finally converges to a constant value of around 0.52 eV for larger sized ribbons ($n > 24$) [see Fig. 4.4(a)]. The same oscillatory behavior has been observed in earlier calculations [288] and it is quite similar to that predicted for BN-ANRs [258]. As n increases we also observe oscillations in the equilibrium lattice constant, which slowly approaches a constant value of $\sim$ 3.132 Å [see Fig. 4.4(b)], similar to that calculated for the infinite MoS_2 single layer. We thus note that the calculated bandgaps for all n-ANRs are much smaller than that of the infinite MoS_2 single layer (1.90 eV), while the lattice constants deviate only marginally. The reason for such a difference is rooted in the fact that both the VB and CB of the ribbons are formed by states strongly localized at the two edges. Indeed these states do not exist in the case of the infinite MoS_2 single layer and they are simply a consequence of the different wave-function boundary conditions.

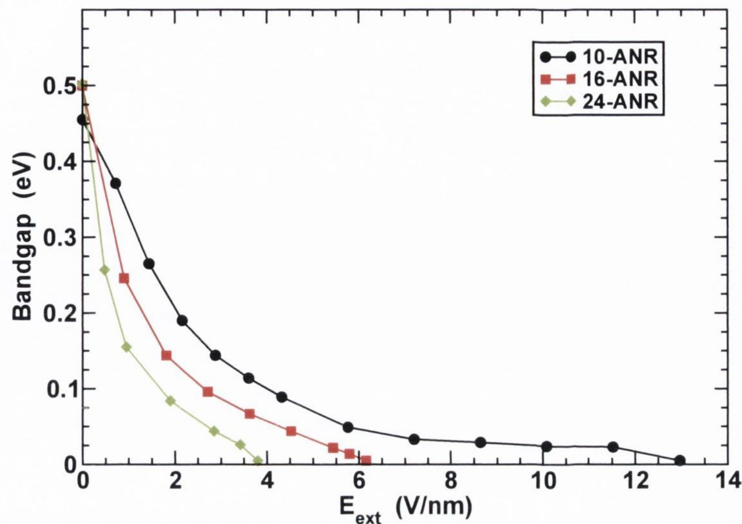

FIGURE 4.5: Variation of the elementary LSDA bandgap with the applied transverse electric field, E_{ext}, for 10-ANR (black circles), 16-ANR (red squares), 24-ANR (green diamonds).

4.2.3 Response of a MoS_2-ANR to E_{ext}

We now discuss the response of the electronic structure of the MoS_2-ANRs to a static external electric field, E_{ext}. As mentioned earlier, the size of the ribbon bandgap is determined by the energy position of the edge states forming the CB and the VB. Thus any change in the ANR bandgap under an applied field would be mainly determined by the response of its edge states. It is worth noting that for $E_{\mathrm{ext}} = 0$, both the CB and VB are doubly degenerate as there are two states in each band corresponding to the two edges of the ribbon (this means that the electron density corresponding to either the CB or the VB is equally distributed over the two opposite edges). We find no gap modulation when E_{ext} is perpendicular to the plane of the ribbon, indicating that a planar MoS_2 nano-structure with a longitudinal gate will not be electronically responsive. In contrast a significant modulation of the bandgap can be obtained by means of a transverse field. This is applied along the z-direction according to the geometry of Fig. 4.1(b). In practice in our calculations a periodic sawtooth-type potential perpendicular to the ribbon edge is used to simulate the transverse electric field in the supercell so that the potential remains homogeneous along the ribbon edges [292].

As the transverse E_{ext} is applied, the bandgap decreases monotonically while remaining direct at Γ [see Fig. 4.3(b) and Fig. 4.5]. Such behavior can be understood by assuming little interaction between the electron densities at the two edges. Under this assumption

the only effect produced by a transverse electric field is that of creating an electrostatic potential difference across the ribbon. As a consequence, the band manifold (either belonging to the VB or the CB) localized at the edge kept at the higher external potential moves upwards in energy, while that kept at the lower potential moves in the opposite direction. Hence, the new bandgap of the system in the presence of an external electric field is formed between the CB manifold localized at the lower potential edge and the VB manifold localized at the opposite one. The edge degeneracy is thus broken. As the field strength increases the bandgap reduces further and eventually vanishes for a critical field, E_c, characteristic of the specific nanoribbon. Note that such a Stark-driven gap modulation has been previously reported for C nanotubes [293] and for nano-ribbons made of different materials such as graphene [272], BN [257, 258, 294], AlN [280] *etc.* Notably, in the case of MoS_2 and in contrast to some other compounds such as BN [294], the gap closure is independent of the field polarity, reflecting the perfect mirror symmetry of the ribbon's edges.

Fig. 4.5 shows the evolution of the bandgap as a function of the external electric field for three selected nano-ribbons, respectively 10-ANR, 16-ANR and 24-ANR. In general we observe that the bandgap drops more rapidly with E_{ext} as the size of the n-ANRs gets larger. Such a width dependence can be easily rationalized by assuming again little interaction between the two ribbon edges. In this case the potential difference between the edges necessary to close the gap is the same regardless of the ribbon size. If one now assumes that the potential drop inside the ribbon is approximately uniform (linear), we will conclude that larger ribbons necessitate smaller electric fields to sustain the same potential difference at the edges. As such the critical field, E_c, decreases with the ribbon width and already for a 24-ANR it assumes a value around 4 V/nm.

Our calculated values for the critical field E_c are quite similar to those obtained before for BN [294] and AlN,[280] despite the fact that the bandgaps in these materials are much larger. Such a fact however should not be surprising. In fact, the bandgap closure occurs because of the almost rigid shift of the edge-localized ribbon CB and VB when the field is applied. As such, the condition for gap closure is that the external field produces a potential difference, ΔV, at the nano-ribbon edges that matches the ribbon bandgap, ΔE_g, *i.e.* $e\Delta V = \Delta E_g$, where e is the electron charge. Under the assumption of a linear potential drop (constant electric field) inside the ribbon, we obtain the relation $e\Delta V = eE_{ext}\frac{d}{\kappa}$, where κ is the ribbon dielectric constant along the transverse direction and d is the ribbon width. The critical field for the gap closure

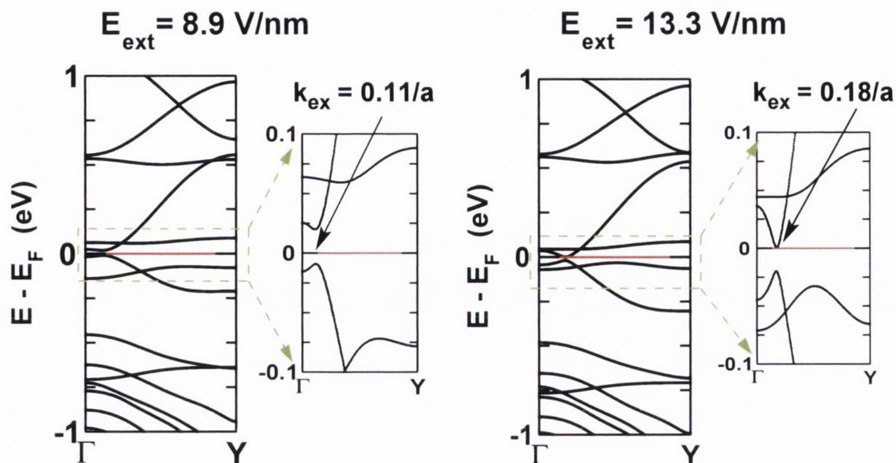

FIGURE 4.6: Non-spin polarized LDA-bandstructure of a MoS_2 10-ANR in presence of a transverse field of magnitude close to that needed for the gap closure: $E_{\text{ext}} = 8.9$ V/nm (left) and $E_{\text{ext}} = 13.3$ V/nm (right). The smaller figures are a zoom around the Fermi level (a is the lattice constant).

then simply reads

$$\Delta E_{\text{g}} = e\Delta V = E_{\text{c}}\frac{ed}{\kappa} \quad \rightarrow \quad E_{\text{c}} \propto \frac{1}{ed}\,, \tag{4.1}$$

where the second equality follows from the fact that the dielectric constant is approximately inversely proportional to the material bandgap. The Eqn. (4.1) has two important consequences. On the one hand, it tells us that the critical field for the gap closure is approximately material independent. On the other hand, it establishes a $1/d$ decay of E_{c} with the ribbon width.

Before the bandgap closes completely with increasing E_{ext} an interesting effect is observed in small sized ANRs (for example in 10-ANR), namely that the gap remains direct but it moves away from Γ towards Y in the 1D Brillouin zone. This shift occurs simultaneously with bandgap reduction and it is seen to become more pronounced as E_{ext} gets larger. Such an effect can be observed in Fig. 4.6 where the band-structure of the 10-ANR is plotted for two different values of the electric field. The bandgap shift away from Γ appears because of the interaction between the two edges of the ribbon and can be explained with the help of a simple tight-binding model, which we develop next.

As already mentioned, the CB and VB are extremely localized at the edges of the ANR, so that their dispersion is solely determined by the longitudinal dimension. Then we can model their electronic structure by considering a simple nearest-neighbor tight

binding model for two linear chains (mimicking the two 1D edges). For simplicity, we take only s orbitals in the model and the CB and VB are simply characterized by two different on-site energies, respectively ϵ_{L} and ϵ_{R} (L and R stand for left and right-hand side edge). This is of course a rather crude model, as both p and d orbitals are excluded. However, the bandgap closure and the formation of a magnetic moment both originate from the one-dimensional nature of the edge states and not from the details of their orbital composition. Our simple model captures the essential features of this problem, while further details related to edge specific nature will be discussed at the end of this section.

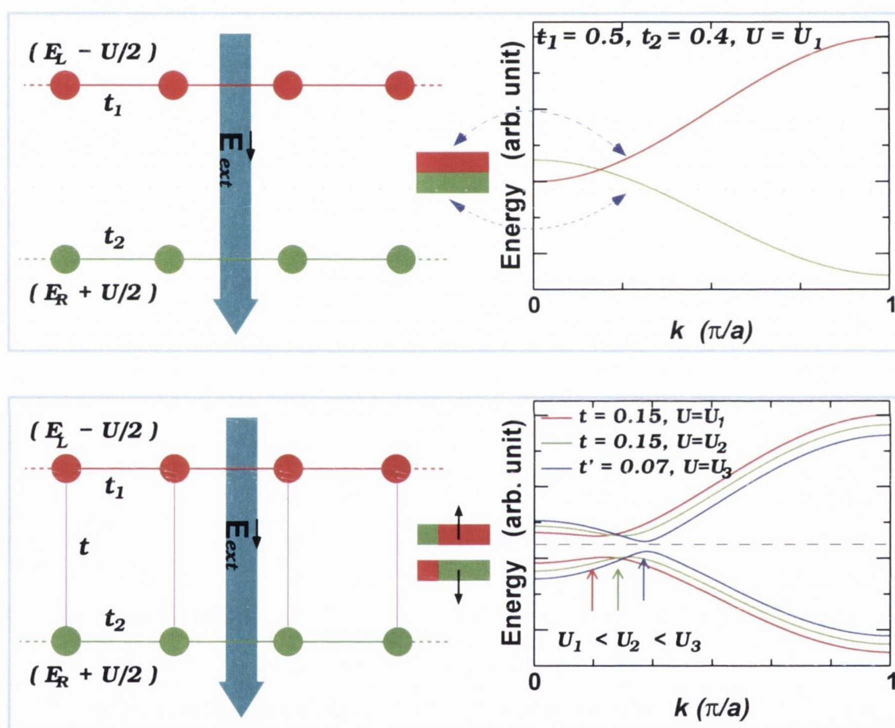

FIGURE 4.7: The band-structure of two linear chains calculated by using a simple tight-binding model. In the top panel the interaction between the chains is assumed to vanish, while in the bottom one there is an additional hopping matrix element between atoms belonging to different chains (the chains are arranged on a square lattice). The horizontal dotted line in the lower panel corresponds to the Fermi level.

The two edges of a nanoribbon interact with each other in two possible ways. On the one hand, electrons can tunnel between the two edges with a probability given by the hopping integral t. This is expected to decrease as the ribbon width becomes larger. On the other hand, upon the application of an external field, the charges at the two ribbon edges will interact electrostatically. Such an interaction is taken into account by

the dielectric response of the ribbon, which is described by the transverse component of the dielectric constant κ. The potential difference between the ribbon edges, ΔV, is related to the external field simply as $\Delta V = E_{\text{ext}}\frac{d}{\kappa}$. The 1D band-structures for the two edges are simply, $E_{\text{L}}^{k} = \epsilon_{\text{L}} - 2t_1 \cos k$, and, $E_{\text{R}}^{k} = \epsilon_{\text{R}} + 2t_2 \cos k$, where $t_1 > 0$ and $t_2 > 0$ are the hopping integrals respectively of the left- and right-hand side chain, and k is the 1D dimensional wave-vector (see Fig. 4.7). Let us assume that $\epsilon_{\text{L}} > \epsilon_{\text{R}}$ so that the left-hand side edge corresponds to the CB and the right-hand one to the VB (the bandgap is at Γ). Let us also assume for the moment that there is no inter-chain interaction, *i.e.* that the hopping integral between the two chains vanishes, $t = 0$. Clearly, if $|\epsilon_{\text{L}} - \epsilon_{\text{R}}| > 2(t_1 + t_2)$ there will be a gap between the CB and VB. The presence of an electric field simply shifts the on-site energy of the two bands. Thus the new on-site energies will be respectively $\epsilon_{\text{L}} - U/2$ and $\epsilon_{\text{R}} + U/2$, with $U = e\Delta V$. This simple model then predicts that the bandgap will close for $U = \epsilon_{\text{L}} - \epsilon_{\text{R}} - 2(t_1 + t_2)$. For electric fields exceeding such values the ribbon will appear as a semi-metal, *i.e.* it will present coexisting electron and hole pockets at the Γ point.

Let us now investigate the situation in which there is inter-chain interaction, *i.e.* $t \neq 0$ between atoms localized on different chains (the atoms are assumed to be arranged on a square lattice). The new band-structure now takes the form

$$E_{\pm}^{k} = \frac{E_{\text{L}}^{k} + E_{\text{R}}^{k}}{2} \pm \frac{1}{2}\sqrt{[E_{\text{L}}^{k} - E_{\text{R}}^{k} - U]^2 + 4t^2}\,, \tag{4.2}$$

where the "+" sign is for the CB and the "−" one is for the VB. Clearly inter-chain hopping opens up a bandgap (of size $2t$) at the point along the Γ-Y line, where the two bands would otherwise cross for $t = 0$ (as shown in Fig. 4.7). It also indicates that, if the applied electric field increases further (U gets larger), the k-point where the direct bandgap appears will shift towards Y, but the value of the bandgap itself will remain constant. It then follows that the bandgap closure occurs only if t is reduced simultaneously as E_{ext} is increased (see the curve in Fig. 4.7 for $t' < t$). This essentially suggests that the polarization of the edge state wavefunctions under the influence of E_{ext} occurs in such a way as to reduce the effective interaction between the two edges of the ribbon. Notably the position in k-space of the bandgap, k_{ex}, can be found by minimizing Eq. (4.2). This gives us $k_{\text{ex}} = \cos^{-1}\left[\frac{U_0 - U}{2(t_1+t_2)}\right]$, with $U_0 = \epsilon_{\text{L}} - \epsilon_{\text{R}}$. Such a qualitative picture agrees quite well with our DFT calculated k_{ex}, which is presented in Fig. 4.8 for small ANRs ($n < 20$). From the figure it is also worth noting, again in agreement with our simple model, that k_{ex} is practically independent of the ribbon

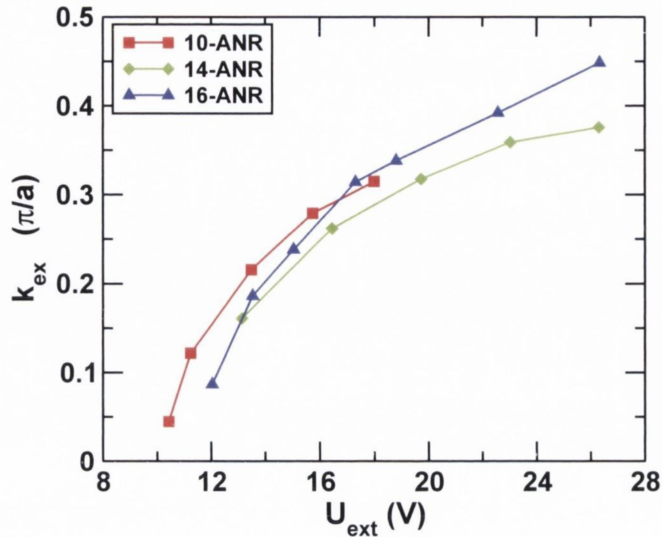

FIGURE 4.8: The variation of the k-vector, $k_{\rm ex}$, corresponding to position of the energy bandgap as a function of applied bias for different n-ANRs. Here $U_{\rm ext} = E_{\rm ext}d$, where d is the nano-ribbon width.

size once the curve is plotted as a function of the external potential at the ribbon edges $U_{\rm ext} = E_{\rm ext}d$.

Next, we make a number of additional observations, which further validate our model. Firstly we note that, as expected, the interaction between the ribbon's edges gets stronger as the ribbon gets smaller. This means that the band repulsion at the bandgap along the Γ-Y direction strengthens for small nano-ribbons. As a consequence the gap-closure occurs for relatively larger fields than those expected by a simple rigid band shift (see figure 4.5). Secondly, the position in k-space of the gap immediately before its closure, $k_{\rm c}$, moves towards Γ as the ribbon becomes wider. This essentially indicates that the inter-edge interaction, parametrized by t, is reduced for large nano-ribbons. In order to prove such a fact, in Fig. 4.9 we plot the bandgap (at relatively large field) as a function of the nano-ribbon size n. This is calculated for an external electrostatic potential, $U_{\rm ext} = 12$ Volt, sufficient to move the bandgap away from Γ for all the ribbons investigated. In this situation the bandgap is a direct measure of the inter-edge hopping t, $\Delta E_{\rm g} \sim 2t$. Notably the decay is rather severe indicating that already for relatively small ribbons ($n > 14$) the inter-edge interaction becomes almost negligible.

Finally we look at the charge density polarization induced in the ANRs by the external electric field. In figure 4.10 we plot the field-induced charge density distribution, $\Delta\rho$, as a function of the position across the ribbon (z-coordinate, see Fig. 4.1). Here $\Delta\rho$

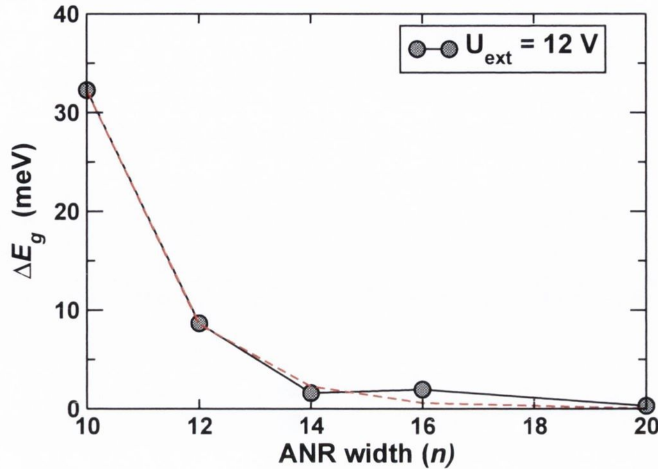

FIGURE 4.9: Variation of the LSDA-bandgap $\Delta E_{\rm g}$ as a function of the n-ANR width, n. Results are plotted for an applied external potential, $U_{\rm ext} = 12$ V, which is sufficient to shift the bandgap away from Γ. In this condition $\Delta E_{\rm g}$ is a direct measure of the inter-chain hopping integral t. The red dashed line is an exponential fit of the calculated data.

is the difference between the charge density calculated in an applied field $\rho(E_{\rm ext})$ and that in no field, $\rho(E_{\rm ext} = 0)$. Also note that all the densities are averaged over the xy plane. Notably there is charge accumulation at the positive potential edge and a corresponding depletion at the negative one. A transverse field induces an electrical dipole across the ribbon, which effectively behaves as a capacitor.

The accumulated charge can be calculated by simply integrating $\Delta\rho(z)$ from one of the edge positions, $z_{\rm L}$, to the ribbon mid-point, $z_{\rm m}$, which is $\Delta\rho_{\rm acc} = \int_{z_{\rm L}}^{z_{\rm m}} \Delta\rho(z)\, dz$. This quantity is presented next in Fig. 4.11 as a function of $E_{\rm ext}$ and for different ANRs. Clearly $\Delta\rho_{\rm acc}$ is found to increase linearly with the field. This is the behavior expected from a parallel plate capacitor. A second important observation, also consistent with viewing the ribbon as a parallel plate capacitor, is that the slope of the $\Delta\rho_{\rm acc}$-$E_{\rm ext}$ curve is almost independent of the ribbon width. Minor variations can be attributed to our arbitrary definition of the ribbon mid-point (this is defined in terms of the planar average of $\Delta\rho(z)$ as the point where $\Delta\rho(z) = 0$) and to the fact that as the field increases and the ribbon bandgap is reduced, the dielectric constant changes.

In summary, the evolution of the electronic properties of MoS_2 armchair nano-ribbons as a function of an external transverse electric field can be understood in terms of the ribbon dielectric response, which is indeed consistent with that of a linear dielectric. These findings are rather general and can be easily transferred to other materials with

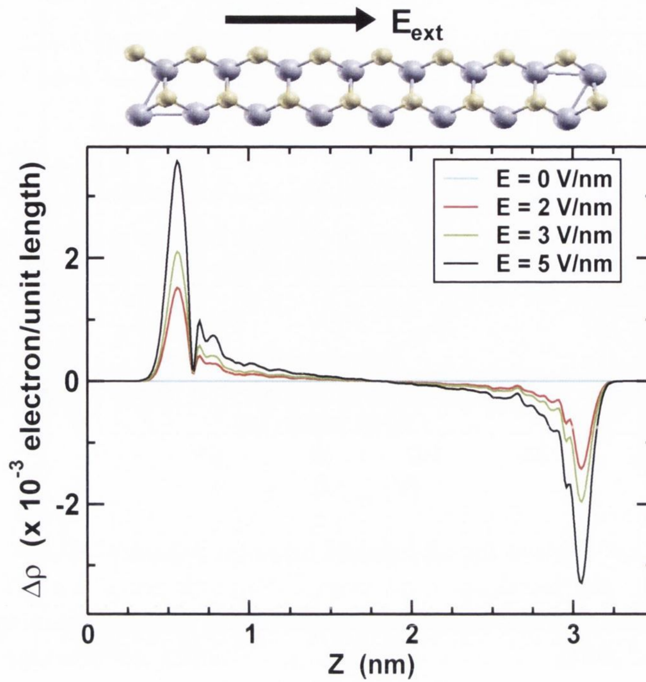

FIGURE 4.10: Field-induced charge density distribution along the nano-ribbon, $\Delta\rho = \rho(E_{\rm ext}) - \rho(E_{\rm ext} = 0)$, for a 16-ANR and different values of $E_{\rm ext}$. Here $\rho(E_{\rm ext})$ is the charge density for an external field $E_{\rm ext}$ averaged over the longitudinal direction (xy-plane) and plotted along the transverse one, z.

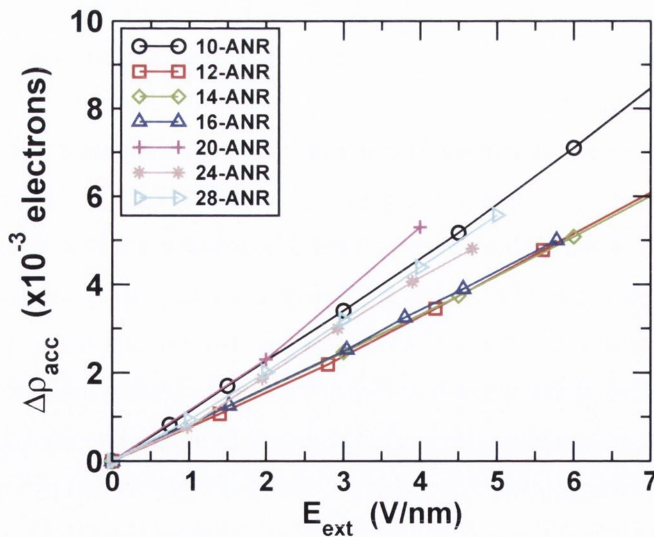

FIGURE 4.11: Charge density accumulation, $\Delta\rho_{\rm acc} = \int_{z_{\rm L}}^{z_{\rm m}} \Delta\rho(z)\,dz$, as a function of the external electric field for n-ANRs of different width. Note the linear dependence with an almost ribbon-independent slope.

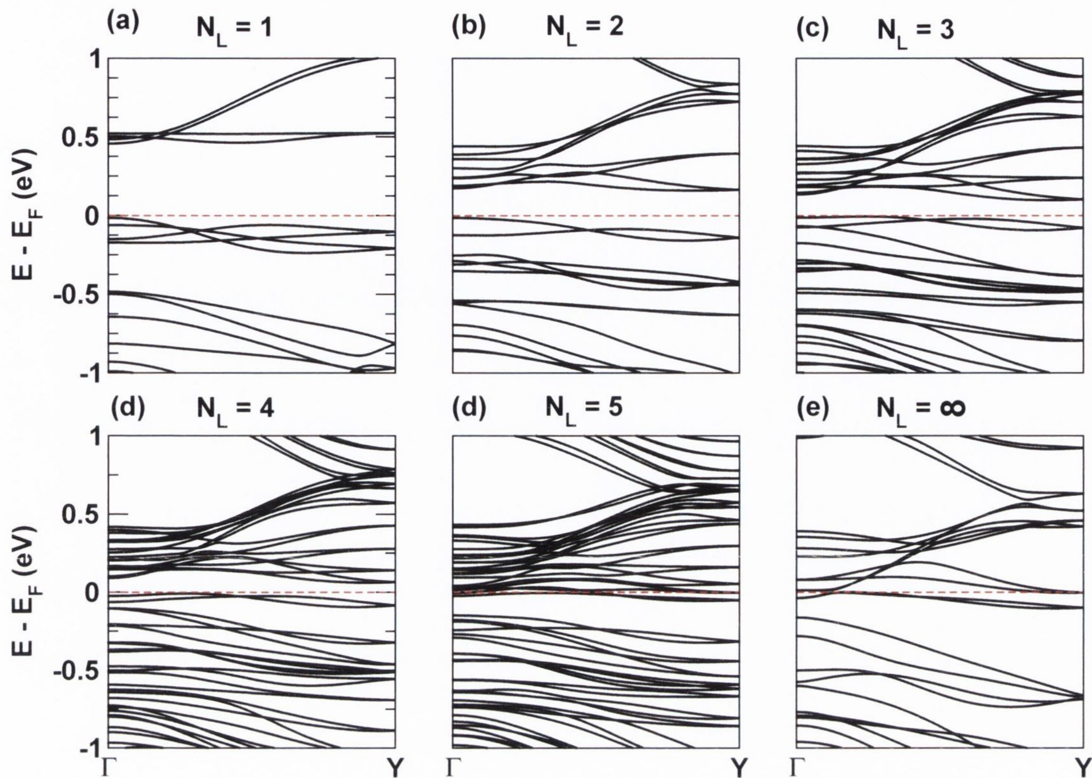

FIGURE 4.12: The LSDA-bandstructure for a multi-layered MoS_2 8-ANR: (a) $N_L = 1$, (b) $N_L = 2$, (c) $N_L = 3$, (d) $N_L = 4$, (e) $N_L = \infty$. Note that now the bandgap is indirect with the conduction band minimum positioned along the Γ-Y direction. The horizontal dashed line denotes the position of the Fermi level.

different bandgaps. Next we examine the effects of stacking multiple MoS_2 nano-ribbon layers.

4.2.4 Bi-layer and multi-layer MoS_2-ANR

In 2D layered compounds the tiny inter-layer interaction is often sufficient to change drastically the electronic properties of the material. A prototypical example is graphene, where the weak π-π interaction is able to turn the linear band-dispersion parabolic [296]. It becomes therefore natural to investigate how the results of the previous section get modified in multi-layered ribbons comprising N_L monolayers.

In order to keep the computational costs reasonable we consider here only the case of 8-ANRs, whose electronic band-structure in a few layers form is presented in Fig. 4.12. As for bulk MoS_2 also multi-layered nano-ribbons display an indirect bandgap, which

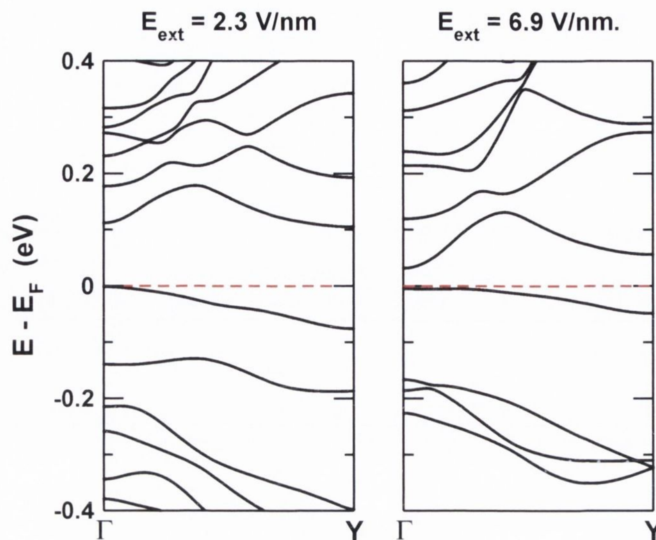

FIGURE 4.13: The LSDA-bandstructure of a MoS_2 8-ANR bi-layer in the presence of a transverse electric field. For $E_{\text{ext}} = 2.3$ V/nm (left) the bandgap is indirect, while it becomes direct at Γ for the larger field of $E_{\text{ext}} = 6.9$ V/nm (right).

is positioned along the Γ-Y direction in the 1D Brillouin zone. We have extended our calculations to ANRs comprising up to five layers and, for comparison, to an infinite (periodic) nano-ribbon stacking. We notice that the bandgap turns indirect already for a bi-layer and then it remains indirect for any other structure. Furthermore, the bandgap decreases monotonically with increasing the number of layers. However, at variance with their parent 2D counterparts and similarly to the single-layer ribbons, also in multi-layered ANRs both the CB and the VB are localized over the ribbon edges. This fact is rather robust with respect to the interlayer-separation, in contrast to what happens to the fine details of the electronic structure of the infinite 2D multi-layers [297], so that the explicit inclusion of van der Waals interaction in the present context is not crucial. The localization of CB and VB at the edges means that, as in the single-layer case, also the multi-layers are sensitive to a transverse electric field.

Such a sensitivity is examined next for the case of the 8-ANR bi-layer in Fig. 4.13. In general the response to E_{ext} is qualitatively similar to that of the single layers as it is determined by the electrostatic potential shift at the nano-ribbon edge. Thus as E_{ext} gets larger the energy shift of both the CB and VB localized at opposite edges results in a bandgap reduction. There is however a difference with respect to the single layer case, namely that the inter-layer interaction lifts the edge-band-degeneracy for $E_{\text{ext}} = 0$. As a consequence the band-dispersion around the bandgap changes in a

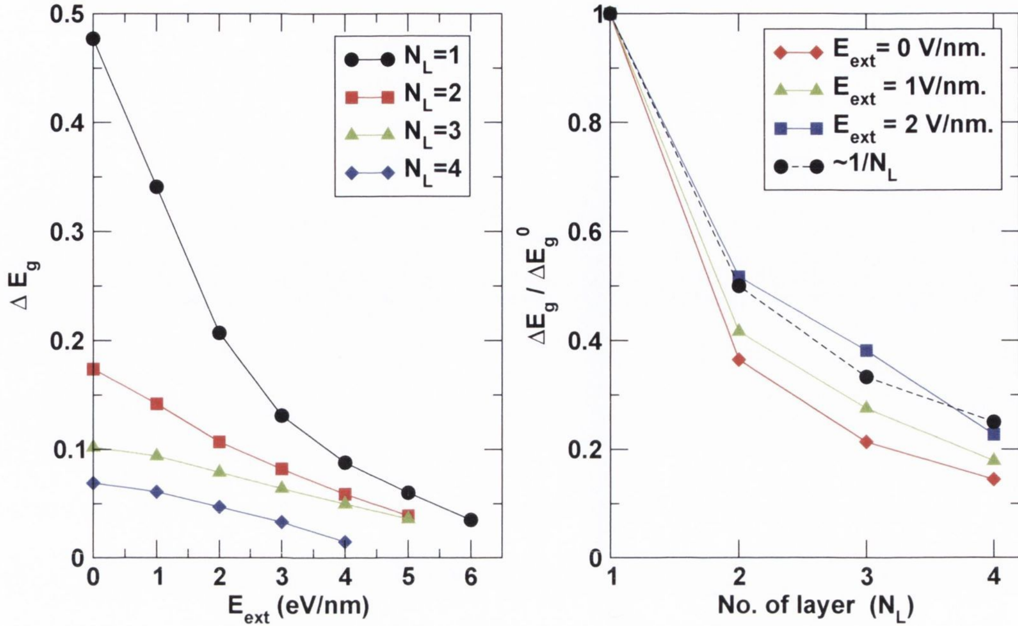

FIGURE 4.14: Left: variation of the elementary LSDA bandgap with the applied transverse electric field, E_{ext}, for monolayer (black circles), bi-layer (red squares), tri-layer (green triangles) and quadri-layer (blue diamonds) of 8-ANR. Right: variation of the normalized elementary LSDA bandgap with different number of layer for $E_{\text{ext}} = 0$ V/nm (red diamonds), $E_{\text{ext}} = 1$ V/nm (green triangles), and $E_{\text{ext}} = 1$ V/nm (black circles). Here Δ_g^0 is the bandgap of the corresponding 8-ANR at the $E_{\text{ext}} = 0$. The black line denotes the perfect $1/\text{N}_L$ variation of the bandgap with N_L being the number of layers

non-trivial way with the electric field. For instance for the case of the bi-layer 8-ANR first the CB minimum moves towards Y, thus strengthening the indirect nature of the gap and then, for larger fields, is reverts back to Γ and eventually the bandgap becomes direct. This is an intriguing feature as it demonstrates that in multi-layers the nature of the bandgap can be manipulated by an external transverse field. One may expect, for instance, that the optical activity of such ribbons may be electrically modulated.

As a final observation we note that the critical fields for closing the gap in multi-layer ANRs are significantly smaller than those needed for the corresponding single-layer ones [see Fig. 4.14(a)]. Furthermore, for a fixed external field the bandgap is found to be inversely proportional to the number of layers [see Fig. 4.14(b)], although a more precise dependence is difficult to establish. Such an inverse dependence is expected if the different layers in the multi-layer ribbon behave effectively like capacitors in parallel, although such an analogy cannot be pushed much further based on our DFT results.

4.2.5 Electrically driven magnetism

As the VB and the CB of a MoS_2-ANR approach each other under the influence of E_{ext} a high DOS is generated at the Fermi level on the verge of the insulator to metal transition. Such high DOS originate from the Van Hove singularities at the band edges owing to the quasi-1D nature of the NRs. For $E_{\text{ext}} = 0$ the ANRs are non-magnetic semiconductors. Thus, for any fields smaller than the critical one for the band closure the system remains semi-conducting and no spin-polarized calculations are needed. However, at and beyond the onset of the metallic phase both spin polarized and non-spin polarized calculations have been performed in order to establish whether the ground state is stable against the formation of a finite magnetic moment. In general, we have found that at the critical electrical field, E_c, where the bandgap closes there is a sufficiently high DOS at the (non-magnetic) Fermi level [see Fig. 4.15] to drive the formation of a magnetic moment according to the Stoner criterion for ferromagnetism.

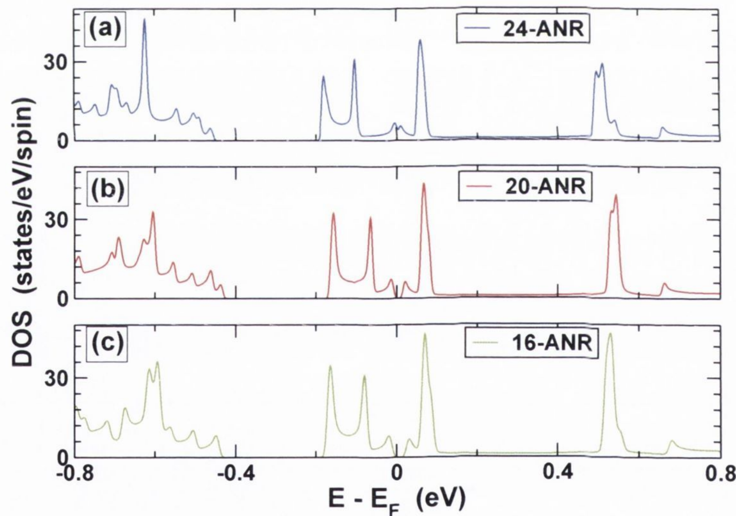

FIGURE 4.15: The non-spin polarized DOS at the critical field E_c for which the first diamagnetic to magnetic transition occurs for the 24-ANR (blue), 20-ANR (red) and 16-ANR (green). The electronic states in DOS are Gaussian broadened by 0.01 eV.

Fig. 4.16 displays the evolution of the ribbon magnetic moment (per ribbon cell), m, as a function of E_{ext} for three different ANRs. For example, one can clearly see that a 24-ANR becomes magnetic for $E_{\text{ext}} = 4$ V/nm, which is the critical field to close the gap completely. Such a transition from a diamagnetic to a magnetic ground state is driven by the Stoner criterion, which reads $I\rho_{\text{F}} > 1$, where I is the Stoner parameter

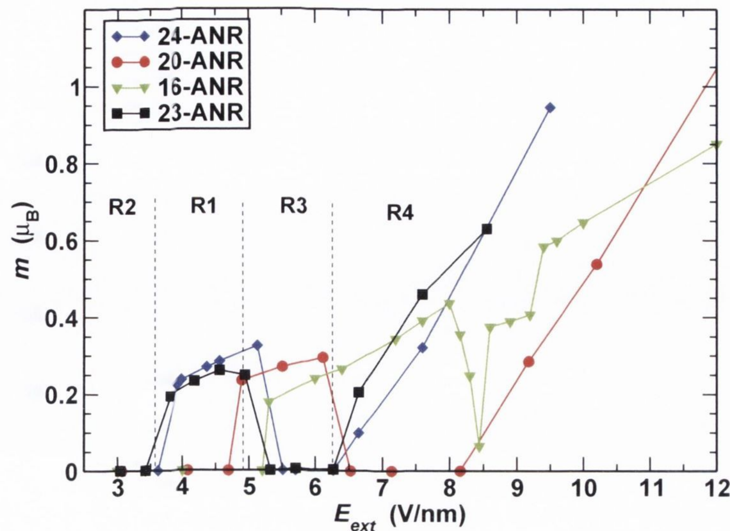

FIGURE 4.16: Variation of the magnetic moment per ribbon cell, m, as a function of the external electric field E_{ext} for 16-ANR (green triangles), 20-ANR (red circles) and 24-ANR (blue diamonds). We also report data for the symmetric 23-ANR (black squares). R1 and R3 (R2 and R4) define the regions of E_{ext} where the 24-ANR is in its diamagnetic (magnetic) state.

(the exchange constant) and ρ_{F} is the DOS at the Fermi level of the diamagnetic state [298, 299]. The Stoner parameter can be estimated from our DFT calculations, since the magnetic exchange splitting, Δ, of the bands is given by $I\bar{m}$ [300], where $\bar{m}$ is the magnetic moment in units of the Bohr magneton μ_{B}. For instance, in the case of the 24-ANR at $E_{\mathrm{ext}} = 4.5$ V/nm we find that $\Delta = 0.14$ eV and $m = 0.27$ μ_{B}/unit cell, so that the estimated value of the Stoner I parameter is ~ 0.5 eV and the required DOS at the Fermi level necessary to satisfy the Stoner instability condition is $\rho_{\mathrm{F}} \geq 1/0.5 = 2$ eV^{-1}.

Also in Fig. 4.16 it can be observed that the critical field for the diamagnetic to magnetic transition corresponds exactly to E_{c}, *i.e.* it coincides with the onset of metallicity (see Fig. 4.5). This is true for both the 20-ANR and the 24-ANR and for any larger ribbon. The situation however is different for the 16-ANR for which the magnetic transition occurs at a field smaller then E_{c}. As noted previously, for small ribbons non-spin polarized calculations reveal that the inter-edge interaction creates a band anti-crossing, so that the critical field for the bandgap closure is larger than that needed for shifting rigidly the CB and the VB by the bandgap. Thus the metallic phase occurs at an E_{c} larger than the one necessary to simply shifting the bands. In contrast, we find that once spin-polarization is allowed in the calculation, the semiconducting to metallic

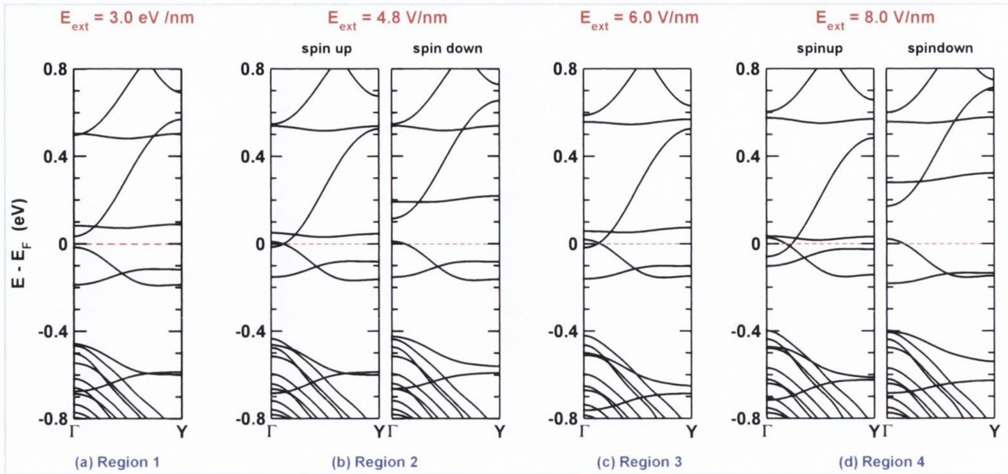

FIGURE 4.17: The band-structure of the 24-ANR plotted for different E_{ext}. In particular we select four representative field strengths corresponding to the four regions defined in Fig. 4.16.

transition occurs virtually with the band edges of the VB and the CB touching at the Γ point. This suggests that the exchange energy gained by spin-polarizing the system is sufficiently large to overcome the inter-edge interaction. Total energy calculations indeed confirm that the spin polarized ground state is energetically more favorable than the diamagnetic one. Hence, the 8-ANR undergoes a magnetic transition at a smaller E_{ext} that the E_{c} calculated from the LDA.

It is also interesting to look at what happens when the electric field is increased beyond the value needed for the diamagnetic transition. Taking the case of the 24-ANR as an example we notice in Fig. 4.16 that there are different magnetic regions depending on E_{ext}. In particular we observe two diamagnetic regions (R1 and R3) and two magnetic ones (R2 and R4). R1 corresponds to the semi-conducting ground state of the ribbon and therefore it is non-magnetic. At the boundary between R1 and R2 the ribbon becomes metallic and the Stoner mechanism drives the electronic structure in a magnetic state. A further increase of E_{ext}, however, destroys the magnetic moment, which returns to zero in R3. Such a return of the diamagnetic phase can be understood by looking at Fig. 4.17, where we present the band-structure for the 24-ANR at four representative electric field strengths, corresponding respectively to the four regions. In R3 the field is strong enough to further shift the CB and VB in such a way that the Van Hove singularities are removed from E_{F}. Now the electronic structure of the ribbon is that of a non-magnetic semi-metal with both an electron and a hole pocket at the Fermi level. As E_{F} cuts now in a region where the bands have relatively large

dispersion (small DOS) the Stoner criterion is no longer satisfied and the magnetic moment disappears. A further increase of the external field drives the system into R4, where now a new band from the CB manifold crosses the Fermi level and it is spin-split by the Stoner exchange. The same mechanism works for the 20-ANR, while anomalies appear for the 16-ANR, again because of the more subtle inter-edge interaction.

Finally we wish to note that, as previously observed, the fact that the ribbon has inversion symmetry about its axis is irrelevant for the magnetic moment formation. This is demonstrated again in Fig. 4.16, where for completeness we report data for the 23-ANR as well. Clearly the 23-ANR and the 24-ANR display an almost identical pattern of magnetic moment formation with E_{ext}, except for minor details in the various critical positions for the on-set of the magnetism, which are mainly due to the slightly different confinement in the two structures.

4.2.6 Edge termination

Then we move to discuss the effects that the different edge terminations have on the onset of the electric field driven magnetism. Experimentally it was reported that MoS_2 single layer clusters present a well defined edge structure [277] (discussed in details later in this chapter). In particular it was shown that clusters above a certain critical size (about 1 nm) all display Mo edges, *i.e.* the ones investigated so far throughout our work. This broadly agrees with earlier density functional theory calculations [301], which however pointed out that alternative edge structures can form depending on the clusters growth environment. In particular it was reported that under hydrodesulfurization conditions S-terminated edges become more stable. It becomes then meaningful and intriguing to explore whether the results presented so far are robust against sulfurization of the edges.

Towards this goal we have repeated our calculations for the 24-ANR by replacing either one or both Mo edges with a different termination. In particular we have looked at three different cases, namely: 1) single 50% S-passivated edge, 2) single 100% S-passivated edge, 3) double 100% S-passivated edges. Furthermore for completeness, we have explored whether hydrogen passivation, alternative to the S one[2], produces any qualitative change.

[2] 50 % and 100 % passivated edge refer to that a Mo edge is passivated with one S (H) or two S (H) respectively.

In general we have found that regardless of the termination, the valence and the conduction bands of the nanoribbon are always made of edge states, while their band dispersion and the actual bandgap do depend on the chemical nature of the edges. These two features suggest that the evolution of the bandgap in an external electric field should present similar qualitative features to those discussed previously, as the gap closure is simply dominated by the shift in the electrostatic potential at the ribbon edges. In contrast the formation of the magnetic moment, which depends on the band dispersion through the density of states and on the exchange interaction of the edge wave-function, may be sensitively affected by the details of the edge structure.

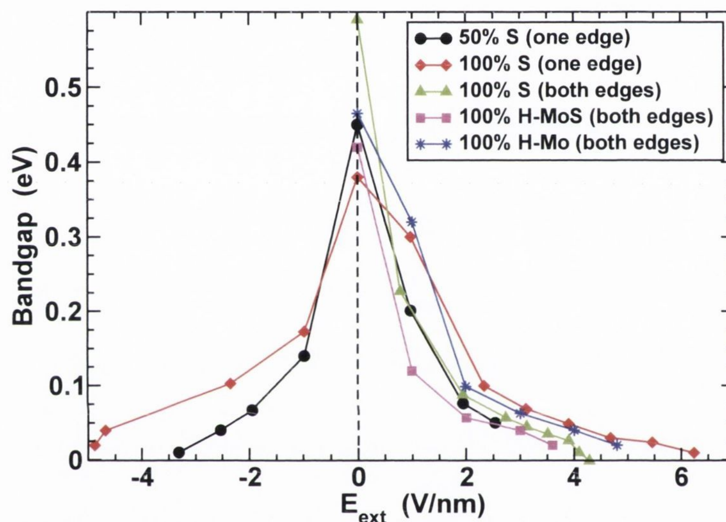

FIGURE 4.18: Evolution of the LSDA-bandgap in an external electric field of a 24-ANR with different edge terminations. In some cases, labelled as "one edge", the new termination is only over one of the two edges, while the other remains in the unsaturated configuration discussed throughout this chapter (Mo edge). In this case we plot the gap as a function of field for both the field polarities.

Fig. 4.18 shows the value of the bandgap as a function of the external electric field for all the terminations investigated. Note that, as some ribbons present different edges, the gap depends not only on the electric field intensity but also on its polarity. For these ribbons we plot results for both positive and negative E_{ext}. In general the figure confirms the intuitive picture presented above, *i.e.* for all the terminations studied we observe gap closure as a function of the electric field. The critical fields are also rather similar ranging between 4 V/nm (the same critical field for the case of two Mo edges) to approximately 6 V/nm.

More intriguing is the influence of the edge termination on the formation of the magnetic moment. Here we find that some edges do not display any Stoner instability so that no magnetism is induced by the external field. This can be appreciated by looking at Fig. 4.19, where we plot the magnetic moment per cell as a function of E_{ext}. From

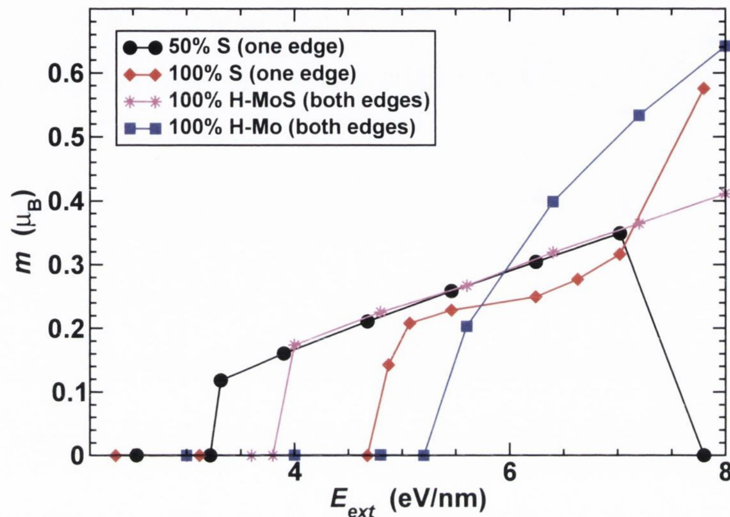

FIGURE 4.19: Magnetic moment as a function of the external electric field for a 24-ANR with different edge terminations.

the figure it appears that ANRs with either 50% or 100% S-rich edges can sustain a magnetic moment. However the figure refers to a 24-ANR in which only one edge has such termination, while the other still displays the Mo one. A closer look at the density of states reveals that the magnetic moment in this case forms only at the Mo edge, but not at the S-rich one. This brings the interesting consequence that the moment formation occurs only for one specific polarity of the electric field, which is the one necessary to bring the band associated to the Mo edge at the Fermi level. A second consequence is that when the sulfurization is at both edges no magnetic moment ever develops.

We then conclude that in S-rich edges the Stoner condition is not met, either because the density of states is not large enough or because the additional S contributes to reduce the Stoner parameter of the edge states. Interestingly H passivisation does not seem to be detrimental to the magnetism. As suggested in Ref. [302] we have investigated two types of passivation differing by whether the double passivation is only at the Mo site (this is labelled in Fig. 4.18 and Fig. 4.19 as "H-Mo") or both at the Mo and the S ones (labelled as "H-MoS"). In this case the magnetic moment forms

at both edges as soon as E_{ext} is large enough to close the gap, *i.e.* H-passivated edges behave identically to the unpassivated Mo ones.

Finally we conclude with some comments on the possible effects of disorder. Throughout this chapter we have investigated only perfect edges, which is justified given the experimental observation of large clusters with perfect edges [277]. However these clusters count at most approximately 20 sites per side and it is very unlikely that much larger nanoribbons can maintain such structural perfection. Defects and inhomogeneities of course break translational invariance so that the one-dimensional nature of the edge states will certainly be affected. One should then expect a general broadening of the edge-related bands with a consequent reduction of the average density of states. Because the magnitude of the density of states determines the Stoner condition, it is reasonable to expect that the formation of the magnetic moment will be rather sensitive to edge defects. In contrast the gap closure in an electric field should be more robust. This in fact depends only on the ability of creating a potential different between the edges, a feature that should not be affected too much by disorder.

4.2.7 Cr doped ANR

In the previous sections we have shed some light on the dependence of the electronic structure (bandgap) of the different kind of edge termination and on an external electric field, E_{ext}. In order to shed additional light on the robustness of the electronic properties under E_{ext} in the presence of external doping, we now discuss a 10-ANR MoS_2 doped with chromium, Cr.

All the calculations for Cr doped nanoribbons are carried out for a 10-ANR, where Mo is replaced by one Cr atom. We perform calculations for three different doping sites: 1) the outer side of the ANR (C_o configuration), 2) the middle of the ANR (C_m configuration) and 3) both sides of ANR (C_b configuration) [see Fig. 4.20]. For every Cr doped 10-ANR, a supercell of 60 atoms is used. This contains one Cr atom for the C_o, and C_m configurations, and two Cr atoms for the C_b one. Our calculations show that doping at the outermost side of the ANR is energetically more favorable than doping in the inner positions. When doping at the C_m position, the 10-ANR has the electronic structure of non-magnetic semiconductor with a bandgap of 0.51 eV. This is similar to the undoped case [see section 4.2.2], where both the CB and VB are localized at the ribbon edges. For this configuration the Cr-related impurity bands are located at

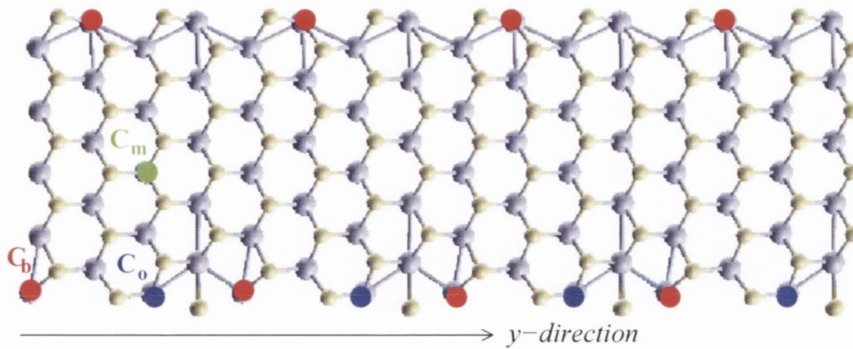

FIGURE 4.20: The atomic structure of the MoS_2-ANR with Cr dopants for the three different configurations investigated. When Mo atoms are replaced by Cr at the blue, green and red position, the corresponding configurations are named C_o, C_m and C_b, respectively.

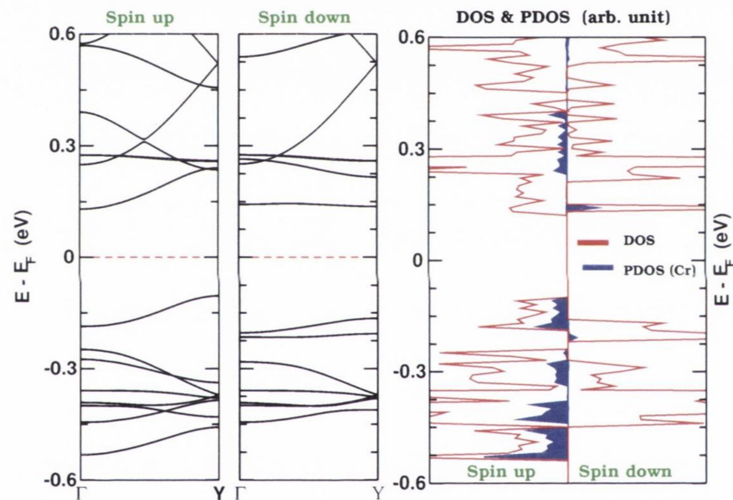

FIGURE 4.21: (a) Bandstructure of a Cr doped 10-ANR in C_o configuration, and the corresponding (b) DOS and PDOS (projected on the Cr atoms). The electronic states in DOS are Gaussian broadened by 0.05 eV.

energies that are not close to the VB and CB. In contrast, the C_o and C_b configurations are both magnetic and insulating. The bandstructure, DOS and the PDOS (projected on the Cr atoms) have been plotted in Fig. 4.21 for the C_o configuration. We note that also for the C_o configuration both the CB and VB originate from the edges of the ribbon. We find a Cr impurity band in the majority spin-band above the VB maximum. The other bands around the Fermi level are located on the Cr atoms and on the different species of the edges atoms. The total magnetic moment per simulation cell is 1.994 μ_B, which is what expected from a Cr^{3+}-d^3 configuration (in fact about 1

μ_B is associated with S atoms). The magnetic moment is localized on the Cr and its surrounding Mo and S atoms.

We now apply an external transverse electric field to the C_o configuration. This can tune the bandgap, as we have seen before for the undoped ANR. Since the spin-up and spin-down bandstructures are different, the response to an E_{ext} of two spin species are expected to be different. In particular, for a certain range of values of E_{ext} a half-metallic solution can be obtained. Also a smaller value of E_{ext} is required to close the bandgap compared to the undoped 10-ANR. By applying a reverse transverse E_{ext}, we expect that the bands would move differently. This is confirmed by our calculation in a transverse E_{ext}. We find that before closing the gap, the orbital character of the VB changes as a function of the field. Therefore, we find the important result that the effective mass of a VB electron can be varied by applying a transverse E_{ext}. This phenomenon demonstrates the possibility of tuning the carrier mobility of Cr doped MoS_2-ANR by applying a E_{ext}.

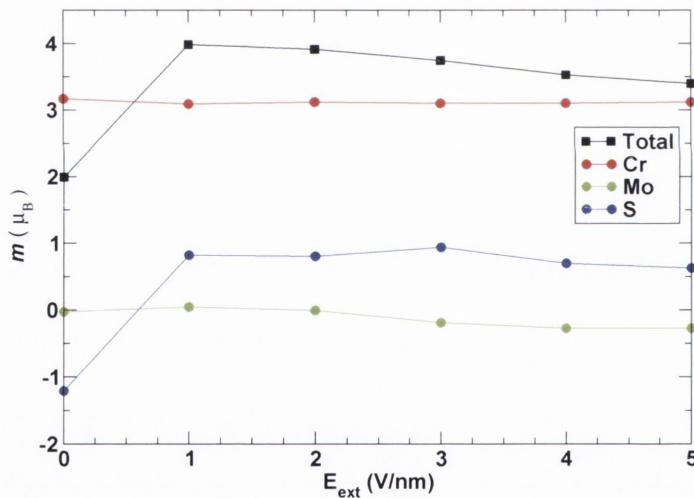

FIGURE 4.22: Variation of the magnetic moment with the electric field for Cr doped MoS_2 10-ANR. Different lines represent the total (black), and the contributions to the magnetic moment from Cr (red), Mo (green), and S (blue).

Fig. 4.22 shows that the total magnetic moment, m, as well as the magnetic moment of the individual species, as a function of the applied field. By applying a small E_{ext}, m_s (the magnetic moment contributed by sulfur atoms in a conventional unit cell) flips from negative to positive, and then remains approximately constant for futher increase of E_{ext}. However, with increasing E_{ext} the magnetic moments of the Cr and Mo species do not change, but the total magnetic moment of the simulation cell changes resulting in

a change of magnetic moment associated to the S atoms, m_s. Such a switch of the total magnetic moment by an E_{ext} may have applications in spintronics devices. Note that for the C_b configuration, where both sides of the 10-ANR are doped, the results are similar to the C_o configuration. The only major difference is that all the previously mentioned magnetic moments are doubled, since we have doubled the number of dopants in the unit cell.

4.2.8 Conclusion

In summary, we have investigated the ground state electronic structure and the electrical field response of MoS_2 nano-ribbon structures. Our first principles calculations show that MoS_2 ANRs are insulators with a direct bandgap regardless of their width. The bandgap in these systems is primarily determined by a pair of edge states and it may be tuned by applying an external transverse electric field. They can eventually drive a metal-insulator transition. This metal-insulator transition is robust against the different percentage of edges passivation with either S or H. It is important to note that the critical electric field for the transition can be reduced to a practical range with increasing ribbon width. Also it is interesting to remark that, as the dielectric constant is approximately proportional to the inverse of the bandgap, the critical fields for the gap closure are expected to be relatively material independent.

The presence of localized edge states that can be moved to the Fermi level suggests that the system can be driven towards magnetic instability. Our spin-polarized calculations show that this indeed happens and that at a certain critical electric field a diamagnetic to a magnetic transition occurs. This follows directly from the Stoner criterion as the Van Hove singularities associated with the edge states have a large density of states. Intriguingly the magnetic phase can be further tuned by the external field and different alternating diamagnetic and magnetic regions can be accessed. Interestingly, the study of an external field induced bandgap-tuning of the ANRs with S, H passivated edges suggests that the Stoner magnetism is very sensitive to edge's reconstruction.

Finally, we study the effect of impurities on the electrical response of a 10-ANR by doping the system with Cr atoms in place of Mo. Our total energy calculations show that Cr preferably locates at the edges and the ribbon and becomes magnetic. By applying an electric field, the magnetic moment as well as the electron effective mass by $\sim$11% can be changed. There is a certain region of E_{ext}, where Cr doped 10-ANRs

(C_o and C_b configurations) become half-metals. These results confirms that tuning of the bandgap of a ANR is robust even external impurity doping.

4.3 Electric Field Effects on Triangular Nanoclusters (TNCs)

As mentioned earlier the edge termination of MoS_2-ANR plays a crucial role in determining their electronic properties and the magnetism induced by an external electric field. Yet there are little existing experimental information about the edge-reconstruction of the MoS_2-NRs. Fortunately, the situation is different for another monolayer nanostructure, namely nanoclusters. Recently Lauritsen *et al.* [277] have managed to show a series of atom-resolved STM images of monolayer MoS_2-TNCs with varying size. These were fully characterized to correspond to atomically scaled structures previously determined by DFT-based STM simulation [190, 205]. Lauritsen *et al.* also observed that the size dependent structure of MoS_2-TNC reflects the change in the edges termination (either Mo or S) and the coordination of S atoms of the nanocluster. In this work, we focus only on the experimentally proposed MoS_2-TNC structures (see Fig. 4.23). The size of the MoS_2-TNCs investigated, are defined in terms of the number (n) of Mo atoms along the TNCs edges. Essentially, all nanocluseters with $n \geq 6$ have appeared to be terminated by a 100% sulfided Mo edges of MoS_2 whereas for nanoclusters with $n \leq 6$, the edges are mostly S terminated having a different percentage of sulfidation [277]. Next, we study the electric field effect on the MoS_2-TNCs.

4.3.1 MoS_2 nanoclusters

First we studied the electronic properties of monolayer MoS_2-TNCs. In Table 4.1, we list the magnetic properties and the gaps between the HOMO and LUMO of different sized TNCs. Our calculations show that the gap varies with increasing TNC size in a nonlinear way (firstly, the gap decreases with size, then it increases leaving the minimum at the size $n = 8$). Because of computational cost, the calculations have been carried out up to the cluster sized $n = 10$. This type of size dependent variation of the gap, in small MoS_2-TNCs, could be an inherent effect in low dimension nanostructures (LDN) as we have also observed a size dependent oscillation of the bandgap in MoS_2

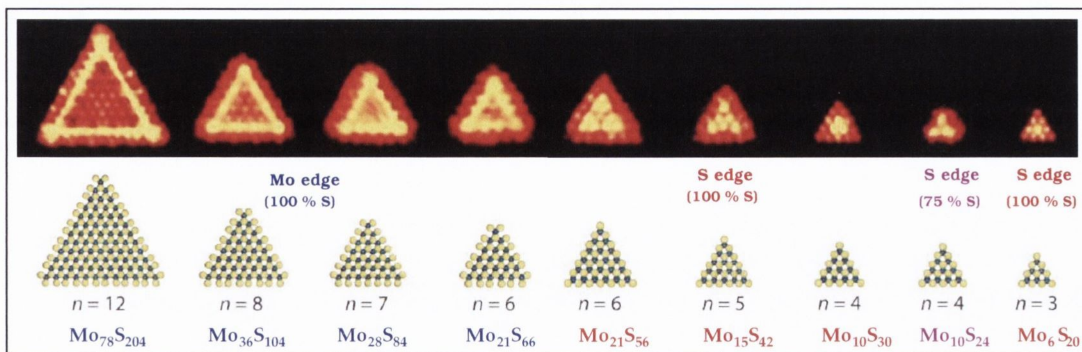

FIGURE 4.23: Size dependent structural progression of single layer MoS_2 nanoclusters. Upper part: STM images of clusters as a function of size, where n denotes the number of Mo atoms on the cluster edge. Lower part: Ball model (top view) with the MoS_2 triangles observed by STM and the corresponding cluster compostion $Mo_X S_Y$ (Mo: blue; S: yellow). Adapted from the Ref. [277].

Size	Edges specification	Magnetic properties	Gap (eV)
n = 2	S edges, 75 % S	Magnetic	-
n = 3, 4	S edges, 100 % S	Magnetic	-
n = 4	S edges, 75 % S	Non-magnetic	0.57
n = 5, 6	S edges, 100 % S	Magnetic	-
n = 6	Mo edges, 100 % S	Non-magnetic	0.22
n = 7	Mo edges, 100 % S	Non-magnetic	0.19
n = 8	Mo edges, 100 % S	Non-magnetic	0.05
n = 10	Mo edges, 100 % S	Non-magnetic	0.16

TABLE 4.1: Theoretically calculated magnetic properties and electronic HOMO-LUMO gap of the TNCs.

nanoribbon (1D) [304], in which the states around the Fermi level are localized at the edges like in the TNC (see later in this section). Therefore, there may be a similar kind of oscillation in the gap with size in MoS_2-TNCs. The D_{3h} point group symmetry, resides in the MoS_2-TNCs, implies that the energy levels are either non-degenerate or doubly-degenerate [305]. Moreover, the wavefunctions of the degenerate levels depend on the type of edges and the orbital symmetry of the TNCs. For an example, in the non-magnetic cluster (n = 4) with S edges and 75% S coverage at edges, the LUMO level is doubly-degenerate, whereas the HOMO level is non-degenerate. As a consequence, the wavefunction of the HOMO level has 3-fold rotational symmetry, whereas the wavefunction of LUMO does not have (see Fig. 4.24). In other word, the non-degenerate LUMO can thus be identified with the A representation of this D_{3h} group, whereas the doubly-degenerate LUMO states belong to the two-dimensional E representation. Of course, superposition of the two degenerate states have the expected

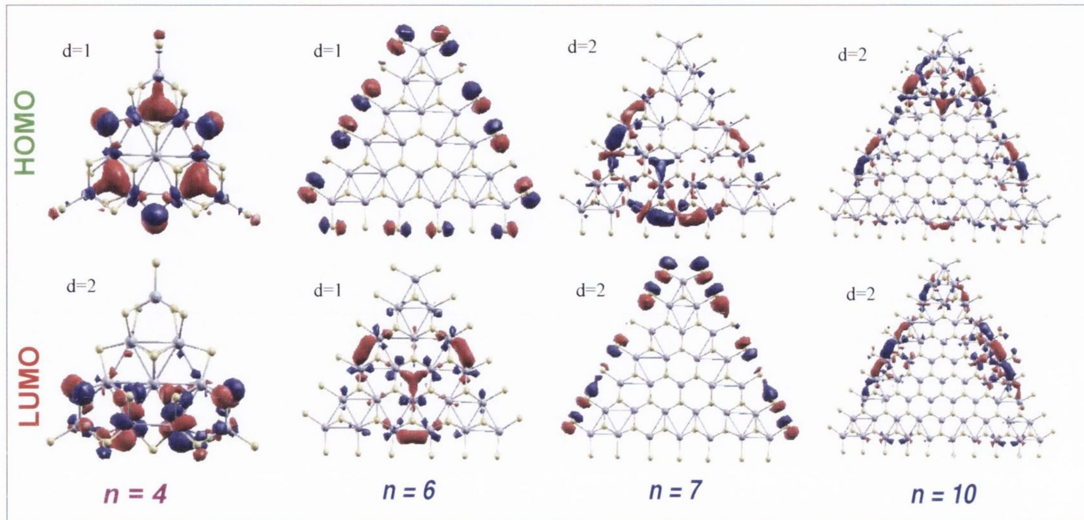

FIGURE 4.24: The Kohn Sham orbitals of the HOMO and LUMO states for different size MoS_2-TNCs. d denote the degenracy of the respective level, either HOMO or LUMO. In the case where the HOMO and LUMO are degenerate, only one of them is plotted. Color code: grey (dark grey) = Mo, yellow (light grey) = S, red and blue = positive and negative amplitude of the wavefunction respectively.

3-fold symmetry. The wavefunctions of the HOMO and LUMO states for different sized TNCs are shown in Fig. 4.24. The HOMOs are mainly localized at the edges atoms. This result is in good agreement with the experimentally observed STM picture (see the ref. [277] and Fig. 4.23). Also, wavefuntions of the HOMO and LUMO for a MoS_2-TNC with Mo edges (n = 6) are in good agreement with the previous theoretical calculations [190].

Now we discuss the effect of an external planer electric field (E_{ext}) on non-magnetic MoS_2-TNCs. In Fig. 4.25, the effect of an E_{ext} (along the y-axis) on the energy levels of a monolayer MoS_2-TNC ($n = 4$) is depicted. Due to a change in potential along the y-axis of the TNC, the D_{3h} symmetry is broken. This lifts the degeneracy of the LUMO level. However, the reflection symmetry of the wavefunctions about the direction of the E_{ext} (y-axis) is preserved. The HOMO level is localized along the edges with higher potential, while the LUMO level is localized on the lower potential edge (see Fig. 4.25). Moreover, upon applying an E_{ext}, both the HOMO and the LUMO level shifts towards each other, resulting in reduction of the gap between them. Both the HOMO and LUMO energy levels shift down in energy monotonically as E_{ext} increases, but the shifting rates are different from each other (as shown in Fig. 4.26). Eventually, for a certain value of E_{ext}, in this case approximately E_{ext} = 1.6 eV/Å, the spin degeneracy

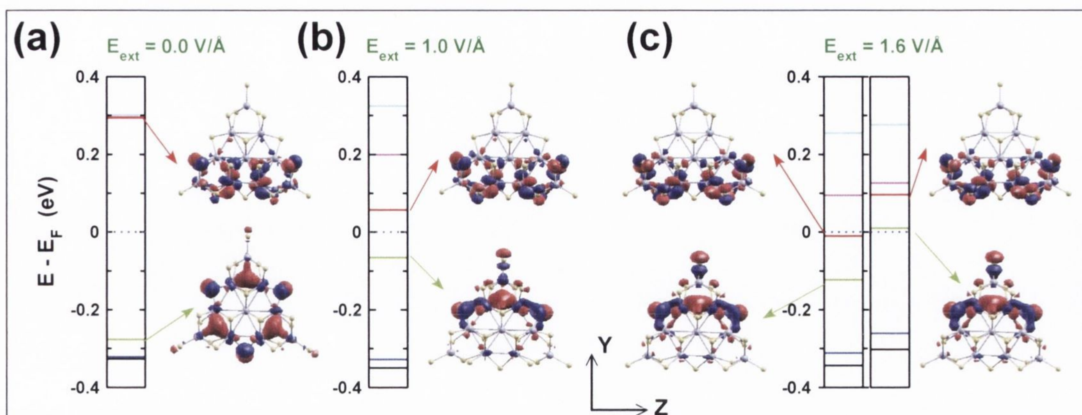

FIGURE 4.25: The effect of an E_{ext} (applied along the y-axis) on the TNC ($n = 4$). The dotted lines, in the energy level diagrams for all E_{ext}, denote the Fermi level E_{F} observed in our calculations. The wavefunction of the HOMO and LUMO are depicted for the $E_{\text{ext}} = 0.0$ V/Å (a), 1.0 V/Å (b), 1.6 V/Å (c). The green and the red arrow indicate the HOMO and the LUMO respectively. The color codes are the same as those indicated in Fig. 4.24.

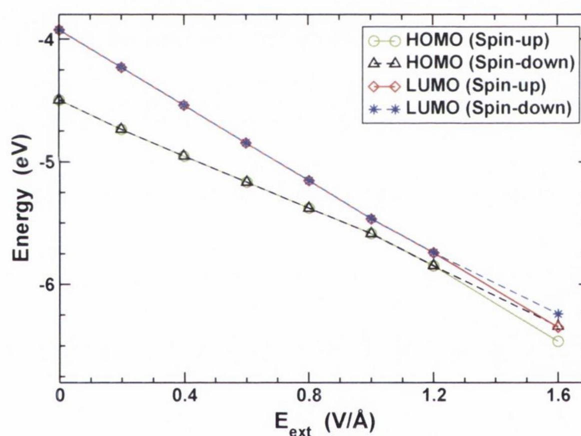

FIGURE 4.26: The spin-polarized HOMO and LUMO energy levels plotted as a function of E_{ext} for the TNC ($n = 4$) with S terminated edge having 75 % sulfidation.

of the HOMO and LUMO levels is lifted. As a consequence, the spin-down HOMO and the spin-up LUMO cross each other (see Fig. 4.26). The spin resolved wavefunctions of these levels are shown in Fig. 4.25 (at $E_{\text{ext}} = 1.6$ V/Å). The spin-down HOMO level becomes unoccupied, whereas the spin-up LUMO level gets occupied by one electron. Therefore, the ground state becomes magnetic with a moment of 2 μ_B.

Next, the external electric field (E_θ) is applied along a different direction. We define the angle θ as one between the direction of the applied E_θ and y-axis in the plane of the TNC ($n = 4$) to study the angular dependence of the gap reduction. Moreover, this study

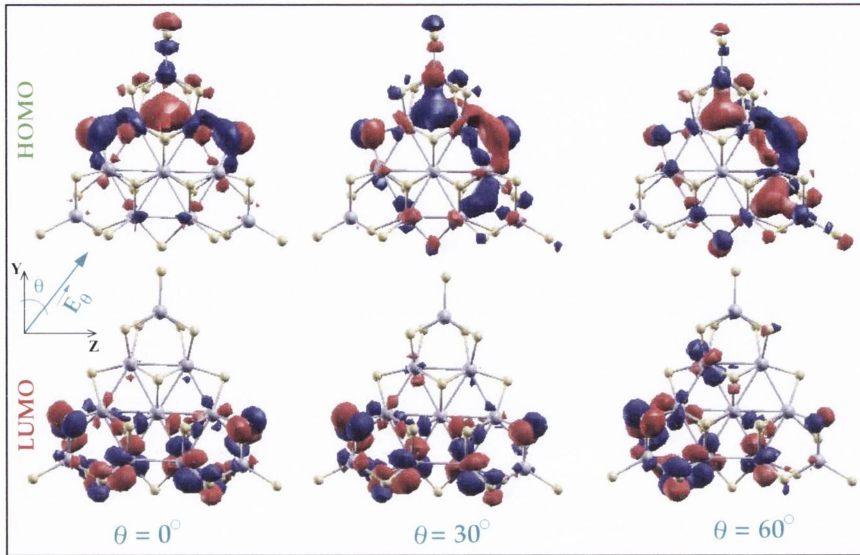

FIGURE 4.27: The effect of a planar E_{ext}, say E_θ = 4.0 V/Å, on the TNCs, where θ is the angle made by the E_θ with the y-axis. Here the wavefunction of the HOMO level (top row) and the LUMO (lower row) for the TNC sized (n = 4) are depicted for an angles of $\theta = 0°$, 30°, 60° respectively from the left to right. The wavefunction rotates by an angle θ (θ = 30°, 60°) with respect to that at θ = 0° along with the direction of E_θ. The color code is same as that in the Fig. 4.24.

would provide useful information for practical purposes in calibrating the response for an arbitrary planar electric field on the electronic structure. The wavefunctions of the HOMO and LUMO (as shown in Fig. 4.27) rotate by an angle θ along with the direction of the applied E_{ext}, and the rate of decrease of the gap is slightly reduced in small steps as θ increases up to 60° (as shown in Fig 4.28). Due to the triangular geometry of the MoS_2 nanoclusters, by studying angles in the ranges 0-60°, one can describe the effects over the entire possible range of θ in the TNC plane. Therefore, the rate of decrease of the gap is identical for angles θ = 30° and θ = 90° (as shown in Fig. 4.28).

In order to get an idea of the response to an E_{ext} of different sizes and types of TNC, we have also studied the electronic properties the n = 6, 7 and 10 TNC. The nanoclusters become magnetic for a certain value of E_c, namely E_c = 0.5 eV/Å, ≈, 0.35 eV/Å , 0.4 eV/Å respectively for n = 6, 7, and 10 respectively. It is difficult to extract the width dependence of E_c as the rate of decrease of the gap depends on the size of the nanocluster, the localization and symmetry of the wavefunctions of HOMO and LUMO, and the initial gap. Nevertheless, we are expecting that the value of E_c may oscillate in a small window of sizes and essentially, it will reduce for large sizes. For example, the value of E_c reduces from 1.6 eV/Å to 0.4 eV/Å as the size increases from n = 4 to

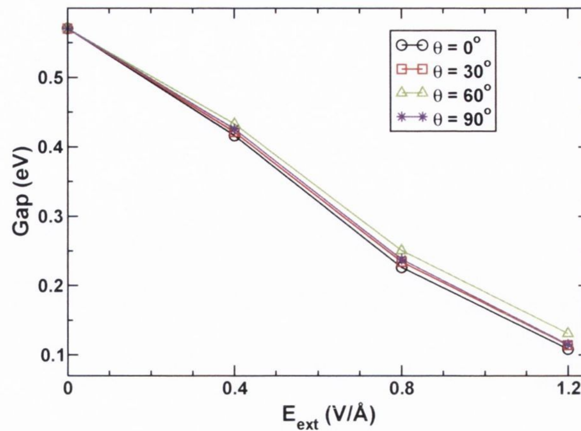

FIGURE 4.28: The variation of the gap (for TNC sized n=4) with the planar E_{ext} (E_θ) in direction θ, where θ is angle between the direction of an E_{ext} and the y-axis.

$n = 10$. Our theoretically calculated value of E_c are large for practical purposes even though, it decreases with size. In this context, we would like mention that recently, Ishii *et al.* managed to apply a very large electric field, say 0.08 V/Å to a polymer thin film without electrical breakdown [306]. Moreover, previous theoretical calculations also studied the stark effect on graphene quantum dots upon the application of an E_{ext} of same order of magnitude as the predicted by our calculations [273].

4.3.2 Hubbard model

In order to understand the physics that leads to ferromagnetism observed in TNC when applying a transverse E_{ext}, we have studied a simple model that describes filling of two single particle states with two interacting electrons. We consider two electrons, in the TNC, occupying two levels with different orbital symmetry, whereas the rest of the electrons are regarded as the vacuum, $|0\rangle$. The two spin degenerate states (of different orbital symmetry) have initially different onsite energies E_1 and E_2 approach each other in energy when one applies an external bias V_{ext}. We describe the situation the situation by using Hubbard Hamiltonian:

$$\begin{aligned}\hat{H} = &\sum_{i\sigma}(E_i - V^i_{\text{ext}})c^\dagger_{i\sigma}c_{i\sigma} + \sum_{<ij>;\sigma} t(c^\dagger_{i\sigma}c_{j\sigma} + \text{h.c.}) \\ &+\sum_i U_i\ \hat{n}_{i\uparrow}\hat{n}_{i\downarrow} + \sum_{i<j;\sigma\sigma'} (W + \delta_{\sigma\sigma'}J)\hat{n}_{i\sigma'}\hat{n}_{j\sigma},\end{aligned} \tag{4.3}$$

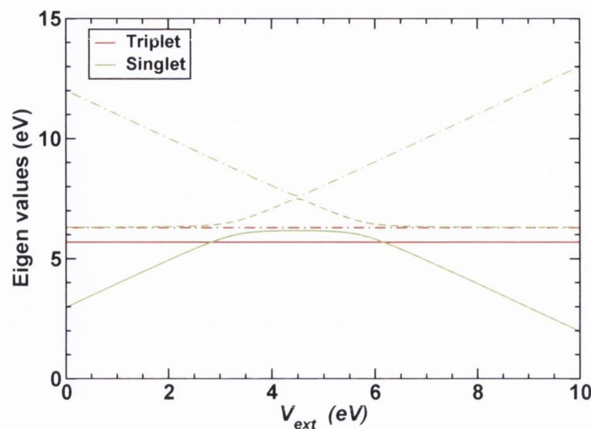

FIGURE 4.29: The eigenvalues are plotted as a function of V_{ext}. Here, E_1=0 eV, E_2=5 eV, U_1=3 eV, U_2=2 eV, W=1 eV, J=0.3 eV, and t=0.1 eV. Green and red colors indicate the singlet and triplet states, respectively, but different lines with same color indicate the eigenvectors with different orbital symmetries.

where $c_i{}^{\dagger}(c_i)$ creates (annihilates) a fermion with spin σ at the ith single particle orbital (i = 1, 2) with onsite energy E_i, V^i_{ext} is the external bias at i^{th} site ($V^1_{\text{ext}} = -V^2_{\text{ext}} = V_{\text{ext}}/2$), t is the hopping, h.c. = hermitian conjugate, U_i and W are the intra-site and inter-site Coulomb repulsion respectively, J is the Hund's exchange energy. In our model, the assumption ($U_1 > U_2$) reflects the fact that the wavefunctions are more localized in the occupied levels as compared to the unoccupied one. Among the six possible states, the three spin singlets ($|S_i\rangle$; i = 1, 2, 3) and the three spin triplet states ($|T_i\rangle$; i=1,2,3) are identified as follows:

$$|S_1\rangle = c^{\dagger}_{1\uparrow}c^{\dagger}_{1\downarrow}|0\rangle\,,$$

$$|S_2\rangle = c^{\dagger}_{2\uparrow}c^{\dagger}_{2\downarrow}|0\rangle\,,$$

$$|S_3\rangle = \frac{1}{\sqrt{2}}(c^{\dagger}_{1\uparrow}c^{\dagger}_{2\downarrow} - c^{\dagger}_{2\uparrow}c^{\dagger}_{1\downarrow})|0\rangle\,,$$

$$|T_1\rangle = c^{\dagger}_{1\uparrow}c^{\dagger}_{2\uparrow}|0\rangle\,,$$

$$|T_2\rangle = c^{\dagger}_{1\downarrow}c^{\dagger}_{2\downarrow}|0\rangle\,,$$

$$|T_3\rangle = \frac{1}{\sqrt{2}}(c^{\dagger}_{1\uparrow}c^{\dagger}_{2\downarrow} + c^{\dagger}_{2\uparrow}c^{\dagger}_{1\downarrow})|0\rangle\,.$$

The exact energy eigenvalues for this problem are presented in Fig. 4.29 as a function of the external bias, V_{ext}. We find that the singlet ground states approaches the first excited state (triplet) with an increasing of V_{ext}. Parallel spin filling can be realized

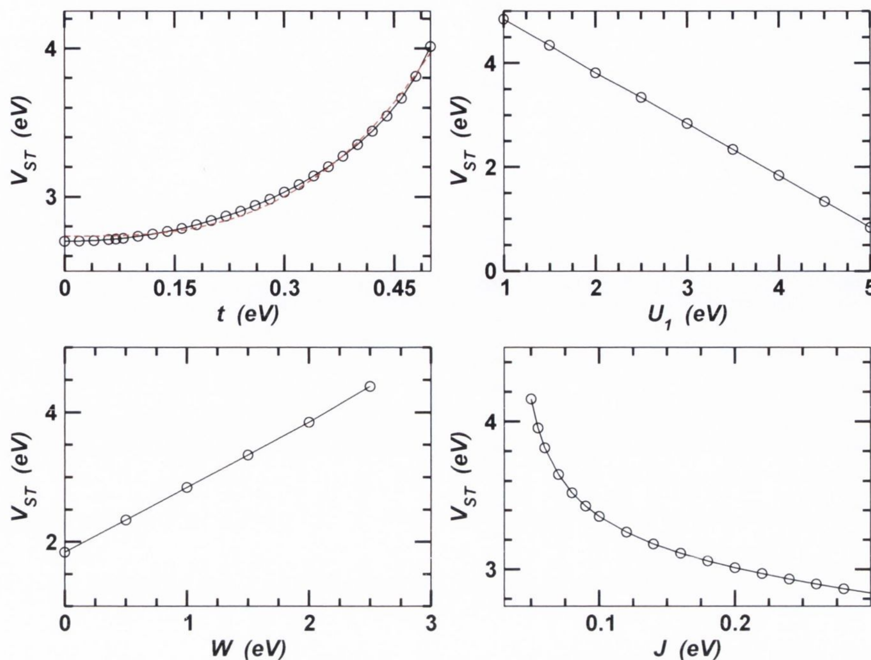

FIGURE 4.30: Variation of V_{ST} with the different parameters of the model t, U, W and J. The other parameters are kept at the fixed values repeated in Fig. 4.29. The red dashed line, in the graph (upper row and left), is a t^3 fit of the data.

when the energy gain in Hunds exchange exceeds the spacing between the two single-particle states ($E_1 - E_2 < |J|$) [312, 313]. This implies that intra-nanocluster exchange is ferromagnetic ($J < 0$) obeying the Hunds rule [314, 315]. When the energy spacing between the potential shifted on-site energies is just less than J, at $V_{\text{ext}}=V_{ST}$ (see Fig. 4.29), the triplet state becomes the new ground state resulting in a singlet to triplet (S-T) transition. This S-T transition corresponds to the ferromagnetic transition observed in our DFT calculations.

In our model, we also present the variation of V_{ST} with the parameters, say t, U_1, W, and J (see Fig. 4.30). Here V_{ST} increases nonlinearly with increasing t and the curve fits to $\sim t^3$. In contrast, there is a linear variation of the V_{ST} with either U_1 and W, namely an increase U_1 and a decrease with W. Interestingly, the value of the V_{ST} does depend on the U_2 explicitly. However, it decreases nonlinearly with increasing J.

4.3.3 Conclusion

We have investigate the ground state electronic structure and the electric field response of single layer MoS_2. Large ($n \geq 6$) MoS_2 TNCs with Mo edges having 100% S coverage are non-magnetic, whereas the magnetic properties of small TNCs ($n \leq 6$) depend on the type of edges and the percentage of S coverage. The gap between the HOMO and the LUMO of non-magnetic TNCs reduces under a transverse E_{ext} and the nanocluster becomes magnetic with a moment of 2 μ_B for a certain critical value of E_{ext}. In general, such a result for TNCs is expected to be valid for an entire class of layered semiconductors, of which MoS_2 are representative. The required value of E_{ext} (E_{c}) for the singlet to triplet transition can be reduced to a practical range with increasing nanocluster's size and the angular dependence of E_{c} for a nanocluster can be ignored. Finally, a two-site two-electron simple Hubbard model explains the magnetic transition, found by DFT.

Chapter 5

The electronic and phonon properties of pristine and oxygen doped TiS_2

5.1 Introduction

TiS_2 is another layered transition metal di-chalcogenide (LTMD). The most stable structure of bulk TiS_2 is the 1T-polytype, whose unit cell contains one monolayer and the metal Ti atom has octahedral coordination [see Fig.5.1(a,b,c)]. It belongs to the space group $P\overline{3}m1$ like other LTMDs such as $TiSe_2$, $TiTe_2$, ZrS_2 and NbS_2. The Brillouin zone of such class of bulk LTMDs, is shown in Fig.5.1(d). TiS_2 has drawn the attention of researchers over the past four decades due its variety of potential applications. For instance, many studies have been carried out on the intercalation of alkali atoms and organic molecules in TiS_2 for applications related to both lightweight and high energy-density batteries [65, 316]. However, many interesting phenomena such as superconductivity and order-disorder or metal-insulator phase transitions commonly emerge in the LTMD materials class because of intercalation [65, 156, 317]. In particular, for TiS_2 the intercalation changes the conductivity [318]. Another interesting area of research is the modulation of the electronic structure and electrical properties under external pressure. In fact, many experimental [319, 320] as well as theoretical

[321, 322, 323] studies illuminate the pressure induced phase transition in TiS_2. For instance, the transition from a semiconductor to semi-metal phase has been demonstrated by Hall measurements on TiS_2 single crystal at 4 GPa [319] pressure.

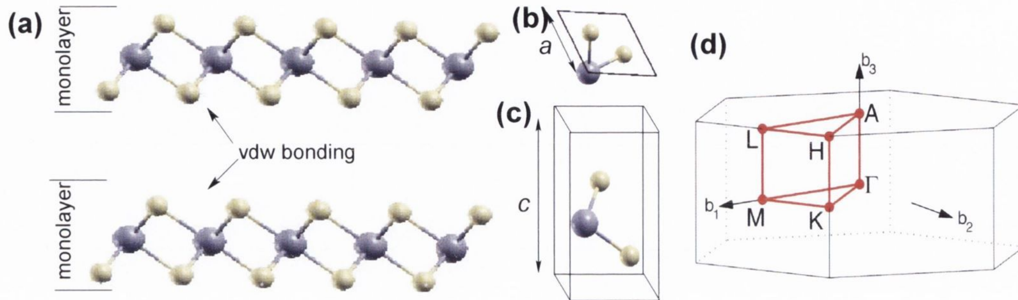

FIGURE 5.1: (a) The structure of bulk TiS_2. (b) Top and (c) side view of the bulk TiS_2 unit-cell. The primitive vector are $\vec{a}_1 = (\frac{1}{2}a, \frac{\sqrt{3}}{2}a, 0)$, $\vec{a}_2 = (\frac{1}{2}a, \frac{\sqrt{3}}{2}a, 0)$, and $\vec{a}_3 = (0, 0, c)$. (d) The Brillouin zone of the hexagonal crystal structure shows the high symmetry points in k-space. Color code: light grey→Ti and yellow →S.

Although significant knowledge has been accumulated on the ways for tuning the physical properties of TiS_2 by intercalation of molecules or alkali atoms and by external pressure, a clear understanding of the electronic properties of the host TiS_2 materials is still to be achieved. Many conflicting results exist on the electronic phase of bulk TiS_2, namely it is still debated whether the material is semi-metallic, metallic, or semiconducting. Surprisingly, all the possible results are obtained either experimentally or theoretically. Even different experimental studies end up with conflicting conclusions. On the one hand, many experimental measurements infer that bulk TiS_2 exhibits a semiconducting phase with a bandgap ranging from 0.05 to 2.5 eV. These observations are supported by angle-resolve photo-emission spectrum (ARPES) [324], optical absorption [325], Hall effect experiments [319, 326], and transport measurements [327]. On the other hand, some other experiments have shown that TiS_2 is a metal or a semi-metal with an indirect bandgap overlap (from Γ to L k-point in the Brillouin zone) ranging from 0.2 to 1.5 eV. This experimental evidence is based on extensive resistivity measurements [328], infrared reflectance [329], and x-ray emission and absorption measurements [330]. From a theoretical point of view, many calculations agree that the electronic phase of bulk TiS_2 is semi-metallic with an indirect band overlap. These studies are based on bandstructure calculations obtain with the linear muffin-tin-orbital (LMTO) method [344], linear augmented plane wave (LAPW) [321, 345], the augmented spherical wave (ASW) [346], full potential linearized augmented plane wave (FLAPW) [347], self-consistent linear combination of atomic orbital (LCAO) [354] and

density functional theory within the local density approximation (DFT-LDA) [322]. Other theoretical works have argued that TiS_2 is a semiconductor with an indirect bandgap. This view is supported by bandstructure calculations based on the self-consistent orthogonalised plane wave method (OPW) [348], Korringa-Kohn-Rostoker (KKR) scheme (non self-consistent) [352], and the atomic orbital (AO) method (self-consistent) [353].

From the experimental knowledge of the bandgap variation, it seems that the electronic structure of bulk TiS_2 largely depends on the experimental conditions. Sometimes Ti-rich stoichiomemtry, *i.e.* $Ti_{1+\delta}S_2$ ($0.1 \leq \delta \leq 0.5$) has been reported for this compound [349, 350] The excess of electrons brought by the excess of Ti atoms might influence the pristine electronic structure. Intrinsic impurities can be responsible for unintentional doping as well. Recently, an experimental observation on $TiSe_2$ [351] has shown that the electronic structure can be tuned from a small gap semiconductor ($\sim$ 0.15 eV) to a semi-metal by adsorption of the polar water molecules. By analogy, it might be suggested that the electronic phase of TiS_2 is very sensitive to the environments, *i.e.* the growth conditions. These include the presence of residual molecules after the growth. In contrast, the variation in electronic structured, predicted theoretically may originate for different treatment of electron-electron correlations in different methods (mentioned above). As it is notoriously known the LTMD family exhibits large electron-phonon coupling. This means that a small change in the atomic structure could affect the properties of the system significantly. Therefore an external perturbation, such as strain and pressure, could play an important role in determining the electronic phases of this system.

Recently, there has been renewed interest in developing oxygen sensing devices based on the change in the electrical or the optical properties of materials induced by their interactions with oxygen. Incidentally, the change in electrical resistivity has been reported for TiS_2 single crystals under an oxygen partial pressure, suggesting possible applications of TiS_2 as an oxygen gas sensor [331]. Moreover, the photo-current can be modulated by oxidizing the TiS_2 crystal ($TiS_{2-x}O_x$) [332]. Recently such desulfurization has been demonstrated in thin-films up to a thickness of approximately 4 nm [333, 334]. Besides this, many studies have been carried out to improve the thermoelectric properties of the TiS_2 via doping [336, 337].

A charge density wave (CDW) ground state based on symmetry-reduction is most commonly found in LTMDs [338]. Below a certain transition temperature, T_{CDW}, the lattice

undergoes a periodic distortion and simultaneously, the electron density exhibits a periodic modulation (see Fig.5.2). The appearance of the CDW phase can be the result of several competing effects such as Peierls instability, an exciton-insulator instability, or Jahn-Teller distortion [56]. All the mechanisms are closely related, especially in LTMD materials, so that identifying the true mechanism is a non-trivial task. For example, in the case of bulk $TiSe_2$, all the mentioned mechanisms for the CDW phase transitions have been proposed by different experimental methods [339, 340, 341]. However, in general, a CDW instability is a competition in reducing energy between the lattice and the electrons. The instability condition for CDW formation with a modulation wave vector $\mathbf{q}$ is governed by the equation [342],

$$\frac{4g_{\mathbf{q}}^2}{\hbar\omega_{\mathbf{q}}} - 2U_{\mathbf{q}} + V_{\mathbf{q}} \geq \frac{1}{\chi_{\mathbf{q}}}, \tag{5.1}$$

where, $g_{\mathbf{q}}$ is the electron-phonon coupling associated with an unnormalized phonon mode with energy of $\omega_{\mathbf{q}}$, $U_{\mathbf{q}}$ and $V_{\mathbf{q}}$ are the electronic Coulomb and the exchange interaction, respectively, $\chi_{\mathbf{q}}$ is the real part of the bare electronic susceptibility defined by $\chi_{\mathbf{q}} = \sum_{\mathbf{k}}[n_F(\epsilon_{\mathbf{k}}) - n_F(\epsilon_{\mathbf{k+q}})]/(\epsilon_{\mathbf{k}} - \epsilon_{\mathbf{k+q}})$. Here, n_F is the Fermi-Dirac distribution function. In a simple scenario where the electron-phonon coupling is sufficient so that the left part of the Eq.(5.1) is positive, a sufficiently large value for the particular vector $\mathbf{q}$ can trigger the CDW instability. Consequently, an unstable soft-phonon mode emerges at the $\mathbf{q}$-vector and a CDW phase exists below the critical temperature, T_{CDW}. The main peculiarity of CDW formation is that electrons and phonons are coupled strongly as compared to the normal phase and propagate together through the materials, producing a collective motion. Thus, the electrical resistance of the materials is reduced, resulting in an improvement of the power dissipation of an electronic device. In fact, a CDW-based field effect transistor (FET) has been demonstrated with both $NbSe_2$ and TaS_2 [166, 343]. The main problem is that the transition temperatures are usually low compared to room temperature. However, a recent experiment shows that T_{CDW} can be increased from 200 to 240 K by reducing the thickness of the materials from bulk to ~100 nm. This is achieved because of the enhancement of the electron-phonon coupling in reduced dimensions.

In this chapter, we study the electronic properties of bulk and monolayer TiS_2 using density functional theory. In order to estimate the fundamental bandgap of the materials, an advanced *ab-initio* technique, namely the Green's functional quasi-particle approach has been employed. Using these *ab-initio* techniques, we further investigate

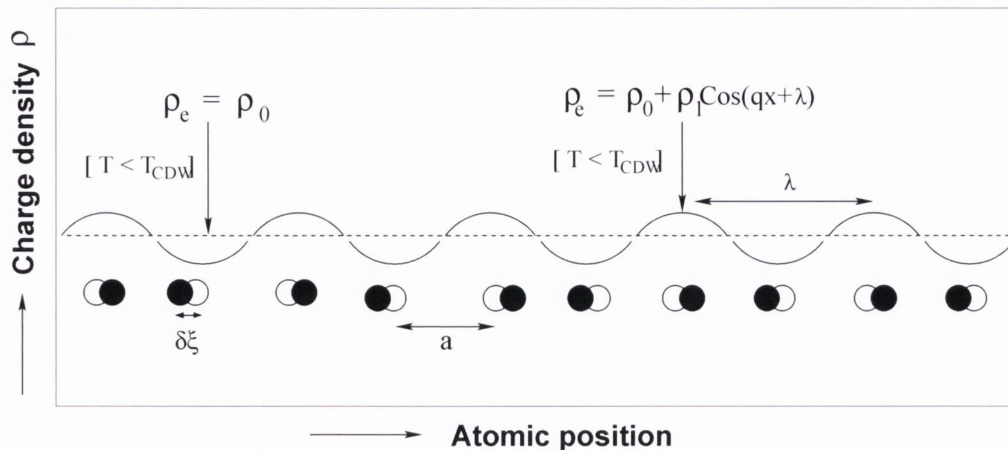

FIGURE 5.2: Schematic view of a one-dimensional charge density wave. Above the transition temperature, T_{CDW}, the material exhibits the normal phase with constant electron density, $\rho_e = \rho_0$. Below T_{CDW}, the atomic positions are distorted by $\delta\zeta$, resulting in modulation of the electron density (solid black line) and of the ion positions (filled black circles).

the electronic properties of an oxygen doped (in place of sulfur) TiS_2 monolayer. Finally, the phonon properties of bulk and monolayer are studied using *ab-initio* density functional perturbation theory.

5.2 Methodology

In order to investigate the electronic properties of TiS_2 monolayers in corporating oxygen impurities, *ab-initio* calculations are performed by using density functional theory [97, 98] within the generalized gradient approximation (GGA) of the exchange and correlation potential (Perdew-Burke-Ernzerhof parametrization [224]) and the Heyd-Scuseria-Ernzerhof [199] (HSE06) hybrid exchange correlation functional, as implemented in the Vienna *ab-initio* simulation package (VASP) code [355]. Projected augmented-wave (PAW) [196] pseudo-potentials are used to describe core electrons. The electronic wavefunction is expanded using plane waves up to a cutoff energy of 400 eV. Brillouin zone sampling is done by using a (5×5×1) Monkhorst-Pack k-grid. Periodic boundary conditions are applied, and a vacuum layer of at least 10 Å is placed above the monolayer to minimize the interaction between the adjacent layers. The conjugate gradient method is used to obtain relaxed geometries. Both atomic positions and cell parameters are allowed to relax, until the forces on each atom are less than 0.02 eV/Å.

In order to calculate the formation energy of O-doping on a TiS_2 monolayer, the following reaction are considered:

$$TiS_2 + xH_2O \rightarrow TiS_{2-x}O_x + xH_2S. \tag{5.2}$$

The formation energy is defined as

$$E_{\text{form}} = E_{\text{tot}}(\text{TiS}_{2-\text{x}}\text{O}_\text{x}) - E_{\text{tot}}(\text{TiS}_2) + E_{\text{mol}}(\text{H}_2\text{S}) - E_{\text{mol}}(\text{H}_2\text{O}), \tag{5.3}$$

where $E_{\text{tot}}(\text{TiS}_{2-x}\text{O}_x)$ is the total energy derived from a calculation with a substitutional atom O in place of S, $E_{\text{tot}}(\text{TiS}_2)$ is the total energy of the corresponding pristine TiS_2 monolayer supercell, $E_{\text{mol}}(\text{H}_2\text{S})$ and $E_{\text{mol}}(\text{H}_2\text{O})$ are the energies of a H_2S and a H_2O molecule, respectively.

Electronic structure calculations based on the Green's function quasi-particle approach, are performed also using the VASP package. The G_0W_0 approximated method is applied as a correction to the KS single particle energies. Both G_0 and W_0 are calculated from the KS orbital energies and wavefunctions within the DFT framework, where the DFT calculations are performed using the hybrid (HSE06) exchange-correlation functional. At least 100 unoccupied bands are used for the (1×1) supercell. The Brillouin zone is sampled using the same k-grid as that used for the DFT calculations.

In order to investigate the vibrational properties of bulk and monolayers of TiS_2, *ab-initio* density functional perturbation theory (DFPT) calculations are performed within the local density approximation (LDA) of the exchange and correlation functional [Ceperley-Alder (CA) parametrization [369]], as implemented in the Quantum Espresso package [356]. Ultra-soft pseudo-potentials are used to describe the core electrons of all the atomic species. The conjugate gradient method is used to obtain relaxed geometries. Both the atomic positions and the cell parameters are allowed to relax, until the forces on each atom are less than 0.01 eV/Å. The electronic integrations are carried out by using a $16\times16\times8$ $(16\times16\times1)$ Monkhorst-Pack k-grid for bulk (monolayer) TiS_2 and a Hermite Gaussian smearing of 0.01 Ryd is used for all the calculations. The dynamical matrix is calculated on a $4\times4\times2$ (4×4) phonon-momentum grid and is interpolated throughout the Brillouin zone in order to plot the bulk (monolayer) phonon bandstructure.

Dimension	Expt.	PBE	HSE06	G_0W_0
Bulk	a=3.41Å, c=5.69Å ΔE_g= -1.5 to 2.5 eV *	a=3.414 Å, c=5.709 Å, ΔE_g=-0.12 eV	a=3.41 Å, c=5.69 Å, ΔE_g=0.41 eV	ΔE_g=1.01 eV
monolayer	-	a=3.41 Å, ΔE_g=-0.06	a=3.407 Å, ΔE_g=0.48 eV	ΔE_g=1.12 eV

TABLE 5.1: The unit-cell parameters and the bandgap of bulk and monolayer TiS_2, calculated with DFT-GGA, DFT-HSE06, and G_0W_0 approach. $\Delta E_g \rightarrow$ bandgap. Negative value of the ΔE_g indicates the band overlap between the conduction and valence band. * The references are mentioned in the introduction of this chapter.

5.3 Electronic Properties with oxygen doping

5.3.1 Pristine bulk and single layer

Our systematic study begins by calculating the electronic properties of bulk TiS_2. In Table 5.1, the optimized lattice parameters and the bandgap for both bulk and monolayer are listed. The optimized bulk TiS_2 unit cell parameters are $a = b$ =3.414 Å, c=5.705 Å. These values are in good agreement with the previous theoretical value of a=3.41 Å [357] and with the experimental ones of $a = b$ = 3.407 Å, c = 5.695 Å [358]. The Ti-S bond length in bulk TiS_2 is found to be 2.425 Å, again it is in close agreement with the experimental value of 2.32 Å [63] and to the previous theoretical (LDA) value of 2.383 Å [323]. The calculated energy bandstructure along the high symmetry lines in the Brilloiun zone of bulk TiS_2 is shown in Fig.5.3(a). Bulk TiS_2 is a semi-metal and we obtain an indirect band-overlap of 0.12 eV (negative bandgap). The valence band maximum (VBM) is found to be located at the Γ point, while the conduction band minimum (CBM) is found to be located at the L point. The partial density of states (PDOS) projected on the different atomic species shows that the valence band and conduction band mainly originate from the S-3p and the Ti-3d orbitals, respectively [see Fig.5.3]. It has been mentioned before that there is ambiguity in the bulk bandgap extracted from the different experimental measurements so that a comparison is different. However our calculated value is in good agreement with existing DFT calculations using semi-local XC functionals (LDA/GGA) [320, 357]. It is well known that LDA/GGA systematically underestimates the bandgap. Therefore, we study the electronic structure using the DFT-hybrid functional (HSE06) and the Green's function quasi-particle approach (G_0W_0 approximation). Fig. 5.3 shows that

for the HSE06 functional, the CBM moves upward in energy, resulting in the opening a bandgap to 0.41 eV. In contrast, in the G_0W_0 approximated quasi-particle approach, the CBM and VBM moves opposite to each other, *i.e.* the CBM becomes higher in energy and the VBM becomes slightly lower in energy. Consequently, there is a further opening of the bandgap (1.01 eV) with respect to the HSE06 one.

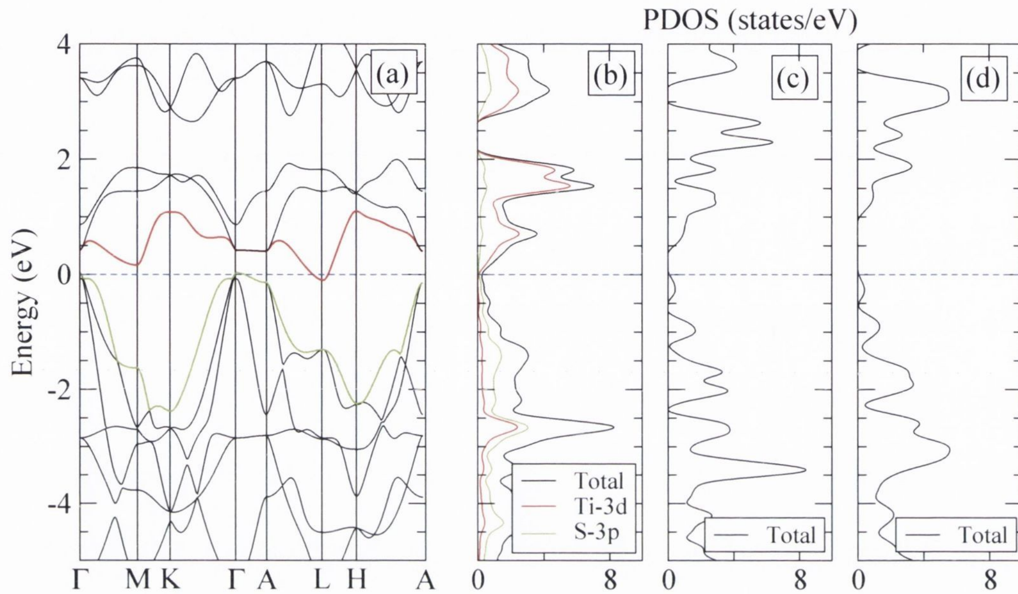

FIGURE 5.3: (a) The GGA-bandstructure of bulk TiS_2. The conduction band (red line) and valence band (green line) overlap between the Γ and the L points. The density of states calculated with (b) the GGA functional, (c) the hybrid-HSE06 functional and (d) the quasi-particle-G_0W_0 approach are plotted for bulk TiS_2. The blue dashed line indicates the VBM. The electronic states in DOS are Gaussian broadened by 0.1 eV.

Next we move to study the electronic properties of a TiS_2 monolayer. Our optimized lattice constant, $a = b$, is now 3.41 Å, *i.e.* it is slightly smaller than that in the bulk. Such a value is in good agreement with the experimentally observed one of 3.40 Å [359]. Our calculations show that unlike MoS_2, as the number of layers is decreased, the electronic property, *i.e.* bandgap do not change significantly. This fact is robust against the choice of methods, *i.e.* DFT-HSE and G_0W_0 method [see Fig.5.4]. Our computed GGA-bandgap of -0.06 eV is in good agreement with the previous theoretical calculations [366]. However, our predicted result conflicts with the DFT-GGA based calculation, in which the bulk is predicted as a semi-metal whereas the monolayer is a semiconductor with an indirect bandgap larger than 1.0 eV [346, 361]. We do not know that reason for this conflict. Both for the bulk and the single layer, the CB and the

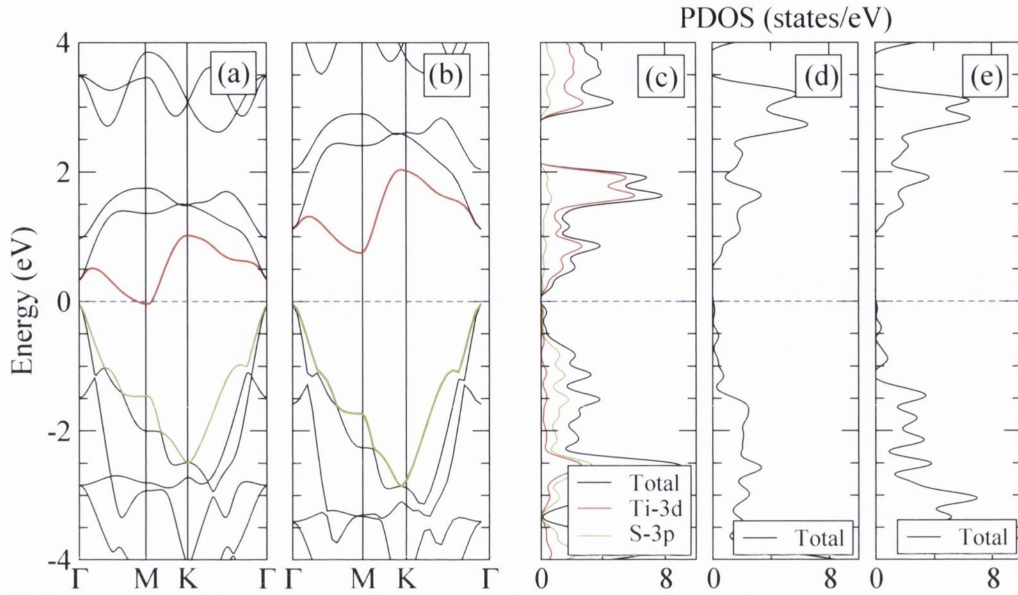

FIGURE 5.4: (a) The GGA- and (b) HSE-bandstructure of TiS_2 monolayer. In the panels (a) and (b), the conduction band and the valence band are denoted by red lines and green lines, respectively. The density of states calculated with (c) the GGA functional, (d) the hybrid-HSE06 functional and the (e) quasi-particle-G_0W_0 approach, are plotted. The blue dashed lines indicate the VBM. The electronic states in DOS are Gaussian broadened by 0.1 eV.

VB are mainly derived from the Ti-3*d* and the S-3*p* orbitals respectively [see Fig.5.3(b) and 5.4(c)]. This is in good agreement with previous calculations [320].

Next, in Sec.5.3.2 we study the effects on the electronic structure of a TiS_2 monolayer due to doping by replacing S with an iso-electronic element, oxygen.

5.3.2 Oxygen doping on a monolayer

An oxygen doped TiO_xS_{2-x} monolayer alloy is modeled by substituting one S atom in a TiS_2 supercell. The oxygen composition x is characterized by varying the supercell size, denoted by $n \times n$, where n goes from 1 to 7. These correspond to x = 1.00 (1×1 supercell), x = 0.125 (2×2 supercell), x = 0.0555 (3×3 supercell), x = 0.03125 (4×4 supercell), x = 0.02 (5×5 supercell), x = 0.01389 (6×6 supercell) and x = 0.010 (7×7 supercell). The optimized lattice constant, the formation energy and the bandgap for different O concentrations are listed in Table 5.2. Interestingly, the formation energy is independent of the O concentration. In contrast, the lattice constant decreases compared to the pristine TiS_2 value due to the fact that the ionic radius of 1.84 Å) is

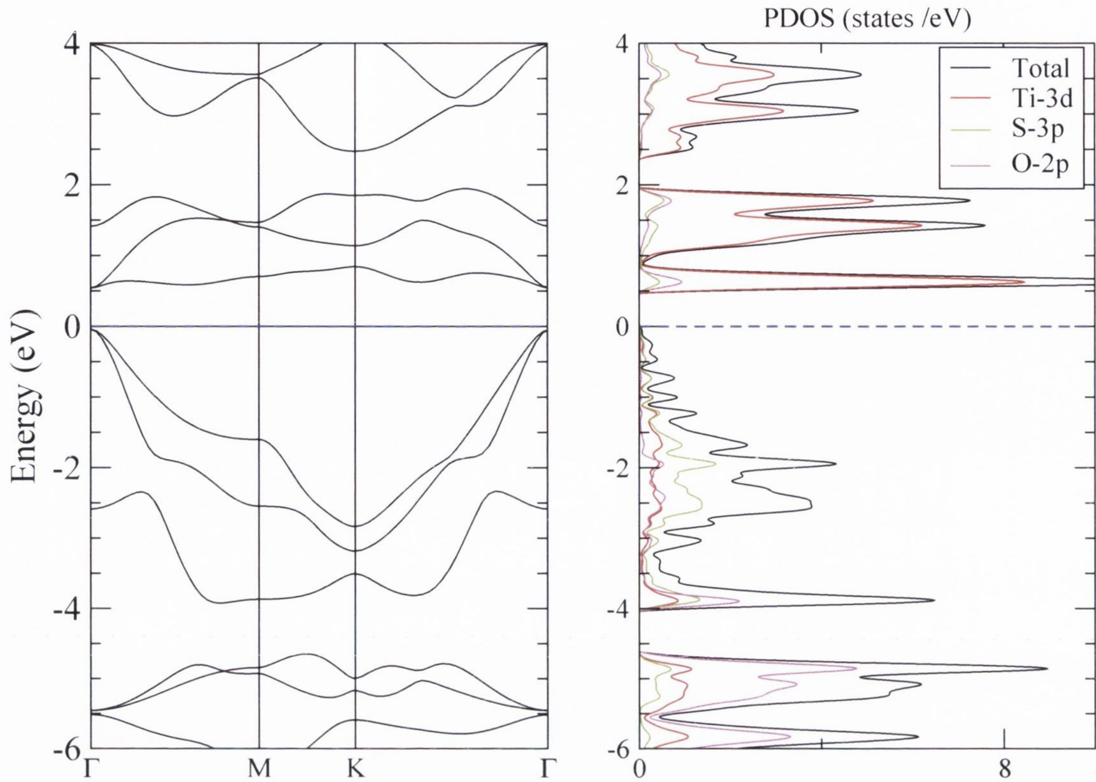

FIGURE 5.5: The GGA-bandstructure (left) and the PDOS (right) of a TiSO monolayer alloy. The blue dashed lines indicate the Fermi level. The electronic states in EDOS are Gaussian broadened by 0.1 eV.

larger than that of O (1.40 Å). Therefore, the bandgap is increased by modifying the valence band and conduction band as they predominantly Tid-S p bonding and anti-bonding states, respectively. In other words, the opening of the bandgap is due to the fact that the O $2p$ shell is located below the S $3p$ shell. Consequently, the bandgap opens monotonically when the O concentration is increased. As a representative situation, for the O doped (1×1) supercell case, the bandstructure as well as the PDOS on different atomic species are shown in Fig. 5.5. The highest bandgap-opening is expected when all the S atoms are replaced by O. This corresponds to formation of a 2D layered hexagonal phase (octahedral symmetry) of TiO_2. 2D-TiO_2 has not been synthesized with this particular crystal structure, the theoretical calculations have shown that it is a metastable phase of TiO_2 [367]. Nevertheless a monolayer hexagonal superstructure of TiO_2 (a nontrivial coordination) has been synthesized from a ferro-electric $SrTiO_3$ surface, where TiO_2 is electrically decoupled from the bulk counterpart [368]. In Fig. 5.6(c), the variation of the bandgap is plotted against the O concentration. Here the concentration is varied by considering a 3×3 supercell in which the S atoms are substituted by the appropriate number of O atoms for a given concentration in

Cell Size ($n \times n$)	S:O	Lattice constant (a) [Å]	Formation energy (E_{form}) [eV]	Bandgap (ΔE_g) [eV]
1×1	1:1	3.18	-0.332	0.54
2×2	7:1	3.35	-0.319	0.21
3×3	17:1	3.39	-0.326	0.08
4×4	31:1	3.40	-0.319	-0.02
5×5	49:1	3.405	-0.328	-0.04
6×6	71:1	3.41	-0.303	-0.05
7×7	98:1	3.41	-0.302	-0.05

TABLE 5.2: The optimized lattice constant, the formation energy, and the bandgap for one oxygen doping on $n \times n$ supercell, where, n runs from 1 to 7.

the 3×3 supercell [see the Fig. 5.6(a), (b)]. For example, in the 3×3 supercell, 9 S atoms are replaced by 9 O atoms for the composition x=1 and the corresponding configuration is shown in Fig. 5.6(b). Interestingly, the bandgap increases linearly with O concentration up to $x = 1.0$. Further increasing the O concentration, the bandgap still results in a bandgap increase, but the slope is larger than that observed for $x \leq 1$. The transition in the slope arises because the nature of the bandgap changes from indirect (from the Γ point to the M point) to direct (at the Γ point) for a concentration $x \simeq 1.0$ (see Fig.5.5).

In order to study the effect of different possible configurations for a particular O concentration, we consider only the O concentration $x = 1$ in the 3×3 supercell depending on the specific substitutional arrangement of the O atoms. Interestingly, we find that the bandgap ranges from 0.54 to 0.44 eV. This implies that the bandgap-variation does not change significantly with the particular site preference under substitution.

Next we calculate the bandgap using the hybrid functional HSE06 and the G_0W_0 quasi-particle approach for two selective configurations, namely for the TiSO and the TiO_2 structures. Fig. 5.6(c) shows that the slope of the bandgap-variation is robust against the different methods, although their initial TiS_2 bandgaps differ significantly from each others.

Then we evaluate the pairing energy between two O atoms in a 6×6 supercell. Here the paring energy is defined as the energy difference, δE, between the configuration where the two impurities are placed at the nearest neighboring positions, and where they are placed as far as possible in the unit-cell. We find that it is energetically preferable by about 20 meV/supercell to two O atoms as close as possible to each other. Based solely on their pairing energy, O-dopants would tend to form clusters, however this cluster

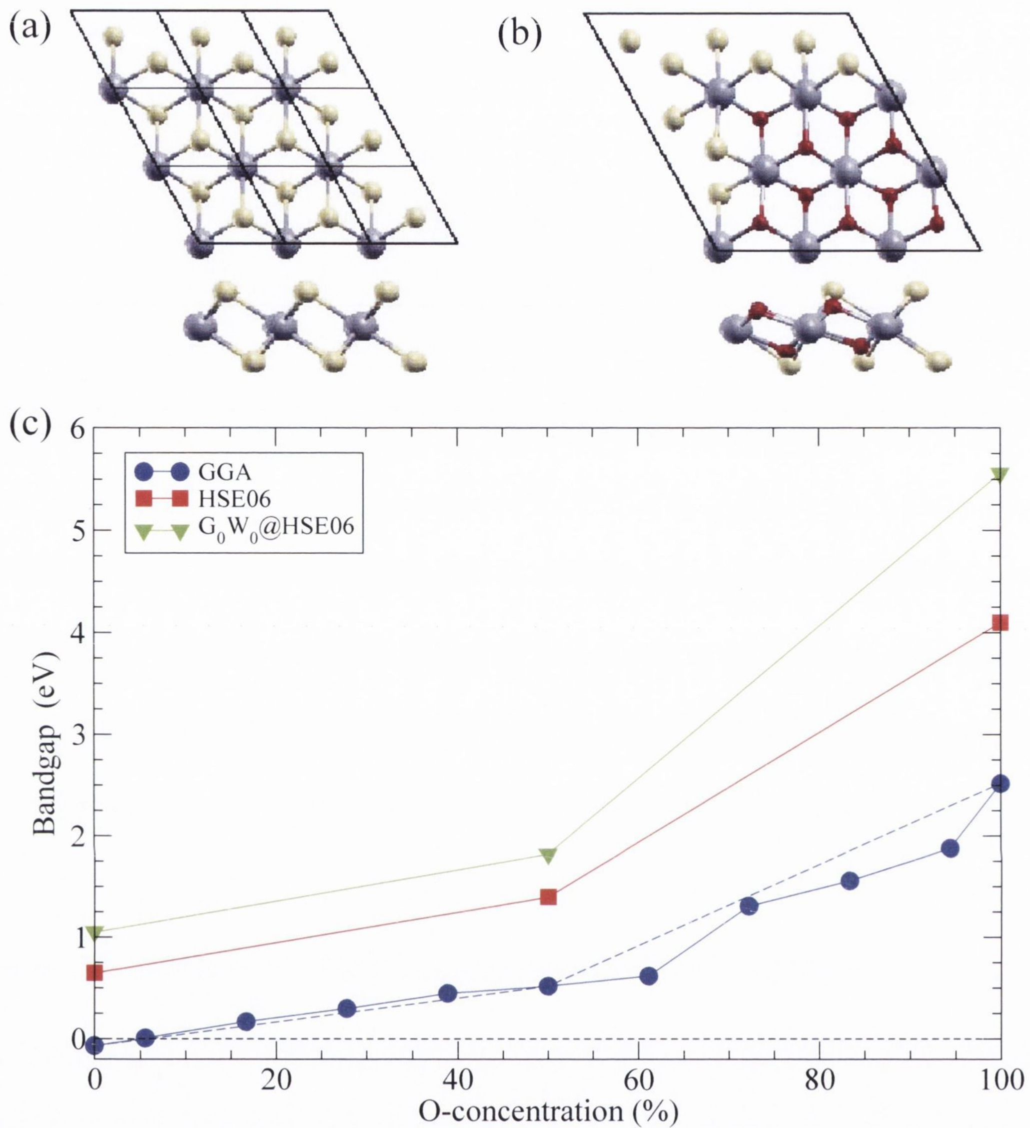

FIGURE 5.6: The top (up) and side (down) view of the (a) pristine and (b) the 50 % O-doped (3×3) supercell. (c) The bandgap-variation against the O-concentration for DFT-GGA (blue), DFT-HSE06, and G_0W_0 approach.

formation is generally controlled in experiments by the energy barrier for moving the oxygen in the TiS_2 monolayer from one site to another one.

5.3.3 Oxygen doping on nanoribbon

In order to shed some light on the effects of placing an O impurity either at the edges or in the middle of a TiS_2 monolayer, we consider a sufficiently long (width about 5

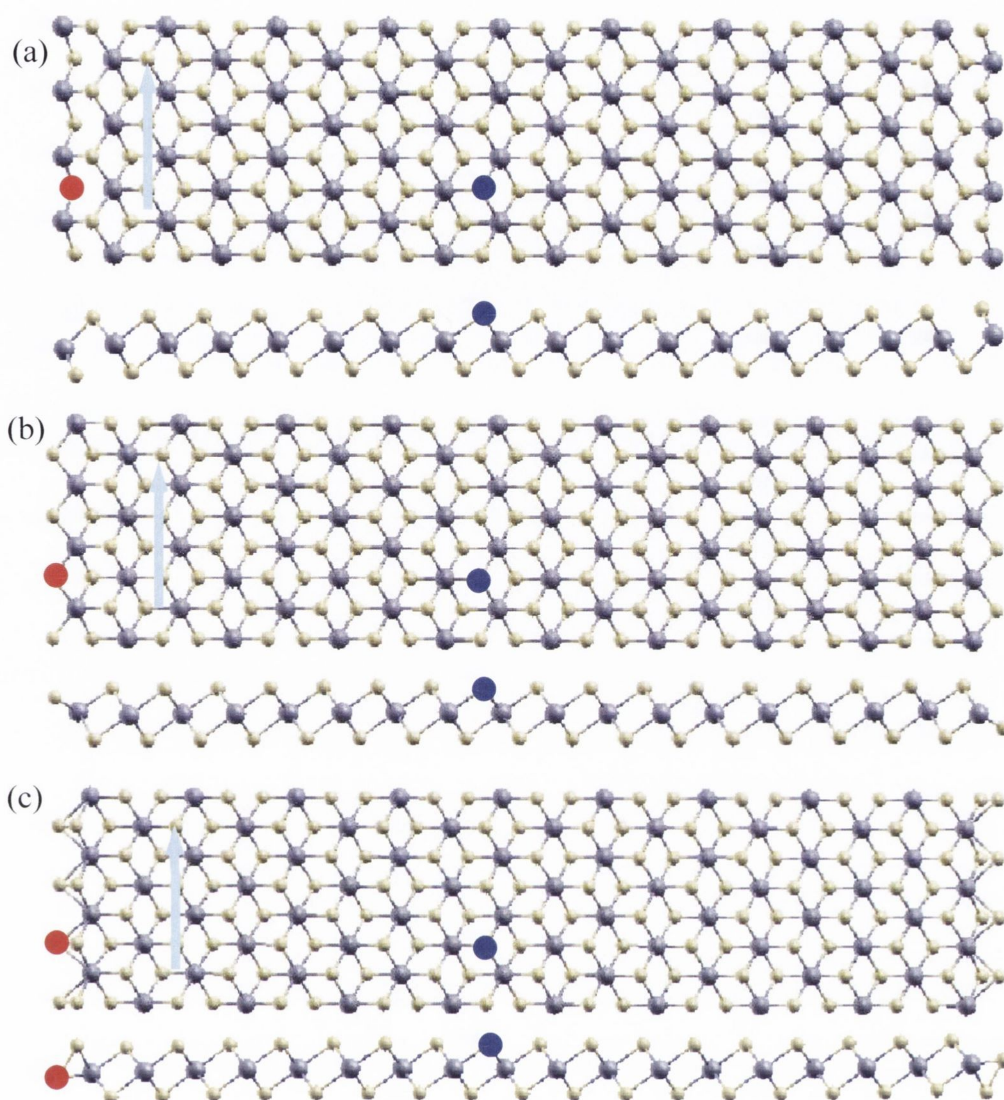

FIGURE 5.7: Top view (up) and side views (down) of 1×4 supercells of (a) 0 %, (b) 50 %, and 100 % S-passivated TiS_2 nanoribbon. The O-doping at the edge site and the middle site of the nanoribbon are denoted by solid red cirles and solid blue circles. Color code: grey →Ti and yellow → S.

nm) nanoribbon. We confirm that the oxygen-doped nanoribbon remains semi-metallic like the monolayer. As we are interested in the edges S atom replacement, we use only the Ti-terminated edges with 0%, 50% and 100% S-passivation as shown in Fig. 5.7. In Table 5.3 we list the formation energy of O doped both at the edges and in the middle of the above mentioned different % S-passivated nanoribbons. In the 100% S passivated nanoribbon, the formation energy is positive for the edge site and is negative for the middle site, *i.e.* oxygen doping is more favorable in the middle of the nanoribbon than that of at the edges. In contrast, O doping is much favorable at the edge site compare

	E_{form} for O-doped at site	
Edge passivation type	Edge	Middle
100% S	1.030	-0.311
50% S	-0.402	-0.321
0% S	-0.467	-0.324

TABLE 5.3: The formation energy for one O doped at the edges and the middle of 100%, 50% and 0% S passivated monolayer TiS_2 nanoribbon.

to the middle one for both 50% and 0% S passivated nanoribbon.

5.4 Phonon Properties of bulk and single layer

In order to study to the effects of dimensionality on the vibrational properties of TiS_2, we study the phonon dispersion of bulk and monolayer TiS_2. The bulk phonon dispersion are plotted along the Γ-K-M-Γ q-path in Fig.5.8(a). The irreducible representation of the zone-center phonon modes reads

$$\Gamma = A_{1g}R + E_gR + 2A_{2u}(IR) + 2E_u(IR), \tag{5.4}$$

where, R and IR denotes respectively Raman and infrared active modes. The atomic displacement of the optical modes at the Γ-point are shown in Fig.5.9. The phonon frequencies of certain modes are measured experimentally by vibrational spectroscopy, such as Raman, infrared and neutron scattering at some high symmetry points in the Brillouin zone [360, 370] and those values are compared with our calculated value [see Fig.5.8(a)]. Our calculations are in good agreement with the experimental values. In addition, our calculated phonon dispersion agrees quite well with the previously theoretical calculation based either on an empirical-valence-force-field method [360] or on a state of the art first principle DFPT [322]. Interestingly, we observe the signature of a soft-phonon mode, generally called Kohn anomaly, along the M point and half the way along the Γ-K direction in the Brillouin zone.

The phonon dispersion of a TiS_2 monolayer is shown in Fig.5.8(b). Similar to the bulk phonon dispersion, there is no energy-gap between the optical and the acoustic phonon of the monolayer. We find that the TiS_2 monolayer is dynamically unstable at the M point. This reflects the fact that the system is stabilized by forming a 2×2 real space superstructure (commensurate charge density wave phase) and the atoms are distorted

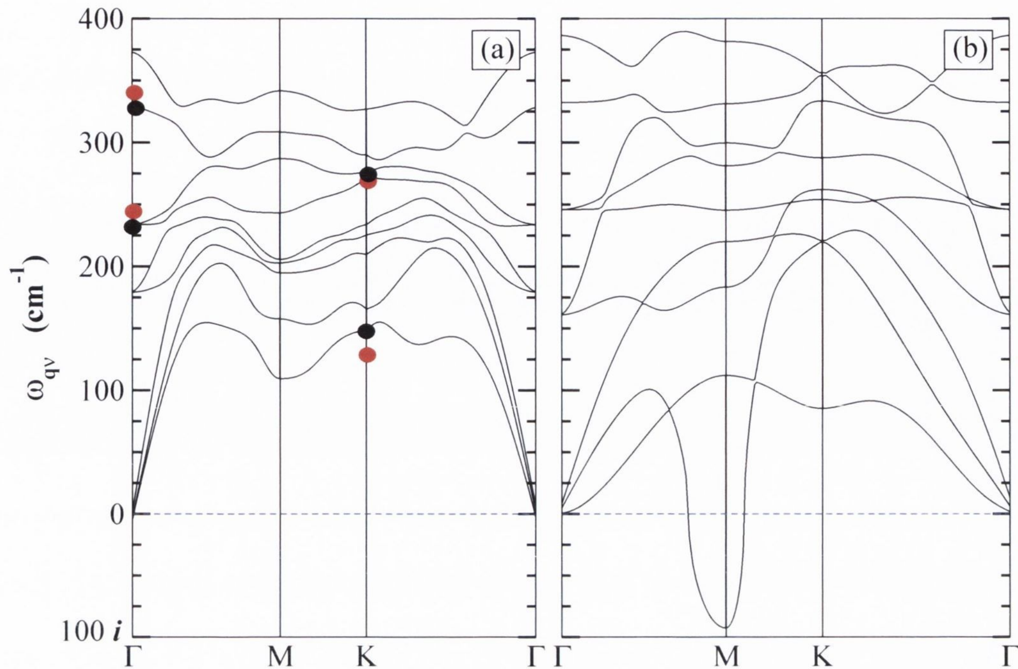

FIGURE 5.8: The phonon dispersion of (a) bulk (b) monolayer TiS_2. The solid red circles represent the experimentally available data correspond to our calculated ones (black solid circles). Note that calculated imaginary frequencies are shown as negative roots of the square phonon frequencies. Lines are guides to the eye

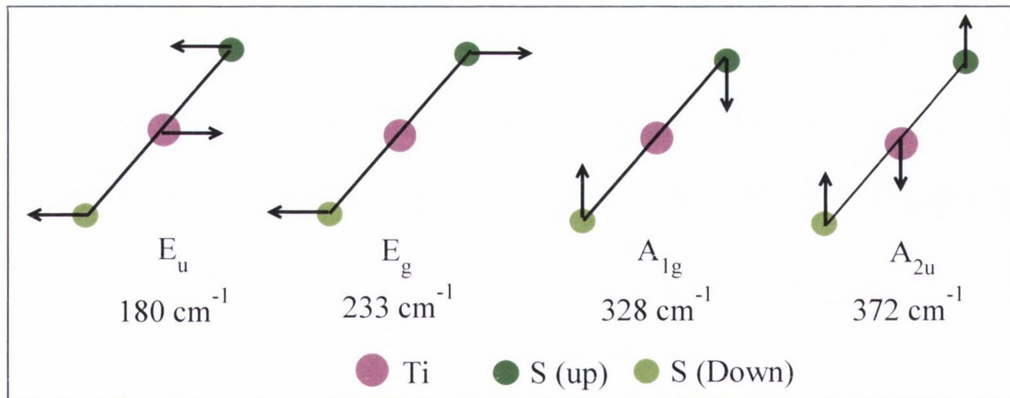

FIGURE 5.9: Schematics of the atomic displacement patterns of the Γ centered optical phonon modes of 1T-TiS_2. The frequencies are reported from our calculations for bulk TiS_2.

to accommodate themselves into their new equilibrium positions. In Fig.5.10(a) the bandstructure of a monolayer in the normal phase and the CDW are shown. In the CDW phase, the material opens a bandgap of 0.09 eV. The macroscopic origin of the CDW phase mainly arises from the strong electron-phonon coupling, generally present in such classes of LTMD materials [362, 363]. Our total energy calculations show that

the 2×2 superstructure is more energetically favorable by 1.1 meV/unit-formula than the undistorted one. Indeed we observe that the unstable phonon mode does exist at the Γ point in the Brillouin zone of an undistorted (2×2) TiS$_2$-supercell. Note that the M point in the Brillouin zone of TiS$_2$-unit-cell is equivalent to the Γ point in the (2×2) TiS$_2$-supercell. As a consequence the unstable mode disappears at Γ in the Brillouin zone of the distorted (2×2) TiS$_2$-supercell. The schematic diagram of the distorted superstructure is shown in Fig.5.10(b). The distortion of the atomic positions are determined by the **q**-vector, at which the unstable phonon mode occurs. The distortion of the Ti atom, $\delta\zeta_{Ti}$ is as large as 0.05 Å compared to that of the S ones ($\leq$ 0.005 Å). The similar CDW phase transition has been observed experimentally in bulk TiSe$_2$, an iso-structural compound to TiS$_2$ and the transition temperature was reported as large as 200 K [364, 365].

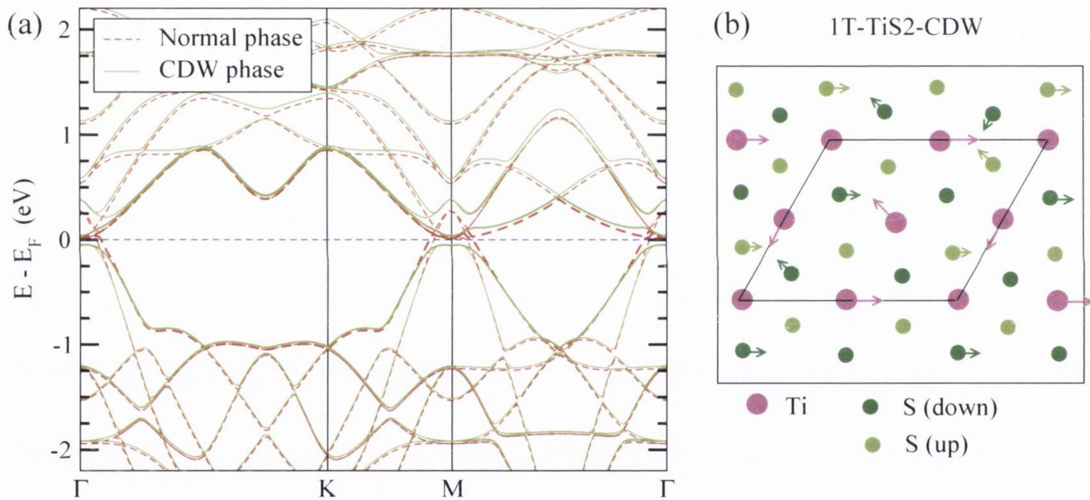

FIGURE 5.10: (a) The LDA-bandstructure of 2×2 supercell of monolayer in the normal (red dashed lines) and the commensurate CDW (green lines) phases. The conduction and valence bands are highlighted with bold lines. (b) The schematic shows the commensurate CDW phase of the TiS$_2$ monolayer. The arrow indicates the displacement of the respective atoms.

Next we move to study the effect of pressure on the CDW phase. In order to simulate the pressure on the system, a compressive strain is applied by reducing the 2D-lattice constant isotropically. It is confirmed that strain weakly affects the bandstructure except for an increase of the S-p bandwidth, but the system remains metallic. In Fig.5.11(a), the phonon dispersion is shown for a 6.6% compressive strain, since the LDA lattice constant of the pristine monolayer is 3.316 Å. Interestingly, the minimum frequency of the soft-phonon mode at the M point have less an imaginary value (-8

cm^{-1}) when compared to the unstrained ones. Consequently, the energy gain due to CDW formation reduces with increase of compressive strain. Eventually, the unstable modes disappear for a compressive strain of 7.1 %, which corresponds to a hydrostatic pressure of $\approx$ 3.9 GPa in the monolayer. The disappearance of the CDW under compressive strain (pressure) can be explained by considering the inter-atomic force constant under a given compressive strain. When the compressive strain increases, the Ti-S bond-length decreases, enhancing the stiffness of the nearest neighbor's Ti-S force constant. Therefore the occurrence of such a soft-phonon mode is strongly influenced by the local environment around the transition metal atoms in the TiS_2 layer. The stiffness also can be varied by iso-electronic doping of the monolayer, *i.e.* by replacing S with oxgyen. The reason is that the Ti-O bondlength is smaller than the Ti-S ones, so that O substitution enhances the inter-atomic (Ti-S/O) stiffness. As a demonstration we plot the phonon dispersion of the TiSO alloy [see Fig.5.11(a)]. We find that the unstable phonon frequency at M point no longer exists.

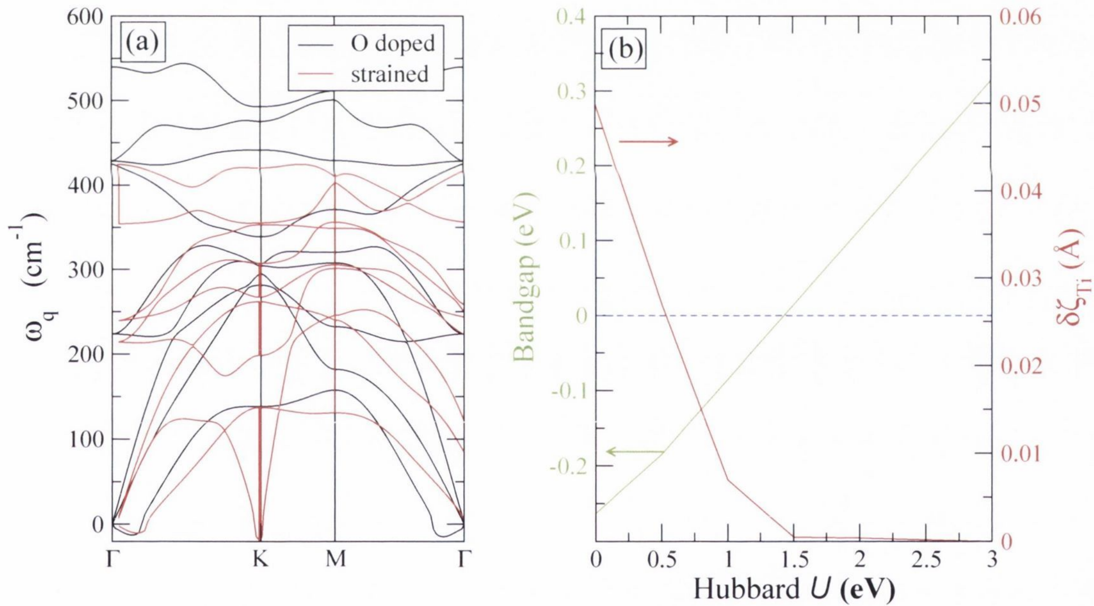

FIGURE 5.11: (a) The phonon dispersion of the O-doped (black) and compressive strained (red) TiS_2 monolayer. (b) The variation of the bandgap (green line) and the Ti-distortion, $\delta\zeta_{Ti}$ (red line) against the Hubbard parameter for LDA+U calculations.

As mentioned in the previous section, the calculated bandgap of a TiS_2 monolayer depends significantly on the choice of exchange correlation functional used for the calculation. In addition, it is known that the charge density wave phase can be present either in a metallic system or in a small-bandgap semiconductor, where the exciton binding energy is sufficient to overcome the energy gain of the lattice distortions. In

this context, in order to investigate the formation of a charge density wave phase as a function of bandgap, we have carried out DFT calculations using the LDA+U functional as the valence has predominantly $3d$ character. We observe that the bandgap opens linearly from -0.25 to 0.33 eV as the U parameter increases from 0.0 to 3.0 eV (the LDA+U corrections are employed only on the Ti atoms). Using the LDA+U method, the $3d$ orbitals become more localized than when calculated with the LDA, resulting in a downward energy-shift of the VB. In Fig.5.11(b) we show the variation of the bandgap and the Ti-lattice distortion, $\delta\zeta_{Ti}$ against the Hubbard U parameter. The lattice distortion vanishes when the bandgap becomes positive, *i.e.* the overlap between the CB and the VB reduced to zero. From these result, we conclude that if the system were a semiconductor, the CDW phase would not exist.

5.5 Conclusion

By using *ab-initio* density functional theory with local (GGA) and non-local (HSE06) exchange and correlation (XC) functional, as well as the Green's function quasi-particle (GW) approach, we have studied the electronic properties of a pristine and an oxygen-doped TiS_2 monolayer. The electronic properties of the bulk and monolayers are sensitive to the choice of DFT-functional. The GGA predicts that both the bulk and monolayers are semi-metallic, whereas both of them turn out to be semiconductors with an indirect bandgap of 0.41 eV (bulk) and 0.48 eV (monolayer) for the HSE06 functional. Moreover, G_0W_0 predicts a bandgap as large as 1.01 eV (bulk) and 1.12 eV (monolayer). Interestingly, the opening of the bandgap, for a given method, is small ($\sim$ 0.06 eV) when the thickness changes from bulk to the single layer limit. This implies that the layer-layer interaction has an insignificant effect on the electronic structure of TiS_2.

The bandgap of a monolayer opens for iso-electronic doping with oxygen (replacing sulfur) and the bandgap opens linearly as the O-concentration increases. Although the absolute value of the bandgap of pristine TiS_2 depends on the choice of the functional in DFT and the G_0W_0 scheme, the variation of the bandgap with O-concentration is robust against them.

Finally, by using *ab-initio* density functional perturbation theory, we have studied the phonon properties of TiS_2 bulk and monolayer. We observe a Kohn anomaly in the

bulk phonon dispersion. In contrast, our LDA calculations show that a monolayer TiS_2 exhibits a CDW instability at the K point, resulting in the formation of 2×2 superstructure. Interestingly, compressive strain (pressure) tunes the CDW instability and a compressive strain of 7.1 % is required for the transition from CDW to a normal metallic state. The CDW can be modulated by an iso-electronic doping with the O or the Se atom in place of the S atom, where Se enhances the CDW instability while O reduces it. In addition, LDA+U calculations show that the bandgap of a monolayer varies linearly as U increases and the bandgap varies from -0.25 eV to 0.33 eV as the U ranges from 0.0 to 3.0 eV. Consequently, the CDW phase disappears for U= 2.0, when the bandgap becomes zero for the undistorted system.

Chapter 6

Conclusions and Future Work

In summary, I have presented a first-principles study on low dimensional nanostructures made of layered transition metal di-chalcogenides. Due to the simultaneous improvements in both synthesis techniques for making atomically-thin structures and the availability of state of the art *ab-onto* electronic structure methods, this branch of materials science has experienced a surge of popularity in recently years. This has been elevated, not only by interest in exploring new fundamental physics, but also by the potential to engineer materials properties suitable for device applications. In this work, I examined the electronic and phonon properties of the layered material's nanostructures and possible ways that can manipulate their properties via external perturbations as well as by reducing dimensions.

In the Chapter 2, I have described briefly the theoretical formalism of both the density functional theory (DFT) and beyond DFT, Green's function quasi-particle approach for electronic structure calculations. In addition, the density functional perturbation theory (DFPT) was introduced for phonon calculations. All the electronic structure calculations were carried out with the SIESTA, VASP and QUANTUM ESPRESSO-DFT codes. The general implementation details for all the codes, were briefly mentioned.

In Chapter 3, I considered a 2D nanostructure made of a prototypical LTMD, namely MoS_2. Interestingly, we observed that the native indirect bandgap became direct when the thickness gets down from bulk to the monolayer limit. In fact, this result had been already confirmed by photo-luminescence experiments. I then carried out a systematic study of the changes of the electronic structure of a MoS_2 monolayer induced by dopants. We considered substitutional doping for both Mo and S, as well as doping

by adsorption. Specifically, on the one hand I considered the Mo atoms substituted by a transition metal Y, Zr and Nb as p-type dopants, and by Re, Rh, Ru, Pd, Ag, and Cd as n-type dopant. On the other hand, S was substituted by nonmetals (P, N and As) as p-type dopants and halogens (F, Cl, Br, and I) as n-type dopants. S substitution with nonmetals and Mo substitution with transition metals creates deep donor levels inside the bandgap of the MoS_2 monolayer for most of the dopants considered. Via substitutional doping I found that it possible to obtain p-type MoS_2 by replacing an Mo atom with Nb. To made MoS_2 n-type we found only rather deep donor levels when substituting Mo with transition metals, with Re being the one with the smallest activation barrier. A n-type character can also be achieved by adsorbing alkali metals. The last class of dopants we considered was adsorption of ionic molecules, which can occur during electric double layer formation when MoS_2 is contrast with in an ionic liquid gate. These show high potential for inducing large carrier concentrations, both electrons or holes, within the MoS_2 monolayer. Moreover, the changes to the carrier densities induced by ionic liquids are expected to be a general property of LTMDs in such environments. Quantum transport across low dimensional structures was recently received a lot of attention as such structures may form the basic building blocks of future logic device and sensors [371]. Therefore in future, we will continue this work by investigating the transport properties of MoS_2 monolayer field effect transistors with a combination of density functional theory and non-equilibrium Greens function methods.

MoS_2-based transistors have appeared always doped, even if no doping is intentionally introduced. Intriguingly this could be both n- and p-type and its origins are unknown. By performing DFT calculations for the complex MoS_2/SiO_2 interface, we found that the clean surface of an SiO_2 substrate did not have a significant effect on MoS_2 electronic properties. However, we were able to identify the interface defects which could generate either n- or p-type doping. Specifically, adsorbed Na or an O vacancy at the SiO_2 surface could change the MoS_2 conductivity to n-type and p-type, respectively. This result has two profound implications: 1) it established that defects at the MoS_2/SiO_2 interface are responsible for doping MoS_2, solving a rather long-standing puzzle, 2) it suggests a new way to fabricate nano-scale logic devices, where the electronic structure of the channel is tuned by controlling surface defects of the substrate.

In Chapter 4, I have investigated the ground state electronic structure and the electrical field response of MoS_2 nanostructures such as nanoribbons (1D) and nanoclusters (0D).

Two types of nanoribbons, namely *zigzag* nanoribbon (ZNR) and *armchair* nanoribbon (ANR), were constructed based on the edge termination of the 2D MoS_2 layers. I predicted that the ground states of ZNR and ANR were metallic and insulating, respectively. Importantly, the bandgap in these systems is primarily determined by a pair of edge states and it might be tuned by applying an external transverse electric field. This could eventually drive a metal-insulator transition. The critical electric field for the transition could be reduced to a practical range with increasing ribbon width. Also it is interesting to remark that, as the dielectric constant was approximately proportional to the inverse of the bandgap, the critical fields for the gap closure are expected to be relatively materials independent. Recently experimental studies have reported applied electric field as large as ~ 0.2 V/Å in BN nanotubes without any dielectric breakdown [372]. This demonstrates that the predicted large critical field is experimentally accessible. We observed that the direct bandgap became an indirect one, when other layers are stacked on the monolayer and subsequently the bandgap reduced inversely with the number of layers. The magnetic properties of the nanoribbon changed from diamagnetic to magnetic via Cr doping at the Mo atoms edges. Interestingly, the modulation of the bandgap is also induced by the Cr doped nanoribbon upon applied external transverse electric field.

The presence of localized edge states that could be moved to the Fermi level by applying a transverse electric field suggested that the system could be driven towards a magnetic instability. Our spin-polarized calculations showed that this indeed happens and that at a certain critical electric field a diamagnetic to magnetic transition occurs. This follows directly from the Stoner criterion as the Van Hove singularities associated with the edge states have a large density of states. Intriguingly the magnetic phase could be further tuned by the external field and different alternating diamagnetic and magnetic regions could be accessed. Although the access of the magnetic region depends on the function of S and H atoms used for the passivation at nanoribbon edges, the modulation of the bandgap is robust against the different type of edges passivation.

I extended the study of electric field effects to 0D monolayer MoS_2 triangular nanoclusters (TNCs). Depending on the edge termination (such as Mo or S edge) and the percentage of S coveraged at the edges, a monolayer MoS_2-TNC is classified as magnetic or non-magnetic. I showed that by applying an external transverse electric field, E_{ext}, the gap between the highest occupied (HOMO) and lowest unoccupied (LUMO) molecular orbitals could be reduced. Eventually, at a certain critical value of E_{ext}, the ground state of a non-magnetic TNC becomes spin-polarized with a moment of $2\mu_{\mathrm{B}}$.

This magnetic transition corresponds to a singlet-triplet transition described by the two-site Hubbard model. Our results suggested that the Stark effect and electrically driven magnetism is expected for the entire class of semiconducting layered materials.

In chapter 5, I considered an another prototypical LTMD, namely TiS_2. Here I investigated the electronic properties of bulk and monolayer TiS_2. I found that both the bulk and monolayer are semi-metallic with an indirect band-overlap within the GGA, whereas both of them are semiconducting according to the HSE06 functional. Concerning the long-standing bandgap issue, *i.e.* the question of whether TiS_2 is a metal, a semi-metal or a semiconductor, we investigated the electronic properties using the advanced *ab-initio* Green's function quasi-particle approach within the G_0W_0 approximation. The G_0W_0 approximated electronic structure predicts TiS_2 to be a semiconductor both in bulk and monolayer form. I observed that the bandgap does not open significantly, unlike the MoS_2 case, when the TiS_2 thickness decreases from bulk to the monolayer limit. This result is robust for all the methods used.
The effect of an oxygen-impurity has been studied by considering TiS_xO_x monolayer alloys. We found that the bandgap opens monotonically when increasing O concentration, although formation energies do not depend on the O concentration. This wide range of bandgap variation opens up the potential of TiS_2 for mainly nanostructured based solar-cell or oxygen-sensing applications.
In the context of an on-going collaboration with the experimental group of Prof. J. Coleman, School of Physics and with one postdoc of our group, Dr. Clotilde S. Cucinotta, in the future we plan to study water evolution processes occurring on the TiS_2 nanoflake. Indeed, electron beam microscopy experiments show that the edge of the flake is oxidized, no oxygen atoms are observed in the middle. The hypothesized reaction product of the oxidation reaction is H_2S, implying that the reagent molecule is H_2O. Having shown that, from a thermodynamic point of view, water evolution can occur (is an exothermic process), not only at the edge of the TiS_2 nanoribbon, but also far from it, our aim is to understand if there is any kinetic hindrance to the oxidation of the nanoflake far from the edge. To this end we plan to study and compare oxidation pathways of the edges of TiS_2 nanoflakes, both in the presence of surface S vacancies and on the clean surface, using the Nudged Elastic Band approach [373], which provides geometries and activation energies of the transition states. The reaction to be studied is

$$TiS_2 + H_2O \rightarrow TiSO + H_2S. \tag{6.1}$$

where TiS_2 represents the clean nanoflake and the TiSO oxidized structure. We expect that this reaction will be characterized by a double proton transfer from water to an S atom of the nanoflake (sitting either at its edge or in the middle of the surface). As a consequence, after the first proton transfer we expect to observe a reaction intermediate characterized by an OH and a SH group adsorbed in neighboring surface sites. An H_2S molecule would be formed after a second proton transfer from the OH group to the close SH group.

Finally, I investigated the phonon properties of bulk and monolayer TiS_2. Bulk TiS_2 exhibits a Kohn anomaly in the phonon dispersion, but all the phonon modes are stable. In contrast, an unstable phonon mode occurs at the M point in the the Brillouin zone for a monolayer. The monolayers are stabilized by forming a 2×2 superstructure. Subsequently, below a certain critical temperature,T_{CDW} both the lattice and the electron density are periodically modulated. The unstable phonon mode can be removed either by applying compressive strain or by oxygen doping in place of S. The disappearance of the phonon-mode could be understood by the stiffness-variation of Ti-S/O bond as it was significantly affected by the environment. As a further study, LDA+U calculations showed that the bandgap of TiS_2 monolayer opens linearly with increasing U, since LDA predicts that monolayer TiS_2 is semi-metallic. The distortion in the CDW phase decreased against the bandgap opening and eventually, the unstable phonon modes disappears, as soon as the monolayer become a semiconductor.

We have mentioned before that the LTMD family exhibits generally strong electron-phonon coupling (λ),

$$\lambda = \frac{N(\epsilon_F)D^2}{M\omega^2}, \tag{6.2}$$

where $N(\epsilon_F)$ is the electron density of states per spin at the Fermi level, D is the deformation potential, M and ω are the effective atomic mass and the average phonon frequency. Therefore it has been commonly found 2D chalcogenides materials display the electron-phonon mediated superconductivity, charge density waves or both in their metallic phases. However, the intercalation of alkali metals or organic molecules could induce/tune the superconductivity in this family. There are two ways to increase electron-phonon coupling by either reducing the dimensionality or by tuning the density of states at the Fermi level. Therefore in future we would like to investigate the effect of doping and dimensionality on the electron-phonon coupling of layered materials.

Chapter 7

Publications stemming from this work

- Kapildeb Dolui, Chaitanya Das Pemmaraju, and Stefano Sanvito, *Electric Field Effects on Armchair MoS_2 Nanoribbons*, ACS Nano **6**, 4823 (2012).
- Kapildeb Dolui, Ivan Rungger, Stefano Sanvito, *Origin of the n-type and p-type conductivity of MoS_2 monolayers on a SiO_2 substrate*, Phys. Rev. B **87**, 165402 (2013), arXiv:1301.2491.
- Kapildeb Dolui, Xi Zhu, Haibin Su, and Stefano Sanvito, *Electrically driven magnetism in triangular nanocluster of MoS_2 and BN*, (manuscript in prepration)
- Kapildeb Dolui, Ivan Rungger, Chaitanya Das Pemmaraju, and Stefano Sanvito *Ab-initio study on the possible doping strategies for MoS_2 monolayers*, (submitted to PRB, arXiv:1304.8056).
- Kapildeb Dolui and Stefano Sanvito, *Ab-initio study of the electronic properties of oxygen doped TiS_2 monolayers* (manuscript in prepration)
- Kapildeb Dolui and Stefano Sanvito, *Effect of dimensionality on phonon properties of TiS_2* (In prepration)

Bibliography

[1] M. A. Topinka, B. J. LeRoy, R. M. Westervelt, S. E. J. Shaw, R. Fleischmann, E. J. Heller, K. D. Maranowski and A. C. Gossard, Nature **410**, 183 (2001).

[2] G. E. Moore, Electronics **38**, 8 (1965).

[3] F. Schwierz, H. Wong, and J.J. Liou, *Nanometer CMOS* (Pan Standford 2010).

[4] I. Appelbaum, B. Huang, and D. J. Monsma, Nature **447**, 295 (2007).

[5] S. M. Goodnick and J. Bird, IEEE Transactions on Nanotechnology **2**, 368 (2003).

[6] F. Schwierz, Nature Nanotechnology **6**, 135 (2011).

[7] P. Avouris, Z. Chen, and V. Perebeinos , Nature Nanotech. **2**, 605 (2007).

[8] D. S. Hecht, L. Hu, and G. Irvin, Adv. Mater. **23**, 1482 (2011).

[9] G. L. Brennecka, J. F. Ihlefeld, J.-P. Maria, B. A. Tuttle, P. G. Clem, J. Am. Ceram. Soc. **93**, 3935 (2010).

[10] R. P. Ortiz, A. Facchetti, and T. J. Marks, Chem. Rev. **110**, 205 (2010).

[11] P. Barber, S. Balasubramanian, Y. Anguchamy, S. Gong, A. Wibowo, H. Gao, H. J. Ploehn, and H. -C. zur Loye, Materials **2**, 1697 (2009).

[12] A. I. Kingon, J. P. Maria, and S. K. Streiffer, Nature **406**, 1032 (2000).

[13] S. K. Kim, S. W. Lee, J. H. Han, B. Lee, S. Han, and C. S. Hwang, Adv. Funct. Mater. **20**, 2989 (2010).

[14] J. -H. Lee, J. Wu, and J. C. Grossman, Phys. Rev. Lett. **104**, 016602 (2010).

[15] N. Nakpathomkun, H. Q. Xu, and H. Linke, Phys. Rev. B **82**, 235428 (2010).

[16] Z. Ma , K. Zhang , J. -H. Seoa, H. Zhoua, L. Suna, H. -C. Yuana, G. Qina, H. Panga and W. Zhou, ECS Transactions **34**, 137 (2011).

[17] T. Zhai, X. Fang, M. Liao, X. Xu, H. Zeng, B. Yoshio, and D. Golberg, Sensors **9**, 6504 (2009).

[18] Zhong Lin Wang, J. Phys.: Condens. Matter **16**, R829 (2004).

[19] M. Osada and T. Sasaki, Adv. Mater. **24**, 210 (2012).

[20] Y. W. Heo, D. P. Norton, and S. J. Pearton, J. Appl. Phys. **98**, 073502 (2005).

[21] D. C. Look, J. Elec. Mater. **35**, 1299 (2006).

[22] S. J. Tans, A. R. M. Verschueren, and C. Dekker, Nature **393**, 49 (1998).

[23] T. Durkop, S. A. Getty, E. Cobas, and M. S. Fuhrer, Nano Lett. **4**, 35 (2004).

[24] A. Javey, H. Kim, M. Brink, Q. Wang, A. Ural, J. Guo, P. McIntyre, P. McEuen, M. Lundstrom, H. J. Dai, Nat. Mater. **1**, 241 (2002).

[25] R. Seidel, A. P. Graham, E. Unger, G. S. Duesberg, M. Liebau, W. Steinhoegl, W. Pamler, and F. Kreupl, *Nanotechnology, 2004. 4th IEEE Conference* **2004**, 7.

[26] Z. Wu, Z. Chen, X. Du, J. M. Logan, J. Sippel, M. Nikolou, K. Kamaras, J. R. Reynolds, D. B. Tanner, A. F. Hebard, and A. G. Rinzler, Science **305**, 5688 (2004).

[27] J. H. Burroughes, D. D. C. Bradley, A. R. Brown, R. N. Marks, K. Mackay, R. H. Friend, P. L. Burns, and A. B. Holmes, Nature **347**, 539 (1990).

[28] J. J. M. Halls, C. A. Walsh, N. C. Greenham, E. A. Marseglia, R. H. Friend, S. C. Moratti, and A. B. Holmes, Nature **376**, 498 (2002).

[29] L. Schmidt-Mende, A. Fechtenkötter, K. Müllen, E. Moons, R. H. Friend, J. D. MacKenzie, Science **293**, 1119 (2001).

[30] N. Stutzmann, R. H. Friend, H. Sirringhaus, Science **299**, 1881 (2003).

[31] L. -L Chua, J. Zaumseil, J. -F. Chang, E. C.-W. Ou, P. K.-H. Ho, H. Sirringhaus, and R. H. Friend, Nature **434**, 194 (2005).

[32] D. G. Lidzey, D. D. C. Bradley, S. F. Alvarado, and P. F. Seidler, Nature **386**, 135 (1997).

[33] A. H. Castro Neto, F. Guinea, N. M. R. Peres, K. S. Novoselov and A. K. Geim, Rev. Mod. Phys. **81**, 109 (2009).

[34] K. F. Mak, M. Y. Sfeir, Y. Wu, C. H. Lui, J. A. Misewich, and T. F. Heinz, Phys. Rev. Lett. **101**, 196405 (2008).

[35] S. Chen, Q. Wu, C. Mishra, J. Kang, H. Zhang, K. Cho, W. Cai, A. A. Balandin and R. S. Ruoff, Nature Materials **11**, 203 (2012).

[36] K. S. Novoselov, A. K. Geim, S. V. Morozov, D. Jiang, Y. Zhang, S. V. Dubonos, I. V. Gregorieva, and A. A. Firsov, Science **306**, 666 (2004).

[37] D. C. Elias *et al.* Nature Physics **7**, 701 (2011).

[38] M. Y. Han, B. Ozyilmaz, Y. Zhang, and P. Kim, Phys. Rev. Lett. **98**, 026805 (2007).

[39] A. Klekachev, M. Cantoro, A. Nourbakhsh, M. H. van der Veen, F. Clemente, A.Stesmans, B. Sels, M. Heyns,a,d and S. De Gendt, ECS Transactions **19**, 201 (2009).

[40] W. Zhang, C.-T. Lin, K.-K. Liu, T. Tite, C.-Y. Su, C.-H. Chang, Y.-H. Lee, C.-W. Chu, K.-H. Wei, J.-L. Kuo, and L. -J. Li,ACS Nano **5**, 7517 (2011).

[41] http: //phycomp.technion.ac.il/~david/thesis/node3.html

[42] http: //www.azom.com/details.asp?articleid=1630

[43] http: //www.ele.uri.edu/Courses/ele533/mobility.html

[44] http://www.matweb.com/search/

[45] http: //en.wikipedia.org/wiki/Silicon

[46] http: //en.wikipedia.org/wiki/Boron_nitride

[47] http: //www.accuratus.com/boron.html

[48] K. Fives, I. T. McGovern, R. McGrath, R. Cimino, G. Hughes, A. McKinley and G. Thornton, J. Phys.: Condens. Matter **4**, 5639 (1992).

[49] R. Fivaz and E. Mooser, Phys. Rev. **163**, 3 (1967).

[50] O. El Beqqali, I. Zorkani, F. Rogemond, H . Chermette, R . Ben Chaabane, M . Gamoudi and G. Guiilaud, Synthetic Metals **90**, 165 (1997).

[51] V. Varshneya, S. S. Patnaikc, C. Muratorea, A. K. Roya, A. A. Voevodina and B. L. Farmer, Computational Materials Sc. **48**, 101 (2010).

[52] D. K. G. de Boer, C. F. van Bruggen, G. W. Bus, R. Coehoorn, C. Haas, G. A. Sawatzky, H. W. Myron, D. Norman, and H. Padmore, Phys. Rev. B **29**, 6797 (1984).

[53] M. M. May, C. Brabetz, C. Janowitz, and R. Manzke, Phys. Rev. Lett. 107, 176405 (2011).

[54] S. Nagata, T. Abe, S. Ebisu, Y. Ishihara, K. Tsutsumi, J. of Phys. and Chem. of Solids **54**, 895 (1993).

[55] D. S. Inosov, V. B. Zabolotnyy, D. V. Evtushinsky, A. A. Kordyuk, B. BÜchner, R. Follath, H Berger and S. V. Borisenko, New Journal Phys. **12**, 125027 (2008).

[56] K. Rossnagel, J. Phys.: Condens. Matter **23**, 213001 (2011).

[57] K. Watanabe, T. Taniguchi and H. Kanda, Nature Materials **3**, 404 (2004).

[58] Y. Chen, J. Zou, S. J. Campbell, and G. L. Caer, Appl. Phys. Lett. **84**, 2430 (2004).

[59] Q. Tang, Z. Zhou, and Z. Chen, J. Phys. Chem. C **115**, 18531 (2011).

[60] S. K. Misra, S. Satpathy, O. Jepson, J. Phys. Condens. Matter **9** 461 (1997).

[61] S. K. Bux, J.-P. Fleurial and R. B. Kaner, Chem. Commun. **46**, 8311 (2010).

[62] D. J. Vaughan and K. M. Rosso, Review in Mineralogy & Geochemistry **61**, 231 (2006).

[63] J.A. Wilson and A.D. Yoffe, Advances in Physics **18**, 193 (1969).

[64] E. A. MArseglia, Iternational Review in Physical Chemistry **3**, 177 (1983).

[65] R. H. Friend and A.D. Yoffe, Advances in Physics **36**, 1 (1987).

[66] Q. H. Wang, K. K. Zadeh, A. Kis, J. N. Coleman, and M. S. Strano, Nature Nanotechnology **7**, 699 (2012).

[67] Jonathan N. Coleman *et al.*, Science **331**, 568 (2011).

[68] A. Kuc, N. Zibouche, and T. Heine, Phys. Rev. B **83**, 245213 (2011).

[69] A. Splendiani, L. Sun, Y. Zhang, T. Li, J. Kim, C.-Y. Chim, G. Galli, and F. Wang, Nano Lett. **10**, 1271 (2010).

[70] H. R. Gutiérrez, N. Perea-Lpez, A. L. Elías, A. Berkdemir, B. Wang, R. Lv, F. López-Urías, V. H. Crespi, H. Terrones, M. Terrones, arXiv.org, arXiv:1208.1325

[71] S. Tongay, J. Zhou, C. Ataca, K. Lo, T. S. Matthews, J. Li, J. C. Grossman, and J. Wu, Nano Lett. **12**, 5576 (2012).

[72] H. S. Lee, S.-W. Min, Y.-G. Chang, M. K. Park, T. Nam, H. Kim, J. H. Kim, S. Ryu, and S. Im ,Nano Lett. **12**, 3695(2012)

[73] S. Alkis, T. özta, L. E. Aygün, F. Bozkurt, A. K. Okyay, and B. Ortaç, Optics Express **20**, 21815 (2012).

[74] C. Lee, H. Yan, L. E. Brus, T. F. Heinz, J. Hone, and S. Ryu, Acs Nano **4**, 2695 (2010).

[75] D. J. Late, B. Liu, H. S. S. R. Matte, C. N. R. Rao, and V. P. Dravid, Adv. Funct. Mater. **22**, 1894 (2012).

[76] Ondrej L. Krivanek *et al.*, Nature **464**, 571 (2010).

[77] I. Childres, L. A. Jauregui, M. Foxe, J. Tian, R. Jalilian, I. Jovanovic, Y. P. Chen, Appl. Phys. Lett. **97**, 173109 (2010).

[78] M. M. Benameur, B. Radisavljevic, J. S. Héron, S. Sahoo, H. Berger, and A. Kis, Nanotechnology **22**, 125706 (2011).

[79] H. Li, Q. Zhang, C. C. R. Yap, B. Kang Tay1, T. H. T. Edwin, A. Olivier, D. Baillargeat, Adv. Funct. Mater. **22**, 1385 (2012).

[80] J. Kibsgaard, A. Tuxen, M. Levisen, E. Lægsgaard, S. Gemming, G. Seifert, J. V. Lauritsen, and F. Besenbacher, Nano Lett.**8**, 3928 (2008).

[81] Q. Li, J. T. Newberg, E. C. Walter, J. C. Hemminger, and R. M. Penner, Nano Lett. **4**, 277 (2004).

[82] Z. Liu, K. Suenaga, Z. Wang, Z. shi, E. Okunishi, and S. Iijima, Nature Communication 2:213 doi:10.1038/ncomms1224 (2011)

[83] X. Wu, Z. Xu, and X. C. Zeng, Nano Lett. **7**, 2987 (2007).

[84] A. Kis, D. Mihailovic, M. Remskar, A. Mrzel, A. Jesih, I. Piwonski, A. J. Kulik, W. Benoît, L. Forró, Adv. Mater. **15**, 733 (2003).

[85] J.V. Lauritsen and F. Besenbacher, Adv. Catal. **50**, 97 (2006).

[86] M. A. Albiter, R. Huirache-Acuña, F. Paraguay-Delgado, J. L. Rico and G. Alonso-Nuñez, Nanotechnology **17**, 3473 (2006).

[87] X. L. Li, *One dimensional metal oxides and sulfides nanomaterials: Sythesis, characterization and their properties*, Beijing Tsinghua University, 2005.

[88] A. Albu-Yaron *et al.*, Angew. Chem. Int. Ed. **50**, 1 (2011).

[89] R. Tenne and M. Redlich, Chem. Soc. Rev. **39**, 1423 (2010).

[90] F. Rosei, J. Phys.: Condens. Matter **16**, S1373 (2004).

[91] A. Logadottir, P. G. Moses, B. Hinnemann, N.-Y. Topsøe,K. G. Knudsen, H. Topsøe, J. K. Nørskov, Catalysis Today **111**, 44 (2006).

[92] F. Besenbacher, M. Brorson, B.S. Clausen, S. Helveg, B. Hinnemann, J. Kibsgaard, J. V. Lauritsen, P.G. Moses, J.K. Nørskov c, H. Topsøe, Catalysis Today **130**, 86 (2008).

[93] E. Merzbacher, *Quantum Mechanics* (John Wiley & Sons Inc., New York, 1998).

[94] R. G. Parr and W. Yang, *Density Functional Theory of Atoms and Molecules*, Oxford University Press, Oxford (UK), 1989.

[95] David J. Griffiths, *Introduction to Quantum Mechanics*, 2nd Edition, Pearson Education (Singapore) Pte. Ltd., 2005.

[96] A. Szabo and N. S. Ostlund, *Modern Quantum Chemistry* (Dover publications Inc., New York, USA, 1996).

[97] P. Hohenberg and W. Kohn, Phys. Rev. **136**, B864 (1964).

[98] W. Kohn and L. Sham, Phys. Rev. **140**, A1133 (1965).

[99] D. M. Ceperley and B. J. Alder, Phys. Rev. Lett. **45**, 566 (1980).

[100] S. H. Vosko, L. Wilk, and M. Nusair, Can. J. Phys. **58**, 1200 (1980).

[101] J. P. Perdew, K. Burke, and M. Ernzerhof, Phys. Rev. B **45**, 13244 (1992).

[102] J. P. Perdew, K. Burke and M. Ernzerhof, Phys. Rev. Lett. **77**, 3865 (1996).

[103] J. P. Perdew, Phys. Rev. B **33**, 8822 (1986).

[104] A. D. Becke, Phys. Rev. A **38**, 3098 (1988).

[105] C. Lee, W. Yang and R. G. Parr, Phys. Rev. B **37**, 785 (1988).

[106] B. Miehlich, A. Savin, H. Stoll and H. Preuss, Chem. Phys. Lett. **157**, 200 (1989).

[107] J. Harris and R. O. Jones, J. Phys. F: Met. Phys. **4**, 1170 (1974).

[108] D. C. Langreth and J. P Perdew, Phys. Rev. B **15**, 2884 (1977).

[109] J. Heyd, G. E. Scuseria, and M. Ernzerhof, J. Chem. Phys. **124**, 219906 (2006).

[110] Hal Tasaki, J. Phys.: Condens. Matter **10**, 4353-4378 (1998).

[111] V. I. Anisimov, J. Zaanen, and O. K. Andersen, Phys. Rev. B **44**, 943 (1991).

[112] V. I. Anisimov, I. V. Solovyev, M. A. Korotin, M. T. Czyzyk, and G. A. Sawatzky,Phys. Rev. B **48**, 16929 (1993).

[113] A. I. Lichtenstein, J. Zaanen, and V. I. Anisimov, Phys. Rev. B **52**, R5467 (1995).

[114] M. Cococcioni and S. de Gironcoli, Phys. Rev. B **71**, 035105 (1996).

[115] S. L. Durarev, G. A. Botton, S. Y.Savrasov. C. L. Humphreys, and A. P. Sutton, Phys. Rev. B **50**, 16861 (1998).

[116] J. P. Perdew and A. Zunger, Phys. Rev. B **23**, 5048 (1981).

[117] M. Stengel and N. A. Spaldin. Phys. Rev. B **77**, 155106 (2008).

[118] D. Vogel, P. Krüger, and J. Pollmann, Phys. Rev. B **54**, 5495 (1996).

[119] C. D. Pemmaraju, T. Archer, D. Snchez-Portal, and S. Sanvito, Phys. Rev. B **75**, 045101 (2007).

[120] A. Filippetti and N. A. Spaldin, Phys. Rev. B **67**, 125109 (2003).

[121] T. Archer, C. D. Pemmaraju, S. Sanvito, C. Franchini, J. He, A. Filippetti, P. Delugas, D. Puggioni, V. Fiorentini, R. Tiwari, and P. Majumdar, Phys. Rev. B **84**, 115114 (2011).

[122] A. Droghetti, C. D. Pemmaraju, and S. Sanvito, Phys. Rev. B **81**, 092403 (2010).

[123] C. D. Pemmaraju, I. Rungger, X. Chen, A. R. Rocha, and S. Sanvito, Phys. Rev. B **82**, 125426 (2010).

[124] R. M. Martin, *Electronic Structure: Basic Theory and Practical Methods,* Cambridge University Press, Cambridge UK (2004).

[125] J. M. Soler, E. Artacho, J. D. Gale, A. García, J. Junquera, P. Ordejón, and D. Sánchez-Porta, J. Phys.: Condense Matter **14**, 2745 (2002).

[126] W. H. Press, B. P. Flsnnery, S. A. Teukolsky, and W. T. Vetterling, NUmerical Recipes in Fortran (Camebridge University Press, Cambridge (UK), 1992), 2nd. Ed.,URL http://library.lanl.gov/numerical/bookfpdf.html.

[127] J. F. Janak, Phys. Rev. B **18**, 7165 (1978).

[128] J. P. Perdew and M. Levy, Phys. Rev. B **56**, 16021 (1997).

[129] L. J Sham and M. Schlünter, Phys. Rev. Lett. **51**, 1888 (1983).

[130] Carsten A. Ullrich, *Time-Dependent Density-Functional Theory: Concepts and Applications.* Oxford University Press.

[131] F. J Himpsel, Adv. Phys. **32**, 1 (1983).

[132] N. V. Smith, Rep. Prog. Phys. **51**,1227 (1988).

[133] L. Heldin Phys. Rev. **139**, A796 (1965).

[134] Patrick Rinke, Abdallah Qteish, Jörg Neugebauer, Christoph Freysoldt and Matthias Scheffle, New J. Phys. **7**, 126 (2005).

[135] R. Sakuma, C. Friedrich, T. Miyake, S. Blügel, and F. Aryasetiawan, Phys. Rev. B **84**, 085144 (2011).

[136] F. Aryasetiawan and O. Gunnarsson **61**, Rep. Prog. Phys. 237-312 (1998).

[137] F. Aryasetiawan and S. Biermann, Phys. Rev. Lett. **100**, 116402 (2008).

[138] J. P. Perdew and S. Kurth, (Sringer, Berlin, 1998), vol. 500 of Lecture Notes in Physics.

[139] S. Yu. Savrasovt, Phys. Rev. Lett. **69**, 2819 (1992).

[140] Stefano Baroni, Stefano de Gironcoli, Andrea Dal Corso, Paolo Giannozzi, Review of Modern Physics **73**, 515 (2001).

[141] N. W. Ashcroft and N. D. Mermin, *Solid State Physics*, Saunders College Publishing, Olland, 1986.

[142] D. R. Hamann, M. Schlüter, and C. Chiang, Phys. Rev. Lett. **43**, 1494-1497 (1979).

[143] L. Kleinman and D. M. Bylander, Phys. Rev. Lett. **48**, 1425 (1982).

[144] D. Vanderbilt, Phys. Rev. B **41**, 7892 (1990).

[145] G. Kresse and J. Hafner, J. Phys. Condens Matter **6**, 8245 (1994).

[146] S. G. Louie, S. Froyen, and M. L. Cohen, Phys. Rev. B **26**, 1738 (1982).

[147] P. E. Blöchl, Phys. Rev. B **50**, 17953 (1994).

[148] G. Kresse, D. Joubert, Phys. Rev. B **59**, 1758 (1999).

[149] D. J. Singh, Plane Waves, Pseudopotential and the LAPW Method, Kluwer Academic, Norwell, MA, 1994.

[150] Jürgen Hafner, J. Computatinal Chemistry **29**, 2044-2078 (2008).

[151] P. Giannozzi et al., J. Phys.: Condens. Matter **21** 395502 (2009); URL http://www.quantum-espresso.org

[152] K. K. Tiong and T. S. Shou, J. Phys.: Condens. Matter **12**, 5043 (2000).

[153] W.O. Winer, Wear **10**, 422 (1967).

[154] H. Topsøe, B. Hinnemann, J. K. Nørskov, J. V. Lauritsen, F. Besenbacher, P. L. Hansen, Glen Hytoft, R. G. Egeberg, and K. G. Knudsen, Catalysis Today **107**, 12 (2005).

[155] X. Fang, X. Guo, Y. Mao, C. Hua, L. Shen, Y. Hu, Z. Wang, F. Wu, and L. Chen, Chem. Asian J. **7**, 1013 (2012).

[156] R. B. Somoano and A. Rembaum, Phys. Rev. Lett. **27**, 402 (1971).

[157] Joh. A. Woollam and R. B. Somoano, Phys. Rev. B **13**, 3843 (1976).

[158] J. V. Lauritsen, J. Kibsgaard, S. Helveg, H. Topsøe, B. S. Clausen, E. Lægsgaard, and F. Besenbacher, Nature nanotechnology **2**, 53 (2007).

[159] Z. Yin, H. Li, H. Li, L. Jiang, Y. Shi, Y. Sun, G. Lu, Q. Zhang, X. Chen, and H. Zhang, Acs Nano **6**, 74 (2012).

[160] Q. H. Wang, K. Kalantar-Zadeh, A. Kis, J. N. Coleman, and M. S. Strano, Nature Nanotechnology **7**, 699 (2012).

[161] A. H. Castro Neto and K. Novoselov, Reports on Progress in Physics **74**, 082501 (2011).

[162] T. Takahashi, T. Takenobu, J. Takeya, and Y. Iwasa, Adv. Funct. Mater. **17**, 1623 (2007).

[163] X. Wang, Y. Ouyang, X. Li, H. Wang, J. Guo, and H. Dai, Phys. Rev. Lett. **100**, 206803 (2008).

[164] S. Y. Zhou, G.-H. Gweon, A. V. Fedorov, P. N. First, W. A. de Heer, D.-H. Lee, F. Guinea, A. H. Castro Neto, and A. Lanzara, Nature Materials **6**, 770 (2007).

[165] S. Adam, E. H. Hwang, V. M. Galitski, and S. Das Sarma, PNAS **104**, 18392 (2007).

[166] A. Ayari, E. Cobas, O. Ogundadegbe, and M. S. Fuhrer, Journal of Appl. Phys. **101**, 014507 (2007).

[167] L. Liu, S. B. Kumar, Y. Ouyang, and J. Guo, IEEE. Trans. Electron Devices **58**, 3042 (2011).

[168] K.-K. Liu, W. Zhang, Y.-H. Lee, Y.-C. Lin, M.-T. Chang, C.-Y. Su, C.-S. Chang, H. Li, Y. Shi, H. Zhang, C.-S. Lai, and L.-J. Li, Nano Lett. **12**, 1538 (2012).

[169] B. Radisavljevic, A. Radenovic, J. Brivio, V. Giacometti, and A. Kis, Nature nanotechnology **6**, 147 (2011).

[170] D. Lembke and A. Kis, ACS Nano **6**, 10070 (2012).

[171] D. Jena and A. Konar, Phys. Rev. Lett. **98**, 136805 (2007).

[172] K. F. Mak, C. Lee, J. Hone, J. Shan, and T. F. Heinz, Phys. Rev. Lett. **105**, 136805 (2010).

[173] Y.-H. Lee, X.-Q. Zhang, W. Zhang, M.-T. Chang, C.-T. Lin, K.-D. Chang, Y.-C. Yu, J. T.-W. Wang, C.-S. Chang, L.-J. Li, and T.-W. Lin, Adv. Mater. **24**, 2320 (2012).

[174] H. Li, Gang Lu, Z. Yin, Q. He, H. Li, Q. Zhang, H. Zhan, Small **8**, 682 (2012).

[175] Z. Zeng, Z. Yin, X. Huang, H. Li, Q. He, G. Lu, F. Boey, and H. Zhang, Angew. Chem. Int. Ed. **50**, 11093 (2011).

[176] Y. Zhan, Z. Liu, S. Najmaei, P. M. Ajayan, and J. Lou, Small **8**, 966 (2012).

[177] C. Ataca and S. Ciraci, J. Phys. Chem. C **115**, 13303 (2011).

[178] Javier D. Fuhr, Andrés Saúl, and Jorge O. Sofo, Phys. Rev . Lett. **92**, 026802 (2004).

[179] J. He, K. Wu, R. Sa, Qiaohong Li, and Y. Wei, Applied Phys. Lett. **96**, 082504 (2010).

[180] H. Ji, J. Wei, and D. Natelson, Nano Lett. **12**, 2988 (2012).

[181] Y. Zhang, J. Ye, Y. Matsuhashi, and Y. Iwasa, Nano Lett. **12**, 1136 (2012).

[182] A. E Somers, P. C. Howlett, D. R. MacFarlane, and M. Forsyth, Lubricants **1**, 3 (2013).

[183] N. Han, F. Wang, J. J. Hou, F. Xiu, S. Yip, A. T. Hui, T. Hung, and J. C. Ho, Acs Nano **6**, 4428 (2012).

[184] P. Joshi, H. E. Romero, A. T. Neal, V. K. Toutam, and S. A. Tadigadapa, J. Phys.: Condens. Matter **22**, 334214 (2010).

[185] T. O. Wehling, A. I. Lichtenstein, and I. Katsnelson, Applied Phys. Lett. **93**, 202110 (2008).

[186] S. Ghatak, Atindra Nath Pal, and Arindam Ghosh, Acs Nano **5**, 7707 (2011).

[187] H. Liu, J. Gu, and P. D. Ye, IEEE Electron Device Lett. **33**, 1273 (2012).

[188] D. C. Look, J. W. Hemsky, and J. R. Sizelove, Phys. Rev. Lett. **82**, 2552 (1999).

[189] C. V. de Walle and J. Neugebauer, J. Appl. Phys. **95**, 3851 (2004).

[190] M. V. Bollinger, K.W. Jacobsen, and J. K. Norskov, Phys. Rev. B **87**, 085410 (2003).

[191] J.P. Perdew and M. Levy, Phys. Rev. Lett. **51**, 1884 (1983).

[192] P.A.G. O'Hare, B. M. Lewis and B.A. parkinson, The Journal of Chemical Thermodynamics **20**, 681 (1988).

[193] D. M Ceperly and B. J. Alder, Phys. Rev. Lett. **45**, 566 (1980).

[194] N. Troullier and J. L. Martins, Phys. Rev. B **43**, 1993 (1991).

[195] J. Junquera, Óscar Paz, D. Sánchez-Portal, and E. Artacho, Phys. Rev. B **64**, 235111 (2001).

[196] P. E. Blø̈chl, Phys. Rev. B 50, 17953 (1994).

[197] G. Kresse and J. Furthmüller, Phys. Rev. B **54**, 11169 (1996).

[198] H. J. Monkhorst and J. D. Pack, Phys. Rev. B **13**, 5188 (1976).

[199] J. Heyd, G.E. Scuseria and M. Ernzerhof, J. Chem. Phys. **118**, 8207 (2003); J. Heyd, G.E. Scuseria and M. Ernzerhof, J. Chem. Phys. **124**, 219906 (2006).

[200] Th. Böker, R. Severin, A. Müller, C. Janowitz, R. ManzkeD, Voess, P. Krüger, A. Mazur, J. Pollmann, Phys. Rev. B **64**, 235305 (2001).

[201] K. Fives, I. T. McGovern, R. McGrath, R. Cimino, G. Hughes, A. McKinley, G. Thornton, J. Phys.: Condens. Matter **4**, 5639 (1992).

[202] K. Kobayashi and J. Yamauchi, Phys. Rev. B **51**, 17085 (1995).

[203] S. Helveg, J. V. Lauritsen, E. Lægsgaard, I. Stensgaard, J. K. Nørskov, B. S. Clausen, H. Topsøe, F. Besenbacher, Phys. Rev. Lett. **84**, 951 (2000).

[204] S. W. Han, H. Kwon, S. K. Kim, S. Ryu, W. S. Yun, D. H. Kim, J. H. Hwang, J. S. Kang, J. Baik, H. J. Shin, and S. C. Hong, Phys. Rev. B **84**, 045409 (2011).

[205] T. Li and G. Galli, J. Phys. Chem. C **111**, 16192 (2007).

[206] H.-P. Komsa, J. Kotakoski, S. Kurasch, O. Lehtinen, U. Kaiser, and A. V. Krasheninnikov, Phys. Rev. Lett. **109**, 035503 (2012).

[207] F. L. Deepak, R. P. Biro, Y. Feldman, H. Cohen, A. Enyashin, G. Seifert, and R. Tenne, Chem. Asian J. **3**, 1568 (2008).

[208] K. K. Tiong, P.C. Liao , C.H. Ho, and Y.S. Huang, J. of Crystal Growth **205**, 543 (1999)

[209] V. V. Ivanovskaya, A. Zobelli, A. Gloter, N. Brun, V. Serin, and C. Colliex, Phys. Rev. B **78**, 134104 (2008).

[210] F. L. Deepak *et. al*, J. Am. Chem. Soc **129**, 12549 (2007).

[211] S. Mathew, K. Gopinadhan, T. K. Chan, X. J. Yu, D. Zhan, L. Cao, A. Rusydi, M. B. H. Breese, S. Dhar, Z. X. Shen, T. Venkatesan, and John T. L. Thong, Appl. Phys. Lett. **101**, 102103 (2012).

[212] K. T. Park, J. S. Hess, and K. Klier, Journal of Chem. Phys. **111**, 1636 (1999).

[213] K. Ueno, H. Shimotani, Y. Iwasa, and M. Kawasaki, Appl. Phys. Lett. **96**, 252170 (2010).

[214] S.-J. Xu, J. M. Nilles, J. H. Hendricks, S. A. Lyapustina and K. H. Bowen, J. of Chemical Phys. **117**, 5742 (2002).

[215] C. Paduani and P. Jena, J. Nanopart. Res. **14** 1035 (2012).

[216] S. Das, H.-Y. Chen, A. V. Penumatcha, and J. Appenzeller, Nano Lett. **13**, 100 (2013).

[217] K. T. Park and J. Kong, Topics in Catalysis **18**, 175 (2002).

[218] R. H Friend and A. D. Yoffe, Advance in Physics **36**, 1 (1987).

[219] H.T. Yuan, M. Tih, K. Morimoto, W. Tan , F. Wei, H. Shimotani, Ch. Kloc, and Y. Iwasa, Appl. Phys. Lett. **98**, 012102 (2011).

[220] K. Ueno, S. Nakamura, H. Shimotani, H. T. Yuan, N. Kimura, T. Nojima, H. Aoki, Y. Iwasa, and M. Kawasaki, Nature Nanotechnology **6**, 408 (2011).

[221] J. Pu, Y. Yomogida, K.-K. Liu, L.-J. Li, Y. Iwasa, and T. Takenobu, Nano Lett. **12**, 4013 (2012).

[222] Kapildeb Dolui, Ivan Rungger, Stefano Sanvito, arXiv:1301.2491

[223] W. S. Yun, S. W. Han, S. C. Hong, I. G. Kim, and J. D. Lee, Phys. Rev. B **85**, 033305 (2012).

[224] J. P. Perdew, K. Burke, and M. Ernzerhof, Phys. Rev. Lett. **77**, 3865 (1996).

[225] N. Troullier and J. L. Martins, Phys. Rev. B **43**, 1993 (1991).

[226] S. Sanvito and C.D. Pemmaraju, Phys. Rev. Lett. **102**, 159701 (2009).

[227] A. Zunger, S. Lany and H. Raebiger, Physics **3**, 53 (2010).

[228] A. Droghetti, C.D. Pemmaraju and S. Sanvito, Phys. Rev. B **78**, 140404(R) (2008).

[229] C.D. Pemmaraju, T. Archer, and D. Sánchez-Portal and S. Sanvito, Phys. Rev. B. **75**, 045101 (2007).

[230] A. Filippetti, C.D. Pemmaraju, S. Sanvito, P. Delugas, D. Puggioni and V. Fiorentini, Phys. Rev. B **84**, 195127 (2011).

[231] A. Droghetti and S. Sanvito, Appl. Phys. Lett. **94**, 252505 (2009).

[232] C.D. Pemmaraju, R. Hanafin, T. Archer, H.B. Braun and S. Sanvito, Phys. Rev. B **78**, 054428 (2008).

[233] K. Nagashio, T. Yamashita, T. Nishimura, K. Kita, and A. Toriumi, Journal of Appl. Phys. **110**, 024513 (2011).

[234] N. T. Cuong, M. Otani, and S. Okada, Phys. Rev. Lett. **106**, 106801 (2011).

[235] T. Björkman, A. Gulans, A.V. Krasheninnikov and R. M. Nieminen, Phys. Rev. Lett.**108**, 235502 (2012).

[236] C. Ataca, M. Topsakal, E. Akturk, and S. Ciraci, J. Phys. Chem. C **115**, 16354 (2011).

[237] J. Robertson and B. Falabretti, J. Appl. Phys. **100**, 014111 (2006).

[238] Narain Arora, *Mosfet Modeling For VLSI Simulation*, World Scientific Publishing Co. Pte. Ltd 2007, pp 128-129.

[239] R. A. McKee, F. J. Walker, and M. F. Chisholm, Science **293**, 468 (2001); Y.-W. Tan, Y. Zhang, K. Bolotin, Y. Zhao, S. Adam, E. H. Hwang, S. DasSarma, H. L. Stormer and P. Kim, Phys. Rev. Lett. **99**, 246803 (2007); K. Nagashio, T. Yamashita, T. Nishimura, K. Kita, and A. Toriumi, J. Appl. Phys. **110**, 024513 (2011).

[240] Horacio E. Bergna, *The Colloid Chemistry of Silica*, Advances in Chemistry, Vol. 234 chapter 1, pp 1-47 (1994)

[241] M. Stapelbroek, D. L. Griscom, E. J. Friebele, and G.H. Sigel, J. Non-Crystalline Solids **32**, 313 (1979).

[242] B. El-Kareh, *Fundamentals of Semiconductor Processing Technologies.* Norwell: Kluwer Academic Publishers, 1995.

[243] A. Ramasubramaniam, Phys. Rev. B **86**, 115409 (2012).

[244] T. Cheiwchanchamnangij and W.R.L. Lambrecht, Phys. Rev. B **85**, 205302 (2012).

[245] Y. Xia, P. Yang, Y. Sun, Y. Wu, B. Mayers, B. Gates, Y. Yin, F. Kim, H. Yan, Adv. Mat. **15**, 353 (2003).

[246] X. Wang X and Y. Li, Inorg. Chem. **45**, 7522 (2006).

[247] F. Cerrina and C. Marrian, MRS Bull. **21**, 56 (1996).

[248] J. M. Gibson, Phys. Today **50**, 56 (1997).

[249] S. Matsui and Y. Ochiai, Nanotechnology **7**, 247 (1996).

[250] M. D. Levenson, P. J. Silverman, R. George, S. Wittekoek, P. Ware, C. Sparkes, L. Thompson, P. Bischoff, A. Dickinson, and J. Shamaly, Solid State Technol.**38**, 81 (1995).

[251] H. S. Nalwa, *Handbook of Nanostructured Materials and Nano-technology*, Eds.; Academic Press: New York, 2000.

[252] X. Duan, C. Niu, V. Sahi, J. Chen, J. Wallace Parce, S. Empedocles, and J. L. Goldman, Nature **425**, 274 (2003).

[253] K. Nakada, M. Fujita, G. Dresselhaus, M. S. Dresselhaus, Phys. Rev. B **54**, 17954 (1996).

[254] K. Wakabayashi, M. Fujita, H. Ajiki and M. Sigrist, Phys. Rev. B **59**, 8271 (1999).

[255] Y. Ding, Y. Wang, and J. Ni, Appl. Phys. Lett. **94**, 073111 (2009).

[256] X. Luo, J. Yang, H. Liu, X. Wu, Y. Wang, Y. Ma, S.-H Wei, X. Gong and H. Xiang, J. Am. Chem. Soc. **133**, 16285 (2011).

[257] C.-H. Park and S. G. Louie, Nano Lett. **8**, 2200 (2008).

[258] V. Barone and J.E. Peralta, Nano Lett. **8**, 2210 (2008).

[259] K.J Erickson, A.L. Gibb, A. Sinitskii, M. Rousseas, N. Alem, J. M. Tour, and A. K. Zettl, Nano Lett. **11**, 3221 (2011).

[260] Z.W. Pan, Z.R. Dai, and Z.L.Wang, Science **291**, 1947 (2001).

[261] A. R. Botello-Méndez, M. T. Martínez-Martínez, F. López-Urías, M. Terrones and H. Terrones, Chem. Phys. Lett. **448**, 258 (2007).

[262] L. Kou, C. Li, Z. Zhang, and W. Guo, ACS Nano **4**, 2124 (2010).

[263] W. Shi, H. Peng, N. Wang, C. P. Li, L. Xu, C. S. Lee, R. Kalish, and S.-T. Lee, J. Am. Chem. Soc. **123**, 11095 (2001).

[264] Y. Ding and J. Ni, Appl. Phys. Lett. **95**, 083115 (2009).

[265] F. Zheng, G. Zhou, Z. Liu, J. Wu, W. Duan, B.-L. Gu, and S. B. Zhang, Phys. Rev. B **78**, 205415 (2008).

[266] A. P. Alivisatos, Science **271**, 933 (1996).

[267] N. Yang, W. E. Angerer, and A. G. Yodh, Phys. Rev. **64**, 045801 (2001).

[268] D. J. Norris and M.G. Bawendi, Phys. Rev. B **53**, 16338 (1996).

[269] A. Srivastava and K. B. Eisenthal, Chem. Phys. Lett. **292**, 345 (1998).

[270] Victor I. Klimov, *Nanocrystal Quantum Dots*, Second edition, CRC press, Page 236.

[271] H. Weller, Angew. Chem. Int. Ed. Engl. **105**, 41 (1993).

[272] Y.-W. Son, M. L. Cohen, and Steven G. Louie, Nature **444**, 347 (2006).

[273] L. A. Agapito, N. Kioussis, and E. Kaxiras, Phys. Rev. B **82**, 201411 (2010).

[274] M. Nath, A. Govindaraj, and C. N. R. Rao, Adv. Mater. 2001, **13**, 283 (2001).

[275] Q. Li, E. C. Walter, W. E. van der Veer, B. J. Murray, J. T. Newberg, E. W. Bohannan, J. A. Switzer, J. C. Hemminger, and R. M. Penner,J. Phys. Chem. B **109**, 3169 (2005).

[276] Y. Sun, S. Wang, and Qiongsheng, Front. Chem. China **4**, 173 (2009).

[277] J. V. Lauritsen, J. Kibsgaard, S. Helveg, H. Topsøe, B. S. Clausen, E. Lægsgaard, F. Besenbacher, Nature Nanotechnology. **2**, 53 (2007).

[278] J. V. Lauritsen, J. Kibsgaard, G. H. Olesen, P. G. Moses, B. Hinnemann, S. Helveg, J. K. Nørskov, B. S. Clausen, H. Topsøe, E. Lægsgaard, F. Besenbacher, J. Catal. **249**, 220 (2007).

[279] M. Chhowalla and G. A. J. Amaratunga, Nature **407**, 164 (2000)

[280] A. J. Du, Z. H. Zhu, Y. Chen, G. Q. Lu, S. C. Smith, Chem. Phys. Lett. **469**, 183 (2009).

[281] Z. Liu, K. Suenaga, Z. Wang, Z. shi, E. okunishi and S. Iijima, Nat. Commun. 2:213 doi:10.1038/ncomms1224 (2011)

[282] Ç. ö. Girit, J. C. Meyer, R. Erni, M. D. Rossell, C. Kisielowski, L. Yang, C.-H. Park, M. F. Crommie, M. L. Cohen, S. G. Louie, and A. Zettl, Scicence **323** 1705 (2009).

[283] X. Liu, T. Xu, X. Wu, Z. Zhang, J. Yu, H. Qiu, J.-H. Hong, C.-H. Jin, J.-X. Li, X.-R. Wang, L.-T. Sun and W. Guo,Nat. Commun. 4:1776 doi: 10.1038/ncomms2803 (2013).

[284] Xing-zhao Dinga, X.T. Zenga, X.Y. Heb, and Z. Chen, Surface and Coatings Technology **205**, 224 (2010).

[285] D. O. Dumcenco, H. Kobayashi, Z. Liu, Y.-S. Huang and K. Suenaga, Nature Communications 4, 1351 (2013) [doi:10.1038/ncomms2351]

[286] S. Iijima, Nature (London) **354**, 56-58 (1991).

[287] Hamada N.; Sawada S.; Oshiyama A., Phys. Rev. Lett. **68**, 1579-1782 (1992).

[288] Li Y.; Zhou Z.; Zhang S.; Chen Z., J. Am. Chem. Soc. **130**, 16739 (2008).

[289] L. Kou, C. Tang, Y. Zhang, T. Heine, C. Chen, and T. Frauenheim, Journal of Physical Chemistry Lett., **3**, 2934 (2012)

[290] Z. Wang *et al.*, J. Am. Chem. Soc. **132**, 13840-13847 (2010).

[291] A. A. Avetisyan, B. Partoens, F. M. Peeters, Phys. Rev. B **79**, 035421 (2009).

[292] C. F. Hart, Phys. Rev. B **38**, 2158 (1988).

[293] J. O'Keeffe, C. Y. Wei, K. J. Cho, Appl. Phys. Lett. **80**, 676 (2002).

[294] Z. Zhang, W. Guo, Phys. Rev. B **2008**, 77, 075403.

[295] S. W. Han *et al.*, Phys. Rev. B **2011**, 84, 045409.

[296] K.S Novoselov, E. McCann, S.V. Morozov, V. I. Fal'ko, M. I. Katsnelson, U. Zeitler, S. Jiang, F. Schedin, A. K. Geim, Nature Physics, **2**, 177-180 (2006).

[297] A. Ramasubramaniam, D. Naveh E. Towe, Phys. Rev. B **84**, 205325 (2011).

[298] E. C. Stoner, Proc. R. Soc. London Ser. A **169**, 339 (1939).

[299] J. F. Janak, Phys. Rev. B **16**, 255 (1977)

[300] Stollhoff G.; Oles A.M.; Heine V., *Phys. Rev. B* **1990**, 41, 7028–7041.

[301] H. Schweiger, P. Raybaud, G. Kresse, and H. Toulhoat, J. Catal. **207**, 76-87 (2002).

[302] A. R. Botello-Méndez, F. López-Urás, M. Terrones, H. Terrones, Nanotech. **20**, 325703 (2009).

[303] C. Ataca, H. Sahin, E. Aktürk, and S. Ciraci, J. Phys. Chem. C **115**, 3934 (2011)

[304] K. Dolui, C. D. Pemmaraju, and S. Sanvito, ACS Nano **6**, 4823 (2012).

[305] *Group Theory and Qunatum Mechanics*, Michael Tinkham, MaGraw-Hill Inc., 1964 pp 71.

[306] H. Ishii *et al.*, Applied Physics Express **4**, 031501 (2011).

[307] http://en.wikipedia.org/wiki/Boronnitride

[308] V. T. Gasparis-Ebeling and H. Noth, Angew. Chem. Int. Ed. Engl. **23**, 303 (1984).

[309] M. Li *et al.*, Journal of materials Chemistry **19**, 8086-8091 (2009).

[310] K. K. Kim, A. Hsu, X. Jia, S. M. Kim, Y. Shi, M. Hofmann, D. Nezich, J. F. Rodriguez-Nieva, M. Dresselhaus, T. Palacios, and J. Kong, Nano Lett. **12**, 161 (2012).

[311] F. Zheng *et al.*, Phys. Rev. B **78**, 085423 (2008).

[312] S. Tarucha *et al.*, Phys. Rev. Lett. **77**, 3613 (1996).

[313] W. Hofstetter and G. Zarand, Phys. Rev. B **69**, 235301 (2004).

[314] M. Eto and Y. V. Nazarrov, Phys. Rev. B **64**, 085322 (2001).

[315] W. Hofstetter and H. Schoeller, Phys. Rev. Lett. **99**, 016803 (2002).

[316] M. S. Whittingham, Science **192**, 1126 (1976).

[317] E. A. Marseglia, International Reviews in Physical Chemistry **3**, 177 (1983).

[318] M. Inoue, H. P. Hughes and A.D. Yoffe, Advance in Physics **38**, 565 (1989).

[319] P. C. Klipstein and R. H. Friend, J . Phys. C : Solid State Phys. **17**, 2713 (1984).

[320] B. Liu, J. Yang, Y. Han, T. Hu, W. Ren, C. Liu, Y. Ma, and C. Gao, J. Appl. Phys. **109**, 053717 (2011).

[321] G. A. BeneshT, A. M. Woolley and C. Umrigar, J . Phys. C: Solid State Phys. **18**, 1595 (1985).

[322] Y. G. Yu and N. L. Ross, J. Phys.: Condens. Matter **23**, 055401 (2011).

[323] F. Yu, J.-X. Sun and Y.-H. Zhou, Solid State Science **12**, 1786 (2010).

[324] C. H. Chen, W. Fabian, F. C. Brown, K. C. Woo, B. Davies, B. DeLong, and A. H. Thompson, Phys. Rev. B **21**, 615 (1980).

[325] D. L. Greenaway and R. Nitsche, J. Phys. Chem. Solids **26**, 1445 (1965).

[326] R. H. Friend, D. Jerome, W. Y. Liang, C. Mikkelsen, and A. D. Yoffe, J. Phys. C **10**, L705 (1977).

[327] J. J. Barry, H. P. Hughes, P. C. Klipstein, and R. H. Friend, J. Phys. C **16**, 393 (1983).

[328] A. H. Thompson, K. R. Pisharody, and R. F. Koehler, Phys. Rev. Lett. **29**, 163 (1972).

[329] G. Lucovsky, R. M. White, J. A. Benda, and J. F. Revelli, Phys. Rev. B **7**, 3859 (1973).

[330] D. W. Fischer, Phys. Rev. B **8**, 3576 (1973).

[331] K. Kishiro, S. Takemoto, H. Kuriyaki and K. Hirakawa, Jpn. J. Appl. Phys. **33**, 1069 (1994).

[332] K. S. Chandra Babu and O. N. Srivastava, Cryst. Res. Technology **23**, 555 (1988).

[333] V. V. Plashnitsa, F. Viermeyer, N. Petchsang, P. Tongying, T. H. Kosel, and M. Kuno, J. Phys. Chem. Lett. **3**, 1554 (2012).

[334] K. H. Park, J. Choi, H. J. Kim, Dong.-H. Oh, J. R. Ahn, and S. U. Son, Small **4**, 945 (2008).

[335] E. E. Abbott, J. W. Kolis, N. D. Lowhorn, W. Sams, A. Rao, and T. M. Tritt, Appl. Phys. Lett. **88**, 261106 (2006).

[336] C. Wan, Y. Wang, N. Wang and K. Koumoto, Materials **3**, 2606 (2010).

[337] J. Zhang, X.Y. Qin, H.X. Xin, D. Li, and C.J. Song, Journal of Electronic Materials **40** (2011).

[338] J. A. Wilson, F. J. Disalvo and S. Mahajan, Phys. Rev. Lett. **32**, 882 (1974).

[339] Jasper van Wezel, Paul Nahai-Williamson, and Siddarth S. Saxena, Phys. Rev. B **81**, 165109 (2010)

[340] C. Monney, C. Battaglia, H. Cercellier, P. Aebi and H. Beck, Phys. Rev. Lett. **106**, 106404 (2011).

[341] O. Anderson, G. Karschnick, R. Manzke, and M. Skibowski, Solid State Communications **53**, 339 (1985).

[342] F. Weber, S. Rosenkranz, J.-P. Castellan, R. Osborn, R. Hott, R. Heid, K.-P. Bohnen, T. Egami, A. H. Said, and D. Reznik, Phys. Rev. Lett. **107**, 107403 (2011).

[343] N. E. Staley, J. Wu, P. Eklund, Y. Liu, L. Li and Z. Xu, Phys. Rev. B **80**, 184505 (2009).

[344] Z. Y. Wu, G. Ouvrard, S. Lemaux, P. Moreau, P. Gressier, F. Lemoigno, and J. Rouxel, Phys. Rev. Lett. **77**, 2101 (1996).

[345] C. Umrigar, D. E. Ellis, D. S. Wang, H. Krakauer, and M. Posternak, Phys. Rev. B **26**, 4935 (1982).

[346] C. M. Fang, R. A. de Groot, and C. Haas, Phys. Rev. B **56**, 4455 (1997).

[347] S. Sharma, T. Nautiyal, G. S. Singh, S. Auluck, P. Blaha, and C. Ambrosch-Draxl, Phys. Rev. B **59**, 14833 (1999).

[348] P. Krusius, J. Von Boehm, and H. Isomaki, J. Phys. C : Solid State Phys. **8**, 3788 (1975).

[349] J. C. Phillips, Phys. Rev. Lett. **28**, 1196 (1972).

[350] A. C. Kukkonen, W. J. Kaiser, E. M. Logothetis, B. J. Blumenstock, P. A. Schroeder, S. P. Faile, R. Colella, and J. Gambold,Phys. Rev. B **24**, 1691 (1981).

[351] Julia C. E. Rasch, T. Stemmler, B. Müller, L. Dudy and R. Manzke, Phys. Rev. Lett. **101**, 237602 (2008).

[352] Myron and A. J Freeman, Phys. Rev. B **9**, 481 (1974).

[353] D. W. Bullett, J. Phys. C: Solid State phys. **11**, 4501 (1978).

[354] A. Zunger and A. J. Freeman, Phys. Rev. B **16**, 906 (1977).

[355] G. Kresse and J. Furthmüller, Phys. Rev. B **54**, 11169, 1996.

[356] P. Giannozzi, S. Baroni, N. Bonini, M. Calandra, R. Car, C. Cavazzoni, D. Ceresoli, G. L. Chiarotti, M. Cococcioni, I. Dabo *et al.*, J. Phys.: Condens. Matter 21, 395502 (2009).

[357] K. Sánchez, P. Palacios, and P. Wahnón, Phys. Rev. B. **78**, 235121 (2008).

[358] R. Aksoy, E. Selvi, R Knudson, Y. Z. Ma, J. Phys. Condense. Matter. **21**, 025403 (2009).

[359] Z. Zeng, Z. Yin, X. Huang, H. Li, Q. He, G. Lu, F. Boey, and H. Zhang, Angew. Chem. Int. Ed. **50**, 11093 (2011).

[360] S. Jiménez Sandoval, and X. K. Chen, and J. C. Irwin, Phys. Rev. B **45**, 14347 (1992).

[361] V. V. Ivanovskaya, G. Seifert, and A. L. Ivanovskií, Semiconductors **39**, 1058 (2005).

[362] Y. Nishio, M. Shirai, Naoshi, and K. Motizuki, Journal of the Physical Society of Japan **63**, 156 (1994).

[363] J. A. Wilson, F. J. DiSalvo and S. Mahajan, Phys. Rev. Lett. **32**, 117 (1975).

[364] M. Calandra and F. Mauri, Phys. Rev. Lett. **106**, 196406 (2011).

[365] P. Goli , J. Khan , D. Wickramaratne , R. K. Lake , and A. A. Balandin, Nano Lett. **12**, 5941 (2012).

[366] F. Güller, C. Helman, A. M. Llois, Physica B **407**, 3188 (2012).

[367] Y. H. Lu, B. Xu, A. H. Zhang, M. Yang , and Y. P. Feng, J. Phys. Chem. C **115**, 18042 (2011).

[368] N. Erdman, O. Warschkow, M. Asta, K. R. Poeppelmeier, D. E. Ellis, and L. D. Marks, J. Am. Chem. Soc. **125**, 10050 (2003).

[369] D.M. Ceperly and B.J. Alder, Phys. Rev. Lett. **45**, 566 (1980).

[370] M. Scharli, and F. Lévy, Phys. Rev. B **33**, 4317 (1986).

[371] L. Venkataraman, J. E. Klare, C. Nuckolls, M. S. Hybertsen and M. L. Steigerwald, Nature (London) **442**, 904 (2006).

[372] M. Ishigami, J. D. Sau, S. Aloni, M. L. Cohen, and A. Zettl, Phys. Rev. Lett. **94**, 056804 (2005).

[373] G. Henkelman and H. Jónsson, J. Chem. Phys. 2000, **113**, 9978 (2000), G. Henkelman,B. Uberuaga, H. Jónsson, J. Chem. Phys. **113**, 9901 (2000).